



AKADEMIA GÓRNICZO - HUTNICZA
IM. STANISŁAWA STASZICA W KRAKOWIE

WYDZIAŁ FIZYKI I INFORMATYKI STOSOWANEJ

UNIVERSITEIT ANTWERPEN

FACULTEIT WETENSCHAPPEN DEPARTEMENT FYSICA

Electronic structure of artificial atoms and molecules: spin-orbit coupling effects

Author:

mgr inż. Michał NOWAK

Advisor:

Dr hab. inż. Bartłomiej SZAFRAN

Co-advisor:

Prof. dr. Francois M. PEETERS

May 28, 2013

to my wife

Abstract

This thesis describes effects of the coupling of spin and spatial degrees of freedom for electrons confined in quantum dots. The discussion is carried mainly in the context of spin control by orbital degrees of freedom. The dissertation consists of eleven chapters: introduction (1) and summary of published articles and manuscript that appeared as a result of PhD research (2). The papers are included in subsequent chapters (3-10) followed by the manuscript (11). Chapters (3-5) study single and multiple few-electron lateral quantum dots in the presence of Rashba and Dresselhaus spin-orbit coupling in terms of mixing of electron orbitals, anisotropy of spin exchange between neighboring quantum dots and impact of the dot orientation with respect to crystal host lattice on effective Landè factor. In next two chapters (6-7) we describe properties of quantum dots shaped as quantum rings in the context of breaking the circular symmetry of the charge density by spin-orbit coupling and possible application of such structures to perform controlled spin rotations. We refer to recent experimental results explaining the anisotropy of spin-orbit coupling observed in a single self-organized quantum dot (8) and the role of tunnel coupling on the observed spectrum of the electric dipole spin resonance in gated nanowires (9). Description of anisotropic spin polarization and lifting of the Pauli blockade due to spin relaxation and electric dipole spin resonance in nanowire quantum dots is given in the last two chapters (10-11).

Streszczenie

Poniższa rozprawa opisuje efekty sprzężenia pomiędzy spinowym i przestrzennym stopniem swobody elektronów uwięzionych w kropkach kwantowych. Dyskusja prowadzona jest głównie w kontekście kontroli spinu poprzez orbitalny stopień swobody. Praca zawiera jedenaście rozdziałów: wstęp (1) oraz podsumowanie artykułów i manuskryptu, które powstały jako efekt badań przeprowadzonych w trakcie doktoratu (2). Publikacje i manuskrypt tworzą kolejne rozdziały (3-11) rozprawy. W rozdziałach (3-5) badamy własności pojedynczych i wielokrotnych kilkuelektronowych kropek kwantowych w obecności oddziaływania Rashby oraz Dresselhausa w kontekście mieszania orbitali elektronowych, anizotropii wymiany spinu między sąsiadującymi kropkami oraz wpływu orientacji kropki w odniesieniu do materiału podłoża na efektywny czynnik Landègo. W kolejnych dwóch rozdziałach (6-7) badamy własności kropek kwantowych w postaci pierścieni kwantowych w kontekście łamania symetrii gęstości ładunku przez sprzężenie spin-orbita i możliwości wykorzystania tych struktur do przeprowadzania kontrolowanych obrotów spinu. Odnosimy się do nowych wyników eksperymentalnych wyjaśniając anizotropię oddziaływania spin-orbita obserwowaną w pojedynczej samozorganizowanej kropce kwantowej (8) oraz wpływ sprzężenia tunelowego na zmierzone widmo elektrycznych rezonansów spinowych w bramkowanych drutach półprzewodnikowych (9). Opis anizotropowej polaryzacji spinowej oraz znoszenia blokady Pauliego poprzez relaksację spinową i rezonanse spinowe w kropkach kwantowych zdefiniowanych w nanodrutach jest przedstawiony w dwóch ostatnich rozdziałach (10-11).

Samenvatting

Dit proefschrift beschrijft gevolgen van de koppeling van de spin en ruimtelijke vrijheidsgraden voor elektronen opgesloten in kwantumstippen. Het centrale thema betreft de spin controle door orbitale vrijheidsgraden. Het proefschrift bestaat uit elf hoofdstukken: inleiding (1) en samenvatting van gepubliceerde artikelen en manuscript, die verschenen als resultaat van dit promotieonderzoek (2). De papers worden in de volgende hoofdstukken (3-10) gevolgd door het manuscript (11). Hoofdstukken (3-5) bestuderen enkelvoudige en meervoudige-elektron laterale kwantumstippen in de aanwezigheid van Rashba en Dresselhaus spin-baan koppeling in termen van de menging van elektronorbitalen, anisotropie van spin-uitwisseling tussen naburige kwantumstippen en de impact van de stip oriëntatie met betrekking tot de kristal gastmatrix op de effectieve Landè factor. In de twee volgende hoofdstukken (6-7) beschrijven we de eigenschappen van kwantumstippen, die de vorm hebben van kwantumringen, in de context van het breken van de cirkelvormige symmetrie van de ladingsdichtheid door spin-baankoppeling en mogelijke toepassing van dergelijke structuren om gecontroleerde spin rotaties uit te voeren. We verwijzen naar recente experimentele resultaten en verklaren de anisotropie van spin-baan koppeling waargenomen in een zelf-georganiseerde kwantumstip (8) en de rol van tunnel koppeling op het waargenomen spectrum van de elektrische dipool spin resonantie in 'gated' nanodraden (9). Een beschrijving van de anisotrope spinpolarisatie en de opheffing van de Pauli blokkade ten gevolg van spin relaxatie en elektrische dipool spin resonantie in nanodraad kwantumstippen wordt gegeven in de laatste twee hoofdstukken (10-11).

Contents

Acknowledgements	2
About the dissertation	3
1 Motivation and context of the thesis	4
2 Summary of the articles	5
2.1 Article A.1, <i>Coupling of bonding and antibonding electron orbitals in double quantum dots by spin-orbit interaction</i>	5
2.2 Article A.2, <i>Time-dependent configuration-interaction simulations of spin swap in spin-orbit-coupled double quantum dots</i>	6
2.3 Article A.3, <i>Singlet-triplet avoided crossings and effective g-factor versus spatial orientation of spin-orbit-coupled quantum dots</i>	7
2.4 Article A.4, <i>Spin-orbit coupling effects in two-dimensional circular quantum rings: Elliptical deformation of confined electron density</i>	8
2.5 Article A.5, <i>Fano resonances and electron spin transport through a two-dimensional spin-orbit-coupled quantum ring</i>	8
2.6 Article A.6, <i>Tuning of the spin-orbit interaction in a quantum dot by an in-plane magnetic field</i>	9
2.7 Article A.7, <i>Resonant harmonic generation and collective spin rotations in electrically driven quantum dots</i>	10
2.8 Article A.8, <i>Spin polarization anisotropy in a narrow spin-orbit-coupled nanowire quantum dot</i>	11
2.9 Manuscript M.1, <i>Spontaneous and resonant lifting of the spin blockade in nanowire quantum dots</i>	12
3 Coupling of bonding and antibonding electron orbitals in double quantum dots by spin-orbit interaction	14
4 Time-dependent configuration-interaction simulations of spin swap in spin-orbit-coupled double quantum dots	28
5 Singlet-triplet avoided crossings and effective g-factor versus spatial orientation of spin-orbit-coupled quantum dots	38

6	Spin-orbit coupling effects in two-dimensional circular quantum rings: Elliptical deformation of confined electron density	47
7	Fano resonances and electron spin transport through a two-dimensional spin-orbit-coupled quantum ring	62
8	Tuning of the spin-orbit interaction in a quantum dot by an in-plane magnetic field	71
9	Resonant harmonic generation and collective spin rotations in electrically driven quantum dots	84
10	Spin polarization anisotropy in a narrow spin-orbit-coupled nanowire quantum dot	90
11	Spontaneous and resonant lifting of the spin blockade in nanowire quantum dots	98

Acknowledgements

I would like to thank my promotor prof. Bartłomiej Szafran. Firstly for the encouragement to do a PhD – I think that you had more faith in me than I had at the time. Thank you for indicating me the directions in the study, for the competence and patience in explanation, for the discussions and support you provided me during these years. I also thank you for motivating for harder work especially in the first years of the study and also for leading the MPD programme that provided the financial support. I would like to thank my co-promotor prof. Francois Peeters for the possibility to work in Condensed Matter Theory Group at University of Antwerp. Thank you for your support, hospitality and devoted time. I also thank prof. Bart Partoens for the collaboration during the stay in Belgium.

I would like to thank my colleagues from the Theory of Nanostructures and Nanodevices Group. Paweł Wójcik, we shared a room at my first year at the University and since then I have always appreciated discussions about physics and all other subjects with you. Paweł Szumniak, you and your wife Sylwia were great companions during our stay in Belgium. I thank both Paweł and Paweł for the great time during the conferences – especially the trip to Japan is a memory for a lifetime. I also thank Maciej Poniedziałek, Michał Zegrodnik, Przemysław Gryniewicz for the time spent at the University. I would like to thank the members of our Group: prof. Janusz Adamowski, prof. Stanisław Bednarek, dr. Tomasz Chwiej and dr. Bartłomiej Spisak and all staff of the Faculty for the friendly atmosphere.

I especially thank my wife. Thank you for the patience and forbearance when I worked late, for your constant support, belief, friendship and love. I could not have done it without you! I would like to thank to my daughter who was born in December 2012 – you brought a new light but also new challenges to my life. Finally I thank my parents and family who have always been supporting me.

I would like to thank Foundation for Polish Science for the financial support provided under START and MPD "Krakow Interdisciplinary PhD-Project in Nanoscience and Advanced Nanostructures" programmes co-financed by the EU European Regional Development Fund. Part of the present work was done under support of Iuventus 2011 programme, Project No. IP2011038671 financed by MNiSW and by PL-Grid Infrastructure.

About the dissertation

The present dissertation is composed of a collection of articles that describes the effects of spin-orbit interaction on the electronic structure of artificial atoms and molecules, i.e. single and systems of quantum dots. The dissertation consist of eight published papers:

- A.1 M. P. Nowak and B. Szafran, *Coupling of bonding and antibonding electron orbitals in double quantum dots by spin-orbit interaction*,
Physical Review B 81, 235311 (2010),
- A.2 M. P. Nowak and B. Szafran, *Time-dependent configuration-interaction simulations of spin swap in spin-orbit-coupled double quantum dots*,
Physical Review B 82, 165316 (2010),
- A.3 M. P. Nowak and B. Szafran, *Singlet-triplet avoided crossings and effective g-factor versus spatial orientation of spin-orbit-coupled quantum dots*,
Physical Review B 83, 035315 (2011),
- A.4 M. P. Nowak and B. Szafran, *Spin-orbit coupling effects in two-dimensional circular quantum rings: Elliptical deformation of confined electron density*,
Physical Review B 80, 195319 (2009),
- A.5 M. P. Nowak, B. Szafran, and F. M. Peeters, *Fano resonances and electron spin transport through a two-dimensional spin-orbit-coupled quantum ring*,
Physical Review B 84, 235319 (2011),
- A.6 M. P. Nowak, B. Szafran, F. M. Peeters, B. Partoens, and W. J. Pasek, *Tuning of the spin-orbit interaction in a quantum dot by an in-plane magnetic field*,
Physical Review B 83, 245324 (2011),
- A.7 M. P. Nowak, B. Szafran, and F. M. Peeters, *Resonant harmonic generation and collective spin rotations in electrically driven quantum dots*,
Physical Review B 86, 125428 (2012),
- A.8 M. P. Nowak and B. Szafran, *Spin polarization anisotropy in a narrow spin-orbit-coupled nanowire quantum dot*,
Physical Rev B 87, 205436 (2013),

and manuscript that is under review at the stage of preparation of the thesis:

M.1 M. P. Nowak and B. Szafran *Spontaneous and resonant lifting of the spin blockade in nanowire quantum dots*,
arXiv:1303.0211 (2013).

The collection of articles is preceded by the introduction and summary of the works.

1 Motivation and context of the thesis

During the last two decades significant progress has been made in confining and isolating single and few charge carriers in three dimensional potential cavities within a semiconducting medium that are called quantum dots. This opened unprecedented opportunity to study quantum phenomena at the nanoscale and to take a step towards quantum information processing. Electrons trapped in quantum dots possess a discrete energy spectrum [1] and such systems are often referred to as artificial atoms. Coupled quantum dots – where the electron wavefunction forms extended orbitals – are called artificial molecules.

The ability to control single carries opens a possibility for quantum computation that utilizes a new class of algorithms [2, 3] that take advantage of quantum parallelism. Spin of the electron confined in a quantum dot is considered as a good candidate [4] for a bit of quantum information – qubit – due to its weak coupling to the environment which increases the coherence time. For realization of quantum algorithms single and two-qubit gates are required. While the latter can be realized relatively simple – by controlling the exchange coupling between the spins [5] – the control of single spin raises more difficulties. First demonstration of single electron spin rotation employed Rabi resonances induced by oscillating magnetic field [6]. This method however cannot be used for the creation of scalable devices as the electrode used for the creation of a local AC magnetic field is of considerable size. For practical implementation of quantum gates electrical control of electron spin would be preferable. This is made possible by spin-orbit coupling. Spin-orbit interaction is an effect of relativistic origin where in the electrons reference frame the external electric field results in an effective magnetic field that depends on the electron momentum and affects the electrons spin. In semiconductor nanostructures

there are two possible sources of the spin-orbit interaction. First of them is Rashba [7] spin-orbit coupling which arises from the external electric fields in the structure. The second is Dresselhaus [8] spin-orbit interaction which results from the inversion asymmetry of the crystal structure in zincblende semiconductors. The strength of the spin-orbit interaction depends on the geometry of the device, and can be controlled by the strength of the external electric [9] or magnetic fields [10]. In recent years a great attention has been paid to spin-orbit coupling in quantum dots which resulted in measurements of i.e. spin precession in an effective magnetic field [11], avoided crossings in the energy spectra [12, 13], their dependence on the orientation of the external magnetic field [14] and first demonstration of coherent electrical spin control [15]. On the other hand spin-orbit interaction leads to coupling of the spin with the environment through orbital degrees of freedom which results in spin decoherence and relaxation [16, 17] and lifts the spin polarization in external magnetic field limiting the ability to store information in the spin degree of freedom.

The present thesis is devoted to spin-orbit interaction effects in quantum dots and its application to the control of the electron spin in artificial atoms and molecules. The present work describes effects of spin-orbit interaction in lateral structures and explains recent experimental results on self-organized quantum dots and gated nanowires.

2 Summary of the articles

2.1 Article A.1, *Coupling of bonding and antibonding electron orbitals in double quantum dots by spin-orbit interaction*

The first experimental demonstration of the control of a single [6] and a pair [5] of spins in a solid state exploited planar quantum dots. These structures are created by tailoring of the confinement potential of the two dimensional electron gas in a doped heterostructure. In article [A.1] we describe effects of spin-orbit interaction in lateral few-electron coupled quantum dots.

To study the two-dimensional quantum dots we developed a computational scheme in which the single electron spin-orbitals are obtained in a basis consisting of Gaussian functions distributed on a square mesh. This approach is applicable to systems without any symmetry and takes into account Rashba and Dresselhaus

spin-orbit interactions. We applied the configuration interaction scheme to obtain the solution for two- and three-electron in a numerically exact manner.

We describe experimentally measurable [18] consequences of spin-orbit interaction on the optical absorption spectra in a microwave regime. We find that spin-orbit coupling results in a mixed character of the states in the single-electron regime that possess bonding and antibonding components. For odd-number of electrons this results in opening avoided crossings between the states of opposite parity and spin visible in the absorption spectra. For the two-electron system the optical transitions are possible only in the presence of spin-orbit coupling that lifts the spin-polarization of the states and opens singlet-triplet anticrossing in the lowest part of the energy spectra.

2.2 Article A.2, *Time-dependent configuration-interaction simulations of spin swap in spin-orbit-coupled double quantum dots*

Laterally coupled quantum dots have been used [5] for realization of two-qubit quantum gates that realize *SWAP* and *SQUARE ROOT OF SWAP* operations that are based on spin exchange [19] between the two electrons confined in adjacent coupled dots. Without spin-orbit coupling the process is described by isotropic Heisenberg Hamiltonian where the spin exchange is controlled by the strength of the tunnel coupling [20]. Spin-orbit interaction is known to introduce anisotropic corrections [21] to the spin exchange that results in a dependence of the process on the initial direction of the spin polarization and limits the fidelity of the *SWAP* operation. The previous works discussed ways to minimize the anisotropy [22, 23] or to utilize it for the construction of quantum gates [24, 25]. Recent work [26] showed that in zero magnetic field the anisotropy vanishes but only for a specific choice of the spin basis. In regard of the ongoing discussion in the work [A.2] we perform a numerical experiment to study the spin swap process as it takes place in time under the presence of spin-orbit interaction.

We adopt a calculation scheme of [A.1] to obtain eigenstates of coupled quantum dots and used them to prepare the initial state for time evolution such that the two electrons are in opposite spin configuration and are localized in adjacent dots. We present that for neglected Coulomb interaction the spin exchange involves

tunneling of spin-opposite electrons between the dots which is accompanied by the precession of their spins in the spin-orbit effective magnetic field. This results in an appearance of additional spin components that depend on the initial spin polarization direction even without the magnetic field. The Coulomb interaction blocks the electron motion but the tunneling of the spin densities accompanied by spin precession is still observed. We find that the Coulomb interaction results in the generation of spin components in the direction of the spin-orbit field which are maximal at the half-time of the spin *SWAP* – altering the *SQUARE ROOT OF SWAP* operation. Moreover we present a way to restore the isotropy of the exchange process by proper choice of the double dot orientation with respect to crystal lattice due to cancelation of the effective Rashba and Dresselhaus fields.

2.3 Article A.3, *Singlet-triplet avoided crossings and effective g-factor versus spatial orientation of spin-orbit-coupled quantum dots*

The orientation of the lateral quantum dots with respect to the crystal axes is defined at the stage of fabrication of the device [27]. In the work [A.3] we demonstrate that in the presence of both Rashba and Dresselhaus coupling the energy splitting between the spin opposite states depends on the orientation of the dot. We explain that in the presence of spin-orbit coupling the strength of the Zeeman interaction that polarizes the spins depends on the extension of the charge density in the (001) plane provided that the length of the dot is comparable with the spin-orbit length (that is inversely proportional to the coupling strength). This results in changes of the effective g-factor calculated from the spin splittings. If the strength ratio of the Rashba and Dresselhaus coupling is detuned from 1 the dependence becomes weaker. The change of spin polarization results in changes of the width of the avoided crossing between singlet and triplet which is observed in the lowest part of the two-electron energy spectrum.

2.4 Article A.4, *Spin-orbit coupling effects in two-dimensional circular quantum rings: Elliptical deformation of confined electron density*

Special case of quantum dots are the circular structures with removed center that form quantum rings. Closed quantum rings have been studied in the context of persistent currents [28] and magnetization [29, 30, 31] in an external magnetic field. Previous studies on spin-orbit coupled quantum rings focused on the one-dimensional approximation of the structure [32]. Recent study [33] showed that spin-orbit interaction leads to breaking of the rotational symmetry of the charge density in the quantum ring. We employ configuration interaction calculations on a Gaussian mesh to describe a realistic quantum ring with finite width channels. We present that the one-dimensional approximation results in several artificial results and find that in the presence of both Rashba and Dresselhaus spin-orbit coupling rotational symmetry of the charge density is broken but *only* in the presence of external magnetic field or in the presence of both couplings with unequal strengths. We find that even for radically reduced channel width the exact results do not tend to the ones obtained in the one-dimensional approximation [33].

Moreover we show that the deformation of the charge density is increased by the electron-electron repulsion in the two electron regime. The breaking of the rotational symmetry of the charge density by the spin-orbit coupling corresponds to changes in experimentally accessible quantities such as the chemical potential of the ring and the magnetization that resembles the dependencies known for rings with defects [34].

2.5 Article A.5, *Fano resonances and electron spin transport through a two-dimensional spin-orbit-coupled quantum ring*

Open quantum rings allow for the realization of two-path interferometers where the phenomena related to phase change in the vector potential of the external magnetic field (Aharonov-Bohm effect [35]) or in the spin-orbit field (Aharonov-Casher effect [36]) results in modification of the conductance. Moreover the spin-orbit-coupled rings are considered for performing controlled rotations of transported electron spin [37]. The work [A.5] studies electron transport through the quantum ring in the

presence of Rashba spin-orbit coupling that results from the electric field present solely in the ring area. This approach allows for well defined spins in the leads and is realized by the addition of an electrode above the ring [38].

We developed a computational scheme that allows for the solution of the electron transport problem through a quantum ring with two-dimensional channels by the solution of time-independent Schrödinger equation with boundary conditions that assume the electron to enter from one of the leads. We find that in contrary to the one-dimensional studies [37] that in the presence of spin-orbit interaction Fano resonances appear in the conductance of the ring. The resonances occurs for Fermi energy that matches the energy of resonance states localized in the ring – whose wavefunctions vanish in the leads – and appear due to the breaking of the symmetry of the localized states by the spin-orbit coupling. We find that in the resonances the spin polarization of transported electron is altered which is due to the coupling to the spin of the resonance states. We demonstrate that the observed Fano resonances are the narrowest when the spin-orbit coupling strength is tuned to the maxima of the Aharonov-Casher oscillations. When the strength is detuned from the maxima the resonances become broader and the spin polarization at the output of the ring strongly depends on the electron Fermi energy which was not the case in the previous studies [37].

2.6 Article A.6, *Tuning of the spin-orbit interaction in a quantum dot by an in-plane magnetic field*

In 2010 the first transport spectroscopy measurement of a *single* self-organized quantum dot was reported [14]. Self-organized quantum dots are formed in the Stranski-Krastanov growth and are known for an almost a decade. The previous studies however were limited to the optical spectroscopy that were performed on ensembles of this objects. The study of Ref. [14] revealed broad anticrossings in the few-electron energy spectra of a single quantum dot opened by spin-orbit interaction that is exceptionally strong in these structures due to their limited height (that increases the strength of Dresselhaus coupling) and potential profile in the dot [39] that results in strong built-in electric fields (that increase the strength of Rashba coupling). The measured anticrossings [14] changed their width as the orientation of the external magnetic field was varied. The experimental work concluded that they are due to

Rashba coupling but did not provide any further explanation. Article [A.6] is the first theoretical description of a spin-orbit coupled three-dimensional quantum dot in a single and two-electron regime and provides a theoretical explanation of the experimental findings of Ref. [14].

For studies performed in work [A.6] a new computational scheme was developed that allowed for the inclusion of the full Rashba and Dresselhaus Hamiltonians into a three dimensional calculation in an efficient way. Two-electron eigenstates are obtained using a configuration interaction scheme where the electron-electron interaction matrix elements are calculated through the solution of the Poisson equation in the quantum dot.

In one-electron energy spectra we find avoided crossings opened separately by Rashba and Dresselhaus couplings whose width changes with the orientation of the in-plane magnetic field. We explain that the width of the anticrossing depends on the mixing ratio between the states of opposite spin and parity and that due to the different form of the Rashba and Dresselhaus Hamiltonians this mixing vanishes for different orientation of the magnetic field. Under the presence of both couplings the magnetic field orientation for which the anticrossing is the narrowest depends on the relative strength of Rashba and Dresselhaus couplings. We compared results of our calculation in the two electron regime with the experimental data and explained that the results indicate the presence of Dresselhaus coupling in the structure. Furthermore we derive analytical formula which allows for the calculation of the relative strength of the spin-orbit couplings from the experimentally accessible data.

2.7 Article A.7, *Resonant harmonic generation and collective spin rotations in electrically driven quantum dots*

For the realization of a complete set of quantum gates the implementation of single qubit quantum gates that require single spin rotations is necessary. Electrical spin rotations are performed by electric dipole spin resonance which relies on transitions between spin states induced by oscillating electric field mediated by spin-orbit coupling when the oscillation frequency matches the Larmor frequency in weak external magnetic field [6]. A lot attention was paid [40, 41, 42, 43, 44, 45] to InAs and InSb nanowire quantum dots that allow for efficient electrical control of electron spin due the strong spin-orbit interaction in this systems [12, 13]. The work [40]

measured maps of the current in function of the magnetic field and electric field frequency that revealed central resonance line due to transition from spin-parallel triplet states to degenerate spin-antiparallel state. Recent experiment [42] presented detailed spectroscopy of the electric dipole spin resonance spectrum revealing the additional resonance line at the fractional frequency and the splitting of the central line. We developed a computational scheme that allowed for simulation of electric dipole spin resonance in a two-electron nanowire artificial molecule for the explanation of this observation and to study the impact of the electron-electron interaction on the spin rotations.

The calculations are based on a quasi-one-dimensional model of the nanowire with the exact inclusion of the Coulomb interaction. The simulation reveals that for non-zero interdot coupling the exchange interaction results in the splitting of the central resonance line which is accompanied by the collective rotation of the spins of both electrons. We also find that in the fourier transform of the driven electron momentum there are harmonics present of the driving frequency. When one of the harmonics matches the resonant frequency a transition appears which is the origin of the experimentally resolved resonances at the half frequency [42]. The fractional resonances appear only if the exchange coupling between electrons is nonzero, i.e., they are accompanied by the splitting of the central resonance line. Moreover we find that the fractional transitions appear also in a single-electron regime also without the spin-orbit coupling – the resonant generation of harmonic frequency is an intrinsic propriety of an electrically driven electron.

2.8 Article A.8, *Spin polarization anisotropy in a narrow spin-orbit-coupled nanowire quantum dot*

The electric dipole spin resonance experiments measure the main resonances at the frequency that corresponds to the energy separation due to Zeeman splitting in an external magnetic field. In experiments [41, 42] this allowed for measurement of the effective Landè factor for different in-plane orientation of the magnetic field. The measurements revealed strong anisotropy of the effective g-factor. In the work [A.8] we study effects of anisotropic spin polarization in nanowire quantum dots in the context of the experimental findings.

We solve the three dimensional Schrödinger equation for single and two-electrons

confined in a cylindrical quantum dot in the presence of Rashba coupling. We find that the degree of spin polarization of the states depends on the orientation of the external magnetic field. Surprisingly we find that the spin polarization becomes almost complete for decreasing radius of the wire. We present an analytical solution for the phenomena in the one-dimensional limit where we present analytical forms of the spin-orbitals that allows us to explain the changes of the effective g -factor. In the two-electron regime we perform configuration interaction calculation and relate our results to the experimental findings [41, 42]. We find that the form of the g -factor dependence on the magnetic field orientation matches the one obtained in the experiment. Moreover calculated width of the avoided crossing between the energy levels of the singlet and triplet states and its dependence on the magnetic field orientation agrees with the findings of Ref. [42].

2.9 Manuscript M.1, *Spontaneous and resonant lifting of the spin blockade in nanowire quantum dots*

Observation of the electric dipole spin resonance [40, 41, 42, 43, 44, 45] relies on the measurement of the current increase associated with the lifting of the Pauli blockade in the two electron coupled quantum dots. The single electron current is blocked when the two electrons initialize in spin parallel configuration forming a triplet state. Spin rotation drives the system into a $S = 0$ state which relaxes to the singlet ground state (with double occupancy of a single dot), which is followed by the escape of one of the electrons to the drain electrode. However, in the presence of spin-orbit coupling, phonon mediated spin-relaxation occurs [17, 46, 47] as a concurrent process to the electric dipole spin resonance, lifting of the blockade also from spin parallel states. So far the latter process has been considered in the context of the leakage current [48, 49]. In work [M.1] we present results of our simulation that describes the time dependent process of electric dipole spin resonance along with phonon mediated relaxation in the presence of spin-orbit coupling.

We find that the spin-nonconserving relaxation occurs provided the energy separation between initial and final states for the relaxation is small enough. This leads to spontaneous lifting of the blockade from one of the Zeeman split triplets. The only remaining blocked state is the spin triplet with spins polarized antiparallel to the magnetic field and in a weak magnetic field the resonances are observed solely

from this state. When the external magnetic field is increased the spin positive triplet becomes the ground state which results in the restoration of the blockade from this state. This results in the appearance of an additional resonance which is related to the spin rotation accompanied by charge reconfiguration. We identify the latter resonance in the recent experimental results [44].

3 Coupling of bonding and antibonding electron orbitals in double quantum dots by spin-orbit interaction

Coupling of bonding and antibonding electron orbitals in double quantum dots by spin-orbit interaction

M. P. Nowak and B. Szafran

Faculty of Physics and Applied Computer Science, AGH University of Science and Technology, al. Mickiewicza 30, 30-059 Kraków, Poland

(Received 4 March 2010; revised manuscript received 13 May 2010; published 9 June 2010)

We perform a systematic exact diagonalization study of spin-orbit coupling effects for stationary few-electron states confined in quasi-two-dimensional double quantum dots. We describe the spin-orbit-interaction induced coupling between bonding and antibonding orbitals and its consequences for magneto-optical absorption spectrum. The spin-orbit coupling for odd electron numbers (one, three) opens avoided crossings between low energy excited levels of opposite spin orientation and opposite spatial parity. For two electrons the spin-orbit coupling allows for low-energy optical transitions that are otherwise forbidden by spin and parity selection rules. We demonstrate that the energies of optical transitions can be significantly increased by an in-plane electric field but only for odd electron numbers. Occupation of single-electron orbitals and effects of spin-orbit coupling on electron distribution between the dots are also discussed.

DOI: [10.1103/PhysRevB.81.235311](https://doi.org/10.1103/PhysRevB.81.235311)

PACS number(s): 73.21.La

I. INTRODUCTION

In a pair of quantum dots¹⁻⁴ defined in semiconducting medium the charge carriers form extended wave functions when their tunneling through the interdot barrier becomes effective enough. In vertically stacked quantum dots the extended electron and hole orbitals are probed by photoluminescence experiments in external electric field.⁴ The electron single-dot orbitals hybridize to bonding ground states similar to the ones found in natural covalent molecules. Recent studies⁵ indicated that the hole in artificial molecules of self-assembled quantum dots behaves in a different manner forming an antibonding ground-state orbital. This peculiar behavior results⁵ of the spin-orbit (SO) coupling-induced mixing of light and heavy hole states.

In the present paper we study the mixing of bonding and antibonding electron orbitals that is induced by SO interaction in planar systems of laterally coupled quantum dots. The coupling between spatial and spin electron degrees of freedom results from inversion asymmetry of the structure⁶ and/or the crystal lattice.⁷ This asymmetry enters into the two-dimensional SO Hamiltonian which does not conserve the spatial parity and couples the electron spin-up bonding orbitals with spin-down antibonding orbitals. In order to indicate experimentally accessible consequences of this coupling we consider optical absorption spectra in the external magnetic field for up to three confined electrons. In parabolic quantum dots the spin-orbit coupling introduces a distinct dependence of the far infrared magneto-optical absorption spectra on the number of confined electrons.⁸ We find that the SO induced modification to the absorption spectra of double dot are qualitatively different for even and odd electron numbers.

Laterally coupled quantum dots^{9,10} are considered candidates for realization of a quantum gate working on electron spins³ since the height/width of the interdot barrier can be tuned by external voltages which is essential for the control of the spin exchange between the electrons confined in adjacent dots. The idea of the spin exchange motivated a number

of theoretical investigations on the properties of electron systems in laterally coupled quantum dots.^{1,2,11-18}

The SO interaction is one of the issues that are investigated in the context of spin-based quantum information processing.^{16-22,25-33} The SO coupling allows for spin manipulation by the spatial electron motion.³⁰⁻³³ Moreover, it leads to the spin relaxation¹⁸⁻²² mediated by phonons, leading to information decay and decoherence. Singlet-triplet induced avoided crossing of two-electron energy levels were observed in electron-transport spectroscopies for gated InAs nanowire quantum dots²³ as well as for double quantum dots.²⁴ The exchange interaction between electrons confined in separate dots was found to contain an anisotropic component originating from the SO coupling,²⁵ which initially motivated a quest for spin processing procedures^{26,27} minimizing its effects. Later on, proposals of using the asymmetry of the exchange interaction for construction of universal quantum gates that could work without single spin operations^{28,29} were formulated. Recently, a theoretical study supported by exact diagonalization results argued that¹⁶ the anisotropy of the exchange interaction is in fact absent in zero magnetic field. The SO coupled double quantum dots were so far studied by the exact diagonalization in Ref. 34, which provides a detailed analysis of single-electron states and in Refs. 16 and 35 which deal with the electron pair in the context of the exchange interaction.

II. THEORY

We consider an effective mass single-electron Hamiltonian of the form,

$$h = \left(\frac{\mathbf{p}^2}{2m^*} + W(\mathbf{r}) \right) \mathbf{1} + \frac{1}{2} g \mu_B B \sigma_z + H_{SIA} + H_{BIA}, \quad (1)$$

where $\mathbf{p} = \hbar \mathbf{k} = -i\hbar \nabla + e\mathbf{A}$, $\mathbf{1}$ is the identity matrix, $W(\mathbf{r})$ stands for the potential, H_{SIA} and H_{BIA} introduce Rashba⁶ (structure inversion asymmetry) and Dresselhaus⁷ (bulk inversion asymmetry) spin-orbit interactions. The vector po-

tential is taken in the symmetric gauge $A = \frac{B}{2}(-y, x, 0)$. The Rashba and Dresselhaus SO interactions have the form

$$H_{SIA} = \alpha \nabla W \cdot (\boldsymbol{\sigma} \times \mathbf{k}), \quad (2)$$

and

$$H_{BIA} = \gamma [\sigma_x k_x (k_z^2 - k_y^2) + \sigma_y k_y (k_x^2 - k_z^2) + \sigma_z k_z (k_y^2 - k_x^2)], \quad (3)$$

respectively. In Eqs. (2) and (3) α and γ are bulk SO coupling constants, σ 's are Pauli matrices and x , y , z axes are oriented parallel to $[100]$, $[010]$, and $[001]$ (growth) crystal directions, respectively.

We assume that the confinement potential forming the quantum dot is separable into an in-plane $V_c(x, y)$ and a growth direction $V_z(z)$ components so that the potential appearing in the Hamiltonian (1) is

$$W(\mathbf{r}) = V_c(x, y) + V_z(z) + |e|\mathbf{F} \cdot \mathbf{r}, \quad (4)$$

where \mathbf{F} is the external electric field vector (below we always take $F_y=0$). In the following we adopt a two-dimensional approximation assuming that the electrons occupy a frozen lowest-energy state of quantization in the growth direction. The two-dimensional SO terms are obtained by averaging H_{SIA} and H_{BIA} over the wave function describing the electron localization in the growth direction. The two-dimensional Rashba terms are usually³⁵ separated into a diagonal

$$\begin{aligned} H_{SIA}^{diag} &= \alpha \sigma_z \left[\frac{\partial W}{\partial y} k_x - \frac{\partial W}{\partial x} k_y \right] \\ &= \alpha \sigma_z \left(\left[\frac{\partial V_c}{\partial y} \right] k_x - \left[\frac{\partial V_c}{\partial x} + |e|F_x \right] k_y \right), \end{aligned} \quad (5)$$

and linear

$$H_{SIA}^{lin} = \alpha \left\langle \frac{\partial W}{\partial z} \right\rangle (\sigma_x k_y - \sigma_y k_x), \quad (6)$$

parts. In this formula the average gradient of the potential calculated for the wave function in the growth direction can be attributed to an effective z component of the electric field $F_z = \frac{1}{|e|} \left\langle \frac{\partial W}{\partial z} \right\rangle$. The two-dimensional Dresselhaus SO interaction contains the linear

$$H_{BIA}^{lin} = \gamma \langle k_z^2 \rangle [\sigma_x k_x - \sigma_y k_y], \quad (7)$$

and the cubic

$$H_{BIA}^{cub} = \gamma [\sigma_y k_y k_x^2 - \sigma_x k_x k_y^2] \quad (8)$$

terms. We assume that the quantum dot is made of $\text{In}_{0.5}\text{Ga}_{0.5}\text{As}$ alloy for which we adopt the SO coupling constants $\alpha=0.572 \text{ nm}^2$ (after Ref. 36) and $\gamma=32.2 \text{ meV nm}^3$ (after Ref. 37). The other material parameters are taken as arithmetic average³⁸ of InAs and GaAs, i.e., we use the electron effective mass $m^*=0.0465m_0$, Landé factor $g=-8.97$ and dielectric constant $\epsilon=13.55$. The considered large value of the g factor is in the order of the one found for in experimental samples^{23,24} in which the SO coupling effects were studied.

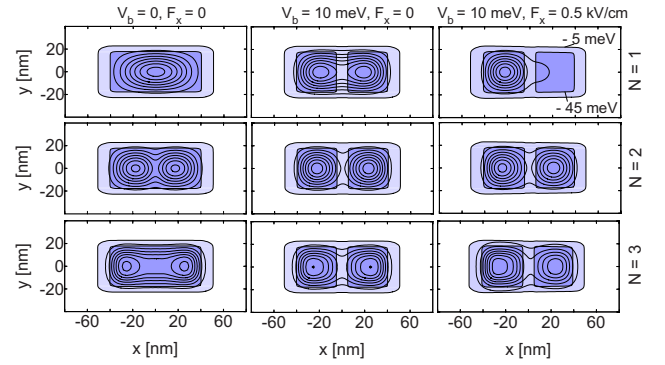


FIG. 1. (Color online) The shades of gray (blue online) show the in-plane potential of a single dot ($V_b=0$ —left column of plots) and of a double dot ($V_b=10 \text{ meV}$ —central and right columns). In the right column of plots an in-plane electric field of $F_x=0.5 \text{ kV/cm}$ is included. Inside the light (darker) blue area the potential falls below -5 meV (-45 meV). The contours indicate the charge density for a single (top row), two electrons (middle row) and three electrons (lowest row of plots) for $B=0$.

For the electron wave function in the growth direction identified with the ground-state of an infinite rectangular potential well of height d one obtains the two-dimensional linear Dresselhaus constant $\gamma^{2D} = \gamma \langle k_z^2 \rangle = \gamma \frac{\pi^2}{d^2}$ [see Eq. (7)]. In the bulk of our calculations we assume a minimal but still realistic value of $d=5.42 \text{ nm}$, for which $\gamma^{2D}=10.8 \text{ meV nm}$.

The in-plane confinement potential is taken in form

$$\begin{aligned} V_c(x, y) &= - \frac{V_0}{\left(1 + \left[\frac{x^2}{R_x^2}\right]^\mu\right) \left(1 + \left[\frac{y^2}{R_y^2}\right]^\mu\right)} \\ &\quad + \frac{V_b}{\left(1 + \left[\frac{x^2}{R_x^2}\right]^\mu\right) \left(1 + \left[\frac{y^2}{R_y^2}\right]^\mu\right)}, \end{aligned} \quad (9)$$

where $V_0=50 \text{ meV}$ is the depth of the dots and V_b is the height of the interdot barrier. We assume $\mu=10$ for which the potential profile has a form of a nearly rectangular potential well, where $2R_x=90 \text{ nm}$ and $2R_y=40 \text{ nm}$ determine the size of the double dot in x and y directions respectively and $2R_b=10 \text{ nm}$ is the thickness of the interdot barrier. We consider two values of the barrier height $V_b=10 \text{ meV}$ —for the double-dot potential and $V_b=0$ —for a single elongated dot. The potential V_c is displayed in Fig. 1 for both the single and double dot. The single elongated dot is discussed here as a limit of the strong interdot tunnel coupling.

Our calculation deals with a single or double quantum dot that is two-dimensional and strongly anisotropic, with the length to width ratio of about 2:1. Such a quantum dot can be defined by an electrical gating of a quantum well for a proper shape of the gate. The profile of the confinement potential for a circular gate was discussed in Ref. 39. Double flat InGaAs quantum dots that are laterally coupled are also produced by etching techniques.⁴⁰ In these⁴⁰ structures the dots nearly

touch one another and the 2:1 ratio of the lengths is preserved.

The singlet/triplet avoided crossings that are due to SO coupling were observed in the charging spectra of InAs quantum-wire-based structures, both a single²³ and double²⁴ dots. These quantum wires^{23,24} are three-dimensional objects of a circular profile of confinement potential. The confinement along the wire is introduced^{23,24} by electrical gating and the magnetic field is applied perpendicular to the axis of the wire. The common point of the geometry of these structures^{23,24} and the present model is the distinct anisotropy of the structure within the plane perpendicular to the external magnetic field. For the single dot²³ the length of the structure along the wire is 180 nm as compared to the wire diameter of 50 nm. For the double dot²⁴ the length and diameter are 220 and 100 nm, respectively. The other common point of the considered model and the quantum-wire dots^{23,24} is the strong Zeeman effect due to the large value of the g factor.

The single-electron eigenfunctions are found by diagonalization of the two-dimensional version of Hamiltonian (1) in a basis of multicenter Gaussian functions⁴¹ with embedded gauge invariance

$$\psi_n = \sum_{ks} c_{ks}^n \chi_s \exp \left[-\frac{(\mathbf{r} - \mathbf{R}_k)^2}{2a^2} + \frac{ieB}{2\hbar}(xY_k - yX_k) \right], \quad (10)$$

where summation over k runs over centers of Gaussian $\mathbf{R}_k = (X_k, Y_k)$, $s = \uparrow, \downarrow$ and χ_s are eigenstates of Pauli σ_z matrix. The centers \mathbf{R}_k are distributed on a rectangular mesh of 25×11 points spaced by $\Delta x = \Delta y = 5.2$ nm. The variationally optimal basis function parameter $a = 4.7$ nm is used in the calculations.

The eigenproblem of N -electron Hamiltonian

$$H = \sum_i^N h_i + \sum_{i=1, j>i}^N \frac{e^2}{4\pi\epsilon_0 \epsilon r_{ij}} \quad (11)$$

is solved using the configuration-interaction approach with a basis constructed of Slater determinants built of single-electron eigenfunctions [Eq. (10)] of SO-coupled Hamiltonian. Convergence of the energies with a precision better than $1 \mu\text{eV}$ is usually reached for inclusion of thirty one-electron eigenstates.

The confinement potential [Eq. (9)] is symmetric with respect to the origin. In the present work the asymmetry effects are introduced by the in-plane electric field F_x . For $F_x = 0$ and without SO coupling the stationary states possess a definite spatial parity with respect to point inversion $P\psi^n(-\mathbf{r}) = \pm \psi^n(\mathbf{r})$, where P is the inversion operator. The eigenvalue $+1$ corresponds to even-parity states and the eigenvalue -1 to the odd-parity states. When SO is introduced the spatial parity eigenvalue is no longer a good quantum number even for $F_x = 0$. For symmetric systems the SO coupled Hamiltonians commute with the operator $P\sigma_z$, which implies that the spin-up and spin-down components still possess definite but opposite spatial parities. We refer to $P\sigma_z$ as the s -parity operator. Eigenstates of this operator with eigenvalue $+1(-1)$ are referred to as even (odd) s -parity states or for brevity

s -even (s -odd) states. The even s -parity states have even-parity spin-up component and odd-parity spin-down component.

We evaluate the optical absorption spectrum using the energies of stationary states and transition probabilities from state k to l that is proportional to the square of the dipole matrix element

$$I_{kl} = \langle \Psi_k | \sum_{j=1}^N (x_j \pm iy_j) | \Psi_l \rangle, \quad (12)$$

where Ψ_k is the N -electron wave function for k th Hamiltonian (11) eigenstate and the signs \pm correspond to opposite circular polarization of the exciting light. The optical transitions conserve the electron spin and invert the spatial parity when it is a well-defined quantity. When the SO coupling is introduced the optical transitions can only occur between states of opposite s -parity.

III. RESULTS

A. Single electron

The single-electron spectrum for a single elongated dot and for the double dot is presented in Fig. 2. For $B = 0$ the ground state and the first excited state are Kramers doublets. In each doublet we find one state of the odd s -parity and the other of the even s -parity. At $B = 0$ the electron in the ground-state (first-excited-state) doublet occupies predominantly a bonding (antibonding) orbital. With the solid (dashed) lines we plotted the even (odd) s -parity energy levels. Black lines show the results without SO coupling. The dark gray (blue online) lines correspond to the case of SO coupling without the linear Rashba term (H_{SIA}^{lin}), i.e., for $F_z = 0$. The light gray (red online) curves in Fig. 2(a) correspond to $F_z = 188.8$ kV/cm, for which the linear two-dimensional Rashba constant is as large as the linear two-dimensional Dresselhaus one. Beyond increased width of the avoided crossing no qualitative difference in the results obtained for these two values of F_z is found. Therefore, below we assume $F_z = 0$ unless stated otherwise.

For illustration of the double-dot wave functions we assumed a presence of a residual magnetic field $B = 10 \mu\text{T}$ which lifts the doublet degeneracy and we chose the states of the ground and excited doublets that correspond to $\langle s_z \rangle > 0$. With the blue lines in Fig. 3 we plotted the spinor components of the even s -parity ground state which is bonding in its spin-up component with or without SO coupling. Its antibonding spin-down component appears when the SO coupling is introduced [Fig. 3(c)]. The red lines in Fig. 3 correspond to the odd s -parity state of the excited doublet which is antibonding in the spin-up component. The SO coupling adds to this state a bonding spin-down component.

In Fig. 2 one observes an avoided crossing of two excited energy levels of the odd s -parity stemming of both the ground and the excited doublets. Without the SO coupling the energy level that goes up in the energy with growing magnetic field corresponds to the spin-down bonding orbital, and the one that goes down—to the spin-up antibonding orbital. The avoided crossing opened by the SO interaction is accompanied by spin and spatial parity mixing.

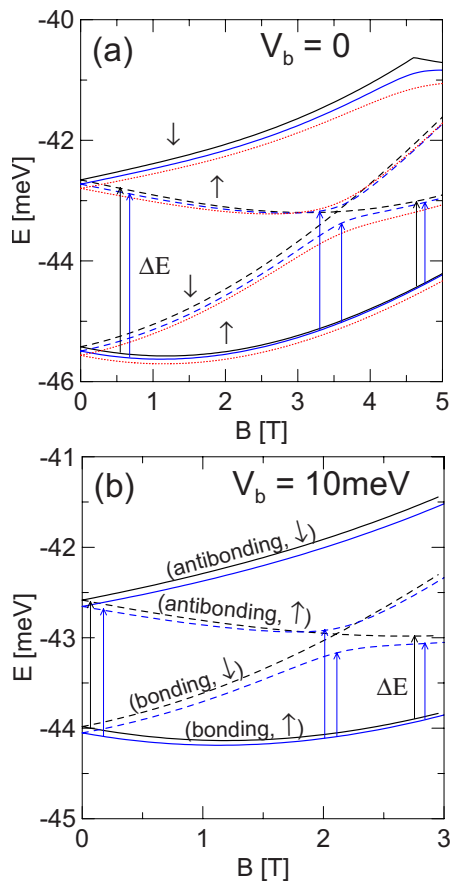


FIG. 2. (Color online) Lowest single-electron energy levels in function of the magnetic field for a single elongated dot ($V_b=0$) (a) and for a double dot ($V_b=10$ meV) (b). Solid (dashed) lines correspond to the even (odd) s -parity. Black lines show the results without SO coupling. The blue curves show the results obtained with SO coupling for $F_z=0$ and the red curves in (a) for $F_z=188$ kV/cm. The spin direction for the energy levels without SO coupling are marked with arrows. The thin vertical lines indicate allowed optical transitions from the ground state.

For the single electron in ideally symmetric pair of dots ($F_x=0$) there is a direct correspondence between the SO-coupling-induced mixing of both the spin states and the occupation of molecular orbitals of opposite spatial parity. The occupation of the even-parity orbitals [$oc(e)$] is calculated as the norm of this component of the spinor that corresponds to the even-parity state. Then the average value of the z component of the electron spin is $\langle s_z \rangle = \hbar [oc(e) - \frac{1}{2}]$ for the even s -parity and $\langle s_z \rangle = \hbar [\frac{1}{2} - oc(e)]$ for the odd s -parity states. Occupation of the even-parity orbitals and $\langle s_z \rangle$ is for the double dot displayed in Fig. 4 as function of the magnetic field. The ground state at higher field becomes a pure bonding spin-up orbital. We notice that the values corresponding to the two odd s -parity energy levels interchange near 2 T which is related to the energy level anticrossing presented in Fig. 2(b). At the center of the avoided crossing these two energy levels correspond to $\langle s_z \rangle = 0$ and bonding and antibonding orbitals are equally occupied.

The discussed anticrossing of the odd s -parity energy levels leaves a clear signature on the optical absorption spec-

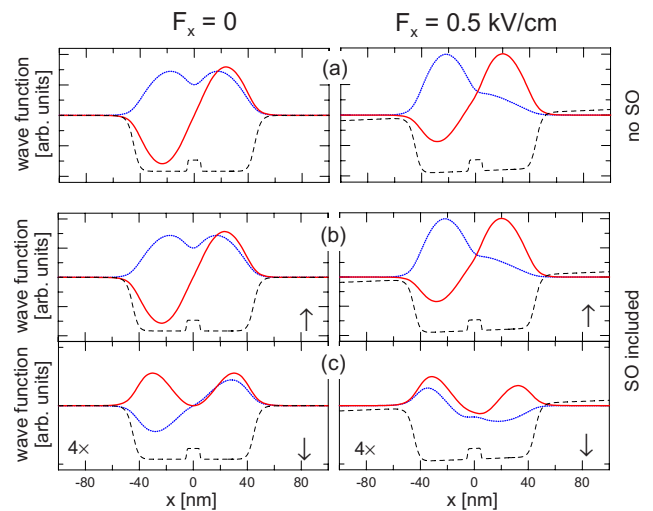


FIG. 3. (Color online) Dashed curves show the potential confinement profile for $V_b=10$ meV calculated for $y=0$. (a) The spin-up components of the even s -parity ground state (red lines) and s -odd parity excited state (blue lines) in the absence of SO coupling (spin-down components exactly vanish). (b) Same as (a) but with SO coupling present. Spin-down components are presented in (c). The scale for the wave function is the same on all the plots, but in (c) the wave functions were multiplied by 4. At right (left) panels an electric field is $F_x=0.5$ kV/cm (zero).

trum. The energy and probability of excitation from the ground state are displayed in Fig. 5. The ground state has the even s -parity hence the absorption is only allowed to the odd s -parity final state. The ground-state is nearly spin-up polarized (Fig. 4) and since electron spin is left unchanged during an optical transition the absorption goes to the s -odd state with spin-up orientation. When the avoided crossing is opened between the s -odd energy levels both of them possess a nonzero spin-up component and the optical transitions to both of them from the ground-state are allowed. Outside the avoided crossing the absorption spectra with or without SO coupling are similar.

The energy range in which the SO-induced avoided crossing is observed in the absorption spectrum corresponds to far-infrared or microwave radiation in which cyclotron reso-

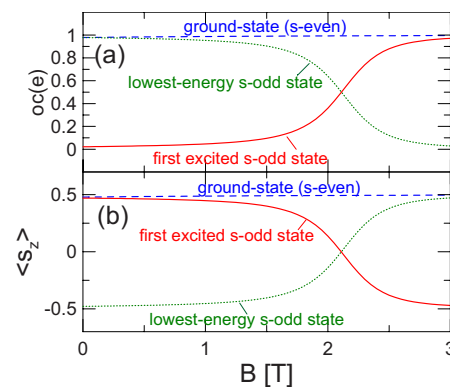


FIG. 4. (Color online) Contribution of even-parity orbitals (a) and average value of the z component of the spin (b) (in \hbar units) in the lowest-energy s -even and s -odd parity eigenstates.

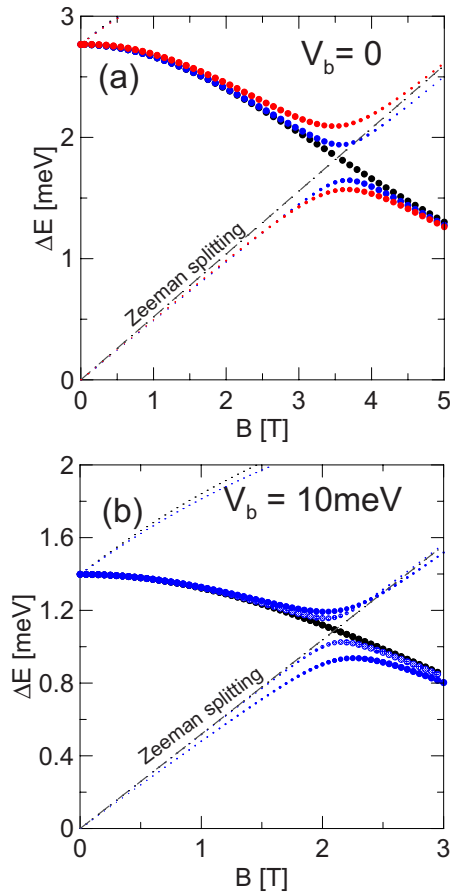


FIG. 5. (Color online) The dots show the low-energy absorption from the ground state at $F_x=0$ for the single dot (a) and for the coupled dots (b) (for the energy spectra see Fig. 2). The area of the dots is proportional to the absorption probability. The black dots show the results without SO coupling. The full blue dots correspond to SO coupling with $F_z=0$. The open blue circles in (b) correspond to height of the dot d increased from 5.42 to 7.67 nm which amounts in a twofold reduction of the two-dimensional Dresselhaus constant. The red dots in (a) correspond to a strong linear Rashba coupling present $F_z=188$ kV/cm. The dashed gray line indicates the Zeeman splitting $g\mu_b B$.

nance experiments are performed.⁴³ One can increase the energy of the avoided crossing twice by applying an electric field of 0.5 kV/cm—see Fig. 6(b). In the presence of the electric field the electron in the ground-state is pushed to the left dot by $F_x > 0$ while the final state in the absorption process is mainly localized in the right dot [see Fig. 3(b)]. The opposite shifts of the electron wave function in the initial and final states are translated by the electric field into an increased transition energy [see Fig. 6(a) for the energy splitting]. The obtained energy increase is accompanied by reduction of the SO-induced avoided crossing.

Figure 6(b) shows also that for nonzero F the absorption probabilities vanish at higher B . The separation of the initial and final states [Fig. 3(b)] by the electric field is enhanced when the magnetic field is applied, since the latter increases the localization of wave functions near the centers of the dots lifting the interdot tunnel coupling. In consequence—the ground state becomes totally localized in one dot and the

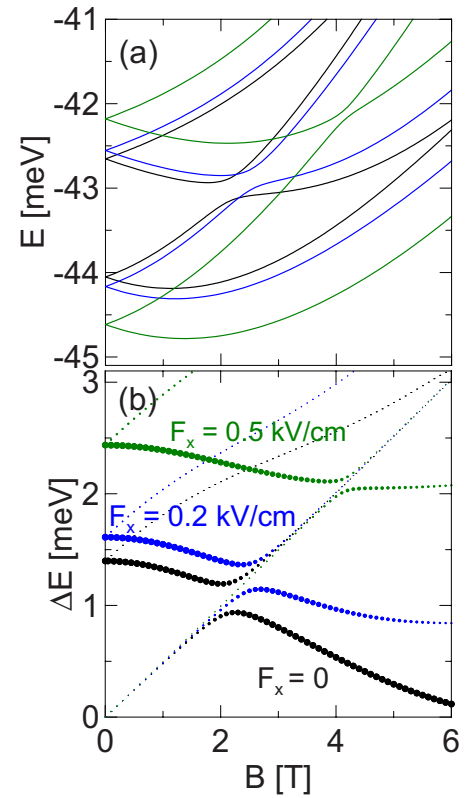


FIG. 6. (Color online) Single-electron energy spectrum (a) and optical absorption spectrum (b) in function of the magnetic field for $F_x=0$ (black color), $F_x=0.2$ kV/cm (blue) and $F_x=0.5$ kV/cm (green) for coupled quantum dots.

final state of the transition in the other. Vanishing overlap between the initial and final state wave function implies vanishing transition probability as calculated by formula (12).

In order to evaluate the importance of separate spin-orbit coupling terms we calculated their contributions to the single-electron ground state. For $B=0$ and $F_x=0$ and $\alpha F_z = \gamma \langle k_z \rangle^2 = \gamma^{2D} = 10.8$ meV nm [red curves in Fig. 2(a)] we find that the expectations values of H_{SIA}^{lin} , H_{BIA}^{lin} , H_{BIA}^{cub} , and H_{SIA}^{diag} are, -0.14 meV, -0.14 meV, 1 μ eV, and -0.01 μ eV, respectively. At 4 T the corresponding values are -0.19 meV, -0.03 meV, 0.13 μ eV, and -6 μ eV. At high magnetic field the energy effects of the Dresselhaus coupling are reduced in consistence with the recent study⁴² of parabolic quantum dots. This reduction is due to the Zeeman effect⁴² which is for the considered material particularly strong. For $F_z=0$ at 4 T [blue curve in Fig. 2(a)] one obtains -27 , 0 , 0.01 , and -6 μ eV. For additionally switched off Zeeman term the numbers are -230 , 0 , 3 , and 6 μ eV, respectively. In fact, only the linear terms of SO interaction introduce significant contributions to the results within the considered range of magnetic field.

B. Electron pair

In the absence of the magnetic field and without SO coupling the first excited state of the electron pair is spin triplet. For $B=0$ we find that the first excited state is threefold de-

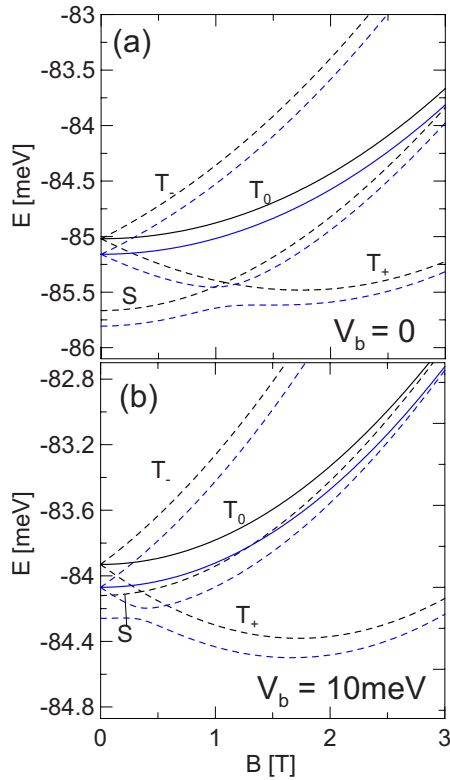


FIG. 7. (Color online) Two-electron energy spectrum for a single elongated dot $V_b=0$ (a) and for a couple of dots separated by $V_b=10$ meV barrier (b). Black (blue) lines show the results without (with) SO coupling. For the results without SO coupling we added labels S for the singlet and T for the triplets (subscript denotes the sign of the z component of the total spin). Dashed (solid) curves correspond to odd (even) s -parity. Results were obtained for $F_x=0$.

generate also with SO coupling present. This applies to both the single elongated dot [Fig. 7(a)] and the double dot [Fig. 7(b)]. Without SO coupling the magnetic field induces a singlet-triplet ground-state transition near 1 T for the single dot and near 0.4 T for the double dot. The crossing singlet and triplet energy levels have the same odd s -parity and an avoided crossing is opened between them when SO coupling is introduced. The calculated width of the avoided crossing is 0.18 and 0.07 meV for the single and double dot, respectively, which is within the order of the ones found in experiments: 0.23 and 0.2 meV for the nanowire quantum dot²³ and for the double dot.²⁴

For a symmetric system ($F_x=0$) the optical transition from the ground-state can only go to the even s -parity eigenstate. In the absence of the spin-orbit coupling in the considered energy range only the triplet with zero z component of the spin (T_0) has the required spatial parity to absorb photons. However, this absorption is excluded anyway on both sides of the singlet-triplet ground-state transition. For B below this transition the matrix element [Eq. (12)] vanishes due to opposite symmetry of the spatial initial and final wave functions with respect to the electron interchange. For B above the singlet-triplet transition the ground-state (triplet with $s_z=\hbar$ denoted as T_+) and T_0 states have the same symmetry with respect to the electron interchange, but the z com-

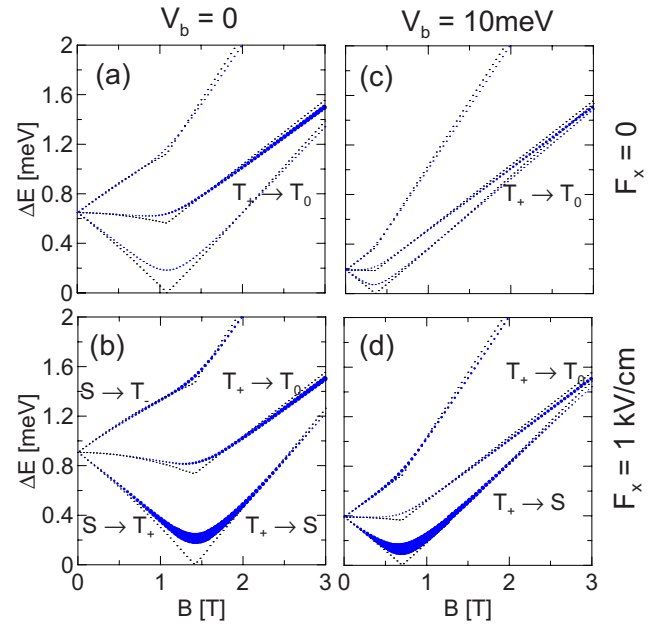


FIG. 8. (Color online) Two-electron ground-state absorption spectrum as a function of the magnetic field for SO coupled single dot (a,b) and double dot (c,d). Panels (a,c) correspond to $F_x=0$ and (b,d) to $F_x=1$ kV/cm. The area of the dots is proportional to the absorption probability. Transitions are denoted by labels of two-electron spin eigenstates which are found without SO coupling. Without SO coupling all the transitions presented in this figure are forbidden.

ponents of the spin are different. Optical transitions between the states corresponding to energy levels presented in Fig. 7 are only allowed by the SO coupling. The calculated absorption spectrum is shown in Fig. 8. For $F_x=0$ [Figs. 8(a) and 8(c)] the absorption probability grows with the magnetic field after the singlet-triplet ground state avoided crossing. Then, the transition corresponds to $T_+ \rightarrow T_0$ excitation in terms of states without SO coupling. When the electric field F_x is switched on [Figs. 8(b) and 8(d)] the parity selection rules no longer apply and we notice appearance of also $S \leftrightarrow T_+$ and $S \rightarrow T_-$ transitions. The probabilities for the discussed transitions—which are all forbidden in the absence of SO coupling—remain very small (less than 0.5%) as compared to the ones found for the single and three electrons.

For two electrons the role of the electric field for the low-energy optical absorption is different from the single-electron case. For $N=1$ the electric field distinctly shifts the energy of the absorption lines (Fig. 6). For $N=2$ the energy shift is very weak, only the transition probabilities are affected. For the single electron the energy shifts resulted from spatial electron-charge displacements of the initial and final states induced by the electric field. For two electrons these shifts are hampered (see Fig. 1) since the charge shift implies appearance of a double occupation of one of the dots. Figure 9 shows the charge localized in the left dot in function of the electric field. For $N=1$ (and $N=3$) the dependence of the charge on F_x is the strongest at zero electric field, while for $N=2$ we find the weakest dependence.

For $B=0$ we did not find any SO coupling influence on the charge distribution as a function of the in-plane electric

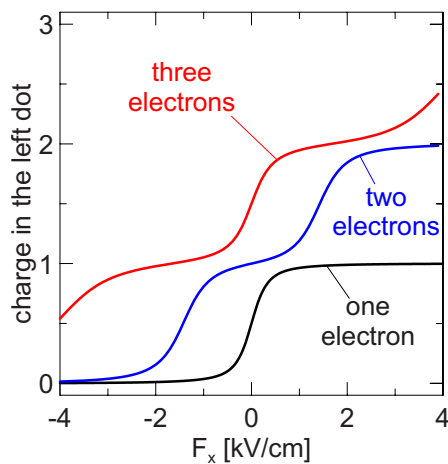


FIG. 9. (Color online) Electron charge localized in the left dot as a function of the electric field for the double dot at $B=0$. Results with and without SO coupling are not distinguishable.

field. Nevertheless, such an effect is observed in the presence of the external magnetic field—see Fig. 10. For $B=0.4$ T the ground-state without SO coupling corresponds already to the spin triplet, in which—due to the Pauli exclusion—localization of both electrons in the same dot requires occupation of an excited single-dot energy level. The charge of the two-electron system for the triplet ground-state is even more resistant to shifts by the electric field than for the singlet state [compare Figs. 10(b) and 10(d)]. For $B=0.4$ T the ground state becomes singlet again near 0.4 kV/cm. The electrons in the singlet state occupy more easily¹¹ the dot made deeper by the electric field which restores the singlet ground state when F_x is applied. We notice [see the dashed line in Fig. 10(d)] a jump in the occupation of the left dot at the singlet-triplet transition. For $B=0.6$ T a similar effect is observed only at higher F_x [the dashed line in Fig. 10(f)]. The SO coupling mixes the singlet and triplet states and we notice that the electron charge in the left dot [blue lines in Figs. 10(b), 10(d), and 10(f)] becomes a smooth function of F_x . As a general rule, when the ground state without SO coupling is singlet (triplet)—the SO coupling reduces (enhances) the occupation of the deeper dot.

At the singlet-triplet transition the SO coupling influences also the probability of finding both the electrons in the same

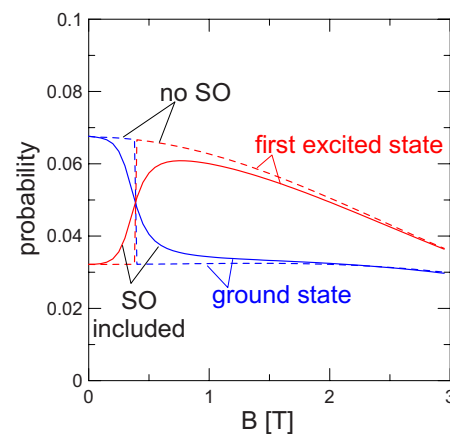


FIG. 11. (Color online) Probability that both the electrons occupy the same dot with and without SO coupling in the ground state and first excited state.

dot (Fig. 11). Without SO coupling the ground-state probability exhibits a rapid drop at the singlet-triplet transition near 0.4 T. The spin-orbit coupling influences the double occupation probability only for nonzero B .

In order to quantify the occupation of the single-electron even- and odd-parity orbitals we first project the two-electron eigenstates of operator [Eq. (11)] into the basis composed of single-electron eigenfunctions obtained without SO coupling (denoted as ψ' in the following). For a state ν we consider the projection in form

$$d_{kl}^{\nu} = \frac{1}{2} \sum_{i,j>i} C_{ij}^{\nu} \langle \psi_i(1)\psi_j(2) - \psi_i(2)\psi_j(1) | \nu \rangle, \quad (13)$$

$$| \psi'_k(1)\psi'_l(2) - \psi'_k(2)\psi'_l(1) \rangle.$$

An eigenfunction ψ'_k has a definite spatial parity and z component of the spin associated with a spinor χ_k which is the s_z eigenfunction of eigenvalue $\hbar/2$ or $-\hbar/2$ ($\chi_k = |\uparrow\rangle$ or $\chi_k = |\downarrow\rangle$). Hence, the occupation of the spin-up even-parity single-electron wave functions can be calculated as

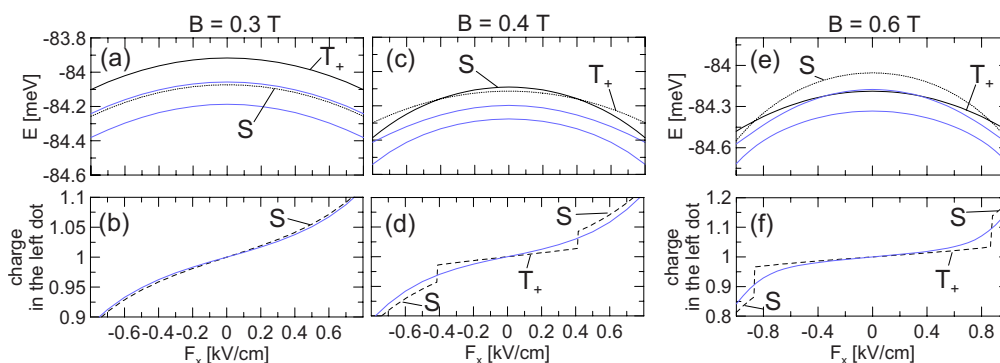


FIG. 10. (Color online) Two-electron energy spectrum of the double dot is shown in (a,c,e) as a function of the electric field. Plots (b,d,f) indicate the charge localized in the left dot. Black (blue) lines show the results without (with) SO coupling. The labels S and T_+ correspond to eigenstates without SO coupling.

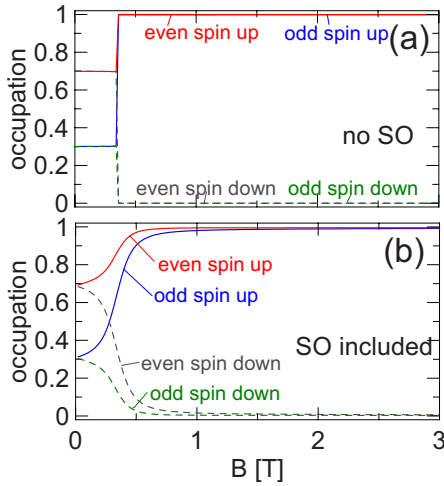


FIG. 12. (Color online) Occupation of the single-electron orbitals of definite spatial parity and spin for two-electron ground state with (b) and without (a) SO coupling for the electron pair in the double dot.

$$oc(e\uparrow) = \sum_{k,l>k} |d_{kl}|^2 [\delta_p(k,+)\delta_s(k,\uparrow) + \delta_p(l,+)\delta_s(l,\uparrow)], \quad (14)$$

where

$$\delta_p(k,\pm) = \frac{1 \pm \int [\psi'_k(r)]^* \psi'_k(-r) dr}{2} \quad (15)$$

and

$$\delta_s(k,\uparrow) = \langle \chi_k | \uparrow \rangle. \quad (16)$$

The occupation of the spin-up odd-parity single-electron states is determined by the formula

$$oc(o\uparrow) = \sum_{k,l>k} |d_{kl}|^2 [\delta_p(k,-)\delta_s(k,\uparrow) + \delta_p(l,-)\delta_s(l,\uparrow)], \quad (17)$$

with an obvious generalization for the spin-down components. The results are displayed in Fig. 12. Without SO coupling (i) below 0.4 T the ground state is even-parity singlet—the electrons occupy mostly the even-parity states (ii) above 0.4 T the ground-state is odd-parity triplet—the spin-down contributions are removed, one of the electrons occupy an even-parity and the other an odd-parity orbital. The jump of the occupations near 0.4 T that is observed in the results without SO coupling is replaced by a smooth transition when SO coupling is applied. The values obtained for orbital occupations in both large and zero B limits are similar.

Nonconservation of the spatial parity in the presence of SO coupling for the two-electron states becomes evident when one considers contributions of the two-electron basis elements. The contributions of the elements in which both electrons occupy orbitals of the same spatial parity are calculated as

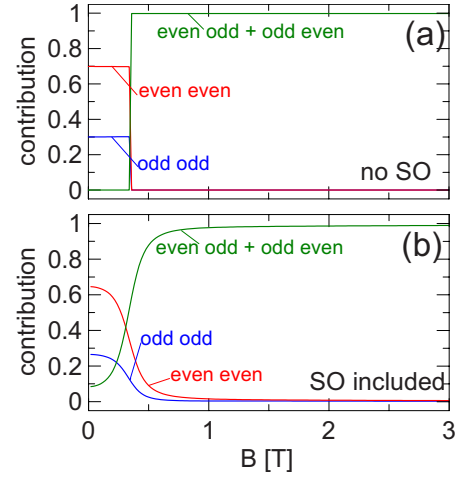


FIG. 13. (Color online) Contributions of the two-electron orbitals to the ground state with (b) and without (a) SO coupling for the electron pair in the double dot.

$$c_{ee} = \sum_{k,l>k} |d_{kl}|^2 \delta_p(k,+)\delta_p(l,+), \quad (18)$$

for the even-parity orbitals and

$$c_{oo} = \sum_{k,l>k} |d_{kl}|^2 \delta_p(k,-)\delta_p(l,-), \quad (19)$$

for the odd-parity orbitals. Contribution of the two-electron basis elements in which the electrons occupy opposite parities is

$$c_{oe+eo} = \sum_{k,l>k} |d_{kl}|^2 [\delta_p(k,-)\delta_p(l,+) + \delta_p(k,+)\delta_p(l,-)]. \quad (20)$$

The results are displayed in Fig. 13. Without SO coupling for $B < 0.4$ T the contribution of the basis elements in which the electrons occupy opposite parity eigenstates is zero. In the triplet ground state for $B > 0.4$ T the electrons are bound to occupy orbitals of opposite parities. When the SO is present for $B=0$ there is a nearly 10% contribution of basis elements in which the electrons occupy orbitals of opposite parities. The c_{oe+eo} grows with the magnetic field, but it stays below 100% in the studied range of B . This result and the ones presented above indicate that for two electrons the SO coupling has a noticeable influence on the ground-state properties in contrast to the single-electron case.

C. Three electrons

For $N=3$ in the absence of SO coupling the magnetic field leads to the ground-state spin-polarization transition near 3 T in both the single (Fig. 14) and double [Fig. 15(a)] dots. For symmetric dots this transition is associated with energy level crossing even when SO coupling is introduced since the ground states on both sides of the transition correspond to opposite s -parities. The in-plane electric field opens an avoided crossing at the ground-state spin-polarization transition [see Fig. 17(a)].

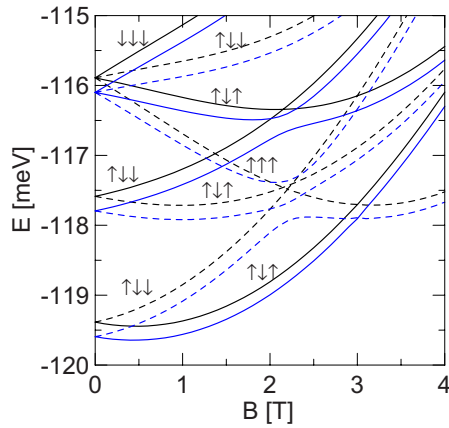


FIG. 14. (Color online) Three-electron energy spectrum for the single elongated dot. Black (blue) lines show the results without (with) SO coupling. Solid (dashed) lines correspond to even (odd) s -parity states. The arrows in the plot indicate the z component of the spin without SO coupling.

For three electrons in a single dot without SO coupling one observes (Fig. 14) crossings of three s -odd energy levels near 2 T. For the double dot [Fig. 15(a)] the crossings appear in more separated magnetic fields. The three crossing levels have different z projections of the spin. Similarly as for $N=1$ the SO coupling opens avoided crossing in the absorption spectrum, but for $N=3$ three energy levels participate in this avoided crossing instead of two. These avoided crossings are accompanied by a smooth variation of the spin [Fig. 15(b)].

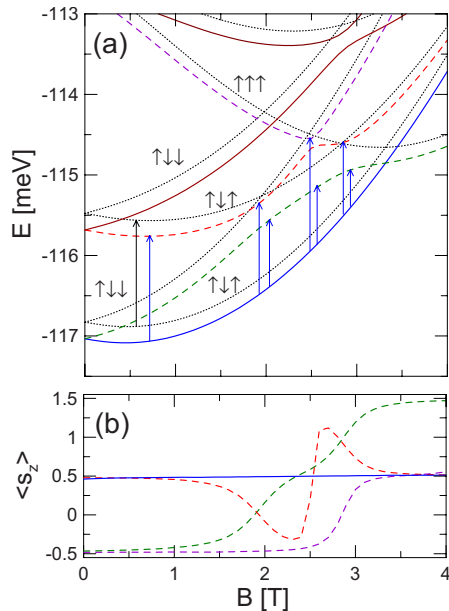


FIG. 15. (Color online) Three-electron energy spectrum (a) for the double dot. Black (color) lines show the results without (with) SO coupling. Solid (dashed) lines correspond to even (odd) s -parity. The short arrows in the plot indicate the z component of the spin without SO coupling and the longer ones show the allowed optical transitions from the ground-state. (b) z component of the spin for the lowest even s -parity and three lowest odd s -parity energy levels. Type and color of curves for these states is adopted of panel (a).

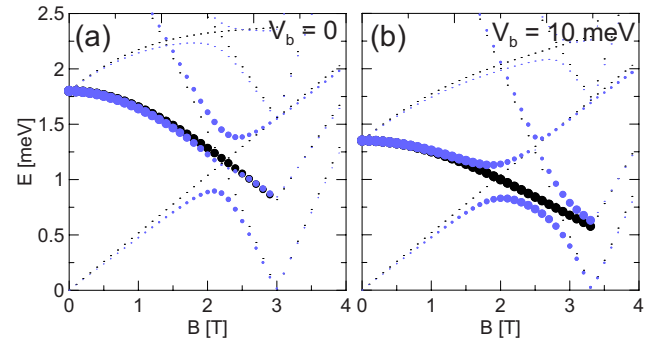


FIG. 16. (Color online) Optical absorption spectrum for the three-electron system in the single dot (a) and in the double dot (b). Black (blue) dots correspond to SO coupling absent (present). Area of the dot is proportional to the absorption probability.

For the spin unpolarized ground-state ($B < 3$ T) the lowest-energy optical transition goes from the ground-state to the odd s -parity states with $\langle s_z \rangle \approx \hbar/2$. Without SO coupling and in terms of occupation of single-electron orbitals we observe (Fig. 16) a transition of one of the electrons occupying a bonding orbital to an occupied antibonding orbital. One finds a single bright line similar to the one found for $N=1$. For $B > 3$ T the principle line in the ground-state

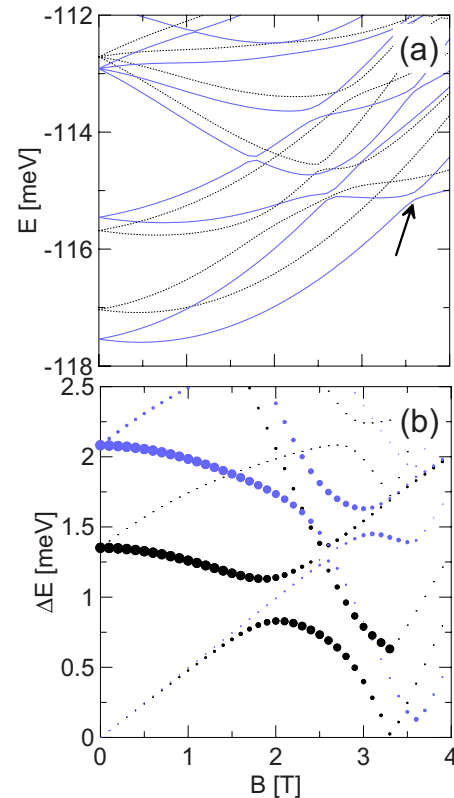


FIG. 17. (Color online) (a) Three electron energy spectrum for SO-coupled double dot at $F_x=0$ (black dotted lines) and for $F_x=0.5$ kV/cm (blue solid curves). The arrow indicates the ground-state avoided crossing which is opened in presence of nonzero F_x . (b) Optical absorption spectrum for the SO-coupled double dot. Black (blue) dots correspond to $F_x=0$ ($F_x=0.5$ kV/cm).

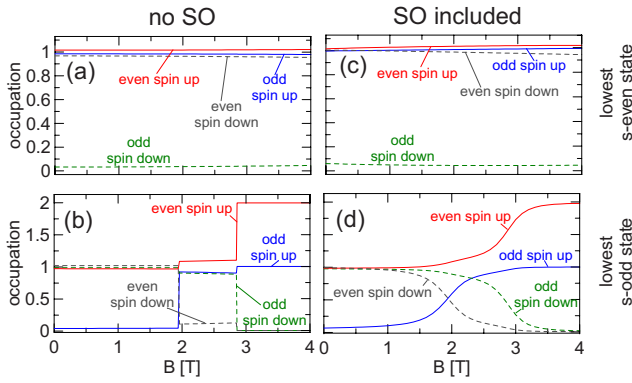


FIG. 18. (Color online) Occupation of the single-electron orbitals of definite spin orientation and spatial parity without (a,b) and with (c,d) SO coupling for the lowest-energy s -even (a,c) and s -odd (b,d) state for three electrons in the double dot.

absorption spectrum disappears due to the ground-state spin polarization.

The in-plane electric field increases the energy splitting between the ground-state and the first excited state leading to an increase of the energy absorbed at the optical transition [Fig. 17(b)]. The form of the avoided crossing is not affected by the field—like in the single-electron case.

For the lowest-energy even s -parity state both occupation of single-electron spin orbitals [Figs. 18(a) and 18(c)] and contribution of three-electron basis elements of definite spatial parity [Figs. 19(a) and 19(c)] are only weakly affected by both the magnetic field and the spin-orbit coupling. The dependence of the studied quantities on the magnetic field is more spectacular for the lowest energy s -odd state [Figs. 18(b), 18(d), 19(b), and 19(d)]. Without SO coupling the lowest-energy s -odd level corresponds to even parity only between 1.9 and 2.8 T, hence the vanishing contribution of the even-parity three-electron basis elements outside this B interval. In the presence of SO coupling the contribution of the even-parity basis elements extends over the entire studied range of the magnetic field.

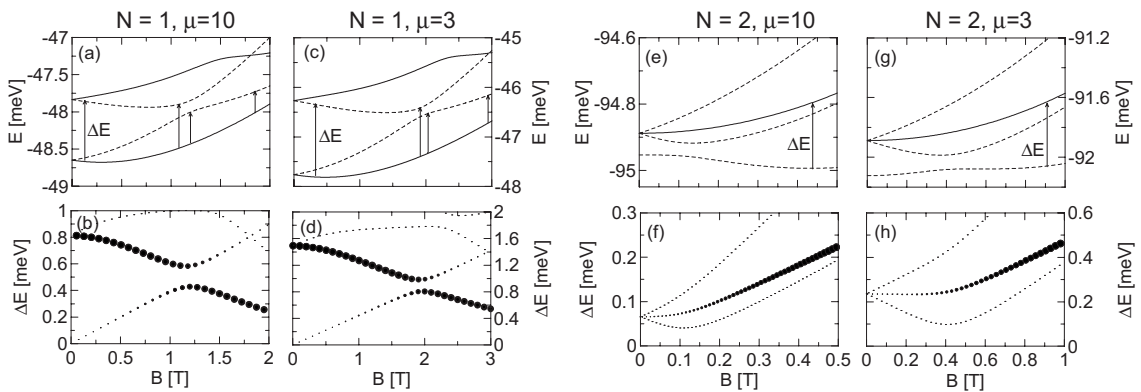


FIG. 20. Energy spectra (a,c,e,g) and the absorption spectra (b,d,f,h) for a single (a–d) and two (e–h) electrons for a single elongated quantum dot with the lateral sizes increased twice $2R_x=180$ nm, $2R_y=80$ nm with respect of the results presented above. In (a,b,e,h) we kept $\mu=10$ in Eq. (9) (as above) for which the lateral confinement profile is a square quantum well and in (c,d,g,h) a smoother profile with $\mu=3$ was adopted.

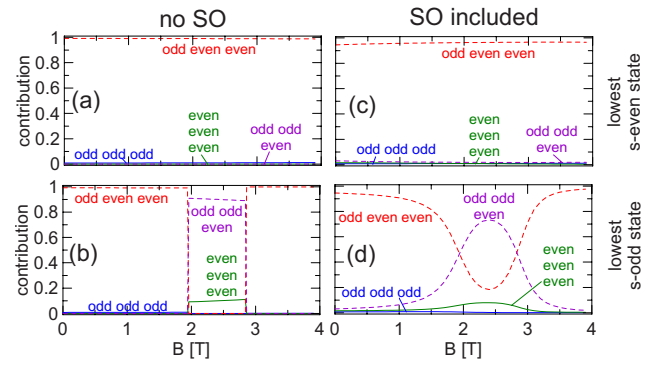


FIG. 19. (Color online) Contributions of single-electron orbitals of a given symmetry to the lowest-energy three electron s -even (a,c) and s -odd (b,d) states, with (c,d) and without (a,b) SO coupling.

D. Results for a larger dot

The results obtained above for the double dot and for the single elongated quantum dot for the energy and absorption spectra are qualitatively similar. In fact the results stay qualitatively the same as long as the strong anisotropy of the confinement potential is present. In order to illustrate this fact we increased the size of the dot twice in both x and y directions. The energy and absorption spectra for $2R_x=180$ nm and $2R_y=80$ nm are displayed in Fig. 20 for one (a–d) and two (e–h) electrons. In Figs. 20(a), 20(b), 20(e), and 20(f) we keep the same nearly square lateral profile of the confinement potential, and in the rest of the plots we made it smoother by replacing the exponent $\mu=10$ by $\mu=3$ in Eq. (9). We can see that the energy and the magnetic fields range changes, but the plots retain their character seen above in Fig. 2, 5, 7, and 8.

IV. SUMMARY AND CONCLUSIONS

We have presented a systematic exact diagonalization study of one, two and three-electron spin-orbit coupled systems in double quantum dots. We discussed the mixing of the bonding and antibonding electron orbitals by the SO cou-

pling. We investigated occupation of even- and odd-parity orbitals, the energy and optical absorption spectra in crossed electric and magnetic fields as well as the electron distribution.

For one and three electrons confined in a pair of identical dots we found that the spin-orbit coupling only weakly affects the ground-state properties. A strong mixing of bonding and antibonding orbitals due to the spin-orbit coupling was found in the lowest-energy excited states.

In contrast to the odd electron numbers, for two electrons the spin-orbit interaction affects the properties of the ground state since the spin polarization becomes a smooth transition instead of an abrupt singlet-triplet transformation. On the contrary, the spin polarization of the three electron system in symmetric dots is not affected by the spin-orbit coupling since the low- and high-spin ground-states correspond to opposite s -parities. For three electrons the SO coupling makes the spin-polarization continuous only when the confinement potential contains an in-plane asymmetry, e.g., introduced by an electric field.

For odd electron numbers the spin-orbit-coupling-induced mixing of spatial parities of the first excited state opens char-

acteristic avoided crossings in the optical absorption spectrum. An in-plane electric field shifts the initial and final states of the optical transition to opposite dots. In consequence it distinctly increases the energy of the optical transition at an expense of a reduced width of the avoided crossing.

The low-energy optical absorption for two electrons is only allowed by the SO coupling. For two electrons the in-plane electric field lifts the spatial parity selection rules but does not essentially perturb the energy of the optical transitions.

ACKNOWLEDGMENTS

This work was supported by the “Krakow Interdisciplinary PhD-Project in Nanoscience and Advanced Nanostructures” operated within the Foundation for Polish Science MPD Programme co-financed by the EU European Regional Development Fund. Calculations were performed in ACK-CYFRONET-AGH on the RackServer Zeus.

-
- ¹X. Hu and S. Das Sarma, *Phys. Rev. A* **61**, 062301 (2000).
²A. Harju, S. Siljamäki, and R. M. Nieminen, *Phys. Rev. Lett.* **88**, 226804 (2002).
³G. Burkard, D. Loss, and D. P. DiVincenzo, *Phys. Rev. B* **59**, 2070 (1999).
⁴H. J. Krenner, M. Sabathil, E. C. Clark, A. Kress, D. Schuh, M. Bichler, G. Abstreiter, and J. J. Finley, *Phys. Rev. Lett.* **94**, 057402 (2005); E. A. Stinaff, M. Scheibner, A. S. Bracker, I. V. Pomonarev, V. L. Korenev, M. E. Ware, M. F. Doty, T. L. Reinicke, and D. Gammon, *Science* **311**, 636 (2006); H. J. Krenner, E. C. Clark, T. Nakaoka, M. Bichler, C. Scheurer, G. Abstreiter, and J. J. Finley, *Phys. Rev. Lett.* **97**, 076403 (2006).
⁵J. I. Climente, M. Korkusiński, G. Goldoni, and P. Hawrylak, *Phys. Rev. B* **78**, 115323 (2008); M. F. Doty, J. I. Climente, M. Korkusiński, M. Scheibner, A. S. Bracker, P. Hawrylak, and D. Gammon, *Phys. Rev. Lett.* **102**, 047401 (2009).
⁶Y. A. Bychkov and E. I. Rashba, *J. Phys. C* **17**, 6039 (1984).
⁷G. Dresselhaus, *Phys. Rev.* **100**, 580 (1955).
⁸P. Pietiläinen and T. Chakraborty, *Phys. Rev. B* **73**, 155315 (2006); T. Chakraborty and P. Pietiläinen, *Phys. Rev. Lett.* **95**, 136603 (2005).
⁹J. M. Elzerman, R. Hanson, J. S. Greidanus, L. H. Willems van Beveren, S. De Franceschi, L. M. K. Vandersypen, S. Tarucha, and L. P. Kouwenhoven, *Phys. Rev. B* **67**, 161308(R) (2003); R. Hanson, L. H. Willems van Beveren, I. T. Vink, J. M. Elzerman, W. J. M. Naber, F. H. L. Koppens, L. P. Kouwenhoven, and L. M. K. Vandersypen, *Phys. Rev. Lett.* **94**, 196802 (2005).
¹⁰J. R. Petta, A. C. Johnson, J. M. Taylor, E. A. Laird, A. Yacoby, M. D. Lukin, C. M. Marcus, M. P. Hanson, and A. C. Gossards, *Science* **309**, 2180 (2005).
¹¹B. Szafran, F. M. Peeters, and S. Bednarek, *Phys. Rev. B* **70**, 205318 (2004).
¹²J. Pedersen, C. Flindt, N. A. Mortensen, and A.-P. Jauho, *Phys. Rev. B* **76**, 125323 (2007).
¹³A. L. Saraiva, M. J. Calderon, and B. Koiller, *Phys. Rev. B* **76**, 233302 (2007).
¹⁴M. Stopa, A. Vidan, T. Hatano, S. Tarucha, and R. M. Westervelt, *Physica E (Amsterdam)* **34**, 616 (2006).
¹⁵D. V. Melnikov, J.-P. Leburton, A. Taha, and N. Sobh, *Phys. Rev. B* **74**, 041309(R) (2006).
¹⁶F. Baruffa, P. Stano, and J. Fabian, *Phys. Rev. Lett.* **104**, 126401 (2010).
¹⁷S. Gangadharaiah, J. Sun, and O. A. Starykh, *Phys. Rev. Lett.* **100**, 156402 (2008).
¹⁸P. Stano and J. Fabian, *Phys. Rev. Lett.* **96**, 186602 (2006).
¹⁹V. N. Golovach, A. Khaetskii, and D. Loss, *Phys. Rev. B* **77**, 045328 (2008).
²⁰K. Shen and M. W. Wu, *Phys. Rev. B* **76**, 235313 (2007).
²¹T. Meunier, I. T. Vink, L. H. Willems van Beveren, K.-J. Tielrooij, R. Hanson, F. H. L. Koppens, H. P. Tranitz, W. Wegscheider, L. P. Kouwenhoven, and L. M. K. Vandersypen, *Phys. Rev. Lett.* **98**, 126601 (2007).
²²J. I. Climente, A. Bertoni, G. Goldoni, M. Rontani, and E. Molinari, *Phys. Rev. B* **75**, 081303(R) (2007).
²³C. Fasth, A. Fuhrer, L. Samuelson, V. N. Golovach, and D. Loss, *Phys. Rev. Lett.* **98**, 266801 (2007).
²⁴A. Pfund, I. Shorubalko, K. Ensslin, and R. Leturcq, *Phys. Rev. B* **76**, 161308(R) 2007.
²⁵K. V. Kavokin, *Phys. Rev. B* **64**, 075305 (2001).
²⁶N. E. Bonesteel, D. Stepanenko, and D. P. DiVincenzo, *Phys. Rev. Lett.* **87**, 207901 (2001).
²⁷G. Burkard and D. Loss, *Phys. Rev. Lett.* **88**, 047903 (2002).
²⁸L.-A. Wu and D. A. Lidar, *Phys. Rev. A* **66**, 062314 (2002).
²⁹D. Stepanenko and N. E. Bonesteel, *Phys. Rev. Lett.* **93**, 140501 (2004).
³⁰S. Debal and C. Emary, *Phys. Rev. Lett.* **94**, 226803 (2005).

- ³¹C. Flindt, A. S. Sorensen, and K. Flensberg, *Phys. Rev. Lett.* **97**, 240501 (2006).
- ³²S. Bednarek and B. Szafran, *Phys. Rev. Lett.* **101**, 216805 (2008).
- ³³P. Földi, O. Kálmán, M. G. Benedict, and F. M. Peeters, *Phys. Rev. B* **73**, 155325 (2006); *Nano Lett.* **8**, 2556 (2008).
- ³⁴P. Stano and J. Fabian, *Phys. Rev. B* **72**, 155410 (2005).
- ³⁵L. Meza-Montes, C. F. Destefani, and S. E. Ulloa, *Phys. Rev. B* **78**, 205307 (2008).
- ³⁶E. A. de Andrada e Silva, G. C. La Rocca, and F. Bassani, *Phys. Rev. B* **55**, 16293 (1997).
- ³⁷S. Saikin, M. Shen, M. Cheng, and V. Privman, *J. Appl. Phys.* **94**, 1769 (2003).
- ³⁸M. Willatzen and L. C. Lew Yan Voon, *J. Phys.: Condens. Matter* **20**, 345216 (2008).
- ³⁹S. Bednarek, B. Szafran, K. Lis, and J. Adamowski, *Phys. Rev. B* **68**, 155333 (2003).
- ⁴⁰L. Wang, A. Rastelli, S. Kiravittaya, P. Atkinson, F. Ding, C. C. Bof Bufon, C. Hermannstädter, M. Witzany, G. J. Beirne, P. Michler, and O. G. Schmidt, *New J. Phys.* **10**, 045010 (2008).
- ⁴¹T. Chwiej and B. Szafran, *Phys. Rev. B* **78**, 245306 (2008).
- ⁴²B. Szafran, M. P. Nowak, S. Bednarek, T. Chwiej, and F. M. Peeters, *Phys. Rev. B* **79**, 235303 (2009).
- ⁴³W. Pan, K. Lai, S. P. Bayrakci, N. P. Ong, D. C. Tsui, L. N. Pfeiffer, and K. West, *Appl. Phys. Lett.* **83**, 3519 (2003).

4 Time-dependent configuration-interaction simulations of spin swap in spin-orbit-coupled double quantum dots

Time-dependent configuration-interaction simulations of spin swap in spin-orbit-coupled double quantum dots

M. P. Nowak and B. Szafran

*Faculty of Physics and Applied Computer Science, AGH University of Science and Technology,
al. Mickiewicza 30, 30-059 Kraków, Poland*

(Received 21 May 2010; revised manuscript received 4 August 2010; published 12 October 2010)

We perform time-dependent simulations of spin exchange for an electron pair in laterally coupled quantum dots. The calculation is based on configuration interaction scheme accounting for spin-orbit (SO) coupling and electron-electron interaction in a numerically exact way. Noninteracting electrons exchange orientations of their spins in a manner that can be understood by interdot tunneling associated with spin precession in an effective SO magnetic field that results in anisotropy of the spin swap. The Coulomb interaction blocks the electron transfer between the dots but the spin transfer and spin precession due to SO coupling is still observed. The electron-electron interaction additionally induces an appearance of spin components in the direction of the effective SO magnetic field which are opposite in both dots. Simulations indicate that the isotropy of the spin swap is restored for equal Dresselhaus and Rashba constants and properly oriented dots.

DOI: [10.1103/PhysRevB.82.165316](https://doi.org/10.1103/PhysRevB.82.165316)

PACS number(s): 73.21.La, 03.67.Lx, 71.70.Gm, 75.70.Tj

I. INTRODUCTION

One of ideas for solid-state quantum computation employs spins of electrons confined in quantum dots^{1,2} for information storage and processing. This idea drives an extensive experimental research on spin manipulation,³ detection,⁴ decoherence, and relaxation.⁵ Construction of a universal quantum gate requires implementation of a controllable spin-exchange operations between electrons confined in adjacent dots. In the absence of spin-orbit (SO) coupling, the spin-spin Hamiltonian possesses an isotropic form,² i.e., depends only on relative orientation of the spins. Anisotropic corrections⁶⁻⁸ are introduced by SO coupling. The spin processing procedures were revised^{9,10} in order to remove or minimize the anisotropy due to the SO coupling. On the other hand a practical use was invented for the anisotropic exchange interaction in construction of quantum gates.¹¹⁻¹³ A recent study¹⁴ reported that the anisotropic part of the exchange interaction vanishes in zero magnetic field which should lift the limitations for spin information processing that were the major concern of the previous work.^{6,9-13} The conclusion was supported by comparison¹⁴ of the double dot energy spectrum as found by the exact diagonalization technique and by a model Hamiltonian.

The spin interactions for two-electron systems are probed by charging experiments¹⁵ that resolve the singlet-triplet avoided crossings due to the SO coupling. These avoided crossings occur in external magnetic field, for which anisotropy of the exchange interaction is evident. At the moment the spin dynamics for double quantum dots in zero magnetic field can only be verified in a numerical experiment which we provide in this work. We present results of simulation in which the spin dynamics is monitored in time. We use the method of configuration interaction to simulate the spin swap in laterally coupled quantum dots. Our numerically exact results indicate that the swap process and result depend on the initial orientation of the spins also in zero magnetic field. We point out that the main source of the anisotropy is the effective magnetic field due to the SO coupling^{16,17} that leads to

precession of spins of moving electrons. The Coulomb interaction blocks the single-electron motion within the double dot. Nevertheless, the collective motion is still observed and we find that it results in the transfer of the spin associated with its precession. Moreover, we demonstrate that the Coulomb interaction leads to an appearance of spin components in the direction of the effective magnetic field which are opposite in both dots.

The effects of the SO coupling for electron energy spectra is lifted and SU(2) symmetry is restored when the Dresselhaus and Rashba interactions acquire the same strength.¹⁸ The Rashba¹⁹ interaction can be controlled by external electric fields and restoration of SU(2) symmetry allows for appearance of helical spin-density waves in the two-dimensional electron gas. Our simulations indicate that for equal Dresselhaus and Rashba coupling constants the spin swap becomes isotropic for carefully chosen spatial orientation of the double dot for which the SO effective magnetic field vanishes.

II. THEORY

We consider a two-dimensional Hamiltonian

$$h = \left[\frac{\hbar^2 \mathbf{k}^2}{2m^*} + V(\mathbf{r}) \right] \mathbf{1} + H_{SIA} + H_{BIA}, \quad (1)$$

where $\mathbf{k} = -i\nabla$, $\mathbf{1}$ is the identity matrix, $V(\mathbf{r})$ stands for the confinement potential, H_{SIA} and H_{BIA} introduce the Rashba and Dresselhaus SO interactions, respectively. For x and y axes oriented parallel to $[100]$ and $[010]$ crystal directions, SO interaction terms are given by $H_{BIA} = \beta(\sigma_x k_x - \sigma_y k_y) + H_{cub}$, and $H_{SIA} = \alpha(\sigma_x k_y - \sigma_y k_x) + H_{diag}$. The cubic Dresselhaus term H_{cub} and the diagonal Rashba terms H_{diag} (for their form see Ref. 20) are included in the calculation but have a negligible influence on the spin evolution. We use $\text{In}_{0.5}\text{Ga}_{0.5}\text{As}$ effective mass $m^* = 0.0465m_0$, dielectric constant $\epsilon = 13.55$ and assume a model confinement potential²⁰ $V(x, y) = -V_0 / [(1 + [x^2/R_x^2]^\mu)(1 + [y^2/R_y^2]^\mu)] + V_b / [(1$

$+[x^2/R_b^2]^\mu)(1+[y^2/R_y^2]^\mu)$, where $\mu=10$, $V_0=50$ meV is depth of dots, and $V_b=10$ meV is the height of the interdot barrier. The size of the double dot system in x and y directions is $2R_x=90$ nm and $2R_y=40$ nm, respectively. $2R_b=10$ nm is the interdot barrier width.

Calculations for the two-electron system start by diagonalization of the Hamiltonian

$$H = h_1 + h_2 + \frac{e^2}{4\pi\epsilon\epsilon_0|\mathbf{r}_1 - \mathbf{r}_2|} \quad (2)$$

in the basis of eigenstates of Eq. (1) that are in turn determined using a multicenter Gaussian variational wave function.²⁰ The eigenvalues E_m of Hamiltonian (2) and the corresponding eigenfunctions $\Psi_m(\mathbf{r}_1, \sigma_1, \mathbf{r}_2, \sigma_2)$ obtained from the configuration interaction scheme are used for simulation of the time evolution as described by the Schrödinger equation $i\hbar \frac{d\Psi}{dt} = H\Psi$

$$\Psi = \sum_m c_m \exp(-iE_m t/\hbar) \Psi_m, \quad (3)$$

where c_m coefficients are determined by the initial condition.²¹ For diagonalization of Hamiltonian (2) we use a basis of 325 two-electron wave functions obtained from 26 lowest energy single-electron eigenstates. The convergence of the results is discussed in the Appendix.

In order to simulate the spin swap, in the initial condition we localize the electrons in separate dots with opposite spin orientations. We denote the initial spatial single-electron wave functions localized in the left and right dots by ψ_l and ψ_r , respectively. Functions ψ_l and ψ_r are obtained by superposition of bonding and antibonding orbitals that are obtained as two lowest energy eigenstates of Hamiltonian (1) *without* the SO coupling. The initial two-electron wave function is taken as an antisymmetrized product $\Psi_{l\downarrow r\uparrow} = \frac{1}{\sqrt{2}}[\psi_l(\mathbf{r}_1)s_+(\sigma_1)\psi_r(\mathbf{r}_2)s_-(\sigma_2) - \psi_l(\mathbf{r}_2)s_+(\sigma_2)\psi_r(\mathbf{r}_1)s_-(\sigma_1)]$, where s_+ and s_- are orthogonal eigenfunctions of a chosen spin component. Projection of these wave functions on eigenfunctions of Hamiltonian (2) defines $c_m = \langle \Psi_{l\downarrow r\uparrow} | \Psi_m \rangle$ used in Eq. (3).

Below we consider precession of a single electron spin in the effective magnetic field due to the SO coupling.¹⁶ For this purpose we solve the Bloch equation

$$\frac{d\langle \mathbf{s} \rangle}{dt} = g\mu_b \langle \mathbf{B}_{\text{SO}} \times \mathbf{s} \rangle / \hbar, \quad (4)$$

where μ_b is the Bohr magneton and \mathbf{B}_{SO} is the effective magnetic field due to the linear (dominating) terms of the SO coupling

$$\mathbf{B}_{\text{SO}} = \frac{2\alpha}{g\mu_B} \begin{pmatrix} k_y \\ -k_x \\ 0 \end{pmatrix} + \frac{2\beta}{g\mu_B} \begin{pmatrix} k_x \\ -k_y \\ 0 \end{pmatrix}. \quad (5)$$

For each time step we evaluate the right-hand side of Eq. (4) using the average values as provided by the time evolution in the basis of single-electron eigenstates

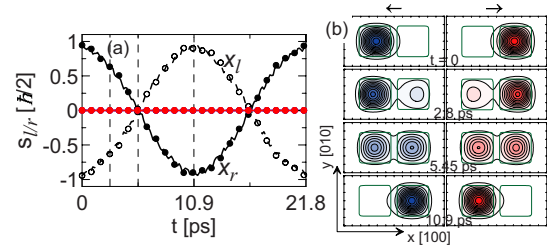


FIG. 1. (Color online) Spin-swap simulation for quantum dots placed on the x axis. In the initial condition one electron is localized in the left dot ($x < 0$) with spin oriented antiparallel to the x axis and the other electron is localized in the right dot ($x > 0$) with the spin parallel to the x axis. Results were obtained for pure Dresselhaus coupling. (a) Black lines show the x component of the spin stored in the left (dashed) and right (solid) quantum dots (Ref. 24). The circles indicate the results obtained without SO coupling. Average values of y and z components is zero with grey (red online) lines or without grey (red online) circles SO coupling. (b) Spin-left (left column) and spin-right (right column) densities in selected moments in time.

$$\begin{pmatrix} \frac{d\langle s_x \rangle}{dt} \\ \frac{d\langle s_y \rangle}{dt} \\ \frac{d\langle s_z \rangle}{dt} \end{pmatrix} = \frac{2\alpha}{\hbar} \begin{pmatrix} -\langle k_x s_z \rangle \\ -\langle k_y s_z \rangle \\ \langle k_x s_x \rangle + \langle k_y s_y \rangle \end{pmatrix} + \frac{2\beta}{\hbar} \begin{pmatrix} -\langle k_y s_z \rangle \\ -\langle k_x s_z \rangle \\ \langle k_x s_y \rangle + \langle k_y s_x \rangle \end{pmatrix}. \quad (6)$$

III. RESULTS

Two-dimensional SO coupling constants depend on the thickness d of the confinement layer $\beta = \gamma(\pi/d)^2$, and on the value of vertical electric field F_z (external or built-in) $\alpha = \alpha_{3D}F_z$, where γ and α_{3D} are bulk Dresselhaus and Rashba constants, respectively. We use $\gamma = 32.2$ meV nm³ for the InGaAs alloy²² and assume $d = 5.4$ nm which gives $\beta = 10.8$ meV nm. This seems a maximal value of the coupling constant that can be practically achieved in an InGaAs quantum dot. The bulk Rashba constant of the alloy is $\alpha_{3D} = 0.572$ nm² (after Ref. 23). The electric field needed to produce $\alpha = 10.8$ meV nm is 18.9 meV/nm, which is equivalent to the confinement potential drop of 102 meV across the dot of the height $d = 5.4$ nm. Results presented below stay qualitatively unaffected for smaller values of the coupling constants or weaker interdot coupling (for the latter—see the Appendix).

A. Quantum dots placed along [100] direction

Let us first assume that the confinement potential is symmetric in the growth direction ($\alpha = 0$) and that the centers of the dots are placed on the x axis. Initially the spin in the left (right) dot is set parallel (antiparallel) to the x axis. Figure 1(a) shows the time dependence of the average spin stored in the left and right dot.²⁴ For $t = 0$ the spins in the left and right

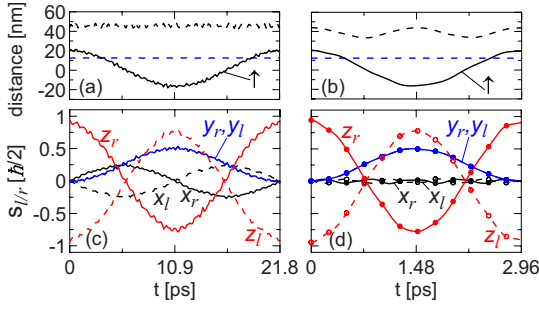


FIG. 2. (Color online) Simulation similar to the one presented in Fig. 1 only for electron spins set initially parallel or antiparallel to the z axis. In the left (right) column of plots the Coulomb interaction is included (neglected). [(a) and (b)] The average position of the spin-up density (black solid line). The electron-electron distance (dashed lines) in the x (black), and y (blue) directions, calculated as $\sqrt{\langle(x_1-x_2)^2\rangle}$ and $\sqrt{\langle(y_1-y_2)^2\rangle}$, respectively. [(c) and (d)] The spin components stored in the left (dashed curves) and right (solid curves) quantum dots (Ref. 24). Here and in all the other plots the x , y , and z components of the spin are given by black, blue, and red lines, respectively. Circles in (d)—see text.

dots are not exactly equal to $\pm\hbar/2$ due to leakage of ψ_l (ψ_r) functions to the right (left) dot [see Fig. 1(b) for $t=0$]. The spin swap is completed at $t=t_s=10.9$ ps and no other component of the spin is generated during the process.

The swap process *exactly* as illustrated in Fig. 1(a) is obtained in the absence of SO interaction independent of the choice of the direction in which the electron spins are initially set antiparallel to each other. In order to present the effects of SO coupling for the spin swap, let us change the initial condition. At $t=0$ the spin in the right (left) dot is now set parallel (antiparallel) to the z axis [see Fig. 2(c)]. At $t=t_s$ the absolute values of $\langle s_z \rangle$ are visibly reduced as compared to the initial condition and the spins in both dots acquire an identical nonzero value of the y component. Moreover, opposite components of the spin in the x direction are generated in both dots during the swap. The x spin components are maximal at $t=t_s/2$ and disappear once the swap is completed.

For $\alpha=0$ the SO effective magnetic field of Eq. (5) is oriented along the x axis—the direction of electron tunneling between the dots. In order to evaluate the effects of the spin precession we performed calculations for a single electron. We localize the electron in the left dot and assume that its spin is oriented antiparallel to the x [Figs. 3(a), 3(d), and 3(g)], y [Figs. 3(b), 3(e), and 3(h)], and z axes [Figs. 3(c), 3(f), and 3(i)]. The electron wave packet oscillates between the left and right dots [Figs. 3(g)–3(i)]. The electron—localized initially in the left dot with the spin aligned with the z (y) direction—acquires a nonzero y (z) component of the spin when it tunnels to the right dot [Figs. 3(e) and 3(f)]. Figures 3(a)–3(c) show that the spin evolution as obtained by integration of the Bloch Eq. (4) describing the spin precession perfectly agrees with the results of the main simulation. For the spin initially set antiparallel to the x axis—i.e., aligned with \mathbf{B}_{SO} —no precession is observed [Figs. 3(a) and 3(d)].

Let us now return to the problem of two electrons with spins initially parallel and antiparallel to the z axis. The re-

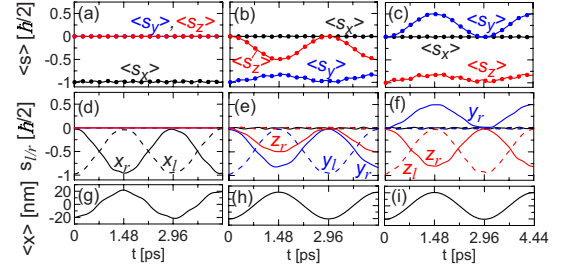


FIG. 3. (Color online) Simulation for a single electron, pure Dresselhaus coupling and dots placed on the x axis. The electron is initially localized in the left dot with spin-oriented antiparallel to the x , y , and z axis in the left, central, and right columns of plots, respectively. [(a)–(c)] Average values of spin components are given by curves. The circles indicate the results obtained from the Bloch Eq. (4). [(d)–(f)] The spin stored in the left (dashed lines) and the right (solid lines) quantum dots. Black, blue, and red lines show the results for x , y , and z components, respectively. [(g)–(i)] The average x position of the electron packet.

sults for noninteracting pair of electrons [given by lines in Fig. 2(d)] are exactly reproduced by the sum of single-electron solutions [dots in Fig. 2(d)]. Figure 2(b) shows that the horizontal electron-electron distance oscillates as the noninteracting electrons tunnel from one dot to the other and meet at the interdot barrier. The same y component of the spin is generated in both dots in any moment of time. The electron spins are initially oppositely oriented with respect to the z axis and move in the opposite directions along the x axis. Accordingly, the change of y spin component as given by Eq. (6) has the same sign for both electrons.

When the Coulomb repulsion is switched on, the oscillation of the electron-electron distance is no longer observed [Fig. 2(a)]—the electrons occupy fixed positions in separate dots. The electron density—the sum of spin-up and spin-down electron densities—is nearly stationary but the components of the sum are not. In Figs. 2(a) and 2(b) with the black solid line we plotted the center of mass of the spin-up electron-density packet. We notice that this center oscillates in a very similar way for both interacting and noninteracting electrons. Also the spin swap as obtained for interacting electrons is similar to the one found in the absence of the Coulomb repulsion [cf. Figs. 2(c) and 2(d)], only the swap time is increased by a factor of 10 as the Coulomb repulsion enhances the effective height of the interdot barrier. The only qualitative feature introduced by the Coulomb interaction is the noticeable oscillation of the x component of the spin. We found as a general rule for interacting electrons that during the spin precession opposite spin components in the direction of \mathbf{B}_{SO} appear in both dots.

Figure 4 shows the results for spins initially antiparallel in the y direction, still for the pure Dresselhaus coupling. The appearance of the z component of the spin during the swap is due to spin precession and is observed for both interacting [Fig. 4(a)] and noninteracting [Fig. 4(b)] electrons. For the Coulomb interaction present the opposite spin components in the x direction (aligned with \mathbf{B}_{SO}) appear in the dots, similarly as presented in Fig. 2(c) for the spins initially aligned with the z axis.

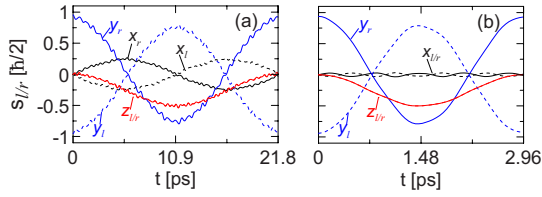


FIG. 4. (Color online) (a) Same as Fig. 2(c). (b) Same as Fig. 2(d) only for electron spins initially antiparallel in the y direction.

To further illustrate the findings of the above paragraph let us consider the case of pure Rashba coupling (Fig. 5). In III-V material the Dresselhaus coupling cannot be completely removed. Nevertheless, it can be small as compared to the Rashba coupling provided that the dots height is large and/or strong electric field is applied in the growth direction. For the pure Rashba coupling and the considered orientation of the dots \mathbf{B}_{SO} is aligned with the y axis [see Eq. (5)]. For the spins initially parallel and antiparallel to this axis, the spin swap [Figs. 5(c) and 5(d)] occurs without generation of neither x nor z spin components. For the spins initially aligned with x (z) axis one observes appearance of z (x) spin component—the same in both dots—for both interacting and noninteracting electrons—see Figs. 5(a) and 5(b) [Figs. 5(e) and 5(f)] that results from the spin precession. According to Eq. (6) for $\beta=0$ the electron spin that is initially parallel to the x axis and moves in the x direction acquires the z component of the same sign as the spin antiparallel to the x axis that moves in the $-x$ direction [Figs. 5(a) and 5(b)]. When the electron-electron interaction is present we additionally observe [see Figs. 5(a) and 5(e)] an appearance of opposite spin components in the y direction (i.e., direction of \mathbf{B}_{SO}) in both dots.

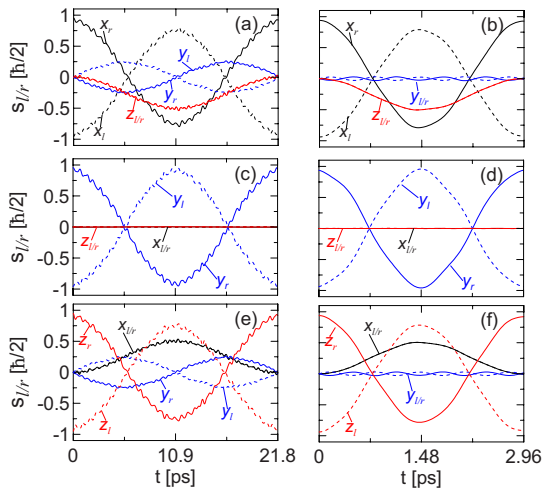


FIG. 5. (Color online) Simulation for pure Rashba coupling and centers of dots placed on the x axis. The electrons in the left and right dots initially possess opposite spins in [(a) and (b)] x , [(c) and (d)] y , [(e) and (f)] and z directions. Black, blue, and red curves show the x , y , and z spin components stored in the left (dashed curve) and the right (solid curve) dots. Plots (b), (d), and (f) were obtained for neglected electron-electron interaction which is included in (a), (c), and (e).

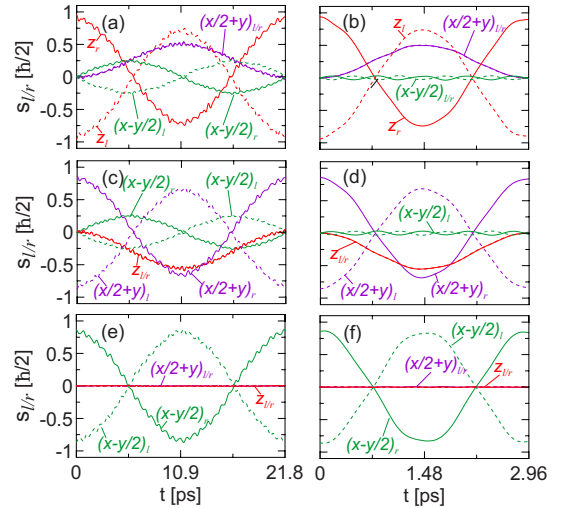


FIG. 6. (Color online) Simulation for both SO coupling types present $\alpha=\beta/2=5.4$ meV nm and centers of dots placed on the x direction. The electrons in the left and right dots initially possess opposite spins along z ($[001]$) direction in (a) and (b), $x/2+y$ ($[1,2,0]$) in (c) and (d), and $x-y/2$ ($[2,\bar{1},0]$) in (e) and (f). Purple, green, and red curves show the $[1,2,0]$, $[2,\bar{1},0]$, and $[0,0,1]$ spin components stored in the left (dashed curve) and the right (solid curve) dots. Plots (b), (d), and (f) were obtained for neglected electron-electron interaction which is included in (a), (c), and (e).

Finally, Fig. 6 shows the results for both coupling types present with $\beta=10.8$ meV nm and $\alpha=5.4$ meV nm. For the electrons moving between the two dots, the SO magnetic field vector is aligned with the $x-y/2$ line, i.e., the $[2\bar{1}0]$ crystal direction. For the discussion of the spin behavior we consider this crystal direction and two orthogonal ones: within the plane of confinement $[120]$, and in the growth direction $[001]$. When the electron spins are initially aligned with the SO field vector, the swap goes without generation of other components of the spin [Figs. 6(e) and 6(f)]. For spins initially antiparallel to the $[001]$ direction [Figs. 6(a) and 6(b)] the precession of the spins leads to an appearance of $[120]$ spin component and vice versa [Figs. 6(c) and 6(d)]. The electron-electron interaction for both initial spin orientations that are orthogonal to \mathbf{B}_{SO} leads to appearance of the spin components parallel to the \mathbf{B}_{SO} direction [see the green curves in Figs. 6(a) and 6(e)] in the form noticed above for the pure Dresselhaus and Rashba coupling: vanishing at $t=t_s$, maximal at $t=t_s/2$, and always opposite in both dots.

B. Spin oscillations due to the electron-electron interaction

The results presented above indicate that during the swap of spins that are initially perpendicular to \mathbf{B}_{SO} , the electron-electron interaction induces appearance of spin components in the direction of this vector that are opposite in both dots [Figs. 2(c), 4(a), 5(a), 5(e), 6(a), and 6(b)]. The net spin in the direction of \mathbf{B}_{SO} remains zero, in contrast to the spin generated in the direction perpendicular to \mathbf{B}_{SO} by the spin precession. The spin components in \mathbf{B}_{SO} direction vanish at

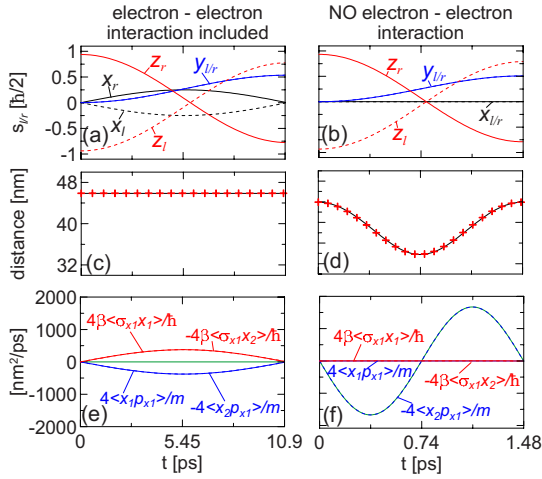


FIG. 7. (Color online) [(a) and (b)] Same as Figs. 2(c) and 2(d) but for the basis limited to four lowest energy two-electron states. [(c) and (d)] Electron-electron distance ($\langle(x_1 - x_2)^2\rangle^{1/2}$) as calculated for the wave function given by Eq. (4) (black line) and integrated using Eq. (7) (red crosses) starting from the initial condition. [(e) and (f)] Real parts of right-hand side terms of Eq. (7).

the end of the swap $t=t_s$, however they are maximal at $t=t_s/2$. Note that the XOR gate employs the square-root-of-a-swap operation,² i.e., the spin-swap process interrupted exactly at $t_s/2$.

Let us analyze the background of the appearance of spin components in the direction of \mathbf{B}_{SO} vector. We focus on the simulation presented in Fig. 2(c), for which $\alpha=0$, the dots are placed along the x axis hence \mathbf{B}_{SO} is aligned with the x axis, and the spins are initially set parallel and antiparallel to the z axis.

By the Ehrenfest theorem the average electron-electron distance in the x direction changes in time as

$$\begin{aligned} \frac{d}{dt}\langle(x_1 - x_2)^2\rangle &= \frac{4}{m^*}\langle x_1 p_{x1} - x_2 p_{x1}\rangle + \frac{4\beta}{\hbar}\langle\sigma_{x1}x_1 - \sigma_{x1}x_2\rangle \\ &\quad - \frac{2i\hbar}{m^*}, \end{aligned} \quad (7)$$

where the last term compensates for the imaginary part due to the non-Hermitian $x_1 p_{x1}$ operator. The electron-electron distance as presented in Fig. 2(a) is nearly constant but contains a rapid oscillation of small amplitude which results from a difference between the electron-electron separation in the initial condition and the equilibrium distance for interacting electrons (see Appendix). For the purpose of analysis of Eq. (7) it is useful to limit the basis used for Eq. (3) to four lowest energy two-electron states, which correctly describes the spin evolution (see Appendix) but is free of this rapid oscillation. The results for the spin evolution, electron-electron distance and the right-hand-side terms of Eq. (7) are displayed in Fig. 7. For noninteracting electrons, at the right-hand side of Eq. (7) only the $\langle x_2 p_{x1}\rangle = \langle x_2\rangle\langle p_{x1}\rangle$ term has a nonzero real part [Fig. 7(f)], which oscillates due to independent tunneling of electrons which go from one dot to the other with periodically changing positions and momenta. On

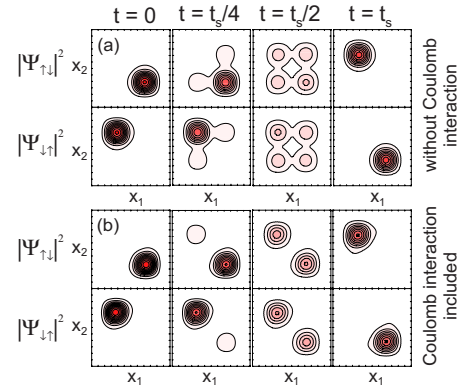


FIG. 8. (Color online) Probability densities for the components of the two-electron wave functions corresponding to opposite spin orientations plotted on x_1, x_2 plane along the axis of the system $y_1=y_2=0$ for chosen moments in time during the spin swap. Parameters are the same as in Fig. 7. The spins are initially oriented parallel and antiparallel to the z axis for (a) noninteracting and (b) interacting electrons. The spin-swap time is $t_s=1.48$ ps for (a) noninteracting electrons and $t_s=10.9$ ps for (b) the interacting ones.

the other hand the average value of $x_1 p_{x1}$ operator is purely imaginary.²⁵ For noninteracting electrons the term of Eq. (7) containing $x\sigma_x$ vanishes [Fig. 7(f)] and so does σ_x in both dots [Fig. 7(b)]. Thus the oscillation of the electron-electron distance observed in Fig. 7(d) is only due to the mean value of $x_2 p_{x1}$ operator.

Interacting electrons keep their relative distance [Fig. 7(c)] so the terms at the right-hand side of Eq. (7) must cancel one another. They indeed do [Fig. 7(e)]. Remarkably, in contrast to the case without Coulomb interaction [Fig. 7(f)], for interacting electrons one finds [Fig. 7(e)]

$$\langle x_1 p_{x1}\rangle = -\langle x_2 p_{x1}\rangle \quad (8)$$

and

$$\langle\sigma_{x1}x_1\rangle = -\langle\sigma_{x1}x_2\rangle. \quad (9)$$

Relations (8) and (9) can be explained by analysis of the electron motion which becomes collective when the electron-electron interaction is introduced. The two-electron wave function of Eq. (3), can be written as a four-component wave function²⁶ $\Psi_1 = \Psi_{\uparrow\uparrow}(\mathbf{r}_1, \mathbf{r}_2)$, $\Psi_2 = \Psi_{\uparrow\downarrow}(\mathbf{r}_1, \mathbf{r}_2)$, $\Psi_3 = \Psi_{\downarrow\uparrow}(\mathbf{r}_1, \mathbf{r}_2)$, and $\Psi_4 = \Psi_{\downarrow\downarrow}(\mathbf{r}_1, \mathbf{r}_2)$, each corresponding to a given direction of the spin for a given electron label [e.g., $\Psi_{\uparrow\downarrow}(\mathbf{r}_1, \mathbf{r}_2)$ corresponds to electron of position \mathbf{r}_1 (\mathbf{r}_2) with spin oriented parallel (antiparallel) to the z axis]. Antisymmetry of the wave function with respect to the electron interchange implies $\Psi_1(\mathbf{r}_1, \mathbf{r}_2) = -\Psi_1(\mathbf{r}_2, \mathbf{r}_1)$, $\Psi_4(\mathbf{r}_1, \mathbf{r}_2) = -\Psi_4(\mathbf{r}_2, \mathbf{r}_1)$, and $\Psi_2(\mathbf{r}_1, \mathbf{r}_2) = -\Psi_3(\mathbf{r}_2, \mathbf{r}_1)$. For the exchange of initially opposite spins Ψ_3 and Ψ_4 components are most relevant. Snapshots of $|\Psi_3|^2$ and $|\Psi_4|^2$ are displayed in Fig. 8 as functions of x_1 and x_2 calculated along the axis of the double dot $y_1=y_2=0$ for noninteracting [Fig. 8(a)] and interacting [Fig. 8(b)] electrons. Figure 8 shows that in the initial condition the electrons occupy separate dots and that the spin contained in the right (left) dot is oriented parallel (antiparallel) to the z direction. Spin orientation is inverted after the

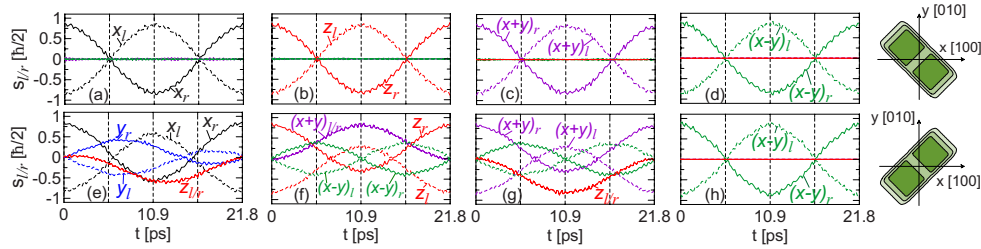


FIG. 9. (Color online) Spin stored in separate dots for two interacting electrons with equal linear Dresselhaus and Rashba constants $\alpha = \beta = 10.8$ meV nm. The first and second rows of plots correspond to different alignments of the double dot as shown schematically at the right end of the figure. In (a) and (e), and (b) and (d) the spins are initially set parallel or antiparallel to the x and z axes, respectively. In (c) and (g) the spins are initially set in the $x+y$ (i.e., $[110]$) direction—within the plane of confinement and perpendicular to \mathbf{B}_{SO} direction ($[1\bar{1}0]$). In (d) and (h) the spins are initially aligned with \mathbf{B}_{SO} vector. The dashed (solid) lines show the results for the left (right) dot. Black, blue, red, purple, and green colors correspond to x , y , z , $x+y$, and $x-y$ components of the spin, respectively.

swap ($t=t_s$). For noninteracting electrons at $t=t_s/4$ and $t=t_s/2$ we notice [Fig. 8(a)] that probabilities to find both electrons in the same dot (i.e., on the diagonal $x_1=x_2$ of the plots) is nonzero, which results from an independent electron tunneling between the dots. Without the Coulomb interaction the spin swap occurs as due to single-electron tunneling.

The interacting electrons do not occupy the same dot [see the vanishing probability density on the diagonal of plots presented in Fig. 8(b)] and the single-electron interdot tunneling is blocked. The interdot tunneling of separate wave function components is still observed [Fig. 8(b) for $t=t_s/4$ and $t=t_s/2$] but it occurs only along the antidiagonal of the plot $x_2=-x_1$. Therefore, one can replace x_2 by $-x_1$ in the right-hand side of Eqs. (8) and (9) which explains these relations. For the electron-electron distance to be unchanged the terms $\langle x_1 p_{x1} \rangle$ and $\langle -x_2 p_{x1} \rangle$ of Eq. (7) need to be canceled by the terms that contain the x component of the spin. The operator $x_1 \sigma_{x1}$ produces a nonzero contribution since the x spin component generated in the left dot ($x < 0$) has opposite sign [see Fig. 7(a)] than the one generated in the right dot ($x > 0$). We conclude that the generation of opposite spin components in the direction of the effective magnetic field is a consequence of fixed electron-electron distance and collective evolution of the two-electron wave function that are both induced by the Coulomb interaction.

C. Spin exchange for $\alpha = \beta$

For $\alpha = \beta$ the linear SO terms of Hamiltonian (1) commute¹⁸ with $\frac{1}{\sqrt{2}}(\sigma_x - \sigma_y)$ operator and the effective magnetic field $\mathbf{B}_{\text{SO}} = \frac{2\alpha}{g\mu_B}(k_x + k_y)(1, -1, 0)^T$ is aligned with $[1\bar{1}0]$ crystal direction. We performed simulations of the spin swap for $\alpha = \beta = 10.8$ meV nm. For the dots aligned in the x direction that were discussed above the results are qualitatively identical to the ones presented in Fig. 6 only with redefined direction of \mathbf{B}_{SO} vector. For $\alpha = \beta$ the direction of \mathbf{B}_{SO} does not depend on the orientation of the dots, however the strength of this field does. For the diagonal ($[110]$) orientation of the dots (the lower row of plots in Fig. 9) the electrons tunnel between the dots with equal k_x and k_y wave vectors so the field should be relatively the strongest. On the other hand for the quantum dots oriented along the $[1\bar{1}0]$

direction (the upper row of plots in Fig. 9) k_x and k_y have opposite sign for the electrons tunneling between the dots, so \mathbf{B}_{SO} should be expected to vanish.

The simulations show that spin exchange occurs in the same manner for the diagonal ($[110]$) and antidiagonal ($[1\bar{1}0]$) orientation of the dots only when the spins of electrons are initially antiparallel in the direction of \mathbf{B}_{SO} ($[1\bar{1}0]$ or $x-y$)—see Figs. 9(d) and 9(h). For the diagonal orientation of the dots and initial alignment of the spins in the direction perpendicular to the \mathbf{B}_{SO} vector: in z direction [Fig. 9(f)] and in $(x+y)$ direction [Fig. 9(g)] one observes generation of $(x+y)$ and z spin components, respectively. The precession is accompanied by generation of opposite spin components in \mathbf{B}_{SO} direction [Figs. 9(f) and 9(g)] in consistence with the results discussed above.

Note, that the anisotropy of the swap for the diagonal orientation of the dots is observed in spite of the fact that for $\alpha = \beta$ the energy spectrum of SO-coupled system is identical¹⁸ to the one obtained in the absence of SO coupling. For $\alpha = \beta$ the SO coupling does not affect the energy spectrum at zero magnetic field but the effective SO magnetic field is still present.

For the antidiagonal ($[1\bar{1}0]$) orientation of the dots (the upper row of plots in Fig. 9) the spin swap becomes perfectly isotropic and occurs in the same manner independent of the initial spin orientation. Not a trace of spin precession is present in accordance with the single-electron picture of the electron tunneling that goes with $k_x = -k_y$ in any moment in time which implies $B_{\text{SO}} = 0$.

D. Discussion

The present study indicates that the spin swap as originally defined for the purpose of controllable coupling of spin qubits² localized in separate quantum dots is generally anisotropic when the spin-orbit coupling is present. The anisotropy of the spin swap results from the effective magnetic field due to the spin-orbit coupling. This field changes the direction of the electron spin as it moves in space. The study of Ref. 14 indicated that for a carefully chosen computational two-electron basis the exchange Hamiltonian becomes formally isotropic at zero magnetic field. The proposed¹⁴ ba-

sis is obtained by a unitary transformation of a separable basis of singlet and triplet states. The unitary transformation [Eq. (13) of Ref. 14] produces basis elements in which the spin and spatial degrees of freedom are entangled, i.e., direction of the electron spin depends on its position in space. For the purpose of the quantum computation any basis can, in principle, be chosen. However, the entangled basis that allows for a simpler form of the Hamiltonian requires a more challenging handling of the quantum information, which in fact should be stored by entangled spin-orbital wave functions rather than by the electron spin itself. The practical usage of the entangled basis calls for new physical procedures for preparation of the initial state and read out of the quantum computation result.

For construction of the universal quantum gate the two-spin operations need to be complemented by single-spin rotations. The direct idea to perform the latter is to put the system in external magnetic field to split the spin states of the single-electron and exploit the Rabi oscillations in resonant radiation of microwave or radio frequency.²⁷ In presence of the external magnetic field (\mathbf{B}) the spin swap becomes anisotropic even without SO coupling, since the electron spins precess in \mathbf{B} unless they are initially aligned with the direction of the external field. In order not to interfere with the spin exchange the single-spin rotations should be applied without the external magnetic field. The original idea for that purpose was the electrically controlled coupling of a selected spin to a ferromagnetic medium.¹ It was also demonstrated that the single-spin rotations can be performed using the spin precession in the SO effective magnetic field which occurs when the electron is made to move, e.g., along closed trajectories.²⁸ This idea for the single-spin rotations²⁸ does not require the external magnetic field or irradiation.

IV. SUMMARY AND CONCLUSIONS

We presented numerically exact simulations of the spin swap for two-electron SO-coupled double quantum dots. The study covered Dresselhaus and Rashba interactions and various spatial orientations of the double dot. The swap of spins as observed in time-dependent simulation involves four mechanisms: (i) direct tunneling which consists in electron carrying its spin from one dot to the other, (ii) the spin tunneling which still occurs when the direct tunneling is blocked by the electron-electron interaction, (iii) the precession of the spin moving in the effective magnetic field due to the spin-orbit coupling, and (iv) generation of opposite spin components in the direction of the effective magnetic field which is observed for interacting pair of electrons. The third and fourth mechanisms of the above list can be switched off for initial spin orientation aligned with the effective magnetic field vector \mathbf{B}_{SO} . For the initial orientation of the spins in one of the directions perpendicular to \mathbf{B}_{SO} the spin in the other perpendicular direction is generated during the swap as a consequence of the spin precession. We argued that mechanism (iv) is necessary to maintain a constant electron-electron distance and is a consequence of a collective motion of the electrons within the inner degrees of freedom which is still observed when the single-electron tunneling between the

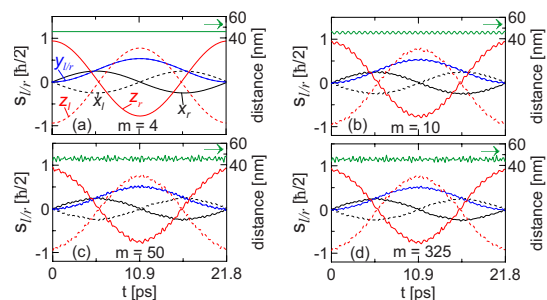


FIG. 10. (Color online) Results of simulations for the pure Dresselhaus coupling and dots placed on the x axis for the interacting electrons with spins initially oriented antiparallel in the z direction. Black, blue, and red curves show the spin components stored in the left (dashed curve) and the right (solid curve) dots. The green curve at the top of the plot is the average electron-electron distance that is referred to the right axis. The results presented in (a), (b), (c), and (d) correspond to the two-electron basis containing $m=4$, 10, 50, and 325 lowest energy eigenstates of Hamiltonian (2).

dots is blocked by the Coulomb repulsion. We also demonstrated that for both coupling types present the spin swap is largely affected by a specific orientation of the double dot system within the (001) plane of confinement via the strength of the effective magnetic field. In particular, we demonstrated that the SO coupling effects can be eliminated from the spin swap process for quantum dots aligned with $[1\bar{1}0]$ crystal direction. For this orientation of the dots and the Rashba constant tuned to match the Dresselhaus constant \mathbf{B}_{SO} vanishes and the spin swap becomes perfectly isotropic.

ACKNOWLEDGMENTS

This work was supported by MPD Programme “Krakow Interdisciplinary PhD-Project in Nanoscience and Advanced Nanostructures” operated within the Foundation for Polish Science and co-financed by the EU European Regional Development Fund and by a research under Project No. N N202 103938 supported by Ministry of Science and Higher Education (MNiSW) for 2010–2013. Calculations were performed in ACK-CYFRONET-AGH on the RackServer Zeus.

APPENDIX

This appendix presents convergence of the results with respect to the energy cutoff used in Eq. (3). Let us consider the dots placed on the x axis and electron spins initially oriented parallel and antiparallel to the z axis that was discussed in the context of Fig. 2(c). Figure 10 shows the results for $m=4$, 10, 50, and 325 two-electron lowest energy eigenstates used as basis elements in Eq. (3). The basis with $m=4$ covers the ground state and threefold degenerate excited state²⁰—which in the absence of SO coupling corresponds to the spin triplet. The energy separation of the ground-state and the excited state is $\Delta E=0.189$ meV, which well corresponds to the spin-swap time² $t_s=\pi/\Delta E=10.9$ ps. The basis of 10, 50, and 325 elements covers all the two-electron eigenstates of the energy that exceeds the ground-state energy by not more than 8.9 meV, 19.4 meV, and 65.2 meV,

respectively. For $m > 4$ a rapid and low amplitude oscillation appears in the results of Fig. 10. This oscillation results from a difference between the electron-electron separation in the initial condition and the equilibrium distance for interacting electrons. The initial condition is taken from single-electron wave function obtained for noninteracting electrons which are projected onto the basis of two-electron eigenstates (see Sec. II). The electron-electron distance is nearly the same in the lowest energy four states (singlet and triplet states). The constant electron-electron distance obtained for $m=4$ [Fig. 10(a)] is the equilibrium distance for interacting electrons in the ground state. For larger m the basis resolves between the equilibrium distances for interacting and noninteracting electrons hence the appearance of the rapid oscillations of electron-electron distance and the resulting oscillations of the spins. The oscillations do not affect the mechanism of the spin swap or the swap time and have a small amplitude which can be further reduced by a choice of confinement parameters. In particular, Fig. 11 shows the results for the barrier height increased from 10 to 50 meV.²⁰ The Coulomb

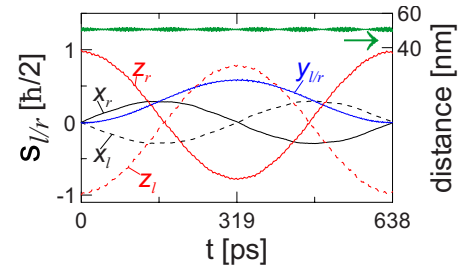


FIG. 11. (Color online) Same as Fig. 10(d) only for interdot barrier height increased from $V_b=10$ meV to $V_b=50$ meV.

interaction affects weakly the electron-electron equilibrium distance and the rapid oscillations have a negligibly small amplitude also for $m=325$. The results presented in this paper were obtained for the fully convergent 325 element basis with the exception of Sec. III B, where we use the four-element basis for simplicity. For $\Delta E=65.2$ meV the shortest oscillation period that can be accounted for is 0.06 ps.

- ¹D. Loss and D. P. DiVincenzo, *Phys. Rev. A* **57**, 120 (1998).
- ²G. Burkard, D. Loss, and D. P. DiVincenzo, *Phys. Rev. B* **59**, 2070 (1999).
- ³J. R. Petta, A. C. Johnson, J. M. Taylor, E. Laird, A. Yacoby, M. D. Lukin, and C. M. Marcus, *Science* **309**, 2180 (2005).
- ⁴J. M. Elzerman, R. Hanson, L. H. W. van Beveren, B. Witkamp, L. M. K. Vandersypen, and L. P. Kouwenhoven, *Nature (London)* **430**, 431 (2004).
- ⁵J. M. Taylor, J. R. Petta, A. C. Johnson, A. Yacoby, C. M. Marcus, and M. D. Lukin, *Phys. Rev. B* **76**, 035315 (2007).
- ⁶K. V. Kavokin, *Phys. Rev. B* **64**, 075305 (2001); **69**, 075302 (2004).
- ⁷Ş. C. Bădescu, Y. B. Lyanda-Geller, and T. L. Reinecke, *Phys. Rev. B* **72**, 161304(R) (2005).
- ⁸S. Gangadharaiah, J. Sun, and O. A. Starykh, *Phys. Rev. Lett.* **100**, 156402 (2008).
- ⁹N. E. Bonesteel, D. Stepanenko, and D. P. DiVincenzo, *Phys. Rev. Lett.* **87**, 207901 (2001).
- ¹⁰G. Burkard and D. Loss, *Phys. Rev. Lett.* **88**, 047903 (2002).
- ¹¹L.-A. Wu and D. A. Lidar, *Phys. Rev. A* **66**, 062314 (2002).
- ¹²D. Stepanenko and N. E. Bonesteel, *Phys. Rev. Lett.* **93**, 140501 (2004).
- ¹³N. Zhao, L. Zhong, J.-L. Zhu, and C. P. Sun, *Phys. Rev. B* **74**, 075307 (2006).
- ¹⁴F. Baruffa, P. Stano, and J. Fabian, *Phys. Rev. Lett.* **104**, 126401 (2010).
- ¹⁵J. Königmann, R. J. Haug, D. K. Maude, V. I. Fa'liko, and B. L. Altshuler, *Phys. Rev. Lett.* **94**, 226404 (2005); C. Fasth, A. Fuhrer, L. Samuelson, V. N. Golovach, and D. Loss, *ibid.* **98**, 266801 (2007); A. Pfund, I. Shorubalko, K. Ensslin, and R. Leturcq, *Phys. Rev. B* **76**, 161308(R) (2007).
- ¹⁶S. D. Ganichev, V. V. Bel'kov, L. E. Golub, E. L. Ivchenko, P. Schneider, S. Giglberger, J. Eroms, J. De Boeck, G. Borghs, W. Wegscheider, D. Weiss, and W. Prettl, *Phys. Rev. Lett.* **92**, 256601 (2004); L. Meier, G. Salis, E. Gini, I. Shorubalko, and

- K. Ensslin, *Phys. Rev. B* **77**, 035305 (2008).
- ¹⁷C. Flindt, A. S. Sorensen, and K. Flensberg, *Phys. Rev. Lett.* **97**, 240501 (2006); P. Földi, O. Kalman, M. G. Benedict, and F. M. Peeters, *Nano Lett.* **8**, 2556 (2008).
- ¹⁸J. Schliemann, J. C. Egues, and D. Loss, *Phys. Rev. Lett.* **90**, 146801 (2003).
- ¹⁹B. A. Bernevig, J. Orenstein, and S.-C. Zhang, *Phys. Rev. Lett.* **97**, 236601 (2006); J. D. Koralek, C. Weber, J. Orenstein, A. Bernevig, S. Zhang, S. Mack, and D. Awschalom, *Nature (London)* **458**, 610 (2009).
- ²⁰Details of the configuration-interaction method and results for stationary states are given in M. P. Nowak and B. Szafran, *Phys. Rev. B* **81**, 235311 (2010).
- ²¹Recently, a time-dependent approach was used for simulation of a single-electron behavior in a one-dimensional model of a SO-coupled double quantum dot perturbed by electric pulses: D. V. Khomitsky and E. Ya. Sherman, *EPL* **90**, 27010 (2010).
- ²²S. Saikin, M. Shen, M. Cheng, and V. Privman, *J. Appl. Phys.* **94**, 1769 (2003).
- ²³E. A. de Andrada e Silva, G. C. La Rocca, and F. Bassani, *Phys. Rev. B* **55**, 16293 (1997).
- ²⁴The spin component i stored in the left dot is calculated as: $s_l = \langle \Psi(\mathbf{r}_1, \sigma_1, \mathbf{r}_2, \sigma_2) | s_l^i \kappa_l(\mathbf{r}_1) + s_l^i \kappa_l(\mathbf{r}_2) | \Psi(\mathbf{r}_1, \sigma_1, \mathbf{r}_2, \sigma_2) \rangle$, where s^i is the spin component i operator and $\kappa_l(x)$ is the step function that takes value 1 in the left dot and 0 in the right dot. Formula for the spin stored in the right dot s_r is the same but with κ_l replaced by $\kappa_r(x) = 1 - \kappa_l(x)$, and $s_l + s_r = \langle s_l^i + s_r^i \rangle$.
- ²⁵This can be explained as follows. The two-electron problem without the Coulomb interaction separates into two single-electron ones. According to the present approach initially the spatial single-electron wave function is a superposition of the ground-state wave function of even parity ψ_0 and the first excited state wave function of odd parity ψ_1 . One can arrange for ψ_0 and ψ_1 to be real valued. In the evaluation of the right-hand side of Eq. (7) for noninteracting electrons the cross terms

$\langle \psi_0 | xp_x | \psi_1 \rangle$ vanish for the parity reason and $\langle xp_x \rangle$ is purely imaginary for any localized real wave function.

²⁶B. Szafran, M. P. Nowak, S. Bednarek, T. Chwiej, and F. M. Peeters, *Phys. Rev. B* **79**, 235303 (2009); S. Moskal, S. Bednarek, and J. Adamowski, *Phys. Rev. A* **76**, 032302 (2007).

²⁷F. H. L. Koppens, C. Buizert, K. J. Tielrooij, I. T. Vink, K. C.

Nowack, T. Meunier, L. P. Kouwenhoven, and L. M. K. Vandersypen, *Nature (London)* **442**, 766 (2006).

²⁸D. Frustaglia and K. Richter, *Phys. Rev. B* **69**, 235310 (2004); P. Földi, B. Molnár, M. G. Benedict, and F. M. Peeters, *ibid.* **71**, 033309 (2005); S. Bednarek and B. Szafran, *Phys. Rev. Lett.* **101**, 216805 (2008).

5 Singlet-triplet avoided crossings and effective g-factor versus spatial orientation of spin-orbit-coupled quantum dots

Singlet-triplet avoided crossings and effective g factor versus spatial orientation of spin-orbit-coupled quantum dots

M. P. Nowak and B. Szafran

*Faculty of Physics and Applied Computer Science, AGH University of Science and Technology,
al. Mickiewicza 30, PL-30-059 Kraków, Poland*

(Received 28 September 2010; revised manuscript received 2 December 2010; published 19 January 2011)

We study avoided crossings opened by spin-orbit interaction in the energy spectra of one- and two-electron anisotropic quantum dots in perpendicular magnetic field. We find that for simultaneously present Rashba and Dresselhaus interactions the width of avoided crossings and the effective g factor depend on the dot orientation within the (001) crystal plane. The extreme values of these quantities are obtained for [110] and $[1\bar{1}0]$ orientations of the dot. The width of singlet-triplet avoided crossing changes between these two orientations by as much as two orders of magnitude. The discussed modulation results from the orientation-dependent strength of the Zeeman interaction, which tends to polarize the spins in the direction of the external magnetic field and thus remove the spin-orbit coupling effects.

DOI: [10.1103/PhysRevB.83.035315](https://doi.org/10.1103/PhysRevB.83.035315)

PACS number(s): 73.21.La

I. INTRODUCTION

Spin-related phenomena in few-electron quantum dots have been under extensive investigation during the past decade. The studies have covered spin relaxation involving spin-orbit interaction and phonon emission,¹ spin dephasing² due to coupling to nuclear spins,³ as well as the spin-exchange interaction.⁴ Besides the fundamental interest, these studies were motivated by an idea to implement quantum computation⁵ on spins of separate electrons confined in quantum dot arrays. The spin-orbit (SO) coupling is considered for spin manipulation within the orbital degrees of freedom⁶ as well as in the context of the anisotropy⁷ of the exchange interaction for quantum gating.⁸

Few-electron systems confined in circular quantum dots undergo ground-state angular momentum transitions in external magnetic field (B).^{9–11} For the electron pair these transitions are observed only in presence of the electron-electron interaction and are accompanied by spin transitions with ground-state changing between singlet and triplet depending on the parity of angular momentum quantum number.¹¹ Singlet-triplet ground-state transitions in two-electron quantum dots are observed in charging experiments.¹² In elliptical quantum dots as well as in double dots,¹³ the angular momentum transitions are replaced by ground-state parity symmetry transformations still accompanied by singlet-triplet transitions.

The SO coupling mixes the eigenstates of opposite parities and spin. In the presence of the SO interaction the singlet-triplet transition occurs through an avoided crossing that for planar quantum dots was discussed in a number of recent theoretical papers.¹⁴ The SO interaction usually introduces energetically weak effects hence the singlet-triplet avoided crossing is narrow and difficult to observe experimentally. The first observations of singlet-triplet avoided crossings due to SO coupling were performed in transport experiments on quantum dots formed in gated InAs quantum wires.¹⁵ A transport experiment resolving this avoided crossing in a planar structure was performed only recently¹⁶ on a single InAs self-assembled quantum dot.

The SO interaction appears due to inversion asymmetry of the crystal lattice (Dresselhaus¹⁷ coupling) and/or of

the nanostructure (Rashba¹⁸ coupling). The resulting SO Hamiltonian is not invariant with respect to rotations within the plane of confinement. The anisotropy of SO interaction was investigated by observation of singlet-triplet avoided crossing for rotated external magnetic-field vector.¹⁶ The study of Ref. 16 extends the previous work¹⁹ in which the spin splittings were controlled by orientation of the external magnetic field superposing the effective magnetic field²⁰ introduced by SO coupling. It was also demonstrated²¹ that in the presence of the SO coupling the nonlinear Kondo conductance depends on the orientation of external magnetic field.

In this paper we consider a planar anisotropic quantum dot in a perpendicular magnetic field and demonstrate that the anisotropy of SO interaction can be used for tuning the width of the singlet-triplet avoided crossing by spatial orientation of the dot. This tunability appears provided that both SO coupling types are present. The discussed effect results from dependence of the effective strength of the Zeeman interaction on the quantum dot orientation within the (001) crystal plane. The Zeeman interaction tends to polarize electron spins in the direction of the magnetic field. A complete polarization amounts in removal of the SO coupling effects. The extent of the spin polarization—and thus also the effective Landé factor²²—vary with the dot orientation. For similar values of SO coupling constants the width of the avoided crossing changes by two orders of magnitude between a few μeV to about 0.5 meV. The dependence of the width of singlet-triplet avoided crossing on spatial orientation of the dot is present for any form of confinement potential (quantum well or parabolic profile) for both single and double quantum dots.

II. THEORY

A. Hamiltonian

We consider a quantum dot defined within the (001) plane with x and y axes identified with [100] and [010] crystal directions, respectively. The magnetic field is oriented parallel to the growth [001] direction (z). We adopt a two-dimensional approximation assuming that the confinement potential is separable into vertical and planar components

$W(\mathbf{r}) = V_z(z) + V(x, y)$ and that the vertical confinement is much stronger than the planar one. Under these conditions the contribution of states excited in the vertical direction that could be introduced by the spin-orbit coupling and by the electron-electron interaction is negligible. The two-dimensional single-electron Hamiltonian takes the form¹⁴

$$H = h\mathbf{1} + \frac{1}{2}g\mu_B B\sigma_z + H_{SIA} + H_{BIA}, \quad (1)$$

where $h = [\frac{\hbar^2 \mathbf{k}^2}{2m^*} + V(x, y)]$ is the spatial Hamiltonian, $\mathbf{1}$ is the identity matrix, $\mathbf{k} = -i(\frac{\partial}{\partial x}, \frac{\partial}{\partial y}) + \frac{e}{\hbar}(A_x, A_y)$, g stands for the Landé factor, and H_{SIA} and H_{BIA} describe Rashba¹⁸ (structure inversion asymmetry) and Dresselhaus¹⁷ (bulk inversion asymmetry) SO interactions. We use the symmetric gauge with $A_x = -y\frac{B}{2}$, $A_y = x\frac{B}{2}$. The two-dimensional Rashba interaction is composed of the diagonal and linear parts $H_{SIA} = H_{SIA}^{\text{lin}} + H_{SIA}^{\text{diag}}$ with

$$H_{SIA}^{\text{lin}} = \alpha(\sigma_x k_y - \sigma_y k_x), \quad (2)$$

and

$$H_{SIA}^{\text{diag}} = \alpha_{3D}\sigma_z \left[\frac{\partial W}{\partial y} k_x - \frac{\partial W}{\partial x} k_y \right]. \quad (3)$$

The two-dimensional coupling constant α in Eq. (2) is related to the bulk coupling constant α_{3D} as $\alpha = \alpha_{3D} \langle \frac{\partial W}{\partial z} \rangle$, where the average value is calculated for the ground-state wave function in the growth direction. The Dresselhaus interaction contains a linear and cubic terms $H_{BIA} = H_{BIA}^{\text{lin}} + H_{BIA}^{\text{cub}}$,

$$H_{BIA}^{\text{lin}} = \beta[\sigma_x k_x - \sigma_y k_y], \quad (4)$$

$$H_{BIA}^{\text{cub}} = \gamma_{3D}[\sigma_y k_y k_x^2 - \sigma_x k_x k_y^2], \quad (5)$$

where γ_{3D} is the bulk coupling constant and the two-dimensional constant is defined by $\beta = \gamma_{3D} \langle k_z^2 \rangle$. We adopt the material parameters for an $\text{In}_{0.5}\text{Ga}_{0.5}\text{As}$ quantum dot, $\alpha_{3D} = 0.572 \text{ nm}^2$ (see Ref. 23) and $\gamma_{3D} = 32.2 \text{ meV nm}^3$ (see Ref. 24), the electron effective mass $m^* = 0.0465m_0$, and the Landé factor $g = -8.97$. For V_z in the form of an infinite quantum well of height d the two-dimensional Dresselhaus constant is $\beta = \gamma_{3D} \frac{\pi^2}{d^2}$. For $d = 5.42 \text{ nm}$ we have $\beta = 10.8 \text{ meV nm}$. The two-dimensional Rashba constant achieves this value when (an external or built-in) vertical electric field acquires 188.8 kV/cm .

Below we consider a model confinement potential

$$V_c(x', y') = -\frac{V_0}{(1 + [\frac{x'^2}{K^2}]^\mu)(1 + [\frac{y'^2}{L^2}]^\mu)}, \quad (6)$$

where $V_0 = 50 \text{ meV}$ is assumed for the depth of the quantum dot. The exponent $\mu = 10$ is applied for which the potential profile has a form of a rectangular potential well with smoothed boundaries. We take $2K = 40 \text{ nm}$ as the smaller length of the dot and the larger length is taken $2L = 90 \text{ nm}$, unless stated otherwise. The primes standing in Eq. (6) are referred to the crystal directions x and y by

$$x' = x \cos(\phi) - y \sin(\phi), \quad y' = x \sin(\phi) + y \cos(\phi). \quad (7)$$

The orientation of the dot with respect to the crystal directions is displayed in Fig. 1 for $\phi = \pi/4$. The effects discussed below remain qualitatively the same for other profiles of the dots. At

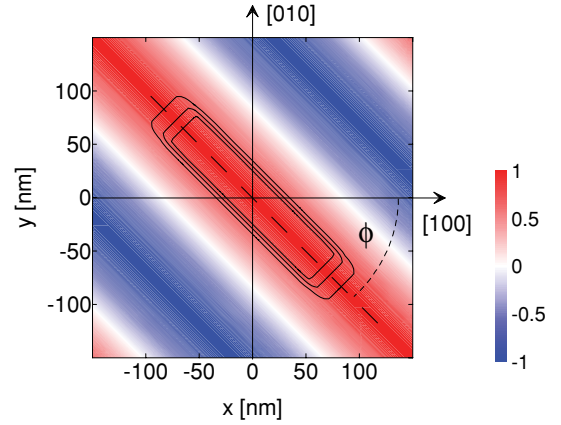


FIG. 1. (Color online) The contour shows a quantum dot of width $2K = 40 \text{ nm}$ and length $2L = 200 \text{ nm}$ placed along $[1\bar{1}0]$ crystal direction [$\phi = \pi/4$ in Eq. (7)]. With the colors we plotted the values of the cosine in the integrand of Eq. (13) for $\alpha = 10.8 \text{ meV nm}$.

the end of next section we present also results for elliptical parabolic confinement potential.

B. Method

The eigenstates of the single-electron Hamiltonian (1) are calculated on a basis of multicenter Gaussian functions which is a precise tool for treatment of confinement potentials of arbitrary or no symmetry,²⁵

$$\phi_v = \sum_{ks} c_{ks}^v \chi_s \exp \left[-\frac{(\mathbf{r} - \mathbf{R}_k)^2}{2a^2} + \frac{ieB}{2\hbar} (xY_k - yX_k) \right], \quad (8)$$

where the centers of Gaussians $\mathbf{R}_k = (X_k, Y_k)$, are distributed on a rectangular array,²⁵ and the localization parameter a is optimized variationally. In Eq. (8) $s = \pm 1$ and χ_s are eigenstates of the Pauli matrix σ_z .

The two-electron states are found by the exact diagonalization approach, which uses the basis of the antisymmetrized products of operator (1) eigenstates,

$$\Phi = \frac{1}{\sqrt{2}} \sum_{\mu=1}^N \sum_{\nu=\mu+1}^N [\phi_\mu(1)\phi_\nu(2) - \phi_\mu(2)\phi_\nu(1)], \quad (9)$$

for diagonalization of the two-electron Hamiltonian $H_2 = H(1) + H(2) + \frac{e^2}{4\pi\epsilon\epsilon_0 r_{12}}$ ($\epsilon = 13.55$ is taken for the dielectric constant). For $2K = 40 \text{ nm}$ and $2L = 90 \text{ nm}$ we use a basis of 25×25 centers, which gives 1250 elements including the spin degree of freedom. In the two-electron calculations we take $N = 30$ lowest-energy single-electron spin orbitals which produces a basis of 435 elements and guarantees the convergence of the variational result better than $1 \mu\text{eV}$.

III. RESULTS AND DISCUSSION

A. Effective g factor and orientation of the dot

In order to explain the dependence of the strength of the Zeeman interaction on the orientation of the dot—which underlies the results to be presented below—let us consider the special case of equal linear SO coupling constants $\alpha = \beta = 10.8 \text{ meV nm}$ and neglect the cubic Dresselhaus and diagonal

Rashba terms of SO interaction, which are small anyway.²⁶ We consider the approximate Hamiltonian for $B = 0$ defined as $H_0 = \hbar\mathbf{1} + H_{SIA}^{\text{lin}} + H_{BIA}^{\text{lin}}$. H_0 commutes with the operator of the $[1\bar{1}0]$ spin component and SO coupling shifts the entire electron energy spectrum by a constant quantity²⁷ $E_N = \epsilon_N - \frac{2\alpha^2 m^*}{\hbar^2}$, where E_N and ϵ_N denote energy eigenvalues with and without SO coupling, respectively. For $B = 0$ the SO coupled eigenfunctions of the H_0 operator $\Psi_{N\pm}$ corresponding to $\pm\hbar/2$ spin eigenvalues in the $[1\bar{1}0]$ direction are related to orbital eigenfunctions φ_N that are obtained in the absence of the SO coupling as

$$\phi_{N\pm}(x, y) = \frac{1}{\sqrt{2}} \left(\pm e^{-i\pi/4} \right) \varphi_N(x, y) e^{\mp(i\sqrt{2}\alpha m/\hbar^2)(x+y)}. \quad (10)$$

The magnetic-field vector parallel to the growth direction introduces the Zeeman interaction with the σ_z matrix to the Hamiltonian, and the $[1\bar{1}0]$ spin component is no longer a good quantum number. Let us try to diagonalize the Hamiltonian including the Zeeman effect $H_z = H_0 + \frac{1}{2}g\mu_B B\sigma_z$ taking H_0 eigenstates (10) as the basis. The shortest reasonable basis contains two degenerate ground-state wave functions $\phi_{1\pm}$ corresponding to opposite spin orientations and the same orbital wave function φ_1 . The matrix of the H_z operator takes the form

$$\mathbf{H}_z = \begin{pmatrix} \langle \phi_{1+} | H_z | \phi_{1+} \rangle & \langle \phi_{1+} | H_z | \phi_{1-} \rangle \\ \langle \phi_{1-} | H_z | \phi_{1+} \rangle & \langle \phi_{1-} | H_z | \phi_{1-} \rangle \end{pmatrix}, \quad (11)$$

where both diagonal terms are $\langle \phi_{1\pm} | H_B | \phi_{1\pm} \rangle = E_1 - \frac{2\alpha^2 m^*}{\hbar^2}$, and the off-diagonal ones are

$$\langle \phi_{1\pm} | H_B | \phi_{1\mp} \rangle = \frac{1}{2}g\mu_B B \int |\varphi_1(x, y)|^2 e^{\pm i(2\sqrt{2}\alpha m^*/\hbar^2)(x+y)} dx dy. \quad (12)$$

For potentials with an in-plane inversional symmetry that are considered in this paper the matrix element (12) is real and is given by

$$\begin{aligned} \langle \phi_{1\pm} | H_B | \phi_{1\mp} \rangle &= \frac{1}{2}g\mu_B B \int |\varphi_1(x, y)|^2 \cos \left[\frac{2\sqrt{2}\alpha m^*}{\hbar^2} (x+y) \right] dx dy. \end{aligned} \quad (13)$$

Figure 1 shows the plot of the cosine term in the integrand. The argument of the cosine has a fixed orientation with respect to the crystal directions and changes sign along $[110]$ with a period of $\lambda_{SO} = \frac{\pi\hbar^2}{2\alpha m^*}$ (for the applied parameters $\lambda_{SO} = 238.4$ nm). For the quantum dot of length $L = 200$ nm oriented along $[1\bar{1}0]$ (see Fig. 1) the cosine has the same sign within the quantum dot area. For this orientation the off-diagonal terms of Hamiltonian matrix (11) are the largest. On the other hand, for the dot oriented along $[110]$ the sign of the integrand oscillates within the quantum dot area and the off-diagonal terms are necessarily smaller. The off-diagonal matrix elements mix the σ_{x-y} eigenstates leading to alignment of the spin along the direction of the field (z). Therefore the spin polarization due to the Zeeman effect should be the strongest for the $[1\bar{1}0]$ dot orientation and the weakest for the dot oriented along the $[110]$ crystal direction.

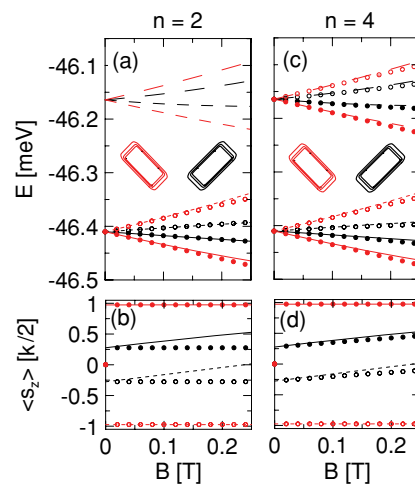


FIG. 2. (Color online) (a) The dots show the eigenvalues of Hamiltonian (11) and the lines present the results of diagonalization of the exact Hamiltonian in function of the external magnetic field for $\alpha = \beta = 10.8$ meV nm, $2K = 40$ nm, and $2L = 350$ nm. The results for $[1\bar{1}0]$ and $[110]$ orientations of the dot are shown by gray (red online) and black lines, respectively. (b) The spin of the two lowest energy levels for both orientations of the dot. The dots in (c) and (d) show the results of diagonalization of 4×4 matrix Hamiltonian with basis including the first excited state (see text).

The results of the diagonalization of matrix Hamiltonian (11) are displayed in Fig. 2(a) for the dot oriented along $[110]$ (black dots) and $[1\bar{1}0]$ (red dots) directions. In Fig. 2(b) we display the average spin for the two lowest-energy states for both orientations of the dot. The lines in Fig. 2 show the results of the exact diagonalization with the basis given by Eq. (8). The eigenvalues of matrix (11) quite well reproduce the exact energy levels and the average spin.²⁸ According to the intuition given by Fig. 1, the electron spin reacts to the application of the external magnetic field in a more pronounced manner for the $[1\bar{1}0]$ orientation of the dot than for the perpendicular orientation $[110]$. As the nonzero magnetic field lifts the ground-state degeneracy, the ground state (the first excited state) becomes nearly spin-up (spin-down) polarized. Polarization of the spin by infinitesimal B for the dot oriented along the $[110]$ direction is much weaker and increases for higher fields. This increase [black lines in Fig. 2(b)] is not very well reproduced by the two-element basis (black dots). Inclusion of the first excited scalar wave function φ_2 to the approximate calculation gives four basis elements of type (10). The results are displayed in Figs. 2(c) and 2(d). The four-element basis reproduces also the excited energy levels and an improvement of the description of $s_z(B)$ dependence is obtained, particularly for the $[110]$ orientation.

The extent of the spin polarization that varies with the dot orientation results in the dependence of the Kramers multiplet splitting induced by weak magnetic fields. This in turn leads to the orientation dependence of the effective g^* factors,²² which in the experiments are estimated by the splitting of energy levels by weak magnetic field. We estimate the effective factor by

$$g^* = \lim_{B \rightarrow 0} \frac{E_2 - E_1}{\mu_B B}, \quad (14)$$

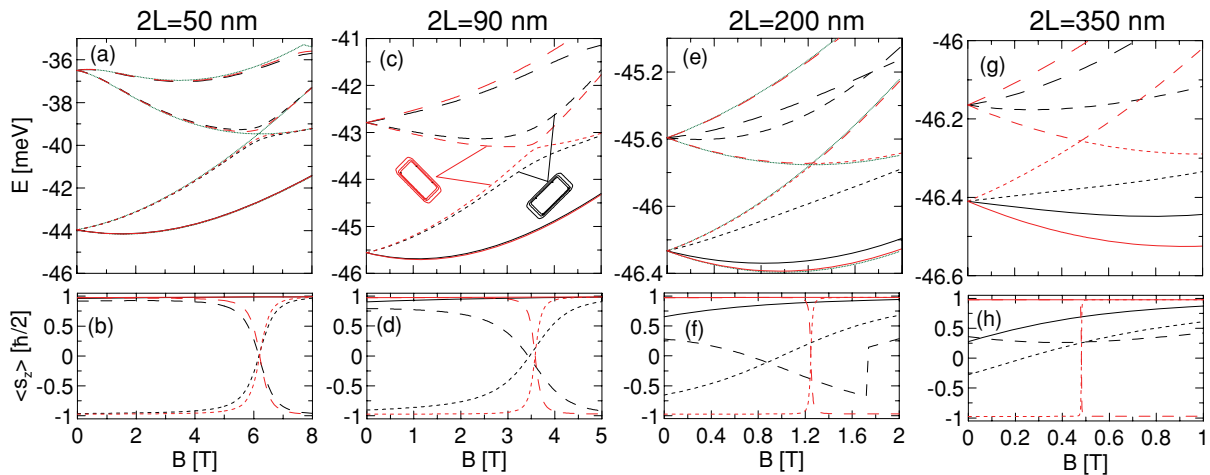


FIG. 3. (Color online) Energy spectrum (upper row) and mean values of the z component of the spin (lower row of plots) for a single electron in a quantum dot of width $2K = 40$ nm and various lengths $2L$. The results for the dot oriented along $[110]$ and $[1\bar{1}0]$ are given in black and gray (red online), respectively. Equal Rashba and Dresselhaus linear coupling constants were assumed, $\alpha = \beta = 10.8$ meV nm. In (a) and (e) the green dotted lines show the energy spectrum in the absence of SO interaction shifted down on the energy scale by 0.142 meV.

which for the antidiagonal $[1\bar{1}0]$ orientation of the dot gives $g^* = -8.7$ (quite close to $g = -8.97$) and for the diagonal orientation $[110]$ $g^* = -2.5$ only.

B. Single-electron results

Let us now consider the results obtained by diagonalization of Hamiltonian (1) with basis (8). Figure 3 shows the energy levels and mean spin z components for various lengths of the dot $2L$ for the diagonal $[110]$ (black color) and the antidiagonal $[1\bar{1}0]$ (red color) dot orientation. For the dot which is close to the square profile [$2K = 40$ nm and $2L = 50$ nm; see Fig. 3(a)] we plotted the results without SO coupling by the green dotted line (shifted down on the energy scale by 0.142 meV). The first and second energy levels correspond to opposite parity and spin. For B below the avoided crossing, the first excited state is of even parity with spin oriented down and the second excited state is of odd parity with spin oriented up. The SO coupling opens an avoided crossing between these two energy levels. This avoided crossing is wider for the diagonal and thinner for the antidiagonal dot orientation [Fig. 3(a)]. The width of this avoided crossing is determined by an extent to which the SO coupling entangles the spin and orbital wave functions. The width varies more strongly with the dot orientation when the anisotropy of the dot is enhanced, i.e., for larger lengths of the dot [Figs. 3(a), 3(c), 3(e), and 3(g)], particularly when it becomes comparable to λ_{SO} . For the antidiagonal orientation of the dots, the strong Zeeman effect quickly polarizes the electron spin and thus removes the SO coupling effects from the energy spectrum. The energy spectra obtained without SO coupling are close to the ones obtained for the antidiagonal orientation of the dot—see Figs. 3(a) and 3(e).

Figure 4 shows the dependence of the effective g^* factor on the orientation of the dots for $2L = 90$ nm and 200 nm. The g^* factor acquires maximal (minimal) absolute value for the antidiagonal (diagonal) dot orientation. For nonequal coupling constants, variation of g^* is reduced, and disappears for a single type of SO coupling present. Note that for the antidiagonal

orientation of the dot the same g^* is obtained for both L considered.

For completeness, in Fig. 5 we display the mean value of the z component of the spin in the function of the dot orientation angle for $\alpha = \beta$, $2L = 90$ nm, and two values of the magnetic field $B = 1$ T (red) and $B = 3$ T (black curves). The spin polarization is the largest for $\phi = \pi/4$ and the smallest for $\phi = -\pi/4$.

The spatial orientation of the dot has a significant influence on the SO-related avoided crossings only when both types of the coupling are of comparable strength. Figure 6 shows the results for the dominant Dresselhaus term $\alpha = 0.2\beta$ for $2L = 90$ nm. The dependence of the width of the avoided crossing on orientation is qualitatively the same as for $\alpha = \beta$ [see Figs. 3(c) and 3(d)], only much weaker. For comparison, the energy spectrum for $\alpha = 0$ and $\beta = 10.8$ meV nm is given in Fig. 6(a) with the black dotted line. For a single type of SO coupling present the same energy spectrum is obtained for any dot orientation.

C. Two-electron results

The two-electron spectrum without SO coupling is given in Fig. 7(a) by the dotted lines (green online). When the magnetic

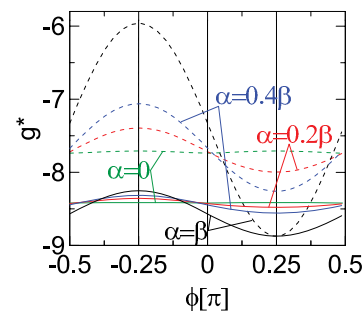


FIG. 4. (Color online) Effective g^* factor estimated by Eq. (14) in function of the spatial orientation of the dot for $2K = 40$ nm, $2L = 90$ nm (solid lines), and $2L = 200$ nm (dashed lines) for $\beta = 10.8$ meV nm and various values of α .

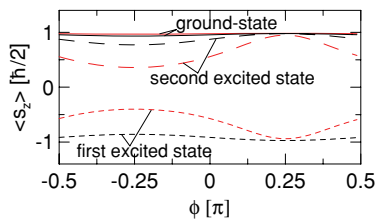


FIG. 5. (Color online) $\langle s_z \rangle$ for $B = 1$ T and 3T plotted in function of angle ϕ with black and gray (red online) lines, respectively, for $2L = 90$ nm and $\alpha = \beta = 10.8$ meV nm.

field is swept across $B = 1.1$ T the ground state changes from the singlet with even spatial parity to the spin-up polarized triplet with odd spatial parity. The dashed and solid lines in Fig. 7 correspond to SO coupling for $\alpha = \beta = 10.8$ meV nm. The results for [110] and $[1\bar{1}0]$ dot orientations are plotted with the black and red lines, respectively. For the $[1\bar{1}0]$ dot orientation the singlet-triplet transition produces a very narrow avoided crossing of width $6 \mu\text{eV}$ as compared to the pronounced (0.37 meV wide) avoided crossing obtained for the [110] orientation. For the [110] orientation the mean values of the spin vary smoothly as functions of B [see Fig. 7(b)], while for $[1\bar{1}0]$ the mean spin is nearly a bivalued function of magnetic field [see Fig. 7(b)], which indicates a removal of the SO coupling effects. The corresponding energy spectrum [red lines in Fig. 7(a)] is very close to the spectrum obtained without SO coupling (green dotted lines) up to a constant energy shift [the energy levels without SO coupling are shifted down by 0.285 meV in Fig. 7(a)]. A similar fact was presented above for the single electron in Fig. 3(a).

In Fig. 8(a) we present two lowest-energy levels as functions of the orientation of the dot for three values of magnetic field: $1 \mu\text{T}$ (residual B), 0.5 T—before the singlet-triplet avoided crossing—and for 1.1 T—at the center of avoided

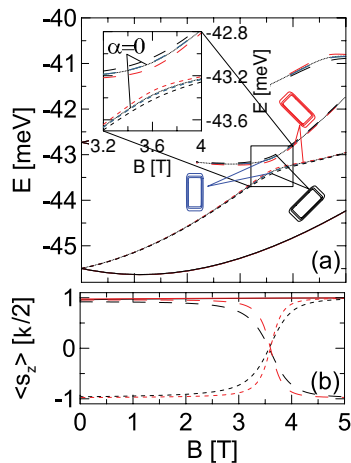


FIG. 6. (Color online) (a) Energy spectrum for a single-electron dot with a larger length aligned with [110] (black), and $[1\bar{1}0]$ (red) crystal directions given by solid and dashed lines. The dot size is $2K = 40$ nm and $2L = 90$ nm, $\beta = 10.8$ meV nm, and $\alpha = 0.2\beta$. The dotted curve shows the results without the linear Rashba term ($\alpha = 0$). (b) Mean value of s_z operator for three lowest energy states, respectively, for [110] and $[1\bar{1}0]$ dot orientations. The results for these geometrical parameters and $\alpha = \beta$ were given in Figs. 3(c) and 3(d).

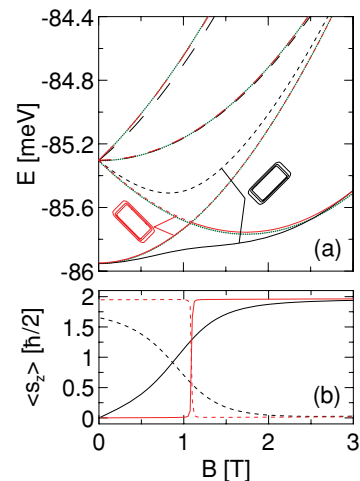


FIG. 7. (Color online) (a) Two-electron energy spectrum for single-elongated dot aligned along [110] (black) and $[1\bar{1}0]$ (dark gray–red online). The dotted curve (green online) shows the results without SO coupling shifted down by 0.285 meV. (b) Mean value of s_z for two lowest-energy states (solid, short dashed, respectively) for [110] (black) and $[1\bar{1}0]$ (dark gray–red online) dot orientation. The value of $\alpha = \beta = 10.8$ meV nm is assumed, $2K = 40$ nm and $2L = 90$ nm.

crossing. The average spins are displayed in Fig. 8(b). For the residual magnetic field the energy spectrum is independent of the dot orientation and the ground-state spin is zero. Nevertheless, a dependence of the spin of the excited state (threefold degenerate at $B = 0$) on the orientation of the dot is noticeable. For 0.5 T the energy levels weakly depend on the dot orientation, but the dependence of the spins is strong. The situation is opposite for 1.1 T. In both the cases for $\phi = \pi/4$ the spins approach closest to 0 and \hbar —values that are found in the absence of SO interaction. For 1.1 T there is a stronger peak or dip structure in the spins displayed in Fig. 8(b), which results from the near degeneracy of energy levels [see Fig. 8(a)] that makes the system particularly susceptible to perturbation by external magnetic field.

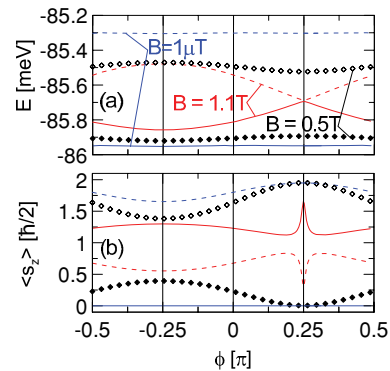


FIG. 8. (Color online) (a) Two lowest two-electron energy levels plotted in blue for $B = 1 \mu\text{T}$, in black for $B = 0.5$ T, and in red for $B = 1.1$ T. (b) s_z mean value. The same parameters as in Fig. 7 were adopted.

D. Parabolic and double quantum dots

The profiles of the confinement potentials depend strongly on the type of quantum dots, their size, and growth conditions. The effects discussed above occur in the low-energy part of the spectrum and appear as functions of the dot orientation. In order to demonstrate that they are not specific to any profile of confinement potential, we considered also an elliptical parabolic quantum dot and a double dot.

Confinement potential of electrostatic quantum dots²⁹ is generally parabolic close to its minimum, although potential profiles closer to a quantum well can also be realized.³⁰ We considered the potential in the form

$$V_p(x',y') = \frac{m^* \omega_x^2}{2} x'^2 + \frac{m^* \omega_y^2}{2} y'^2, \quad (15)$$

with $\hbar\omega_x = 2$ meV and $\hbar\omega_y = 5$ meV. The results for x' identified with $[110]$ and $[\bar{1}\bar{1}0]$ directions are given in Fig. 9. The avoided crossing between the first and second excited states of the single-electron [Fig. 9(a)] as well as the singlet-triplet [Fig. 9(b)] avoided crossing vary strongly with the orientation of the dots in consistence with the above discussion for the confinement potential given by Eq. (6).

We model a double dot by introducing a barrier in the center of the quantum dot,

$$V_d(x',y') = V_c(x',y') + \frac{V_b}{(1 + [\frac{x'^2}{K^2}]^\mu)(1 + [\frac{y'^2}{B^2}]^\mu)}, \quad (16)$$

where V_c is defined by Eq. (6) with $2K = 40$ nm and $2L = 90$ nm, $V_b = 10$ meV, and $2B = 10$ nm is taken for the barrier width. For comparison, the results for the single dot were presented in Fig. 3(c) for the single electron and in Fig. 6(a) for the electron pair. Both the single- and two-electron avoided crossings that were discussed above involved mixing of even and odd spatial parity states by SO interaction. For the double dot these states correspond to bonding and antibonding orbitals, respectively. The avoided crossings observed for the double dot are considerably thinner than in the single-dot case which is due to the introduction of the interdot barrier (in the limit of an impenetrable interdot barrier the bonding and antibonding orbitals are degenerate). In Fig. 10 we find the

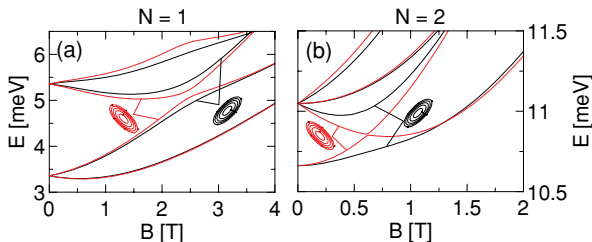


FIG. 9. (Color online) One- (a) and two-electron (b) energy spectrum for elliptical dot aligned along $[110]$ (black) and $[\bar{1}\bar{1}0]$ (gray-red online) for the elliptic parabolic confinement potential given by Eq. (15). Results are obtained for $\alpha = \beta = 10.8$ meV nm. The insets present the equipotential lines.

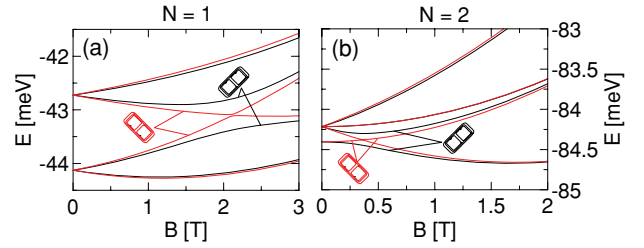


FIG. 10. (Color online) Same as Fig. 9 only for the double dot potential (16).

dependence of the width of avoided crossing on the orientation of the dot that agrees with the precedent results.

E. Discussion

The presented results indicate that the width of SO-related avoided crossings can be designed by specific orientation of the dot with respect to the crystal axes. The choice of the orientation has to be made at the sample fabrication stage. In gated quantum dots with confinement potential of the electrostatic origin²⁹ the orientation of the dot can be chosen quite arbitrarily by the shape of electrodes defined on the sample surface. Orientation of quantum dots with structural confinement can also be intentionally controlled. For instance, InGaAs/GaAs double quantum dots are formed on pre-patterned substrates along either $[110]$ or $[\bar{1}\bar{1}0]$ directions,³¹ for which the width of the SO-related avoided crossing acquires extremal values. In electrostatic quantum dots with a multielectrode setup,²⁹ rotation of the confinement potential should be possible to realize by voltages applied to the gates on a single sample.

We find that the orientation of the dot influences the width of avoided crossings provided that both the linear SO coupling constants are similar. The Rashba interaction constant can be adjusted by external electric fields,³² to match the Dresselhaus constant in particular for observation³³ of persistent spin helix states in quantum wells.³⁴ When only a single type of SO coupling is present, the orientation of the dots has no influence on the energy spectrum. In presence of the SO coupling, the orbital angular momentum is not a good quantum number even for circular confinement potentials. Nevertheless, both the spin components of a single-electron wave function do possess a definite, albeit different, angular momenta. In consequence, the charge density reproduces the circular symmetry of the confinement potential.³⁵ In potentials of circular symmetry the charge density becomes anisotropic only when both SO coupling types are present and additionally the Zeeman effect is introduced by external magnetic field.³⁵

The effect of the dot orientation on the energy spectrum is obtained in external magnetic field. For $B = 0$, the dot orientation has no influence on the Kramers-degenerate energy spectrum even when both SO coupling types are present. For $\alpha = \beta$ the effective magnetic field introduced by SO coupling is oriented along the $[\bar{1}\bar{1}0]$ direction independent of the orientation of the dot, nevertheless, its strength is dot-orientation dependent.³⁶ The electron spins precess in the effective magnetic field. Therefore the orientation of the dot does matter for the spin manipulation at zero magnetic field,^{27,36} even though no effect on the energy spectrum is present.

IV. SUMMARY AND CONCLUSIONS

We studied the avoided crossings opened by SO interaction in the single- and two-electron planar (001) quantum dots as functions of the external perpendicular magnetic field. We demonstrated that the width of these avoided crossings can be tuned within a range of two orders of magnitude by orientation of the quantum dot with respect to the crystal directions.

The tunability is achieved provided that (i) both Rashba and Dresselhaus interactions are present with comparable values of linear coupling constants ($\alpha \simeq \beta$), (ii) the dot is anisotropic, and (iii) its larger length is comparable to $\lambda_{SO} = \pi\hbar^2/(2\alpha m^*)$. The dependence of the width of avoided crossings on the orientation of the dot results from a different strength of the Zeeman interaction, which more or less efficiently polarizes the electron spin. The spin polarization removes the spin-

orbital entanglement from wave functions along with the SO coupling effects from the energy spectrum. Thus the dot orientation affects simultaneously the width of avoided crossings and the effective Landé factor g^* . As a general rule, the dot orientations producing large $|g^*|$ values correspond to narrow avoided crossings.

ACKNOWLEDGMENTS

This work was supported by the Krakow Interdisciplinary Ph.D. Project in Nanoscience and Advanced Nanostructures' operated within the Foundation for Polish Science MPD Programme co-financed by the EU European Regional Development Fund. Calculations were performed in ACK-CYFRONET-AGH on the RackServer Zeus.

-
- ¹P. Stano and J. Fabian, *Phys. Rev. Lett.* **96**, 186602 (2006); V. N. Golovach, A. Khaetskii, and D. Loss, *Phys. Rev. B* **77**, 045328 (2008); K. Shen and M. W. Wu, *ibid.* **76**, 235313 (2007); T. Meunier, I. T. Vink, L. H. Willems van Beveren, K.-J. Tielrooij, R. Hanson, F. H. L. Koppens, H. P. Tranitz, W. Wegscheider, L. P. Kouwenhoven, and L. M. K. Vandersypen, *Phys. Rev. Lett.* **98**, 126601 (2007).
- ²W. Yao, R.-B. Liu, and L. J. Sham, *Phys. Rev. B* **74**, 195301 (2006); W. M. Witzel and S. Das Sarma, *ibid.* **74**, 035322 (2006); L. Cywiński, W. M. Witzel, and S. Das Sarma, *ibid.* **79**, 245314 (2009).
- ³A. C. Johnson, J. R. Petta, J. M. Taylor, A. Yacoby, M. D. Lukin, C. M. Marcus, M. P. Hanson, and A. C. Gossard, *Nature (London)* **435**, 925 (2005).
- ⁴X. Hu and S. Das Sarma, *Phys. Rev. A* **61**, 062301 (2000).
- ⁵D. Loss and D. P. DiVincenzo, *Phys. Rev. A* **57**, 120 (1998); G. Burkard, D. Loss, and D. P. DiVincenzo, *Phys. Rev. B* **59**, 2070 (1999).
- ⁶S. DeBald and C. Emary, *Phys. Rev. Lett.* **94**, 226803 (2005); C. Flindt, A. S. Sorensen, and K. Flensberg, *ibid.* **97**, 240501 (2006); S. Bednarek and B. Szafran, *Nanotechnology* **20**, 065402 (2009); P. Földi, O. Kalman, M. G. Benedict, and F. M. Peeters, *Nano Lett.* **8**, 2556 (2008).
- ⁷K. V. Kavokin, *Phys. Rev. B* **64**, 075305 (2001).
- ⁸N. E. Bonesteel, D. Stepanenko, and D. P. DiVincenzo, *Phys. Rev. Lett.* **87**, 207901 (2001); G. Burkard and D. Loss, *ibid.* **88**, 047903 (2002); L. Wu and D. A. Lidar, *Phys. Rev. A* **66**, 062314 (2002); D. Stepanenko and N. E. Bonesteel, *Phys. Rev. Lett.* **93**, 140501 (2004).
- ⁹M. Wagner, U. Merkt, and A. V. Chaplik, *Phys. Rev. B* **45**, 1951 (1992).
- ¹⁰P. A. Maksym, *Phys. Rev. B* **53**, 10871 (1996).
- ¹¹S. M. Reimann and M. Manninen, *Rev. Mod. Phys.* **74**, 1283 (2002).
- ¹²S. Tarucha, D. G. Austing, T. Honda, R. J. van der Hage, and L. P. Kouwenhoven, *Phys. Rev. Lett.* **77**, 3613 (1996); L. P. Kouwenhoven, T. H. Oosterkamp, M. W. S. Danoesastro, M. Eto, D. G. Austing, T. Honda, and S. Tarucha, *Science* **278**, 1788 (1997).
- ¹³A. Harju, S. Siljamäki, and R. M. Nieminen, *Phys. Rev. Lett.* **88**, 226804 (2002).
- ¹⁴L. Meza-Montes, C. F. Destefani, and S. E. Ulloa, *Phys. Rev. B* **78**, 205307 (2008); F. Qu, G. L. Iorio, V. Lopez-Richard, and G. E. Marques, *Appl. Phys. Lett.* **95**, 083101 (2009); M. P. Nowak and B. Szafran, *Phys. Rev. B* **81**, 235311 (2010); F. Baruffa, P. Stano, and J. Fabian, *ibid.* **82**, 045311 (2010).
- ¹⁵C. Fasth, A. Fuhrer, L. Samuelson, V. N. Golovach, and D. Loss, *Phys. Rev. Lett.* **98**, 266801 (2007); A. Pfund, I. Shorubalko, K. Ensslin, and R. Leturcq, *Phys. Rev. B* **76**, 161308(R) (2007).
- ¹⁶S. Takahashi, R. S. Deacon, K. Yoshida, A. Oiwa, K. Shibata, K. Hirakawa, Y. Tokura, and S. Tarucha, *Phys. Rev. Lett.* **104**, 246801 (2010).
- ¹⁷G. Dresselhaus, *Phys. Rev.* **100**, 580 (1955).
- ¹⁸Y. A. Bychkov and E. I. Rashba, *J. Phys. C* **17**, 6039 (1984).
- ¹⁹V. I. Fal'ko, B. L. Altshuler, and O. Tsypliyatyev, *Phys. Rev. Lett.* **95**, 076603 (2005); J. Königmann, R. J. Haug, D. K. Maude, V. I. Fal'ko, and B. L. Altshuler, *ibid.* **94**, 226404 (2005).
- ²⁰L. Meier, G. Salis, I. Shorubalko, E. Gini, S. Schön, and K. Enslin, *Nature Phys.* **3**, 650 (2007).
- ²¹J. Paaske, A. Andersen, and K. Flensberg, *Phys. Rev. B* **82**, 081309(R) (2010).
- ²²R. Hanson, B. Witkamp, L. M. K. Vandersypen, L. H. Willems van Beveren, J. M. Elzerman, and L. P. Kouwenhoven, *Phys. Rev. Lett.* **91**, 196802 (2003); M. Val'in-Rodr'iguez, A. Puente, and L. Serra, *Phys. Rev. B* **69**, 085306 (2004).
- ²³E. A. de Andrada e Silva, G. C. La Rocca, and F. Bassani, *Phys. Rev. B* **55**, 16293 (1997).
- ²⁴S. Saikin, M. Shen, M. Cheng, and V. Privman, *J. Appl. Phys.* **94**, 1769 (2003).
- ²⁵T. Chwiej and B. Szafran, *Phys. Rev. B* **78**, 245306 (2008).
- ²⁶For $2K = 40$ nm and $2L = 90$ nm [see Fig. 3(c)], $\alpha = \beta = 10.8$ meV nm, the four lowest eigenvalues of Hamiltonian (1) are (in meV) for $B = 0$ -45.5662 , -45.5662 , -42.7978 , -42.7978 , and for $B = 5$ T -44.3195 , -43.0897 , -41.6678 , -41.1676 . When one removes the cubic Dresselhaus and diagonal Rashba terms of Eq. (1) leaving only the linear terms of SO interaction, one obtains for 0 T -45.5661 , -45.5661 , -42.7996 , -42.7996 , and for 5 T -44.3061 , -43.0753 , -41.6817 , -41.1612 , respectively.
- ²⁷J. Schliemann, J. C. Egues, and D. Loss, *Phys. Rev. Lett.* **90**, 146801 (2003).

- ²⁸Note that the results with lines and symbols of Fig. 2 are obtained for different Hamiltonians. The symbols of Fig. 2 are obtained by diagonalization of matrix (11) operator in which the magnetic field enters *exclusively* through the Zeeman term. The lines are obtained for the exact Hamiltonian, in which the magnetic field modifies also the spatial operator h and the SO coupling terms. Nevertheless, this modification is very weak in the range of the magnetic field considered for the discussion of Fig. 2.
- ²⁹J. M. Elzerman, R. Hanson, J. S. Greidanus, L. H. Willems van Beveren, S. De Franceschi, L. M. K. Vandersypen, S. Tarucha, and L. P. Kouwenhoven, *Phys. Rev. B* **67**, 161308(R) (2003).
- ³⁰S. Bednarek, B. Szafran, K. Lis, and J. Adamowski, *Phys. Rev. B* **68**, 155333 (2003).
- ³¹L. Wang, A. Rastelli, S. Kiravittaya, P. Atkinson, F. Ding, C. C. Bof Bufon, C. Hermannstädter, M. Witzany, G. J. Beirne, P. Michler, and O. G. Schmidt, *New J. Phys.* **10**, 045010 (2008).
- ³²M. Studer, G. Salis, K. Ensslin, and D. C. Driscoll, and A. C. Gossard **103**, 027201 (2009).
- ³³J. D. Koralek, C. Weber, J. Orenstein, A. Bernevig, S. Zhang, S. Mack, and D. Awschalom, *Nature (London)* **458**, 610 (2009).
- ³⁴B. A. Bernevig, J. Orenstein, and S.-C. Zhang, *Phys. Rev. Lett.* **97**, 236601 (2006).
- ³⁵M. P. Nowak and B. Szafran, *Phys. Rev. B* **80**, 195319 (2009).
- ³⁶M. P. Nowak and B. Szafran, *Phys. Rev. B* **82**, 165316 (2010).

6 Spin-orbit coupling effects in two-dimensional circular quantum rings: Elliptical deformation of confined electron density

Spin-orbit coupling effects in two-dimensional circular quantum rings: Elliptical deformation of confined electron density

M. P. Nowak and B. Szafran

*Faculty of Physics and Applied Computer Science, AGH University of Science and Technology, al. Mickiewicza 30,
30-059 Kraków, Poland*

(Received 2 October 2009; published 23 November 2009)

We study electron states confined in two-dimensional circular quantum rings in the presence of spin-orbit coupling due to both structure and crystal inversion asymmetry in the external magnetic field. It is demonstrated that the confined electron density loses the circular symmetry of the confinement potential provided that both Rashba and Dresselhaus coupling constants are nonzero, with the exception of a special case of equal coupling constants and absence of the spin Zeeman interaction. An elliptical deviation from the circular symmetry—present already for a single confined electron—is for two electrons strengthened by the Coulomb repulsion. We discuss signatures of the charge-density deformation in the experimentally accessible quantities: magnetization and charging properties of the ring. Relevance of the results of one-dimensional ring models for description of spin-orbit coupling effects is also discussed.

DOI: [10.1103/PhysRevB.80.195319](https://doi.org/10.1103/PhysRevB.80.195319)

PACS number(s): 73.40.Gk, 73.21.Hb

I. INTRODUCTION

Spin-orbit coupling in semiconductor nanostructures is considered useful for spintronics and quantum information processing since it translates the spatial motion of an electron into rotation of its spin.^{1–6} In quantum dots the spin-orbit coupling^{7–14} leads to decay of confined electron spin polarization.¹⁵ Spin-orbit-coupled open quantum rings and their arrays are studied in the context of the Aharonov-Casher effect^{16,17} and other spin-related transport phenomena^{18–21} as well in quantum gates design.⁵ Persistent currents in closed semiconductor quantum rings attracted a lot of theoretical attention^{22–31} and the interest in this field is renewed by the recent observation of the magnetization produced by self-assembled quantum rings.³² The effect of spin-orbit coupling on the magnetization, persistent spin, and charge currents in closed quantum rings^{33–39} was extensively studied within strictly one-dimensional approximations of the ring confinement.

The spin-orbit interaction in semiconductor nanostructures—although crucial for spin manipulation and relaxation—has energetically weak effects. In particular for quantum rings the spin-orbit coupling energy is by at least two orders of magnitude smaller than the energy spacing between the ground and the first-excited states of radial quantization. This fact is usually accepted as a natural argument for strictly one-dimensional approximations^{33–40} in the discussion of the spin-orbit coupling effects. The one-dimensional models are based on an effective energy operator derived by averaging the actual Hamiltonian with the ground-state radial wave function.³⁹

In the present paper we perform a systematic exact diagonalization study of one and two electrons confined in two-dimensional circular quantum rings in the presence of the spin-orbit coupling due to the inversion asymmetry of both the structure (Rashba coupling) and the crystal lattice (Dresselhaus coupling). The exact diagonalization results are confronted with the ones produced by the lowest-radial-state approximation, which turns out to introduce a number of

artificial effects in the spectra and charge densities of the confined system, particularly when both spin-orbit coupling types are present. The case of comparable contributions of the Dresselhaus and the Rashba types of coupling is the one for which persistent helical spin densities waves appear in the two-dimensional electron gas.^{41,42}

In the presence of spin-orbit coupling the stationary states—even when confined in circular potentials—are no longer orbital angular-momentum eigenstates. However, when only a single type of the coupling—Rashba or Dresselhaus—is present both the spin-up and spin-down components of the wave function do have definite angular momenta, and in consequence the spin and charge densities retain the circular symmetry of the confinement potential. When both types of the spin-orbit interaction are simultaneously present the spin densities lose the circular symmetry, and thus a possibility of deviation of the charge density from the circularity is also opened. Indeed such a pronounced deformation of the charge density was found in Ref. 34, in particular for equal Rashba and Dresselhaus coupling constants and in the absence of the Zeeman spin interaction. We identify this result as an artifact of the lowest-radial-state approximation. The deformation of the charge density is indeed found in two-dimensional rings but only in the presence of the spin Zeeman effect and/or for nonzero but unequal coupling constants. Moreover, the actual deformation occurs in a perpendicular direction to the one predicted by the lowest-radial-state approximation. We demonstrate that the charge-density deformation distinctly influences experimentally accessible ground-state properties including the chemical potential which determines the single-electron charging of the ring⁴³ and the magnetization³² produced by persistent currents, especially for two electrons for which the deformation is radically enhanced by the Coulomb interaction.

II. THEORY

We consider a two-dimensional single-electron Hamiltonian with the magnetic field perpendicular to the plane of confinement

$$h = \left(\frac{\mathbf{p}^2}{2m^*} + V(r) \right) \mathbf{1} + \frac{1}{2} g \mu_B B \sigma_z + H_R + H_D, \quad (1)$$

where $\mathbf{p} = -i\hbar \nabla + e\mathbf{A}$, the vector potential is taken in the symmetric gauge $\mathbf{A} = B(-y/2, x/2, 0)$, $\mathbf{1}$ is the identity matrix, $V(r)$ stands for the confinement potential, and H_R and H_D introduce the linear Rashba and Dresselhaus spin-orbit interactions. For x and y axes oriented parallel to $[100]$ and $[010]$ crystal directions, respectively, the spin-orbit terms have the form

$$H_R = \alpha(p_y \sigma_x - p_x \sigma_y) / \hbar \quad (2)$$

and

$$H_D = \beta(p_x \sigma_x - p_y \sigma_y) / \hbar. \quad (3)$$

The two-dimensional Dresselhaus coupling constant $\beta = (\frac{\pi}{d})^2 \beta_{3D}$ depends on d —the thickness of the layer of confinement in the growth direction—and the bulk Dresselhaus constant β_{3D} . For the most popular value of GaAs bulk constant⁴⁴ $\beta_{3D} = 27.5 \text{ eV \AA}^3$ and $d = 5 \text{ nm}$ one has $\beta = 10.8 \text{ meV nm}$, which is used below as the maximal realistic value (for the alloyed InGaAs material constant β_{3D} is slightly increased⁴⁵). The value of the Rashba constant α depends on the slope of the potential along the growth direction, which is partially defined by the growth conditions (asymmetric doping or indium concentration profile) but can be tuned by electrical gating,⁴⁶ in particular to match the Dresselhaus coupling constant for observation of the helical spin-density waves.^{41,42}

We consider a circular quantum ring potential

$$V(r) = -V_0 \{ \exp[-(r/R_o)^\gamma] - \exp[-(r/R_i)^\gamma] \} \quad (4)$$

and apply parameters corresponding to etched $\text{In}_{0.1}\text{Ga}_{0.9}\text{As}/\text{GaAs}$ quantum rings:⁴⁷ potential depth $V_0 = 50 \text{ meV}$, electron effective mass $m^* = 0.063m_0$, dielectric constant $\epsilon = 13.125$, and Landé factor $g = -2.15$. We assume the outer and inner ring radii of $R_o = 60 \text{ nm}$ and $R_i = 40 \text{ nm}$, respectively. In Eq. (4) we apply parameter $\gamma = 35$, for which the radial potential is close to a rectangular quantum well.

The spectrum for the single electron without spin-orbit coupling is given in Fig. 1. The ground-state angular-momentum transitions occur nearly ideally periodically, which is a characteristic feature of nearly one-dimensional rings. The magnetic period of the ground-state Aharonov-Bohm oscillation is 0.565 T , which corresponds to a flux quantum threading a strictly one-dimensional ring of radius $R_{1D} = 48.3 \text{ nm}$. In Fig. 1 more or less 25 meV above the ground state we observe a branch of energy levels corresponding to the first radial excitation.

For $\beta = 0$ ($\alpha = 0$) Hamiltonian (1) commutes with the total angular momentum J_+ (J_-) operator defined as $J_\pm = L_z \pm S_z$, where $S_z = \frac{\hbar}{2} \sigma_z$ is the operator of the z component of the spin and $\mathbf{L} = -i\hbar \mathbf{1}(\mathbf{r} \times \nabla)$ is the orbital angular-momentum operator. For a single type of the spin-orbit coupling present the single-electron Hamiltonian eigenstates are therefore of the form

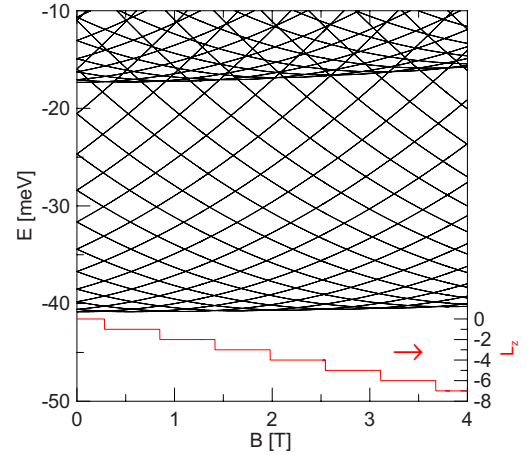


FIG. 1. (Color online) Single-electron energy spectrum for the ring defined by Eq. (4) without spin-orbit coupling. The red line near the bottom of the plot shows the ground-state angular momentum.

$$\psi = \begin{pmatrix} \psi_{l_\uparrow}(r) \exp(il_\uparrow \phi) \\ \psi_{l_\downarrow}(r) \exp(il_\downarrow \phi) \end{pmatrix} \quad (5)$$

with $l_\downarrow = l_\uparrow + 1$ for the Rashba and $l_\downarrow = l_\uparrow - 1$ for the Dresselhaus coupling. When both types of the spin-orbit coupling are present the Hamiltonian still commutes with the s -parity operator $P_s = P \sigma_z$, where P is the scalar parity operator [$Pf(\mathbf{r}) = f(-\mathbf{r})$]. The spin-up and spin-down components of the Hamiltonian eigenstates possess opposite parities.

The single-electron spin orbitals are found by diagonalization of the Hamiltonian in a basis of multicenter Gaussian functions⁴⁸

$$\psi_\nu = \sum_{ks} c_{ks}^\nu \chi_s \exp \left[-\frac{(\mathbf{r} - \mathbf{R}_k)^2}{2a^2} + \frac{ieB}{2\hbar} (xY_k - yX_k) \right], \quad (6)$$

where summation over k runs over centers of Gaussians $\mathbf{R}_k = (X_k, Y_k)$, $s = \pm 1$ and χ_s are eigenstates of the Pauli matrix σ_z . In Eq. (6) integer ν numbers the Hamiltonian eigenstates. The imaginary term in the exponent is due to the magnetic translation which ensures equivalence of all the centers in the presence of the external magnetic field. The centers \mathbf{R}_k are distributed on a square array⁴⁸ of 31×31 centers spaced by $\Delta x = \Delta y = 5.2 \text{ nm}$. We use the basis function localization parameter a equal to the variationally optimal value of 5.7 nm .

The two-electron eigenproblem for the Hamiltonian $H = h(1) + h(2) + (e^2/4\pi\epsilon\epsilon_0 r_{12})$ is diagonalized in the basis of antisymmetrized products of operator (1) eigenstates,

$$\Psi = \frac{1}{\sqrt{2}} \sum_{\mu=1}^K \sum_{\nu=\mu+1}^K [\psi_\mu(1) \psi_\nu(2) - \psi_\mu(2) \psi_\nu(1)]. \quad (7)$$

Convergence of the calculation up to 0.01 meV is usually reached for $K = 22$, and the present approach allows for inclusion of up to at least $K = 52$ single-electron states. Typically, the difference between the two-electron energies as calculated for 52 and 22 single-electron basis states is smaller than $1 \text{ } \mu\text{eV}$. Discussion of the applicability of the

multicenter basis to the two-electron problem is given in Ref. 48.

III. RESULTS AND DISCUSSION

The presentation of the results is organized in the following way. First we consider the single-electron states in the absence of the Zeeman interaction ($g=0$). We begin by the case of a single type of the spin-orbit coupling present (Sec. III A), then we discuss the symmetry breaking as found in the lowest-radial-state approximation for $\alpha=\beta$ (Sec. III B), the case of nonzero but not-equal coupling constants is discussed in Sec. III C. In Sec. III D the effects of the Zeeman interactions are explained. The two-electron states are discussed in Sec. III E. Results for magnetization and chemical potentials are provided in Sec. III F.

A. $\beta=0, g=0$,

Red (dashed) lines in Fig. 2(a) show the energy spectrum for a single type of the spin-orbit coupling present—pure Dresselhaus or pure Rashba case. In Fig. 2(b) we additionally plotted the J quantum number (eigenvalue of the total angular-momentum operator J_{\pm}), the average values of the orbital angular momentum (both expressed in \hbar), and the z component of the spin (in $\hbar/2$ units). Figure 2(b) was produced for the pure Rashba coupling—for the Dresselhaus coupling J and $\langle L \rangle$ values stay the same, but the average value of the z component of the spin is inverted. With the black lines in Fig. 2(a) we plotted the results of the analytical formula¹⁸ for the pure Rashba coupling spectrum within the one-dimensional approximation

$$E_l^s = \frac{\hbar\omega_0}{2} \left\{ \left[\left(n' + \frac{1}{2} \right)^2 + \frac{1}{4} \right] + s \left(n' + \frac{1}{2} \right) \sqrt{1 + \left(\frac{\omega_R}{\omega_0} \right)^2} \right\}, \quad (8)$$

where $\omega_0 = \hbar / (m^* r_0^2)$, $\omega_R = 2\alpha / (\hbar r_0)$, $n' = l + \Phi / \Phi_0$, $l = 0, \pm 1, \pm 2, \dots$ and $s = \pm 1$ are the angular momentum and spin quantum numbers, respectively, r_0 is the effective radius of the ring, Φ is the magnetic flux threading the ring, and Φ_0 is the flux quantum. The results of Eq. (8) as given in Fig. 2 were obtained for $r_0 = R_{1D} = 48.3$ nm in consistence with the average ring radius estimated above from the period of the ground-state Aharonov-Bohm oscillation of Fig. 1. The results of the one-dimensional formula (8) were shifted on the energy scale by -40.94 meV to coincide with the two-dimensional results for $B=0$. As B grows the energy as obtained in the two-dimensional model rise due to the diamagnetic effect, absent for strictly one-dimensional rings. Moreover, we notice that avoided crossings are opened in the exact spectrum above the ground state. For instance near $B=2$ T there is an avoided crossing between the second- and third-excited energy levels, which both correspond to $J = -3.5$ and differ by the majority-spin orientation [this can be noticed by inspecting $\langle S_z \rangle$ in Fig. 2(b) when they become ground states, i.e., near 1.5 and 2.25 T, respectively].

Formula (8) predicts no avoided crossings within the spectrum, and those as found in the exact diagonalization are

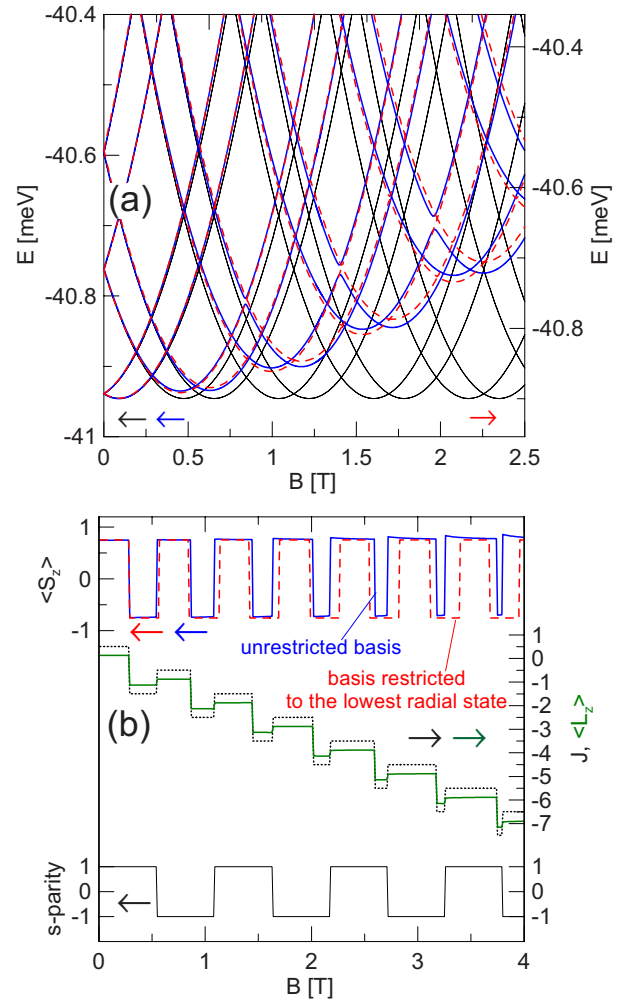


FIG. 2. (Color online) (a) Blue solid curves show the energy spectrum for a single type of the spin-orbit coupling [$\alpha = 10.8$ meV nm, $\beta=0$ or equivalently $\alpha=0$, $\beta=10.8$ meV nm] for $g=0$ as obtained by the present approach. The black lines show the results given by the analytical formula Eq. (8) for a strictly one-dimensional quantum ring shifted down on the energy scale by -40.94 meV. The dashed red curves indicate the results obtained in the lowest-radial-state approximation (see text) referred to the right axis. (b) Solid blue and red dashed curves at the top of the plot show the value of the average spin as obtained for the two-dimensional quantum ring with the exact diagonalization approach and with the basis restricted to the lowest radial state, respectively. The black dotted line and the solid green line indicate the ground-state total and orbital angular momentum, respectively. The black solid line near the bottom of the plot shows the s parity of the ground state. Pure Rashba coupling was applied for this figure ($\alpha = 10.8$ meV nm, $\beta=0$).

due to the contribution of the excited radial states. In order to illustrate this fact further we performed a reference calculation restricted to the lowest-radial state. The reference calculation was performed in the following way: (1) We diagonalize the single-electron Hamiltonian *excluding the spin-orbit coupling*. (2) We form a basis of the obtained eigenfunctions selecting only those without zeroes outside the origin—thus excluding the excited radial states. (3) The basis obtained in

this way is used for diagonalization of the full Hamiltonian (1) including the spin-orbit coupling.

Results of the above procedure (lowest-radial-state approximation) were plotted in Fig. 2(a) with the dashed red curve with respect to the right axis. These results are shifted up on the energy scale by about 0.05 meV with respect to the exact result (mind the shift of the left and right energy scales), and the avoided crossings present in the exact spectrum are closed. In both the lowest-radial approximation and the exact calculation in the ground state one obtains only crossings of energy since the subsequent ground states correspond to different total angular momentum J quantum numbers [see Fig. 2(b)]. With each J transformation (ground-state level crossing) we observe a reorientation of the average spin [see the blue line in Fig. 2(b)]. We notice that the strict periodicity of the ground-state symmetry transformations as given by the one-dimensional formula (8) is perturbed at higher magnetic fields in the exact diagonalization spectrum. The Rashba interaction promotes ground states with spin-up orientation⁵¹ and enlarges their ground-state stability range at the magnetic field scale at the expense of the spin-down oriented ground states. The magnetic fields for which the ground-state crossings are obtained in the lowest-radial-state approximation coincide with the ones produced by the analytical formula [see Fig. 2(a)] and the strict periodicity of the average spin oscillation is conserved [see the red dashed line in Fig. 2(b)].

For strictly one-dimensional rings the energy spectrum and the ground-state properties are ideally periodic with or without the spin-orbit coupling. For the two-dimensional ring considered here the ground-state angular-momentum transitions without the spin-orbit coupling appear nearly ideally periodically on the magnetic field scale (Fig. 1). The spin-orbit coupling destroys this periodicity [see the orbital angular momentum and the spin oscillation plotted with the blue line in Fig. 2(b)]. The periodicity is reproduced within the lowest-radial-state approximation [see the red dashed line for the average spin plotted in Fig. 2(b)] and not by the unrestricted basis.

We find that the first-excited state of the radial quantization contributes mostly to the minority-spin component of the ground-state wave function and we observe a shift of the maximum of the minority-spin density to a larger distance of the ring center with respect to the maximum of the majority-spin density (see Fig. 3). This shift is naturally overlooked by the lowest-radial-state approximation.

B. $\alpha=\beta$, $g=0$

Figure 4 shows the spectrum as obtained for $\alpha=\beta=10.8$ meV nm with the exact approach (blue solid curves) and with the basis restricted to the lowest-radial-state (red dotted curves) shifted down by 0.088 meV. For equal coupling constants both the exact and approximate energy levels are twofold degenerate. The restricted basis produces avoided crossings between the two lowest-energy levels and the rest of the spectrum (near $B=0, 0.6, 1.2$ T, etc.). The results obtained with the unrestricted basis do not contain any avoided crossings.

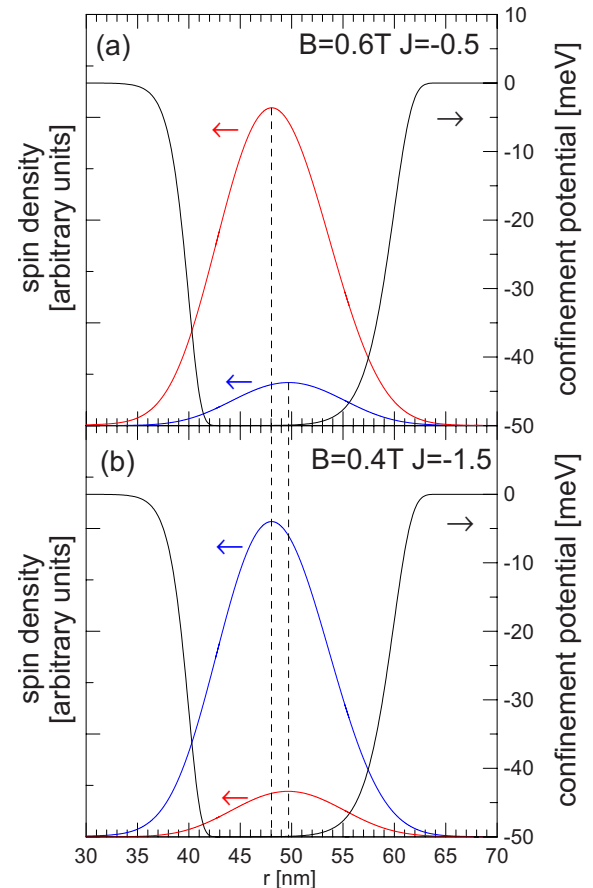


FIG. 3. (Color online) Spin-up (red curves) and spin-down densities (blue curves) as obtained in the ground-state for $B=0.6$ T (a) and $B=0.4$ T (b) for the pure Rashba coupling and $g=0$ (parameters of Fig. 2). The dashed vertical lines show the positions of the maxima of the majority and minority-spin distributions. The black solid lines show the confinement potential.

Figure 4(b) shows the ground-state charge density calculated as a function of the angle along the circumference of the ring for $r=50$ nm in the presence of the magnetic field of 0.75 T. We can see that the restricted basis produces deformation of the charge density, with no counterpart in the exact result. In Fig. 5 we additionally plotted the charge and spin densities for the odd s-parity ground state⁴⁹ at $B=0.75$ T, as obtained in the lowest-radial-state approximation [Fig. 5(a)] and by the exact diagonalization [Fig. 5(b)]. Although the spin densities in the approximate and exact results similarly deviate from the circular symmetry, in the exact result they are distributed in a way that their sum is exactly circularly symmetric, which is not reproduced in the restricted basis [Fig. 5(a)].

We found that the deviation of the charge density from circular symmetry that occurs due to the spin-orbit coupling has an elliptic character, i.e., the charge density is symmetric with respect to both the diagonal line $x=y$ (crystal direction $[110]$) and the antidiagonal line $y=-x$ (crystal direction $[\bar{1}\bar{1}0]$). In consequence the charge density acquires extremal values on the crossing of the average ring radius and the

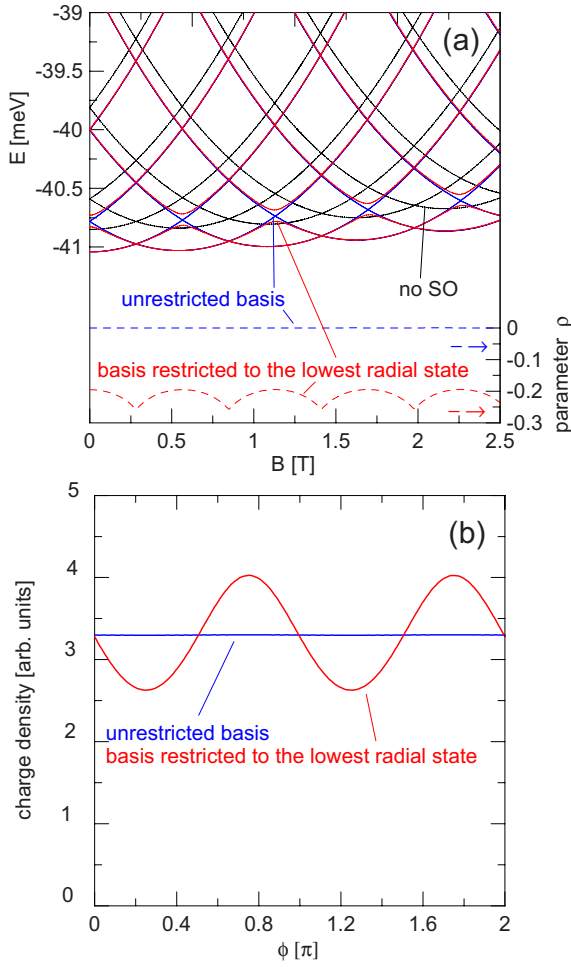


FIG. 4. (Color online) (a) Blue solid curves show the spectrum for $\alpha=\beta=10.8$ meV nm and $g=0$ as obtained with the unrestricted basis. Red dotted curves indicate the results of the lowest-radial-state approximation shifted down on the energy scale by 0.088 meV. The black dotted curves show the results for the spin-orbit coupling excluded. The dashed lines show the parameter ρ characterizing deviation of the charge density from the circular symmetry [Eq. (9)], as obtained by the exact diagonalization (blue line) and with the lowest-radial-state approximation (red line). (b) Charge density obtained for $B=0.75$ T plotted along the center of the ring $r=50$ nm as obtained by the exact diagonalization (blue curve) and with the basis restricted to the lowest radial state (red line) for the ground state of odd s parity.

symmetry axes. Therefore, in order to quantify the elliptic deformation of the charge density we use a parameter

$$\rho = \frac{|\Psi(\pi/4)|^2 - \langle |\Psi|^2 \rangle}{\langle |\Psi|^2 \rangle}, \quad (9)$$

where $\langle |\Psi|^2 \rangle$ is the average electron density calculated over the angle along the circumference of the ring at a distance of 50 nm of its center, and $|\Psi(\pi/4)|^2$ is the value obtained for the angle $\pi/4$, i.e., in point of Cartesian coordinates $x=y=35.33$ nm [see Fig. 5]. The ρ values as obtained with the restricted and unrestricted bases are plotted at the lower part of Fig. 4(a). In the lowest-radial-state approximation the pa-

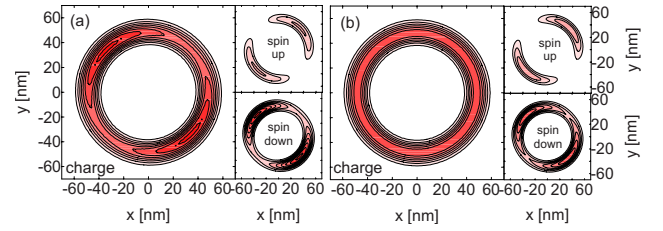


FIG. 5. (Color online) Charge and spin densities as obtained for $g=0$, $\alpha=\beta=10.8$ meV nm and $B=0.75$ T in the basis restricted to the lowest-radial-state (a) and in the unrestricted basis (b) for the ground state of odd s parity (for the ground state of even s parity the spin-up and spin-down densities are inverted).

rameter is negative (one obtains density minima at $[110]$ direction), and the strongest deformation is obtained near the ground-state-symmetry transformations—at odd multiples of half of the flux quantum. In the discussed case of equal coupling constants and $g=0$ the unrestricted basis produces ideally circular results and parameter ρ is found equal to zero.

The effects found in the basis restricted to the lowest radial state, i.e., the opening of the avoided crossings in the energy spectrum [Fig. 4(a)] and the charge-density deformation [Figs. 4(b) and 5(a)], including the orientation of the charge-density maxima on the antidiagonal of the ring ($y=-x$ line) agree with the results of the one-dimensional model presented in Fig. 7(a,b) of Ref. 34 obtained for $\alpha=\beta$ and $g=0$. However, none of these results is reproduced by the unrestricted basis [see Figs. 4(a) and 5(b)]. These effects turn out to be artifacts of the basis restricted to the lowest radial state. In fact, both the appearance of the avoided crossings in the energy spectrum and the charge-density deformation are excluded by the intrinsic symmetry of the Hamiltonian (1) present for $\alpha=\beta$ and $g=0$ as pointed out in Ref. 2. For $\alpha=\beta$ and $g=0$ (i) the Hamiltonian commutes with $\sigma_x - \sigma_y$ operator.^{2,50} (ii) The spin-orbit coupling shifts down the entire spectrum by a constant value $2\alpha^2 m^* / \hbar^2$. (iii) The charge density for each of the Hamiltonian eigenstates is not affected by the spin-orbit coupling.

The results presented above for the nonrestricted basis exactly reproduce all the above features including the constant downshift of the spectrum [for $\alpha=10.9$ meV nm equal to 0.19 meV—the spectrum without spin-orbit coupling is plotted with the black dotted lines in Fig. 4(a)].

For $\alpha=\beta$ and $g=0$ the circular symmetry of the charge density results from the intrinsic symmetry of the Hamiltonian and its deformation is excluded independent of the thickness of the ring. In consequence there does not exist a ring thickness w small enough for which the exact results could reproduce the deformation of the charge density produced by the lowest-radial-state approximation. In other words, the limitation of the basis to the lowest radial state does not become a good approximation even in the limit of small w , although the energy spacing between the lowest-energy and first-excited state diverge as $1/w^2$, which seems quite counterintuitive. A related fact—a nonvanishing contribution of the excited Landau levels in the infinite magnetic field limit of spin-orbit coupled quantum dots for $g=0$ —was recently indicated in Ref. 51.

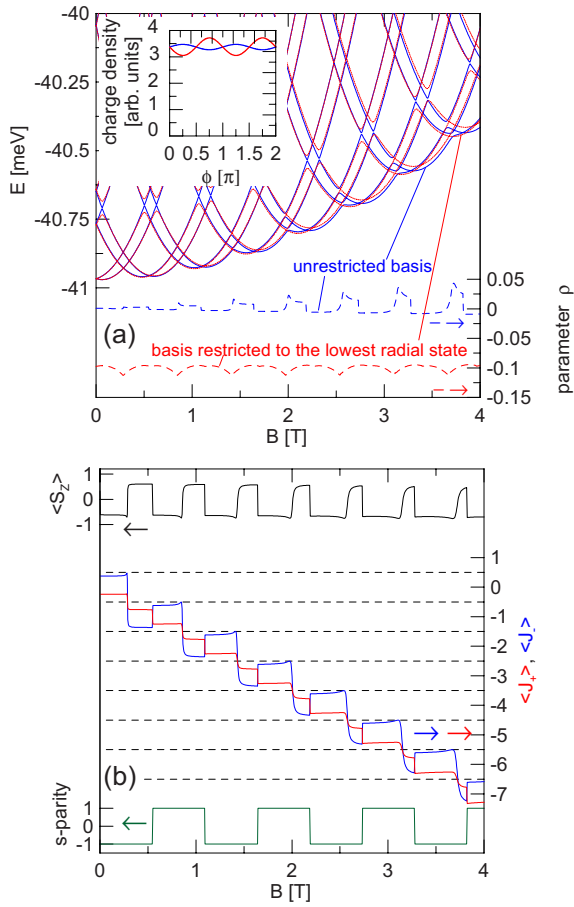


FIG. 6. (Color online) (a) The blue solid and the red dotted curves show the spectrum as calculated for $\alpha = \beta/2 = 5.4$ meV nm with the unrestricted basis and in the lowest-radial-state approximation, respectively. The dashed curves indicate the value of the ρ parameter as calculated by the exact (blue) and restricted (red) bases. The inset shows the ground-state charge density for $B = 3.77$ T along the circumference of the ring as obtained by the basis restricted to the lowest radial state (red curve) and for unrestricted basis (blue curve). (b) The black line at the top of the plot show the average value of the z component of the spin, the blue and red lines the average values of the J_- and J_+ total angular-momentum operators, and the green line near the bottom of the plot the ground-state s -parity obtained in the exact calculation.

C. $\alpha \neq \beta, g=0$

When both coupling types are present but nonequal, there does not exist a direction in which the spin component would commute with the Hamiltonian, and in general energy levels in the external magnetic field are nondegenerate. The spectrum for $\alpha = 5.4$ meV nm and $\beta = 10.8$ meV nm is plotted in Fig. 6—the blue curves show the exact results and the dotted red ones indicate the results obtained with the basis restricted to the lowest radial state shifted down by 0.057 meV. In the ground state we observe regular s -parity transformations [Fig. 6(b)] like in the case of pure Rashba coupling of Fig. 2. However, the total angular momentum is no longer quantized in the Hamiltonian eigenstates [Fig. 6(b)]. Since the considered case corresponds to the dominant Dresselhaus coupling

the J_- average values are closer to the stepwise dependence observed for a single coupling type present of Fig. 2 than J_+ . Also, since the Dresselhaus coupling dominates—the stability of spin-down ground states is observed at high field, like in the case of parabolic quantum dots.⁵¹

Let us now focus our attention on the first ground-state transformation observed near 0.25 T. For the pure and weak Dresselhaus coupling⁵³ one obtains here a crossing of spin-down $l=0$ eigenstate and spin-up $l=-1$ energy levels. Both these levels correspond to odd s -parity symmetry; however there is no avoided crossing between them since they correspond to different quantum numbers $J_- = 1/2$ and $J_- = -3/2$ (opposite spin orientation) before and after the crossing, respectively. For nonzero Rashba coupling accompanying the dominant Dresselhaus coupling that is considered in Fig. 6 the drop of J_- value from about $1/2$ to about $-3/2$ near 0.25 T is continuous since the two energy levels enter into a narrow avoided crossing. The actual crossings in the spectrum are obtained only when the ground-state s -parity changes [see Fig. 6(b)] and they are accompanied by jumps in the average value of J_- . For instance near $B = 2.75$ T there is a ground-state crossing and for $B = 3.1$ T—an avoided crossing occurs [see Fig. 6(a)]. The ground-state energy-level anticrossings are overlooked by the lowest-radial-state approximation [see the red dotted lines in Fig. 6(a)].

The deformation of the ground-state charge density as obtained by the exact diagonalization occurs only near the ground-state avoided crossings and becomes more pronounced at higher field—see the deformation parameter ρ plotted in Fig. 6(a) with the blue dashed line. The exact value of the deformation parameter is a few times smaller than the one obtained in the lowest-radial-state approximation. Moreover, a detectable elliptical deformation of the charge density in the exact result is only obtained for finite magnetic field, while in the lowest-radial-state approximation the parameter ρ takes a nonzero value already at $B=0$. Parameter ρ as obtained by the exact diagonalization occasionally acquires positive sign, opposite to the one obtained in the lowest-radial-state approximation. Then, the maxima of the charge density as calculated by the exact diagonalization appear on the diagonal line $x=y$, while in the lowest-radial-state approximation charge-density minima are found on the antidiagonal $x=-y$. The exact and approximate charge densities are plotted in the inset to Fig. 6 for $B = 3.77$ T, when a maximal deformation is obtained in the exact calculation.

For a ring of smaller width the results of the lowest-radial-state approximation should be closer to the exact ones. In order to verify this expectation we considered a ring with the inner radius $R_i = 55$ nm and the outer one $R_o = 60$ nm with potential depth $V_0 = 200$ meV. The ground-state avoided crossing becomes too thin to be observed (see Fig. 7). The spectrum in the lowest-radial-state approximation becomes nearly identical to the exact one with the exception of a constant variational overestimate of about 0.067 meV and an artificial energy gap opened near -281.8 meV. The ground-state spin oscillation as calculated in the unrestricted basis retains its periodicity in the considered magnetic field range [Fig. 7(b)]. A pronounced difference is still found in the confined charge density. The deformation of the exact charge density disappears with narrowing of the ground-state

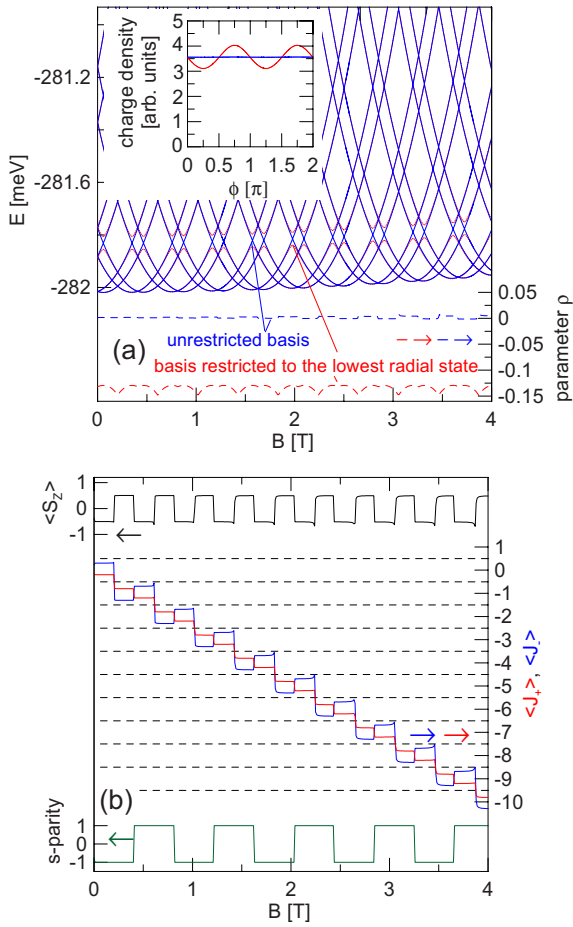


FIG. 7. (Color online) Same as Fig. 6 but for a ring of four times smaller width: $R_i=55$ nm and $R_o=60$ nm. The energy spectrum obtained by the restricted basis in (a) was shifted down by 0.067 meV.

energy-level crossings and becomes too weak to be observed (inset to Fig. 7), while the deformation obtained in the lowest-radial-state approximation not only remains, but is increased by a factor of 50% with respect to the case of Fig. 6 [see the deformation parameters in Figs. 6(a) and 7(a)]. In the context of the charge-density deformation the results of the lowest-radial-state approximation do not really become closer to the results of the exact diagonalization in the limit of small ring width.

D. $g=-2.15$

The spin Zeeman effect for perpendicular magnetic field introduces σ_z operator into the Hamiltonian. With the Zeeman effect and the spin-orbit coupling present there does not exist any spin component whose operator would commute with the Hamiltonian even for $\alpha=\beta$, which lifts the hidden symmetry of the Hamiltonian² discussed above. The spectrum for $g=-2.15$ and $\alpha=\beta=10.8$ meV nm is plotted in Fig. 8(a). We can see that two lowest-energy levels separate from the rest of the spectrum and the ground state undergoes s -parity oscillations [see Fig. 8(c)] in the external magnetic field. The Zeeman effect promotes the spin-up orientation

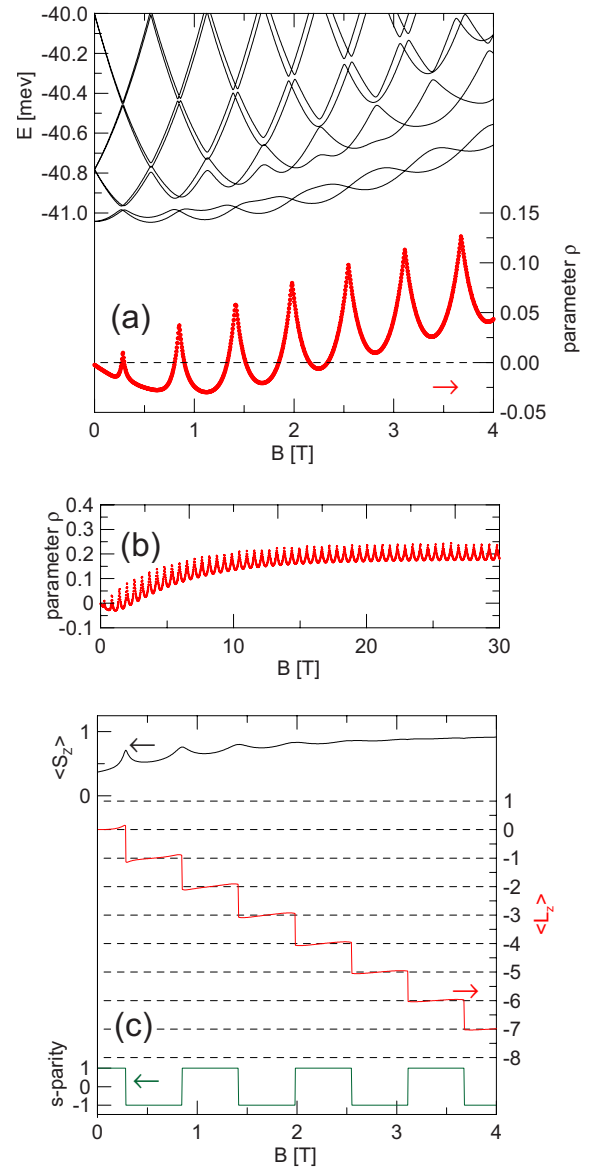


FIG. 8. (Color online) (a) Black curves show the energy spectrum as calculated by the exact diagonalization for $\alpha=\beta=10.8$ meV nm and $g=-2.15$. The red symbols show the deformation parameter ρ , which in wider B range is presented also in panel (b). (c) The black curve at the top of the plot shows the ground-state average value of the spin component, the red curve presents the average orbital angular momentum and the plot at the bottom of the plot indicates the s parity.

[Fig. 8(c)] at high field. The charge density distinctly deviates from the circular symmetry [cf. deformation parameter plotted in Fig. 8(a)]. The deformation parameter takes on maximal values at the ground-state s -parity transformations and it stays positive above 2.5 T [see Fig. 8(b)], i.e., with charge-density maxima localized on the diagonal of the ring—see Fig. 9 for $B=2$ T. The maximal value of ρ parameter at the ground-state s -parity transformations implies that the deviation from the circular symmetry is stronger in the excited state than in the ground-state—see Fig. 9.

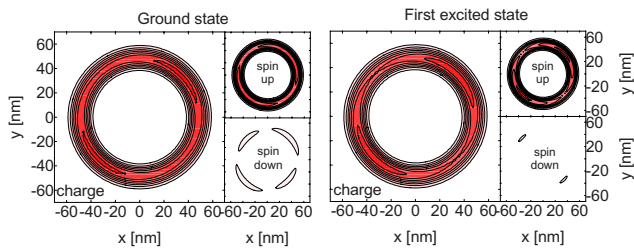


FIG. 9. (Color online) Charge and spin densities for the parameters considered in Fig. 8 at $B=2$ T.

For $\alpha=\beta=0$ the electron density remains circular, no avoided crossings are observed in the spectrum of definite orbital angular momenta [see Fig. 10(a)], and a complete ground-state spin polarization is observed for any nonzero B .

The energy spectrum, the ground-state spin, orbital angular momentum, and s -parity are presented in Fig. 11 for non-equal and nonzero coupling constants, namely, for $\alpha=\beta/2=5.4$ meV nm. The results qualitatively agree with the ones

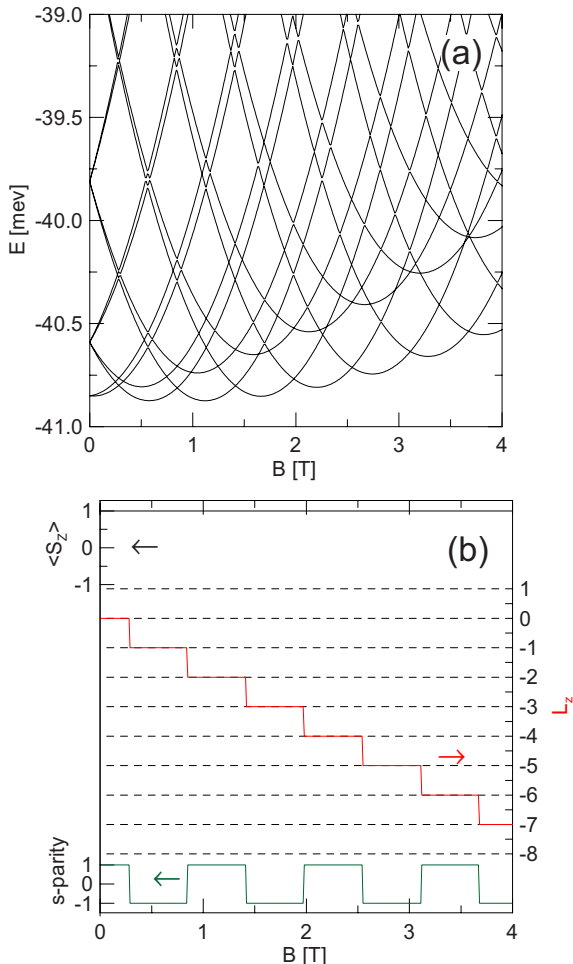


FIG. 10. (Color online) (a) Black curves show the energy spectrum as calculated by the exact diagonalization for $\alpha=\beta=0$ and $g=-2.15$. (b) The black curve at the top of the plot shows the ground-state value of the spin component, the red curve presents the orbital angular momentum and the plot at the bottom of the plot indicates the s -parity.

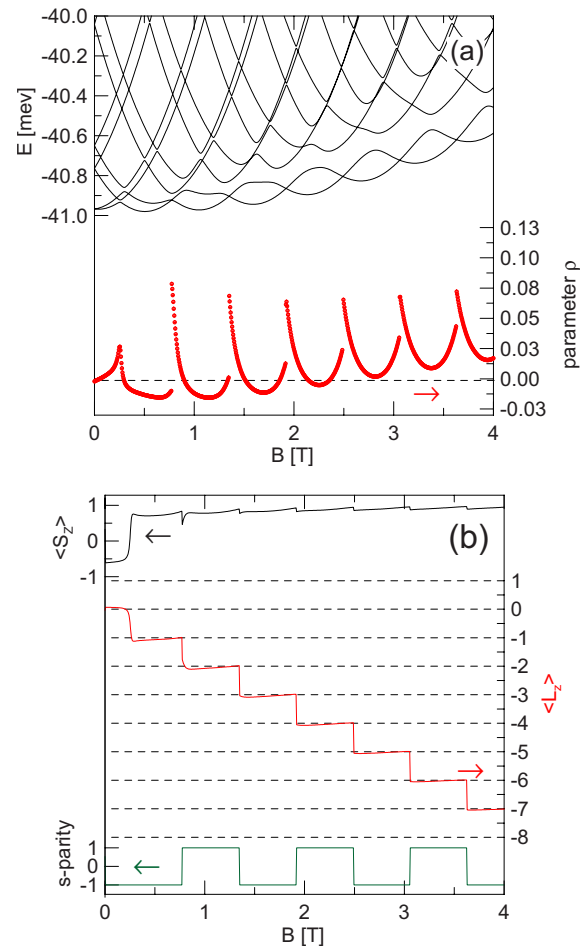


FIG. 11. (Color online) Same as Fig. 8 but for $\alpha=\beta/2=5.4$ meV nm, $g=-2.15$.

obtained for $\alpha=\beta$ in Fig. 8. In particular, an energy gap between two lowest-energy states of opposite parities and the rest of the spectrum is opened and maximal deformation of the electron density is found at the ground-state s -parity transformations. However, the ρ parameter is no longer continuous at the symmetry transformations [cf. the case of $\alpha=\beta$ of Fig. 8(a)]

For one of the coupling constants equal to zero either J_+ or J_- operator commutes with Hamiltonian, hence no deformation of the electron density is found, and the energy spectrum (Fig. 12) does not contain any energy gap between two lowest-energy levels and the rest of the spectrum—in contrast to Figs. 8 and 11.

E. Two confined electrons

Figure 13(a) shows the two-electron spectrum for $g=0$ in the absence of the spin-orbit coupling. The magnetic period of the ground-state transitions is halved²² with respect to the single-electron case (compare Figs. 1 and 13). Figure 13(b) presents the spectrum for the highly symmetric spin-orbit coupling of $\alpha=\beta=10.8$ meV nm. In Fig. 13 the two-electron

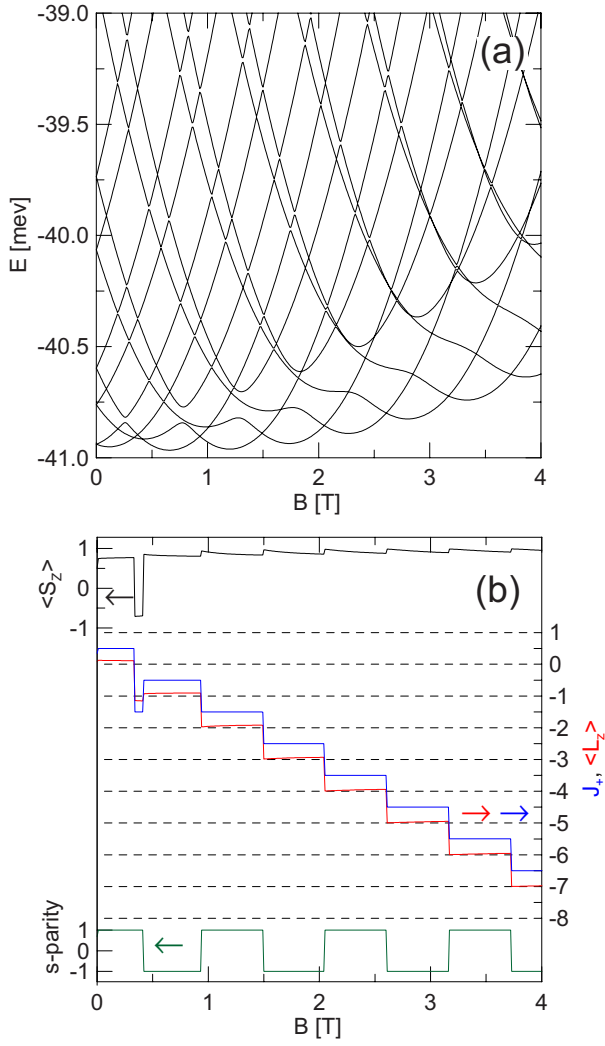


FIG. 12. (Color online) Same as Fig. 11 but for $\alpha = 10.8$ meV nm, $\beta = 0$ and $g = -2.15$.

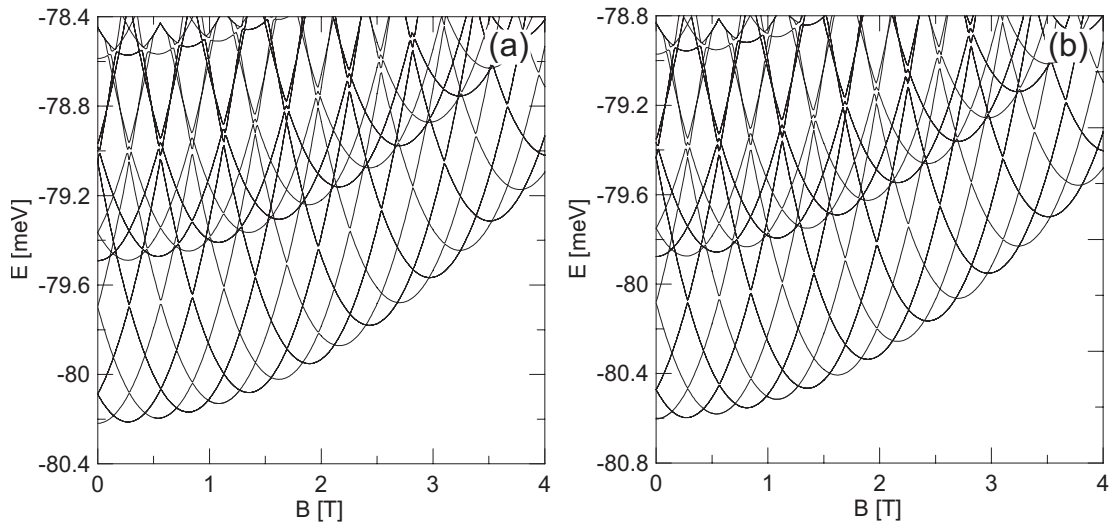


FIG. 13. Two-electron spectrum for $g = 0$ in the absence of the spin-orbit coupling (a), and for $\alpha = \beta = 10.8$ meV nm (b).

spectrum is only shifted down by the spin-orbit coupling by the energy of 0.38 meV, which is twice the value of the shift $2(\alpha^2 m^* / \hbar^2)$ for a single electron (see Sec. III B). No other difference is found between the spectra presented in Figs. 13(a) and 13(b). The invariance of the spectrum although due to the symmetry of the Hamiltonian, in the exact diagonalization calculation is only reproduced by a fully convergent two-electron basis, which illustrates the strength of the present numerical approach.

In the absence of the spin-orbit coupling, in two-electron quantum rings as well as in quantum dots the ground-state spin triplets (singlets) correspond to odd (even) orbital angular momenta, and the ground-state total spin quantum number oscillates between 0 and 1 in the external magnetic field. When the Zeeman effect is included the spin oscillations vanish at higher field and the state with spins polarized parallel ($g < 0$) to the magnetic field vector is established as the ground state. This spin-up polarized ground state of the odd orbital angular momentum corresponds to the odd s -parity symmetry. The even and the odd s -parity energy levels for $g = -2.15$ are plotted in Fig. 14(a) for $\alpha = \beta = 0$ with the red and blue curves, respectively. Note that the Zeeman effect lifts the fractional²² Aharonov-Bohm oscillation for two confined electrons and leaves an integral period shifted by half of the flux quantum with respect to the single-electron oscillation. For $\alpha = \beta = 10.8$ meV nm [see Fig. 14(b)] the ground-state crossings—which for $\alpha = \beta = 0$ are due to the orbital angular-momentum transitions—are replaced by avoided crossings between the odd s -parity energy levels. Opening of avoided crossings is more evident for a case of a weaker spin-orbit coupling $\alpha = \beta = 5.4$ meV nm presented in Fig. 14(c).

In Fig. 15 the two-electron ground-state charge and spin densities for $B = 4$ T are presented for $\alpha = \beta = 10.8$ meV nm. The left column of plots [Figs. 15(a) and 15(c)] corresponds to $g = 0$, the right column to $g = -2.15$ [Figs. 15(b) and 15(d)]. In the upper row of plots [Figs. 15(a) and 15(b)] the electron-electron interaction is neglected and it is included in the lower row of plots [Figs. 15(c) and 15(d)]. For $g = 0$ both the

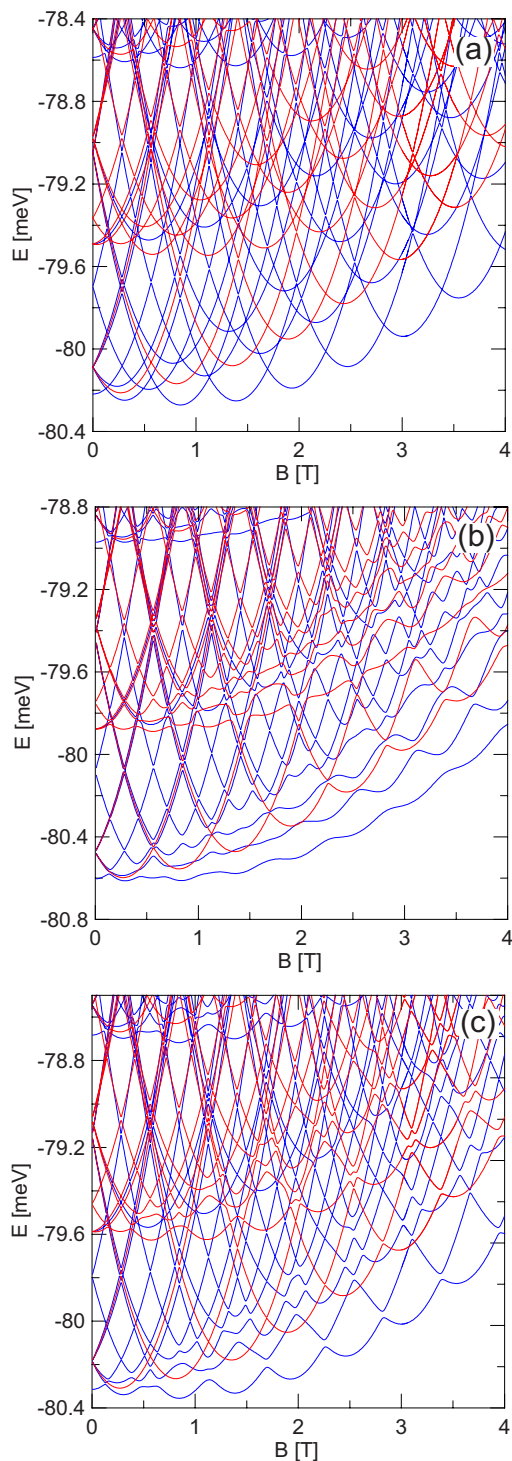


FIG. 14. (Color online) Two-electron energy spectrum for $g = -2.15$ and equal coupling constants $\alpha = \beta$. Blue (red) curves show the energy levels of odd (even) s -parity. Plots (a), (b) and (c) correspond to $\alpha = 0$, $\alpha = 10.8$ meV nm, and $\alpha = 5.4$ meV nm, respectively.

spin and charge density remain circularly symmetric. In the case of single-electron s -parity eigenstates the spin-up and spin-down densities were noncircular although their sum reproduced the circular symmetry [Fig. 5(b)]. For a single elec-

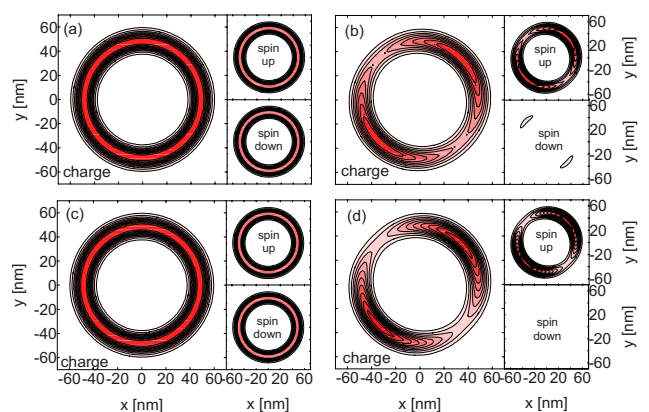


FIG. 15. (Color online) Two-electron charge and spin ground-state densities for $B = 4$ T for $\alpha = \beta = 10.8$ meV nm. $g = 0$ is assumed in (a) and (c), and $g = -2.15$ in (b) and (d). Electron-electron interaction is neglected in (a), (b) and accounted for in (c), (d).

tron ($\alpha = \beta$, $g = 0$) the ground state is twofold degenerate with interchanged spin densities for the odd and even s -parity ground states. For two confined electrons one of them occupies the odd s -parity state and the other the even s -parity state. The two-electron ground state is therefore nondegenerate and the spin densities sum up to a circularly symmetric distribution. For nonzero g , and $\alpha = \beta$ the two-electron ground-state density—even without the electron-electron interaction—is more strongly deformed than the single-electron ground-state density. This is because in the first-excited single-electron state—which is also occupied in the two-electron ground state—the elliptic deformation is stronger than in the single-electron ground state. Moreover the single-electron ground state and the first-excited state possess charge-density maxima at the same $y = x$ line [see the maximal value of the deformation parameter at the ground-state symmetry transformations presented in Fig. 8(a)]. The electron-electron interaction makes the elliptic deformation of the charge density even stronger [cf. Figs. 15(b) and 15(d)].

The elliptic deformation parameter ρ for two electrons and $g = -2.15$ is plotted in Fig. 16. The blue curves correspond to $\alpha = \beta = 10.8$ meV nm with (solid curve) and without (dashed curve) electron-electron interaction. The electron-electron interaction strongly enhances the elliptic deformation of the charge density particularly at odd multiples of half quantum (0.565 T), which correspond to crossings of triplet states in the absence of the spin-orbit coupling [see Fig. 14(a)]. The black line in Fig. 16 shows the result obtained for $\alpha = \beta / 2 = 5.4$ meV nm (electron-electron interaction included). Dependence of the parameter ρ on the magnetic field is very similar to the one found for equal coupling constants.

F. Magnetization and single-electron charging properties

Theoretical analysis of the spin-orbit coupling effects presented above required discussion of the special case of $g = 0$. For the experimentally relevant quantities we limit the

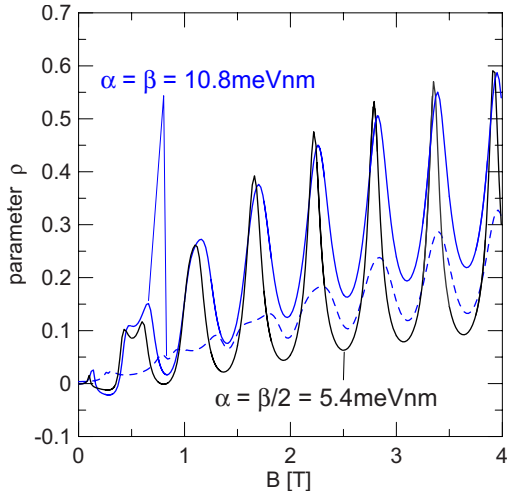


FIG. 16. (Color online) Parameter ρ quantifying the deviation of the electron density from the circular symmetry as obtained for two electrons for $\alpha=\beta=10.8$ meV nm and $g=-2.15$ with (blue solid line) and without electron-electron interaction (blue dashed line). The black solid line corresponds to $\alpha=\beta/2=5.4$ meV nm (electron-electron interaction included).

discussion to the case of negative Landé factor specific to InGaAs structures.

Figures 17 and 18 show the magnetization ($M=-\frac{dE}{dB}$) produced by a single and two electrons. Figure 17 presents the case of pure Rashba and pure Dresselhaus coupling as compared to the results obtained without the spin-orbit interaction. For $B > 2$ T the magnetization for both pure Rashba and pure Dresselhaus interactions acquire the same periodicity as in the absence of spin-orbit coupling only the magnetic fields for which the discontinuities appear (due to the ground-state total angular-momentum transitions) are slightly shifted to lower (for Dresselhaus coupling) or higher (for Rashba coupling) values.

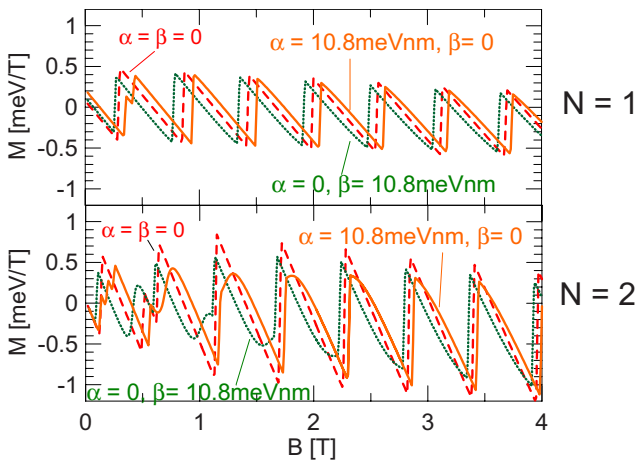


FIG. 17. (Color online) Magnetization for a single (upper plot) or two confined electrons (lower plot) without the spin-orbit coupling and for a single type of the spin-orbit coupling present. $g=-2.15$ is assumed for the Landé factor.

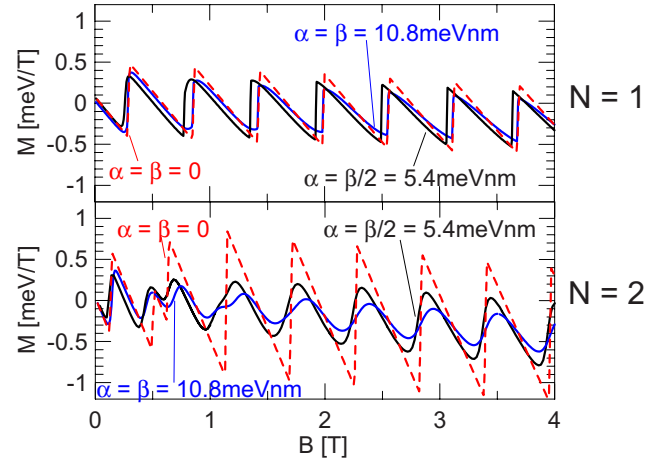


FIG. 18. (Color online) Magnetization for a single (upper plot) or two confined electrons (lower plot) without the spin-orbit coupling and for both types of spin-orbit coupling present. $g=-2.15$ is assumed for the Landé factor.

For both coupling constants nonzero the magnetization discontinuities result from the s -parity transformations. For a single electron the magnetization dependence on the magnetic field (see upper panel of Fig. 18) is similar to the one presented in Fig. 17 for a single type of spin-orbit coupling present. A qualitatively different result between the case of a single and both types of spin-orbit coupling present is obtained for two confined electrons (cf. lower panels of Figs. 17 and 18). For both coupling constants nonzero the ground state already for relatively weak magnetic field becomes permanently s -odd and the ground-state crossings due to the s -parity transformations disappear of the ground-state energy level [see Figs. 14(b) and 14(c)]. In consequence the two-electron magnetization becomes a continuous function of the magnetic field, in contrast to both the case of $\alpha=\beta=0$ and a single type of the spin-orbit coupling present. We also observe that the amplitude of the magnetization oscillations is reduced when both spin-orbit coupling types are present (Fig. 18). This reduction results from hindered circulation of the persistent currents around the ring due to appearance of the charge-density minima. The magnetization reduction is slight for a single electron and more pronounced for two electrons, in accordance with the relative strength of the elliptic deformation for one and two confined electrons.

In the single-electron charging experiments⁴³ the quantum rings embedded in a charge tunable structure are occupied by subsequent electrons when the chemical potentials of N -electron system is aligned with the Fermi energy of the electron reservoir. The chemical potential is defined as $\mu_N = E_N - E_{N-1}$, where E_N stands for the ground-state energy of N confined electrons. The chemical potentials for one- and two-electron systems are plotted in Fig. 19 for a single type of spin-orbit coupling and in Fig. 20 for nonzero values of both α and β coupling constants. The single-electron chemical potential depends on the magnetic field in a qualitatively the same manner in all the cases considered in Figs. 19 and 20. A qualitative difference is obtained for two electrons. The chemical potential for $N=2$ without the spin-orbit coupling

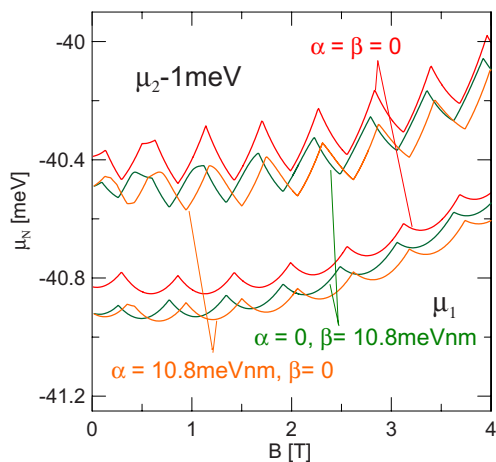


FIG. 19. (Color online) Chemical potentials for one (three lower curves) and two (three upper curves) confined electrons without the spin-orbit coupling and for a single type of spin-orbit coupling present ($g=-2.15$). The chemical potential for two electrons is shifted down by 1 meV.

has cusps (discontinuous derivatives) whenever the ground-state symmetry transformations occur for one or two electrons. The ground-state symmetry transformations for $N=1$ result in V -shaped cusps and the transformations for $N=2$ in Λ -shaped cusps. In Fig. 20 we notice that when both spin-orbit coupling types are present the Λ -shaped cusps in μ_2 are replaced by smooth maxima, which is related to the avoided crossings between s -odd-parity energy levels that are opened in the low part of the energy spectrum [Figs. 14(b) and 14(c)].

Both the magnetization and the chemical potential as presented in Figs. 17–20 indicate that the case of two electrons for both spin-orbit coupling types present differs qualitatively from the case when a single or no type of spin-orbit coupling is present. Above we demonstrated that for

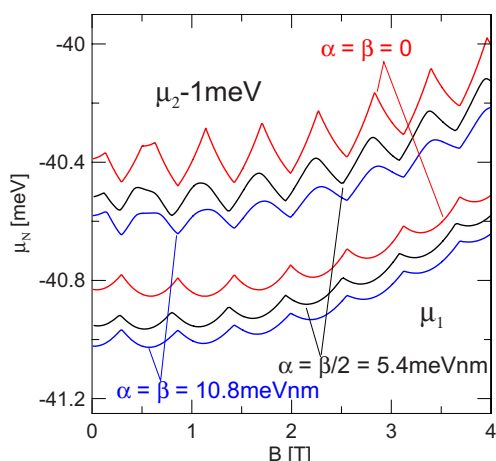


FIG. 20. (Color online) Chemical potentials for one (three lower curves) and two (three upper curves) confined electrons without the spin-orbit coupling and for both types of spin-orbit coupling present ($g=-2.15$). The chemical potential for two electrons is shifted down by 1 meV.

$g=-2.15$ when both coupling constants are nonzero the ground-state electron density is subject to an elliptical deformation. For a single type of spin-orbit coupling present as well as in the absence of the spin-orbit coupling no elliptical deformation is found. Magnetization and chemical potential as obtained for two electrons and both spin-orbit coupling types present have qualitatively the same dependence on the magnetic field as the one found recently for a circular quantum ring with two symmetrically placed repulsive defects⁵² in the absence of the spin-orbit coupling. Figure 15(c) of Ref. 52 shows that the Λ -shaped cusps disappear of the two-electron chemical potential, and Fig. 16(c) of the same work demonstrates that the two-electron magnetization becomes a continuous function of the magnetic field when the ground state acquires the odd spatial parity for stronger magnetic field. Reference 52 also demonstrates that for a single electron confined in a circular ring with two symmetrically placed defects, both the chemical potential and the magnetization remain qualitatively the same as for the clean—circular quantum ring—due to the spatial parity ground-state transformations replacing the angular-momentum transitions for the clean ring. Therefore, at least for one and two electrons, the elliptical deformation of the charge density, which is found in a circular ring when both spin-orbit coupling types are present, results in the same consequences for both the charging and the magnetic properties of the ring as an elliptical perturbation of the circular quantum ring potential in the absence of the spin-orbit coupling.

IV. SUMMARY AND CONCLUSIONS

We have performed a systematic exact diagonalization study of spin-orbit coupling effects for one and two electrons confined in a circular quantum ring of finite width. We discussed validity of one-dimensional models assuming that the radial functions of confined carriers can be identified with the lowest-energy radial state as obtained without the spin-orbit coupling. For a single type of spin-orbit coupling present the lowest-radial-state approximation overlooks rather secondary effects: (i) some avoided crossings that appear in the excited part of the spectrum, (ii) nonideal periodicity of the ground-state oscillation of the average spin obtained for $g=0$, and (iii) relative radial shifts of the majority and minority-spin densities. The performance of the lowest-radial-state approximation is worse when both Rashba and Dresselhaus coupling types are present. In that case the lowest-radial-state approximation produces charge densities which differ qualitatively from the exact ones. In particular for equal coupling constants in the absence of the Zeeman effect the basis restricted to the lowest radial state produces charge densities with artifactually broken circular symmetry, which at least for some applications excludes the usage of the one-dimensional models when Dresselhaus and Rashba spin-orbit interactions are simultaneously present. We have demonstrated that the charge density as obtained by the exact diagonalization deviates from the circular symmetry only when the Zeeman effect is present or when the coupling constants are nonequal. The elliptical deformation of the single-electron density that is found by the exact diagonal-

ization is generally weaker than in the lowest-radial-state approximation and with a different orientation of the density maxima. Moreover, the actual elliptic deformation of the charge density is only obtained for finite magnetic fields, while in the lowest-radial-state approximation the deformation is already found at $B=0$. We have considered signatures of the charge-density deformation on experimentally relevant quantities. We have found that the elliptical deformation of the charge density that appears due to the interplay of the spin-orbit coupling and the Zeeman effect has similar consequences for the magnetization and charging properties of the ring as an elliptical deformation of the circular quantum ring

confinement potential in the absence of the spin-orbit coupling.

ACKNOWLEDGMENTS

This work was supported by the “Krakow Interdisciplinary Ph.D.-Project in Nanoscience and Advanced Nanostructures” operated within the Foundation for Polish Science MPD Programme, co-financed by the EU European Regional Development Fund. Calculations were performed in ACK-CYFRONET-AGH on the RackServer Zeus.

-
- ¹S. Datta and B. Das, *Appl. Phys. Lett.* **56**, 665 (1990).
²J. Schliemann, J. C. Egues, and D. Loss, *Phys. Rev. Lett.* **90**, 146801 (2003).
³K. C. Nowack, F. H. L. Koppens, Yu. V. Nazarov, and L. M. K. Vandersypen, *Science* **318**, 1430 (2007).
⁴S. Bednarek and B. Szafran, *Phys. Rev. Lett.* **101**, 216805 (2008).
⁵P. Földi, B. Molnar, M. G. Benedict, and F. M. Peeters, *Phys. Rev. B* **71**, 033309 (2005); P. Földi, O. Kalman, M. G. Benedict, and F. M. Peeters, *Nano Lett.* **8**, 2556 (2008).
⁶S. Bellucci and P. Onorato, *Phys. Rev. B* **77**, 165305 (2008).
⁷E. Tsitsishvili, G. S. Lozano, and A. O. Gogolin, *Phys. Rev. B* **70**, 115316 (2004).
⁸P. Pietiläinen and T. Chakraborty, *Phys. Rev. B* **73**, 155315 (2006).
⁹M. S. Kushwaha, *J. Appl. Phys.* **104**, 083714 (2008).
¹⁰W. H. Kuan, C. S. Tang, and W. Xu, *J. Appl. Phys.* **95**, 6368 (2004).
¹¹T. Chakraborty and P. Pietiläinen, *Phys. Rev. Lett.* **95**, 136603 (2005).
¹²M. Valin-Rodriguez, A. Puente, and L. Serra, *Phys. Rev. B* **69**, 153308 (2004).
¹³P. Lucignano, B. Jouault, A. Tagliacozzo, and B. L. Altshuler, *Phys. Rev. B* **71**, 121310(R) (2005).
¹⁴C. F. Destefani, S. E. Ulloa, and G. E. Marques, *Phys. Rev. B* **70**, 205315 (2004).
¹⁵D. V. Bulaev and D. Loss, *Phys. Rev. B* **71**, 205324 (2005); M. Florescu and P. Hawrylak, *ibid.* **73**, 045304 (2006); J. I. Climente, A. Bertoni, G. Goldoni, M. Rontani, and E. Molinari, *ibid.* **76**, 085305(R) (2007); M. Prada, R. H. Blick, and R. Joynt, *ibid.* **77**, 115438 (2008).
¹⁶T. Bergsten, T. Kobayashi, Y. Sekine, and J. Nitta, *Phys. Rev. Lett.* **97**, 196803 (2006).
¹⁷M. F. Borunda, X. Liu, A. A. Kovalev, X. J. Liu, T. Jungwirth, and J. Sinova, *Phys. Rev. B* **78**, 245315 (2008).
¹⁸D. Frustaglia and K. Richter, *Phys. Rev. B* **69**, 235310 (2004).
¹⁹O. Kalman, P. Földi, M. G. Benedict, and F. M. Peeters, *Phys. Rev. B* **78**, 125306 (2008).
²⁰R. Citro and F. Romeo, *Phys. Rev. B* **75**, 073306 (2007).
²¹U. Aeberhard, K. Wakabayashi, and M. Sigrist, *Phys. Rev. B* **72**, 075328 (2005).
²²K. Niemelä, P. Pietiläinen, P. Hyvönen, and T. Chakraborty, *Europhys. Lett.* **36**, 533 (1996).
²³J. I. Climente, J. Planelles, and W. Jaskólski, *Phys. Rev. B* **68**, 075307 (2003).
²⁴A. Puente, L. Serra, and R. G. Nazmitdinov, *Phys. Rev. B* **69**, 125315 (2004).
²⁵S. Viefers, P. Koskinen, P. Singa Deo, and M. Manninen, *Physica E (Amsterdam)* **21**, 1 (2004).
²⁶T. Chakraborty and P. Pietiläinen, *Phys. Rev. B* **50**, 8460 (1994).
²⁷A. O. Govorov, S. E. Ulloa, K. Karrai, and R. J. Warburton, *Phys. Rev. B* **66**, 081309(R) (2002).
²⁸J. I. Climente, J. Planelles, and J. L. Movilla, *Phys. Rev. B* **70**, 081301(R) (2004).
²⁹Y. V. Pershin and C. Piermarocchi, *Phys. Rev. B* **72**, 125348 (2005).
³⁰V. M. Fomin, V. N. Gladilin, S. N. Klimin, J. T. Devreese, N. A. J. M. Kleemans, and P. M. Koenraad, *Phys. Rev. B* **76**, 235320 (2007).
³¹V. M. Fomin, V. N. Gladilin, J. T. Devreese, N. A. J. M. Kleemans, and P. M. Koenraad, *Phys. Rev. B* **77**, 205326 (2008).
³²N. A. J. M. Kleemans, I. M. A. Bominaar-Silkens, V. M. Fomin, V. N. Gladilin, D. Granados, A. G. Taboada, J. M. Garcia, P. Offermans, U. Zeitler, P. C. M. Christianen, J. C. Maan, J. T. Devreese, and P. M. Koenraad, *Phys. Rev. Lett.* **99**, 146808 (2007).
³³J. Splettstoesser, M. Governale, and U. Zülicke, *Phys. Rev. B* **68**, 165341 (2003).
³⁴J. S. Sheng and K. Chang, *Phys. Rev. B* **74**, 235315 (2006).
³⁵G. H. Ding and B. Dong, *Phys. Rev. B* **76**, 125301 (2007).
³⁶Q. F. Sun, X. C. Xie, and J. Wang, *Phys. Rev. Lett.* **98**, 196801 (2007).
³⁷G. Y. Huang and S. D. Liang, *EPL* **86**, 67009 (2009).
³⁸A. G. Aronov and Y. B. Lyanda-Geller, *Phys. Rev. Lett.* **70**, 343 (1993).
³⁹F. E. Meijer, A. F. Morpurgo, and T. M. Klapwijk, *Phys. Rev. B* **66**, 033107 (2002).
⁴⁰S.-R. Eric Yang, *Phys. Rev. B* **74**, 075315 (2006).
⁴¹J. D. Koralek, C. Weber, J. Orenstein, A. Bernevig, S. Zhang, S. Mack, and D. Awschalom, *Nature (London)* **458**, 610 (2009).
⁴²B. A. Bernevig, J. Orenstein, and S. C. Zhang, *Phys. Rev. Lett.* **97**, 236601 (2006).
⁴³A. Lorke, R. J. Luyken, A. O. Govorov, J. P. Kotthaus, J. M. Garcia, and P. M. Petroff, *Phys. Rev. Lett.* **84**, 2223 (2000).
⁴⁴W. Knap, C. Skierbiszewski, A. Zduniak, E. Litwin-Staszewska,

- D. Bertho, F. Kobbi, J. L. Robert, G. E. Pikus, F. G. Pikus, S. V. Iordanskii, V. Mosser, K. Zekentes, and Yu. B. Lyanda-Geller, *Phys. Rev. B* **53**, 3912 (1996).
- ⁴⁵S. Saikin, M. Shen, M. C. Cheng, and V. Privman, *J. Appl. Phys.* **94**, 1769 (2003).
- ⁴⁶M. J. Snelling, E. Blackwood, C. J. McDonagh, R. T. Harley, and C. T. B. Foxon, *Phys. Rev. B* **45**, 3922 (1992).
- ⁴⁷M. Bayer, M. Korkusinski, P. Hawrylak, T. Gutbrod, M. Michel, and A. Forchel, *Phys. Rev. Lett.* **90**, 186801 (2003).
- ⁴⁸T. Chwiej and B. Szafran, *Phys. Rev. B* **78**, 245306 (2008).
- ⁴⁹For $\alpha=\beta$ and $g=0$ each energy level is twofold degenerate with respect to the s parity. The degenerate states corresponding to even and odd s parities have the same charge densities, and the spin-up and spin-down densities are exchanged.
- ⁵⁰The eigenstates of $\sigma_x-\sigma_y$ can be constructed from the odd and the even s -parity eigenstates which in the case of $\alpha=\beta$ and $g=0$ correspond to degenerate energy levels. The eigenstates of $\sigma_x-\sigma_y$ are no longer s -parity eigenstates.
- ⁵¹B. Szafran, M. P. Nowak, S. Bednarek, T. Chwiej, and F. M. Peeters, *Phys. Rev. B* **79**, 235303 (2009).
- ⁵²T. Chwiej and B. Szafran, *Phys. Rev. B* **79**, 085305 (2009).
- ⁵³Figure 2 presents the case of pure Rashba coupling and $g=0$. For the pure Dresselhaus coupling the energy spectrum is identical, the average z component of the spin and the s parity are inverted.

**7 Fano resonances and electron spin transport through
a two-dimensional spin-orbit-coupled quantum ring**

Fano resonances and electron spin transport through a two-dimensional spin-orbit-coupled quantum ring

M. P. Nowak,^{1,2} B. Szafran,¹ and F. M. Peeters²¹*AGH University of Science and Technology, Faculty of Physics and Applied Computer Science, al. Mickiewicza 30, PL-30-059 Kraków, Poland*²*Departement Fysica, Universiteit Antwerpen, Groenenborgerlaan 171, B-2020 Antwerpen, Belgium*
(Received 20 October 2011; revised manuscript received 5 December 2011; published 29 December 2011)

Electron transport through a spin-orbit-coupled quantum ring is investigated within linear response theory. We show that the finite width of the ring results in the appearance of Fano resonances in the conductance. This turns out to be a consequence of the spin-orbit interaction that leads to a breaking of the parity of the states localized in the ring. The resonances appear when the system is close to maxima of Aharonov-Casher conductance oscillations where spin transfer is heavily modified. When the spin-orbit coupling strength is detuned from the Aharonov-Casher maxima the resonances are broadened resulting in a dependence of the spin transport on the electron Fermi energy in contrast to predictions from one-dimensional models.

DOI: [10.1103/PhysRevB.84.235319](https://doi.org/10.1103/PhysRevB.84.235319)

PACS number(s): 73.23.Ad, 73.63.Nm

I. INTRODUCTION

Electrical manipulation of spin polarization of carriers is one of the key elements for semiconductor spintronics devices. Since the proposal of the spin-field-effect transistor by Das and Datta¹ particular attention has been addressed to Rashba spin-orbit (SO) coupling.² This interaction—a relativistic consequence of the presence of the electric field within the device—produces an effective magnetic field³ for the moving electrons which makes their spins precess. The Rashba coupling has been successfully implemented in quantum devices that operate on an electron spin through the control of voltages applied to the electrodes in the system, such as quantum gates⁴ and valves.⁵

Proposals of spin-operating devices concern also spin-orbit-coupled quantum rings as a realization of universal quantum gates,⁶ spin beam splitters,⁷ or spin filters.⁸ The electron transfer through quantum rings involves both the spin precession due to the SO interaction and the quantum interference effects related to Aharonov-Bohm^{9,10} and Aharonov-Casher (AC) effects.¹¹ The latter spin-interference effect^{12,13} results from the fact that the relative phase shifts for the wave function passing through both arms of the ring are spin dependent in the presence of SO interaction. The AC oscillations were probed experimentally in a HgTe single quantum ring,¹⁴ in a single¹⁵ and in an array of InGaAs quantum rings,¹⁶ or in an array of Bi₂Se₃ topological insulator quantum rings.¹⁷

Although the theoretical work on SO-coupled quantum rings is rich, it is based mostly on the idealized case of a ring with infinitesimal narrow channels, i.e., the one-dimensional approximation. This approach allowed one to obtain analytical description of charge¹⁸ and spin⁶ transport through the ring as function of the electron Fermi energy and the Rashba SO coupling strength. Theoretical studies concerning two-dimensional channels showed however that for an accurate description of transport through the spin-orbit-coupled ring, the finite width of the channels cannot be neglected.^{13,14,19} This is mainly due to the fact that for a finite-width ring the spin is no longer well defined. Nonetheless, full calculations are rather scarce. A ring with two-dimensional channels has been studied within a tight-binding formalism in Ref. 13 or

in the framework of the scattering matrix method in Ref. 20. Reference 19 investigated the transport within the multiband Landauer-Büttiker formalism. This was later extended to describe the experimental data obtained in the presence of an external magnetic field.¹⁴

In this paper we develop a calculation scheme that allows us to study spin transport through a SO-coupled ring with two-dimensional channels. We show that the finite width of the channels along with SO interaction results in the appearance of Fano resonances in the conductance around the AC oscillation maxima. These sharp peak-dip structures have been previously studied in the presence of an external magnetic field, where they were the result of the broken symmetry of states localized in the ring,²¹ in systems of a quantum ring coupled to a quantum dot,²² or in one-dimensional quantum rings containing impurities²³ and magnetic structures.²⁴ Here we find that the Fano resonances originate from the coupling of the transmitted electron with the resonance states localized in the ring that have broken parity as a consequence of the SO interaction.

We find that in the resonance region the spin transport through the ring is strongly modified. We argue that the modification is caused by the coupling of the electron spin with the spin of the resonance states which is revealed by the application of an external magnetic field. When the SO coupling strength is detuned from the AC oscillation maxima the Fano resonances are broadened which results in a dependence of the spin transport on the electron Fermi energy. This particular result was not present in previous studies on spin transformations in one-dimensional rings⁶ and is of importance for spintronics devices based on SO-coupled rings.

II. THEORY

A. System

We consider a system described by the effective mass Hamiltonian

$$H = \left(\frac{\hbar^2 \mathbf{k}^2}{2m^*} + V_c(\mathbf{r}) \right) \mathbf{1} + \frac{1}{2} g \mu_B B \sigma_z + H_{SIA}, \quad (1)$$

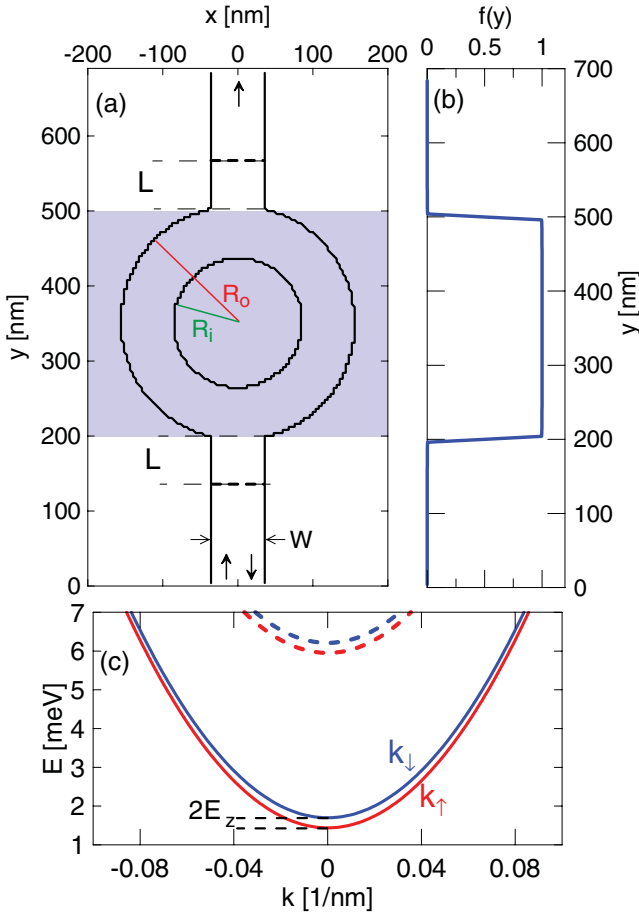


FIG. 1. (Color online) (a) The contour of the confinement potential of the ring and the leads shown by the black curves. The region where Rashba coupling is present is marked with blue color. The dashed thick lines in the leads present the closed system of leads with length L used to obtain the energies of the localized states (see text). (b) Function $f(y)$ that controls the spatial presence of the Rashba coupling. (c) Dispersion relation in the lead obtained for $B = 0.5$ T.

where $V_c(\mathbf{r})$ defines the confinement potential of the ring (with outer radius $R_o = 152$ nm, inner radius $R_i = 88$ nm, and mean radius $R = 120$ nm) and the leads, both with channel width $W = 64$ nm. We adopt a hardwall potential with $V_c = 0$ inside the channels and $V_c = 200$ meV outside (effectively an infinite barrier). The contour of the confinement potential is depicted in Fig. 1(a) by the black curve.

The kinetic momentum operator is $\mathbf{k} = -i\nabla + \frac{e\mathbf{A}}{\hbar}$. We include magnetic field B directed perpendicular to the plain of the device. We choose the Lorentz gauge $\mathbf{A} = (A_x, A_y, 0) = (0, Bx, 0)$.

We include Rashba SO interaction with the Hamiltonian $H_{SIA} = \alpha \nabla V \cdot (\boldsymbol{\sigma} \times \mathbf{k})$ resulting from the electric field felt by the propagating electron. In order to allow for a well-defined spin in the leads we assume that the Rashba coupling is present solely in the ring area by applying the electric field only therein. Experimentally this is realized¹⁵ by applying a voltage between the substrate and a gate that is restricted to the ring area.

In the considered two-dimensional system we describe the potential that enters the Rashba Hamiltonian H_{SIA}

by $V(x, y, z) = V_c(x, y) + |e|F_z z f(y)$. We include inhomogeneous electric field $F_z(y) \equiv F_z f(y)$ that controls the coupling strength. In Fig. 1(a) in the blue region the electric field is approximately equal to F_z . The function that controls $F_z(y)$ has the form $f(y) = 1/\pi^2 [\arctan(y - y_1) + \pi/2] [-\arctan(y - y_2) + \pi/2]$, where $y_1 = 200$ nm and $y_2 = 500$ nm; see Fig. 1(a). The function is nearly steplike. We depict $f(y)$ by the blue curve in Fig. 1(b). Finally, we obtain the Rashba operator for the electric field in the growth direction that depends on the y position [we neglect the derivatives of $V_c(\mathbf{r})$ as the wave function disappears in the proximity of the edges of the confinement potential]:

$$H_{SIA} = \alpha |e| F_z z \frac{\partial f(y)}{\partial y} (\sigma_z k_x - \sigma_x k_z) + \alpha |e| F_z f(y) (\sigma_x k_y - \sigma_y k_x). \quad (2)$$

We average over the z direction assuming that the electron is in the ground state for motion in the vertical excitation ($\langle z k_z \rangle = \frac{1}{2}i$), obtaining

$$H_{SIA} = -\frac{i\alpha |e| F_z}{2} \frac{\partial f(y)}{\partial y} \sigma_x + \alpha |e| F_z f(y) (\sigma_x k_y - \sigma_y k_x). \quad (3)$$

Note that the first term in the latter equation guarantees that the two-dimensional Rashba Hamiltonian is Hermitian when the strength of the coupling is varied along the y direction. In this way we avoid artificial symmetrization needed in the previous work with nonhomogeneous Rashba coupling.²⁵

We employ material parameters for $\text{In}_{0.5}\text{Ga}_{0.5}\text{As}$ alloy, i.e., $m^* = 0.0465m_0$, $g = -8.97$. The Rashba coupling parameter $\alpha = 0.572$ nm² is adopted from Ref. 26.

B. Lead eigenstates

We use a finite-difference approach with Hamiltonian Eq. (1) discretized on a grid with $\Delta x = \Delta y = 4$ nm, employing gauge-invariant discretization of the kinetic energy operator for each of the spinor Ψ components:

$$\frac{\hbar^2 \mathbf{k}^2}{2m^*} \Psi_{i,j} = \frac{\hbar^2}{2m^* \Delta x^2} (4\Psi_{i,j} - C_y \Psi_{i,j-1} - C_y^* \Psi_{i,j+1} - C_x \Psi_{i-1,j} - C_x^* \Psi_{i+1,j}), \quad (4)$$

where $\Psi_{i,j} = \Psi(x_i, y_j)$, $C_y = \exp[-i\frac{e}{\hbar} \Delta x A_y] = \exp[-i\frac{e}{\hbar} \Delta x Bx]$, and $C_x = \exp[-i\frac{e}{\hbar} \Delta x A_x] = 1$. The derivatives in the SO Hamiltonian (3) are discretized straightforwardly.

We obtain the asymptotic states in the leads far away from the ring (i.e., for $y = 0$), where $[-i\hbar \frac{\partial}{\partial y}, H] = 0$ and the spinor of propagating wave can be written as

$$\Psi(x, y) = e^{iky} \begin{pmatrix} \Psi_\uparrow^k(x) \\ \Psi_\downarrow^k(x) \end{pmatrix}. \quad (5)$$

We insert this form of the spinor in the discretized Hamiltonian (1) and obtain a one-dimensional eigenproblem for transverse quantization in the lead. We plot the dispersion relation in Fig. 1(c). The energies of the (split by the Zeeman energy $2E_z$) spin-up and spin-down states are plotted with the red and blue curves, respectively.

In the present work we consider the range of Fermi energies such that E_f lies below the energy of the third subband [the dashed red curve in Fig. 1(c)]. In this case there are four possible values of the electron wave vector for a given electron Fermi energy. It can either belong to the lowest subband having k_\uparrow or $-k_\uparrow$ and spin oriented along the z direction or belong to the second subband having k_\downarrow or $-k_\downarrow$ and spin oriented antiparallel to the z direction.

We solve the transport problem through the solution of the stationary Schrödinger equation $H\Psi = E\Psi$ assuming boundary conditions such that the electron enters the system from the bottom electrode and can either be backscattered or be transmitted through the system. Details on the boundary conditions and on the approach applied to solve the transport problem can be found in the Appendix.

Unless stated otherwise in the calculations we lift the spin degeneracy of the states in the leads by applying a residual magnetic field with $B = 0.1$ mT, which does not induce any observable orbital effects.

III. RESULTS

A. Fano resonances

Let us start with the case of no SO coupling. In the ring there are two types of localized states: states with positive and negative parity with respect to the $y = 0$ axis. We inspect these states by diagonalization of Hamiltonian (1) for a closed system with varied length of the leads given by L [see Fig. 1(c)] and plot the energy spectrum with black dotted curves in Fig. 2(b). Note that in fact each curve corresponds to the energies of two spin-opposite states. In Fig. 2(c) we plot the real part of the wave function of the spin-up states whose energies we mark by A, B, and C. The A and C states are

the states of positive parity and due to the fact that their wave function is nonzero in the leads their energy changes with L . On the other hand the wave function of negative-parity state B is zero in the leads and its energy is independent of L .

When the electron is transmitted through the ring the current-carrying state from the lead (which is a state of positive parity, i.e., the ground state of transverse excitation) couples to the localized states with positive parity. The conductance of the ring as function of electron Fermi energy [see black dotted curve in Fig. 2(a)] exhibits wide resonances due to this coupling. In the absence of SO interaction the localized states of the negative parity are *bound*; i.e., their lifetime is infinite in spite of the fact that their energy lies in the energy continuum—above the lowest subband transport threshold. On the other hand the energy of those states is still below the transport threshold for the next subband with wave functions of negative parity with respect to the axis of the channel.

When the SO coupling is introduced (we discuss first the case of weak Rashba coupling with $F_z = 50$ kV/cm) the parity of the localized states is no longer well defined. For instance mean values of parity operator for states A, B, C are 0.939, -0.962 , 0.957, respectively. Due to the broken symmetry, the current-carrying state from the lead couples now to all the localized states. This results in the appearance of sharp peaks in the conductance, plotted by the red curve in Fig. 2(a), in addition to the wide resonances. These sharp peaks are Fano resonances with characteristic asymmetric dip-peak structures. Their energy corresponds to the energy of states localized purely in the ring. The small width of the resonances is reflected in a finite but long lifetime of the resonance state. In Fig. 2(b) the red curves present the energy spectrum of a closed system as function of L in the presence of SO coupling. Note that now due to the fact that the states lack a well-defined parity anticrossings appear in the spectrum.

B. Spin transport

Let us now inspect spin transport through the ring. We consider the transmission of the electron with spin initially polarized along the z direction (from the k_\uparrow subband) and study the spin state at the output of the system.²⁷ However, for the considered residual magnetic field $B = 0.1$ mT the transfer probabilities from both subbands are exactly the same and the spin at the output of the ring is exactly opposite.

In Fig. 3 we plot the conductance (black curve) and mean spin components at the output lead by solid colored curves. Notice that outside the resonance regions the output spin orientation remains unchanged when E_f is varied—see the red and green curves—which is in agreement with the results of Ref. 6. However, when the electron Fermi energy is tuned to a resonance value the spin at the output is modified, as seen clearly in Figs. 3(b) and 3(c).

In order to further explore the spin changes in the narrow resonance regions let us increase the magnetic field, such the spin splitting of the localized resonance states is pronounced; namely, we apply $B = 0.02$ T. Now the transfer probabilities for an electron incoming from the subband k_\uparrow and k_\downarrow are no longer the same. In Fig. 4(a) with the purple curve we plot the transfer probability for an electron incoming from the lowest subband in the lead, i.e., k_\uparrow with spin polarized parallel to the z direction. With the green curve we show the transfer

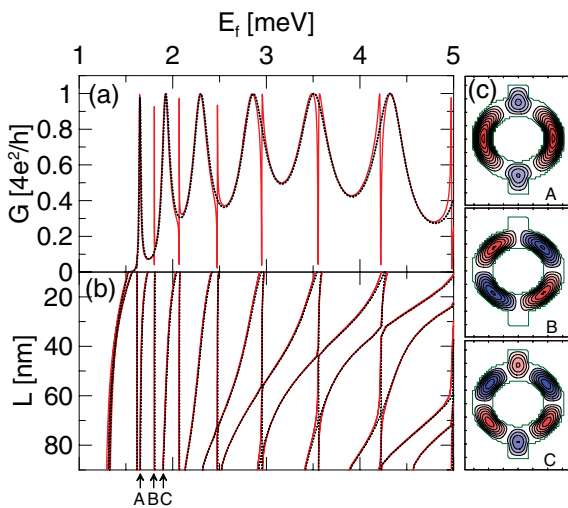


FIG. 2. (Color online) (a) Conductance of the ring as function of the Fermi energy. (b) Energy spectrum for a closed system of a ring with leads of length L . In (a) and (b) black dotted curves represent results obtained for $F_z = 0$ and red solid curves for $F_z = 50$ kV/cm. (c) Real part of the spin-up wave function corresponding to the states A, B, and C marked with blue arrows on (b) obtained without SO coupling for $L = 80$ nm. Green contours depict the profile of the confinement potential.

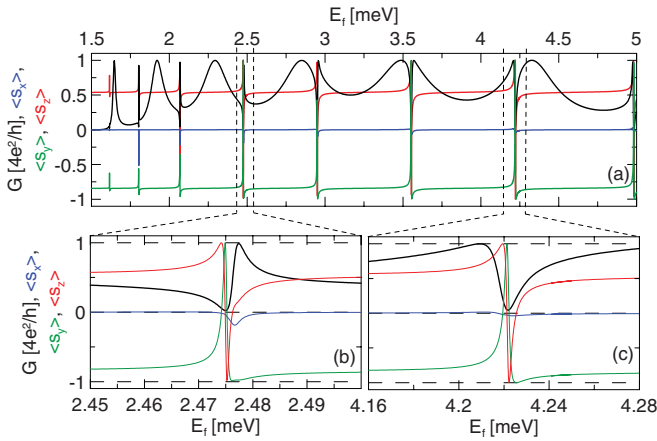


FIG. 3. (Color online) (a) Conductance through the ring (black curve) and mean spin components (blue, green, and red solid curves) at the output lead for the electron with initial spin polarization along the z direction. (b), (c) Close-ups of the resonances in plot (a).

probability for an electron incoming from the second subband, i.e., k_{\downarrow} with spin polarized antiparallel to the z direction. We find that the Fano resonances from Figs. 2(a) and 3(a) are now converted to sharp peaks in the transfer probabilities occurring separately in both $T_{k_{\uparrow}}$ and $T_{k_{\downarrow}}$. In Fig. 4(c) we plot the energy spectrum of the closed system with varied length of the leads. Notice that the magnetic field splits the spin doublets of the localized states. The states have nonzero average spin component in the z direction (with $|\langle s_z \rangle| \simeq 0.9$). The states lying lower in energy have $\langle s_z \rangle < 0$; the states with higher energies have $\langle s_z \rangle > 0$. The splitting energy of the doublet is not equal to the Zeeman splitting as the spin and orbital parts of the wave function of the states are mixed by the Rashba coupling present in the ring. Namely, the energy of twice the Zeeman splitting is

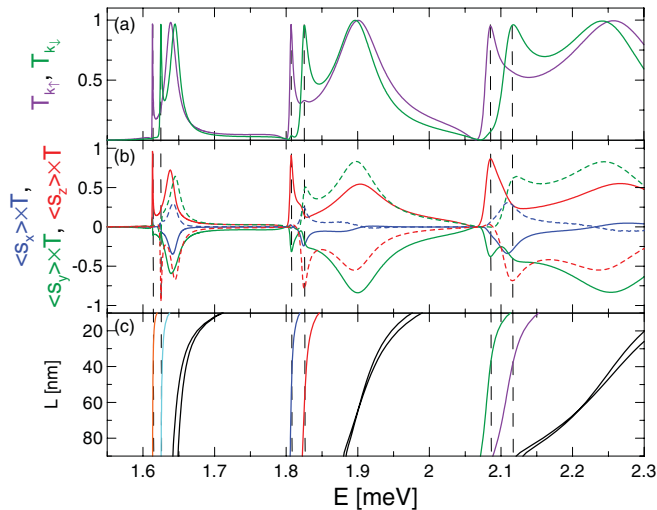


FIG. 4. (Color online) (a) Transfer probability for electron incoming with spin polarized parallel (purple curve) and antiparallel (green curve) to the z direction. (b) Mean values of the spin components in the x , y , and z directions at the end of output lead multiplied by the transfer probabilities. Solid curves are obtained for transport from k_{\uparrow} , dashed curves for k_{\downarrow} . (c) Eigenenergies of closed system with leads of length L . The results are obtained for $B = 0.02$ T.

$2E_z = |g\mu_B B| = 10 \mu\text{eV}$ and the energy difference between the states whose energies we mark with orange and light blue curves is $12 \mu\text{eV}$ and for the pair plotted with blue and red curves the energy difference is $17 \mu\text{eV}$. The mean values of the spin operators in the x and y direction are zero.

The peaks in the transport probabilities for an electron with initially spin polarized parallel to the z direction [see purple curve in Fig. 4(a)] appear for energies equal to those of the resonance states marked with orange, blue, and green colors in Fig. 4(c), with positive $\langle s_z \rangle$. For opposite spin orientation peaks are present for energies corresponding to the second state from the spin doublet (with energies marked with light blue, red, and purple curves), with negative $\langle s_z \rangle$. This indicates that resonances in the transfer probability appear when the spin of the localized state matches the orientation of the spin of the incoming electron.

Let us now inspect the average spin components at the output of the system. In Fig. 4(b) we present the mean x , y , and z spin components multiplied by the conductance with blue, green, and red curves, respectively. Solid curves correspond to initial spin-up polarization and the dashed one to initial spin-down polarization. We observe that when the transported electron couples to the resonance states localized in the ring the spin at the output is close to the average spin of the resonance state (see the peaks marked with vertical dashed lines). Outside of the resonances we observe that the spin of the transferred electron deviates from the z or $-z$ direction.

C. Dependence of the spin orientation on the Fermi energy for increased SO strength

Lets go back to the case of residual magnetic field $B = 0.1$ mT and inspect the dependence of the spin transport on the electron Fermi energy for increased strength of the SO coupling. In Fig. 5 we plot the mean spin components for four F_z values. We observe distinct broadening of the spin changes at the Fano resonances. The broadening of the resonances corresponds to a reduction of the lifetime of the resonance states in the ring.

Although the Fermi energy affects the spin evolution in the ring, the spin measured at the output (i.e., multiplied by the G) remains unchanged as function of E_f for $F_z < 200$ kV/cm. This is made clear by the contour maps of the mean spin components multiplied by the conductance presented in Fig. 6(a) for the y component and in Fig. 6(d) for the z component. Outside the narrow Fano region spin changes are masked by the blocked transport through the ring.

Figures 6(a) and 6(b) show that as the strength of the Rashba coupling is varied the conductance of the ring is changed due to the phase shift of the wave functions traveling in the left and right arm of the ring—the AC effect that modifies the conductance by a factor of¹³

$$G_{AC} = \frac{e^2}{h} \left[1 - \cos \left(\pi \sqrt{1 + \left(\frac{2Rm^*\alpha|e|F_z}{\hbar^2} \right)^2} \right) \right]. \quad (6)$$

For appropriately chosen strength of the SO coupling transport through the ring is quenched.^{18,19} For parameters taken in the present calculation the first AC oscillation minimum ($G_{AC} = 0$) is present around $F_z = 200$ kV/cm which can be observed

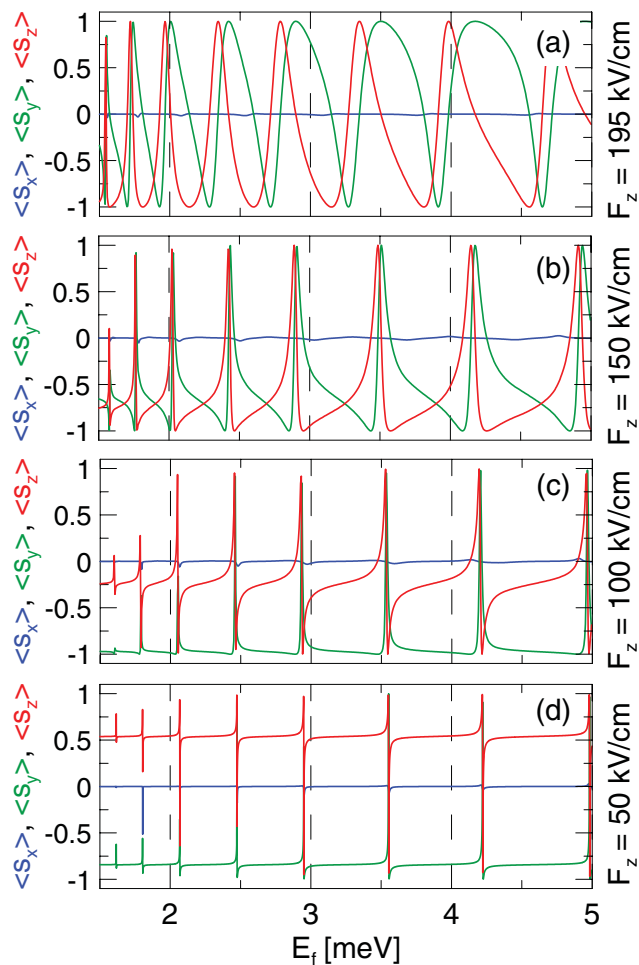


FIG. 5. (Color online) Mean values of the spin components at the output lead obtained for different strengths of the Rashba coupling (as marked on the right side of plots).

in Figs. 6(a) and 6(d). On the other hand the first maxima of the AC oscillations appear for $F_z = 0$ and around $F_z = 340$ kV/cm (note that the quenching of the conductance is found at slightly lower values of F_z for higher Fermi energy).

Similarly to the dependence of the spin on the electron Fermi energy observed before the first AC oscillation minimum ($F_z < 200$ kV/cm) we find that the spin changes for $F_z > 200$ kV/cm—after the first AC oscillation minimum [see Figs. 6(b) and 6(e)]. Similarly to the spin dependence in Fig. 5, they originate in the Fano resonances. Only now the resonances are associated with the second AC oscillation maximum around $F_z = 350$ kV/cm. Moreover now the dependence of the spin on the Fermi energy is no longer masked by the quenched transfer probabilities and it is visible in the contour maps of Figs. 6(a) and 6(d).

We conclude that the changes in the spin orientation originate at the Fano resonances appearing around and in the AC oscillation maxima and are broadened for SO coupling strength detuned from the AC oscillation maxima.

D. Comparison with one-dimensional model

In Ref. 6 it was found that when the electron is transferred through a one-dimensional spin-orbit-coupled ring

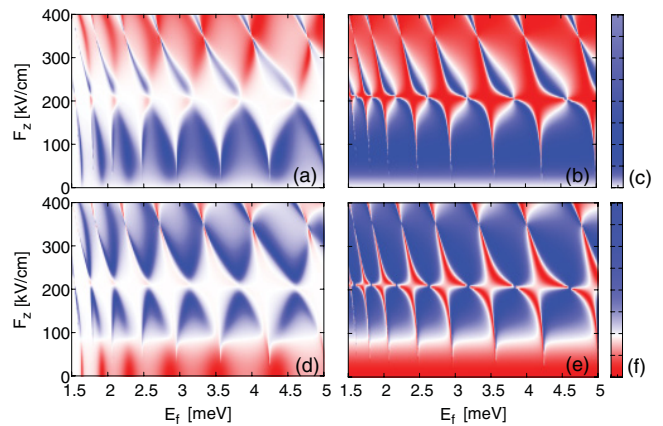


FIG. 6. (Color online) Mean spin components [(a) $\langle s_y \rangle$, (d) $\langle s_z \rangle$] at the output of the system multiplied by the conductance as function of the Rashba coupling strength and the Fermi energy. Plots (b) and (e) shows mean spin components at the output of the ring ($\langle s_y \rangle$ and $\langle s_z \rangle$) respectively. (c) and (d) are the spin components independent of E_f as calculated from the 1D approximation (see text).

its spin precesses around the y direction by an angle $2\theta = 2 \arctan(-F_z |e| \alpha 2m^* R / \hbar^2)$ which is independent of the electron Fermi energy. We calculated the spin after the rotation (taking R as the external radius of the ring, the area where the SO is present) about the angle 2θ and plot the spin components in Figs. 6(c) and 6(f). We observe that before the first AC oscillation minimum both of the present results—of the two-dimensional model and the results for the one-dimensional ring—are similar with the exception of the spin resonances that are present in the first case. However, as the SO coupling strength is increased—the entanglement of the orbital and spin part of the wave function present for the system with finite-width channel increases—the discrepancy between our calculation and the results of the one-dimensional model increases. Namely, we find positive values of the y spin component, which is not seen in the one-dimensional approximation [note that the predictions of Eq. (6) for AC oscillation maxima and minima still hold for this strength of SO coupling].

E. Impact of the channel width and the ring radius

Let us now inspect the influence of the channel width on the spin behavior. We perform calculations in which we keep the mean radius of the ring constant and modify the channel width W . We observe that the dependence of the spin orientation on the Fermi energy is changed. In Fig. 7 we plot the spin components at the output of the ring for different channel width. The wide resonances of the spin at the output as function of Fermi energy found for the wide-channel ring [see Fig. 7(c)] are transformed to sharp peaks for a ring with narrow channels [see Fig. 7(a)]. As the strength of the Rashba coupling and the mean radius of the ring are kept constant, we conclude that the dependence of the spin on the electron Fermi energy is an effect of the two-dimensional character of the channels which gets weaker for decreased W ; i.e., the resonances become narrower. This is in agreement with the intuition that for infinitesimal narrow channels the dependence of E_f should vanish (the peaks should be infinitesimally narrow) and the spin changes

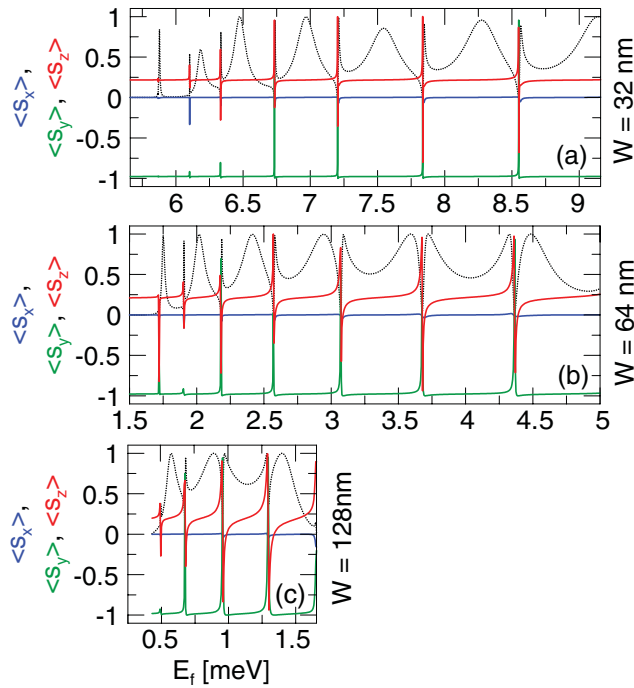


FIG. 7. (Color online) The mean spin components at the output ($\langle s_x \rangle$ with blue, $\langle s_y \rangle$ with green, and $\langle s_z \rangle$ with red curve) for $F_z = 70$ kV/cm and varied channel width W . Dotted black curves present the transport probabilities.

should not depend on the electron Fermi energy as found in the one-dimensional model. Note that in Fig. 7(c) we plot only the Fermi energy range below the energy of the third subband in the lead.

As expected from Eq. (6) the position of the AC oscillation minima and maxima with respect to the Rashba coupling strength is inversely proportional to the ring radius. In Fig. 8 we present the results obtained for a ring with mean radius $R = 220$ nm. First, we observe that spin components oscillate more frequently as function of the Fermi energy which can be attributed to the lower spacings between the energies of the localized states of a larger ring. Nevertheless, we observe a similar qualitative spin behavior with respect to the Fermi energy as in the case of a smaller ring [compare Figs. 8(b) and 8(e) with Figs. 6(b) and 6(e)]. Only now we are able to observe more periods of AC oscillations. We again find that the spin changes originate from the Fano resonances, which appear when the SO strength is tuned to the AC conductance oscillation maxima, i.e., for $F_z \simeq 185$ kV/cm and $F_z \simeq 320$ kV/cm. However, in terms of the mean spin values multiplied by the conductance, we observe a dependence on the Fermi energy only for strong SO coupling (namely $F_z > 200$ kV/cm) similarly to the case of a smaller ring. Also the correspondence with the one-dimensional results [see Figs. 8(c) and 8(f)] remains the same as for smaller ring radius.

IV. SUMMARY AND CONCLUSIONS

In summary, we have studied the spin and charge transport through a spin-orbit-coupled quantum ring with two-dimensional channels. We found Fano resonances of the

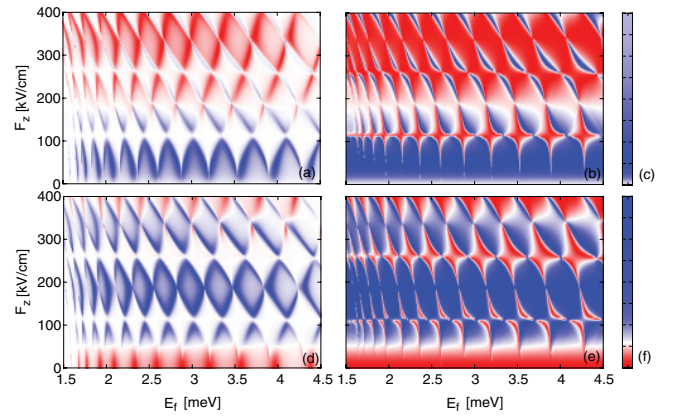


FIG. 8. (Color online) Mean spin components [(a) $\langle s_x \rangle$, (d) $\langle s_x \rangle$] at the output of the system multiplied by the conductance as function of the Rashba coupling strength and the Fermi energy. Plots (b) and (e) show the mean spin components at the output of the ring ($\langle s_y \rangle$ and $\langle s_z \rangle$), respectively. (c) and (f) are the spin components as calculated from the one-dimensional approximation (see text). Results are for a ring with radius $R = 220$ nm.

conductance which are present for nonzero SO coupling strength tuned to the maxima of AC oscillations. These narrow resonances are an effect of coupling of the current-carrying states from the leads with the localized states in the ring that have a long lifetime. The coupling is possible due to the breaking of the parity of these states by the SO interaction.

In the Fano resonances spin transport through the ring is modified. We argue that the modification is due to the coupling of the transferred electron spin with the spin of the resonance states which we investigated in the presence of finite external magnetic field.

When the SO coupling strength is such that system is outside the AC oscillation maxima the Fano resonances are broadened. In that case the spin modification is translated into a wide dependence of the spin transport on the Fermi energy. The latter result is in contrast to the findings of the one-dimensional model⁶ which employed spin transformations (independent of E_f) performed in a quantum ring to realize a universal set of quantum gates. However, when the width of the channels is decreased the resonances that result in the dependence of spin transport on the Fermi energy become narrower; the results tend toward the prediction of the one-dimensional model.

Moreover, by the direct comparison of the results of the one-dimensional model and the two-dimensional calculation we found that for strong SO coupling the spin evolution proves to behave in a way exceeding the predictions for a one-dimensional ring even outside the resonance region.

ACKNOWLEDGMENTS

This work was supported by the ‘‘Krakow Interdisciplinary PhD Project in Nanoscience and Advanced Nanostructures’’ operated within the Foundation for Polish Science MPD Programme cofinanced by the EU European Regional Development Fund, Project No. N N202103938 supported by the Ministry of Science and Higher Education (MNiSW) for 2010–2013, the Belgian Science Policy (IAP), and the Flemish

Science Foundation (FWO-V1). This research was supported in part by PL-Grid Infrastructure.

APPENDIX

This Appendix describes the applied boundary conditions and the method which are used for a solution of the electron transport through system described by Hamiltonian (1).

1. Boundary conditions

The boundary conditions applied in the method assume that the electron enters the system with a given wave vector k_{inc} (corresponding to a given energy) and can exit the system with the combination of wave vectors available for this given energy.

Let us first consider the output channel. The wave function in such channel is a combination of channel eigenstates with positive wave vectors (as we assume no backscattered waves in the output lead). Let us subtract from the derivative

$$\frac{\partial \Psi(x, y)}{\partial y} = \sum_{k>0} ikc_k^{\text{out}} \exp[iky] \begin{pmatrix} \Psi_{\uparrow}^k(x) \\ \Psi_{\downarrow}^k(x) \end{pmatrix} \quad (\text{A1})$$

$ik_{\text{inc}}\Psi(x, y)$, obtaining

$$\frac{\partial \Psi(x, y)}{\partial y} = \sum_{k>0} i(k - k_{\text{inc}})c_k^{\text{out}} \exp[iky] \begin{pmatrix} \Psi_{\uparrow}^k(x) \\ \Psi_{\downarrow}^k(x) \end{pmatrix} + ik_{\text{inc}}\Psi(x, y). \quad (\text{A2})$$

From the discretized form of the derivative

$$\frac{\partial \Psi(x, y)}{\partial y} = \frac{\Psi(x, y + \Delta y) - \Psi(x, y - \Delta y)}{2\Delta y}, \quad (\text{A3})$$

we obtain

$$\Psi(x, y + \Delta y) = 2\Delta y \sum_{k>0} i(k - k_{\text{inc}})c_k^{\text{out}} \exp[iky] \begin{pmatrix} \Psi_{\uparrow}^k(x) \\ \Psi_{\downarrow}^k(x) \end{pmatrix} + \Psi(x, y - \Delta y) + 2\Delta y ik_{\text{inc}}\Psi(x, y). \quad (\text{A4})$$

The same procedure leads to the form of the boundary condition in the bottom of the computational box. Only now we *add* $ik_{\text{inc}}\Psi(x, y)$ and the sum includes a positive wave vector of incoming electron k_{inc} and the two backscattered waves with negative wave vector. For instance, for transport of an electron with wave vector k_{\uparrow} ,

$$\Psi(x, y - \Delta y) = -2\Delta y \sum_{k \neq k_{\downarrow}} i(k + k_{\text{inc}})c_k^{\text{in}} \exp[iky] \begin{pmatrix} \Psi_{\uparrow}^k(x) \\ \Psi_{\downarrow}^k(x) \end{pmatrix} + \Psi(x, y + \Delta y) + 2\Delta y ik_{\text{inc}}\Psi(x, y). \quad (\text{A5})$$

We use the above forms of the wave functions to obtain the boundary conditions, i.e., $\Psi(x, y + \Delta y)$ for the top edge of the computational box and $\Psi(x, y - \Delta y)$ at the bottom of the computational box (at the left and right edge of the mesh we assume $\Psi = 0$). The used boundary conditions are transparent; i.e., the transport results do not depend on the length of the leads.

2. Solving the transport problem

We solve the system of equations produced by the discretization of the Schrödinger equation with the boundary conditions described above. In the present method on the one hand the amplitudes c_k^{in} and c_k^{out} are required for the boundary condition and on the other hand they can be obtained from the solution of the Schrödinger equation. Thus we assume initial values of the amplitudes (namely, $c_{k_{\uparrow}}^{\text{in}} = c_{k_{\uparrow}}^{\text{out}} = 1/\sqrt{2}$ for $k_{\text{inc}} = k_{\uparrow}$; however, we checked that the particular choice of the initial values does not change the final result) and put them into the boundary conditions. Then we solve the Schrödinger equation. From the solution we extract new values of the amplitudes by projection (in the input and output leads) of the function

$$\Psi(x, y) = \sum_k c_k \exp[iky] \begin{pmatrix} \Psi_{\uparrow}^k(x) \\ \Psi_{\downarrow}^k(x) \end{pmatrix} \quad (\text{A6})$$

(which accounts all possible wave vectors for a given energy) onto the solution and solve again the Schrödinger equation. Such procedure is repeated until convergence is reached—the extracted amplitudes do not change in the subsequent iterations, and the amplitudes c_k are such that in the input channel there is only one incoming wave and in the output lead there are no backscattered waves.

We calculate transport probability from the ratio of the probability currents j_k in the leads for respective wave vectors:

$$T_{k \rightarrow k'} = \left| \frac{c_{k'}^{\text{out}}}{c_k^{\text{in}}} \right|^2 \frac{j_{k'}}{j_k}. \quad (\text{A7})$$

The conductance G is calculated as a sum of the transmission probabilities over available subbands; i.e., $G = \frac{2e^2}{h} \sum_i^{k_{\uparrow}, k_{\downarrow}} \sum_j^{k_{\uparrow}, k_{\downarrow}} T_{i \rightarrow j}$.

The described approach allows one to study the electron transport for a given Fermi energy in contrast to the methods involving transmission of a wave packet¹⁰ that consists of the superposition of H eigenstates. Also, as the approach is based on an exact solution of the Schrödinger equation it naturally includes evanescent modes that can appear in the ring.

¹S. Datta and B. Das, *Appl. Phys. Lett.* **56**, 665 (1990).

²Y. A. Bychkov and E. I. Rashba, *J. Phys. C* **17**, 6039 (1984).

³L. Meier, G. Salis, I. Shorubalko, E. Gini, S. Schön, and K. Enslin, *Nature Phys.* **3**, 650 (2007); L. Meier, G. Salis, E. Gini, I. Shorubalko, and K. Enslin, *Phys. Rev. B* **77**, 035305 (2008).

⁴K. C. Nowack, F. H. L. Koppens, Yu. V. Nazarov, and L. M. K. Vandersypen, *Science* **318**, 1430 (2007); S. Bednarek and

B. Szafran, *Phys. Rev. Lett.* **101**, 216805 (2008); S. Nadj-Perge, S. M. Frolov, E. P. A. M. Bakkers, and L. P. Kouwenhoven, *Nature (London)* **468**, 1084 (2010).

⁵P. P. Das, K. B. Chetry, N. Bhandari, J. Wan, M. Cahay, R. S. Newrock, and S. T. Herbert, e-print [arXiv:1107.2540v1](https://arxiv.org/abs/1107.2540v1); S. Kim, Y. Hashimoto, Y. Iye, and S. Katsumoto, e-print [arXiv:1102.4648](https://arxiv.org/abs/1102.4648).

⁶P. Földi, B. Molnár, M. G. Benedict, and F. M. Peeters, *Phys. Rev. B* **71**, 033309 (2005).

- ⁷P. Földi, O. Kálmán, M. G. Benedict, and F. M. Peeters, *Phys. Rev. B* **73**, 155325 (2006).
- ⁸O. Kálmán, P. Földi, M. G. Benedict, and F. M. Peeters, *Physica E* **40**, 567 (2009); V. Moldoveanu and B. Tanatar, *Phys. Rev. B* **81**, 035326 (2010).
- ⁹A. Führer, S. Lüscher, T. Ihn, T. Heinzel, K. Ensslin, W. Wegscheider, and M. Bichler, *Nature (London)* **413**, 822 (2001).
- ¹⁰B. Szafran and F. M. Peeters, *Phys. Rev. B* **72**, 165301 (2005); B. Szafran and M. R. Poniedzialek, *ibid.* **80**, 155334 (2009); A. Chaves, G. A. Farias, F. M. Peeters, and B. Szafran, *ibid.* **80**, 125331 (2009).
- ¹¹Y. Aharonov and A. Casher, *Phys. Rev. Lett.* **53**, 319 (1984).
- ¹²J. Nitta, F. E. Meijer, and H. Takayanagi, *Appl. Phys. Lett.* **75**, 695 (1999).
- ¹³D. Frustaglia and K. Richter, *Phys. Rev. B* **69**, 235310 (2004).
- ¹⁴M. König, A. Tschetschetkin, E. M. Hankiewicz, J. Sinova, V. Hock, V. Daumer, M. Schäfer, C. R. Becker, H. Buhmann, and L. W. Molenkamp, *Phys. Rev. Lett.* **96**, 076804 (2006).
- ¹⁵J. Nitta, T. Koga, and H. Takayanagi, *Physica E* **12**, 753 (2002).
- ¹⁶J. Nitta and T. Bergsten, *New J. Phys.* **9**, 341 (2007).
- ¹⁷F. Qu, F. Yang, J. Chen, J. Shen, Y. Ding, J. Lu, Y. Song, H. Yang, G. Liu, J. Fan, Y. Li, Z. Ji, C. Yang, and L. Lu, *Phys. Rev. Lett.* **107**, 016802 (2011).
- ¹⁸B. Molnár, F. M. Peeters, and P. Vasilopoulos, *Phys. Rev. B* **69**, 155335 (2004).
- ¹⁹S. Souma and B. K. Nikolić, *Phys. Rev. B* **70**, 195346 (2004).
- ²⁰B. H. Wu and J. C. Cao, *Phys. Rev. B* **74**, 115313 (2006).
- ²¹M. R. Poniedzialek and B. Szafran, *J. Phys. Condens. Matter* **22**, 465801 (2010).
- ²²K. Kobayashi, H. Aikawa, S. Katsumoto, and Y. Iye, *Phys. Rev. Lett.* **88**, 256806 (2002).
- ²³S. Bellucci and P. Onorato, *J. Phys. Condens. Matter* **19**, 395020 (2007).
- ²⁴E. Faizabadi and A. Najafi, *Solid State Commun.* **150**, 1404 (2010).
- ²⁵A. Pályi, C. Péterfalvi, and J. Cserti, *Phys. Rev. B* **74**, 073305 (2006).
- ²⁶E. A. de Andrada e Silva, G. C. La Rocca, and F. Bassani, *Phys. Rev. B* **55**, 16293 (1997).
- ²⁷Mean values of the x , y , and z spin components are calculated on a normalized wave function on a stripe at the end of the output lead.

8 Tuning of the spin-orbit interaction in a quantum dot by an in-plane magnetic field

Tuning of the spin-orbit interaction in a quantum dot by an in-plane magnetic fieldM. P. Nowak,^{1,2} B. Szafran,¹ F. M. Peeters,² B. Partoens,² and W. J. Pasek¹¹*Faculty of Physics and Applied Computer Science, AGH University of Science and Technology, al. Mickiewicza 30, PL-30-059 Kraków, Poland*²*Departement Fysica, Universiteit Antwerpen, Groenenborgerlaan 171, BE-2020 Antwerpen, Belgium*

(Received 7 February 2011; revised manuscript received 28 April 2011; published 30 June 2011)

Using an exact-diagonalization approach we show that one- and two-electron InAs quantum dots exhibit an avoided crossing in the energy spectra that is induced by the spin-orbit coupling in the presence of an in-plane external magnetic field. The width of the avoided crossings depends strongly on the orientation of the magnetic field, which reveals the intrinsic anisotropy of the spin-orbit-coupling interactions. We find that for specific orientations of the magnetic field avoided crossings vanish. A value of this orientation can be used to extract the ratio of the strength of Rashba and Dresselhaus interactions. The spin-orbit anisotropy effects for various geometries and orientations of the confinement potential are discussed. Our analysis explains the physics behind the recent measurements performed on a gated self-assembled quantum dot [S. Takahashi *et al.*, *Phys. Rev. Lett.* **104**, 246801 (2010)].

DOI: 10.1103/PhysRevB.83.245324

PACS number(s): 73.21.La

I. INTRODUCTION

Over the past decade there has been a growing interest in the study of the spin-orbit (SO) interaction in semiconductor low-dimensional systems motivated by the possibility of coherent spin manipulation.¹⁻¹³ The Hamiltonians describing the SO coupling resulting from the inversion asymmetry of the material (Dresselhaus¹⁴ coupling) or the specific structure of the device (Rashba¹⁵ interaction) are not invariant with respect to the rotation of the spin or the momentum operators separately, and, consequently, spin-orbit-coupled systems possess intrinsic anisotropic properties. This anisotropy has been thoroughly studied for delocalized systems.^{4,5} In particular, in transport experiments, the dependence of the conductance of a narrow quantum wire on the direction of the external magnetic field can be used to determine the reciprocal strengths of the Rashba and Dresselhaus couplings.⁶ The anisotropy of the spin-orbit interaction is translated into an anisotropic effective magnetic field⁷ for a moving electron modifying the electron spin state. This effective magnetic field can be used to perform rotations of spin and thus to construct quantum gates⁸ or a spin-field effect transistor.^{9,10} Moreover, the spin-orbit coupling is responsible for anisotropic corrections¹¹ to the spin swap in a two-qubit quantum gate¹² because it results in the precession of spin-packets tunneling between the two quantum dots.¹³

For electrons localized in a quantum dot, the SO coupling results in avoided crossings (AC) in the energy spectra¹⁶ and spin relaxation¹⁷ mediated by phonons with a relaxation rate dependent on the orientation of the external magnetic field.¹⁸ The energetic effects of the SO interaction are usually weak. Only recently SO-induced AC were experimentally measured on quantum dots that were situated in gated nanowires^{19,20} and gated self-assembled quantum dots.²¹ The latter experiment studied changes of the width of AC for different orientations of the magnetic field, which extended the previous studies that were focused on a comparison of the spin-splittings for vertical and in-plane alignment of a magnetic field^{22,23} in circularly symmetric confinement potentials.

In the present work, we explain the physics underlying the observations of Ref. 21. To the best of our knowledge, the present paper explains for the first time the oscillatory dependence of the width of AC on the direction of the in-plane magnetic field. The latter turns out to be the consequence of the influence of the individual SO couplings and the anisotropy of the confinement potential. This conclusion is supported by an exact three-dimensional calculation of the energy spectra of one- and two-electron spin-orbit-coupled quantum dots.

We show that for quantum dots with a confinement potential elongated in [100] direction for pure Rashba (or pure Dresselhaus) coupling, the AC disappears when the magnetic field is aligned along the short (or long) axis of the dot. We show how this can be understood from the form of the SO Hamiltonians and the approximate parity of the one-electron wave functions. The dependence of the AC width on the direction of the magnetic field turns to be a $|\sin\phi|$ -shaped function, and when both couplings are present, this function is shifted by an amount that depends on the relative strength of both interactions. This shift is affected by the orientation of the dot within the [001] plane due to the SO bulk-induced anisotropy (Dresselhaus term). For completeness, we also study the influence of the dot shape. We show that for a square-based quantum dot the anisotropic dependence of the AC width is only observed when both couplings are present.²³ Moreover, we show that for increased height of the dot, the orbital effect of the magnetic field modifies the energy spectrum, but the shape of the dependence of the anticrossing width on the direction of the in-plane magnetic field remains unaltered.

The present work is organized as follows: we start with an outline of our theoretical approach in Sec. II. In Sec. III, we present our numerical results starting from the single-electron case, which provides us with a physical insight of the reasons for the SO-coupling anisotropy. We continue by studying different orientations and geometries of the dot, and we end the section with the two-electron case that allows for a direct comparison with the recent experimental data of Ref. 21. We end with a concluding discussion in Sec. IV and a summary in Sec. V.

II. THEORY

A. Model

Our aim is to calculate the energy spectra of one and two electrons confined in a three-dimensional quantum dot in the presence of SO coupling and a magnetic field oriented within the quantum-dot plane. The effect of the spin-orbit coupling on the energy is very small, requiring a very high numerical precision when evaluating the energy spectrum. We assume that the quantum dot is cuboid in shape and that the confinement potential is separable, namely, $V(\mathbf{r}) = V_x(x) + V_y(y) + V_z(z)$. Moreover, we assume that the one-dimensional confinement potentials V_x , V_y , and V_z can be described by an infinite quantum-well model. This is a reasonable approximation for not too small quantum dots. Under these assumptions one can construct a sufficiently precise solver for the two-electron problem. We consider a quantum dot with a varied in-plane orientation with respect to the crystal host. The z axis is taken along the [001] crystal direction, which is also the vertical axis of the dot. The orientation of the dot is described by a rotation of the x and y directions (which are the axes of the dot) with respect to the [100] and [010] crystal directions. The outline of our quantum dot and the coordinate system used is depicted in Fig. 1.

B. Method

We employ the effective mass approximation with a single-electron Hamiltonian of the form

$$h = \left[\frac{\hbar^2 \mathbf{k}^2}{2m^*} + V(\mathbf{r}) \right] \mathbf{1} + \frac{1}{2} g \mu_B \mathbf{B} \boldsymbol{\sigma} + H_{\text{BIA}} + H_{\text{SIA}}, \quad (1)$$

where $\mathbf{k} = -i\nabla + e\mathbf{A}/\hbar$, $\mathbf{1}$ is the identity matrix, $V(\mathbf{r})$ defines the confining potential, and H_{BIA} and H_{SIA} are the spin-orbit-coupling Hamiltonians. The x , y , and z directions are taken

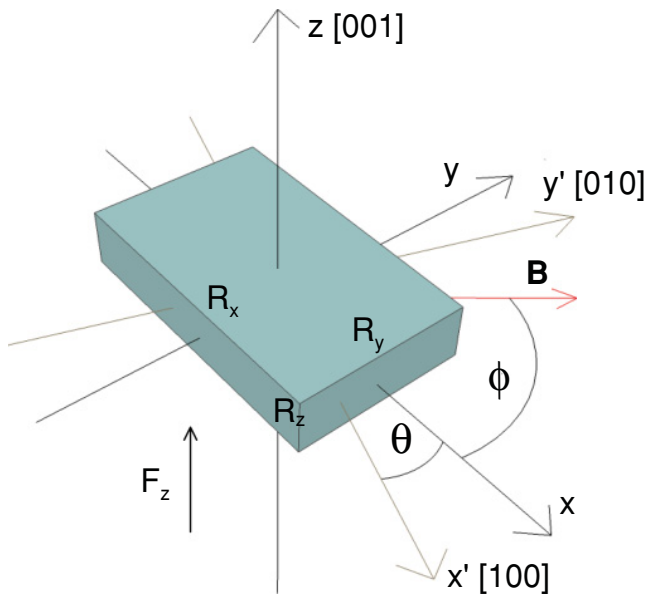


FIG. 1. (Color online) Schematics of the quantum dot system with the used coordinate system fixed to the quantum dot. The crystallographic directions of the InAs host lattice are also indicated together with the direction of the in-plane magnetic field.

along the axes of the dot. But notice that the SO-interaction Hamiltonians are defined in a coordinate system with axes parallel to the [100], [010], and [001], which we denote with x' , y' , and z . Both coordinate systems are transformed into each other by an in-plane rotation by an angle θ .

We introduce the Rashba coupling with Hamiltonian,

$$H_{\text{SIA}} = \alpha \nabla' V \cdot (\boldsymbol{\sigma}' \times \mathbf{k}'), \quad (2)$$

where α defines the coupling strength. For infinite-quantum-well confinement the term $\nabla' V$ within the dot is equal to the external electric field. We neglect the influence of the in-plane component of the electric field²⁴ and obtain the Rashba Hamiltonian in the form

$$H_{\text{SIA}} = \alpha \frac{\partial V}{\partial z} (\sigma_{x'} k_{y'} - \sigma_{y'} k_{x'}). \quad (3)$$

Thus the electric field is in the z direction, which is incorporated by taking a nonzero slope of the bottom of $V_z(z)$.

Inversion asymmetry of the crystal lattice results in a Dresselhaus SO coupling that is described by the Hamiltonian

$$H_{\text{BIA}} = \gamma [\sigma_{x'} k_{x'} (k_z^2 - k_{y'}^2) + \sigma_{y'} k_{y'} (k_x'^2 - k_z^2) + \sigma_z k_z (k_{y'}^2 - k_{x'}^2)], \quad (4)$$

where γ is the coupling constant.

The coordinate system used for the SO coupling can be transformed into the coordinate system used for the quantum dot through the transformation:

$$\begin{aligned} x' &= x \cos \theta - y \sin \theta, \\ y' &= x \sin \theta + y \cos \theta, \end{aligned} \quad (5)$$

which applies both to the Pauli matrices $\boldsymbol{\sigma}$ and the coordinates of the momentum operator.

We include an in-plane magnetic field of orientation $\mathbf{B} = B(\cos \phi, \sin \phi, 0)$, which is described by the gauge $\mathbf{A} = B(z \sin \phi, 0, y \cos \phi)$. The magnetic field vector, \mathbf{B} , for $\phi = 0$ is oriented along the x direction (see Fig. 1).

The one-electron Hamiltonian, Eq. (1), can be rewritten in the form $h = h_x + h_y + h_z + h_{\text{ns}}$, where

$$h_x = -\frac{\hbar^2}{2m^*} \frac{\partial^2}{\partial x^2} + V_x(x), \quad (6)$$

$$h_y = -\frac{\hbar^2}{2m^*} \frac{\partial^2}{\partial y^2} + V_y(y) + \frac{e^2 B^2}{2m^*} y^2 \cos^2 \phi, \quad (7)$$

$$h_z = -\frac{\hbar^2}{2m^*} \frac{\partial^2}{\partial z^2} + V_z(z) + \frac{e^2 B^2}{2m^*} z^2 \sin^2 \phi, \quad (8)$$

are spin-independent parts separable in the x , y , and z directions, and

$$\begin{aligned} h_{\text{ns}} &= -\frac{i\hbar e B}{m^*} \left(z \sin \phi \frac{\partial}{\partial x} + y \cos \phi \frac{\partial}{\partial z} \right) \\ &\quad + \frac{1}{2} g \mu_b B [\sigma_x \cos \phi + \sigma_y \sin \phi] + H_{\text{SIA}} + H_{\text{BIA}} \end{aligned} \quad (9)$$

is the nonseparable part that contains the spin-dependent terms.

The eigenenergies and the eigenvectors, $\psi_x(x)$, $\psi_y(y)$, and $\psi_z(z)$, of the Hamiltonians, h_x , h_y and h_z , are calculated

separately on an one-dimensional mesh of $N_{1D} = 1000$ points. In a next step, we diagonalize h_{ns} in a basis of products of the eigenstates, $\psi_x(x)$, $\psi_y(y)$, and $\psi_z(z)$, resulting in three-dimensional spin-orbitals $\psi(\mathbf{r}, \sigma)$. We typically take $N_x = N_y = 20$ and $N_z = 10$ one-dimensional eigenstates (we assumed $R_z \ll R_x, R_y$), which, including the degeneracy of the spin, gives a basis consisting of 8000 elements that results in an accuracy better than $5 \mu\text{eV}$.

We solve the two-electron problem as described by the Hamiltonian

$$H = h_1 + h_2 + \frac{e^2}{4\pi\epsilon\epsilon_0|\mathbf{r}_1 - \mathbf{r}_2|} \quad (10)$$

using the configuration-interaction approach. In our numerical calculation, we take the dielectric constant $\epsilon = 14.6$ for InAs. The Hamiltonian in Eq. (10) is diagonalized in a basis constructed of antisymmetrized single-electron spin-orbitals $\psi(\mathbf{r}, \sigma)$,

$$\Psi = \frac{1}{\sqrt{2}} \sum_{i=1}^n \sum_{j=i+1}^n [\psi_i(\mathbf{1})\psi_j(\mathbf{2}) - \psi_i(\mathbf{2})\psi_j(\mathbf{1})], \quad (11)$$

where $\mathbf{1}$ and $\mathbf{2}$ are the spatial (\mathbf{r}) and spin (σ) coordinates of the corresponding electron. The electron-electron interaction matrix element requires the calculation of integrals of the form

$$\begin{aligned} & \frac{e^2}{4\pi\epsilon_0} \langle \psi_i(\mathbf{r}_1)\psi_j(\mathbf{r}_2) | \frac{1}{\epsilon|\mathbf{r}_1 - \mathbf{r}_2|} | \psi_k(\mathbf{r}_1)\psi_l(\mathbf{r}_2) \rangle \\ &= e \int d^3\mathbf{r}_1 \psi_i^*(\mathbf{r}_1)\psi_k(\mathbf{r}_1) \int d^3\mathbf{r}_2 \frac{e}{4\pi\epsilon_0} \frac{\psi_j^*(\mathbf{r}_2)\psi_l(\mathbf{r}_2)}{\epsilon|\mathbf{r}_1 - \mathbf{r}_2|} \\ &= e \int d^3\mathbf{r}_1 \psi_i^*(\mathbf{r}_1)\psi_k(\mathbf{r}_1)V_{jl}(\mathbf{r}_1). \end{aligned} \quad (12)$$

A direct calculation of these six dimensional integrals requires an enormous numerical cost. Therefore, we use a method²⁵ in which the innermost integral is attributed to an electric potential, $V_{jl}(\mathbf{r}_1)$, originating from an electric charge distribution, $\psi_j^*(\mathbf{r}_2)\psi_l(\mathbf{r}_2)$. We calculate the electric potential by solving the Poisson equation $\nabla^2 V_{jl}(\mathbf{r}_1) = -e/(\epsilon\epsilon_0)\psi_j^*(\mathbf{r}_1)\psi_l(\mathbf{r}_1)$ with the boundary condition

$$V_{jl}(\mathbf{r}_b) = \frac{e}{4\pi\epsilon_0} \int d^3\mathbf{r}_1 \frac{\psi_j^*(\mathbf{r}_1)\psi_l(\mathbf{r}_1)}{\epsilon|\mathbf{r}_b - \mathbf{r}_1|}, \quad (13)$$

where \mathbf{r}_b lays within the boundary of the the computational box. The Poisson equation is solved on a grid that covers the dot area. The calculation accuracy is carefully monitored²⁶ and a configuration-interaction calculation convergence better than $10 \mu\text{eV}$ is reached for $n = 20$.

C. Parameters

The bulk of our results presented in the following sections are obtained for the parameters described below. In the experiment of Ref. 21, an anisotropic InAs self-organized quantum dot (SOQD) grown on a [001] GaAs substrate is studied with a confinement potential that is elongated due to the source and drain electrodes placed above the dot. The orientation of the dot with respect to the in-plane crystal

directions is not well resolved and in the present work, this is taken as an additional parameter that is studied. We take $R_x = 100 \text{ nm}$ as the long and $R_y = 60 \text{ nm}$ as the short size of the dot.²¹ We take $R_z = 10 \text{ nm}$ as a reasonable estimate of the dot height (note that the SOQD has a nominal pyramidal shape²¹ with height 20 nm , but our model is limited to a potential with a rectangular shape of vertical cross section). R_z influences the effective strength of the Dresselhaus-coupling constant and the orbital effects of the in-plane magnetic field. Results for $R_z > 10 \text{ nm}$ are also discussed below.

For the purpose of the present study, it is important to notice that the electric field in the growth direction defines the strength of the Rashba coupling. The electric field is influenced by the potential profile within the dot,²⁷ the Schottky barrier at the dot-electrode interface, surface charges, and the applied potentials.²⁴ The electrostatics of the actual device is complex and its complete description is out of the scope of the present work. Nevertheless, we are able to estimate the external electric field present in the system by considering the stability diagram and the width of the systems.²⁸ We estimated the maximal value of the external electric field to be of order -30 kV/cm , for which the electrons are still present in the dot.²⁹ From the gate voltage, $V_g = -0.4 \text{ V}$, of two-electron spectroscopy, we estimated $F_z = -13.6 \text{ kV/cm}$, and this value is used in our numerical calculation. Finally, in this paper we indicate that the ratio of the Rashba-coupling strength (that is proportional to F_z) to the strength of the Dresselhaus coupling can be extracted from the experimentally measured orientation of the magnetic field for which the SO-induced AC vanishes.

We take the SO coupling parameters as $\alpha = 1.1 \text{ nm}^2$, from Ref. 30, for the Rashba coupling and $\gamma = 26.9 \text{ meV nm}^3$, from Ref. 31, for the Dresselhaus coupling constant. The material parameters for InAs are adopted from Ref. 32, with values $m^* = 0.026$ and $g = -17.5$.

III. RESULTS

A. Without SO coupling

We consider first a dot aligned such that the x axis is oriented along [100] (y axis along [010]), namely, $\theta = 0$. The energy spectrum obtained in the absence of the SO coupling (we take $\alpha = \gamma = 0$) for a single-electron anisotropic quantum dot is presented in Fig. 2 by the black solid curves. In the absence of the magnetic field, the ground state is doubly degenerate with respect to spin and the spatial wave function is of even symmetry with respect to plane inversions: $\psi(x, y, z) = \psi(-x, y, z)$, $\psi(x, y, z) = \psi(x, -y, z)$, and $\psi(x, y, z) = \psi(x, y, -z)$. We denote the state of even symmetry with respect to all inversions by $|\psi_+\rangle$. The first excited state is a spin-doublet with wave functions meeting the symmetry conditions: $\psi(x, y, z) = -\psi(-x, y, z)$, $\psi(x, y, z) = \psi(x, -y, z)$, and $\psi(x, y, z) = \psi(x, y, -z)$. We will refer to this state as $|\Psi_-\rangle$. The nonzero magnetic field lifts the spin-degeneracy splitting of the states of the same parity by the Zeeman energy. The energy levels depicted by the black lines in Fig. 2 are obtained regardless of the ϕ value in spite of the lateral anisotropy of the dot. Due to the small R_z value and the

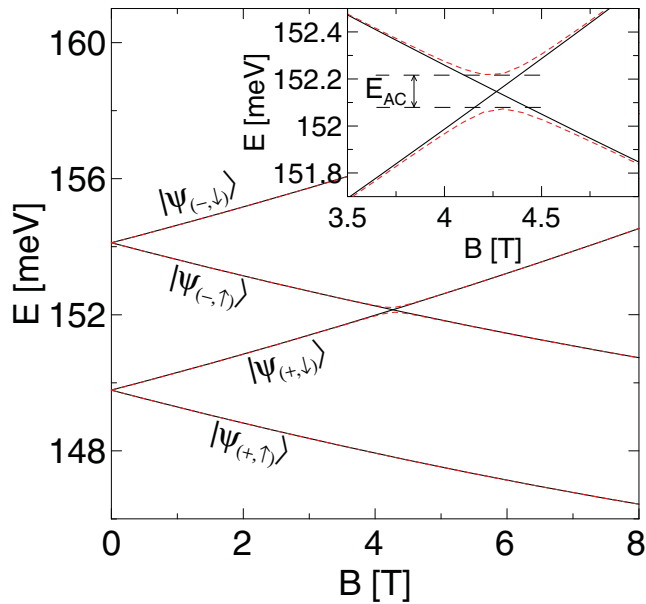


FIG. 2. (Color online) The black solid curves represent the one-electron-energy spectrum obtained without spin-orbit coupling for the in-plane magnetic field, regardless of the ϕ value. The red dashed curves are the energy levels when only Dresselhaus coupling with $\gamma = 26.9 \text{ meV nm}^3$ is included with the magnetic field aligned along the y direction ($\phi = 90^\circ$). The inset shows a zoom-in view of the energy levels in the vicinity of the anticrossing.

in-plane alignment of \mathbf{B} , no orbital effects of the magnetic field are observed (the influence of the height of the dot is studied in Sec. III F).

Generally, in the presence of an in-plane magnetic field, the Hamiltonian in Eq. (1), even without SO interaction, does not commute with the plane-inversion operators P_x and P_y [defined as $P_x f(x, y, z) = f(-x, y, z)$ and $P_y f(x, y, z) = f(x, -y, z)$]. However, due to the insignificance of the orbital effect of the magnetic field for this flat quantum dot, the parity with respect to reflection through the $x = 0$ and $y = 0$ planes is approximately preserved (with $\langle P_x \rangle$ and $\langle P_y \rangle$ above 0.97) even for nonzero B . For the following discussion, we denote the four lowest-energy states for a small magnetic field aligned parallel to the y direction as $|\Psi_{(+,\uparrow)}\rangle$, $|\Psi_{(+,\downarrow)}\rangle$, $|\Psi_{(-,\uparrow)}\rangle$, and $|\Psi_{(-,\downarrow)}\rangle$ with corresponding energies $E_{(+,\uparrow)}$, $E_{(+,\downarrow)}$, $E_{(-,\uparrow)}$, and $E_{(-,\downarrow)}$, where the arrow denotes the spin state aligned parallel (\uparrow) or antiparallel (\downarrow) to the magnetic-field vector.

B. Single type of SO coupling

Inclusion of the SO interaction lifts the spin polarization of the states and changes the crossing observed between the energy levels of $|\Psi_{(+,\downarrow)}\rangle$ and $|\Psi_{(-,\uparrow)}\rangle$ around $B = 4.25 \text{ T}$ into an anticrossing. The inset of Fig. 2 shows the anticrossing energy levels for $\phi = 90^\circ$ (\mathbf{B} parallel to the y axis) represented by the red curves when only Dresselhaus coupling with

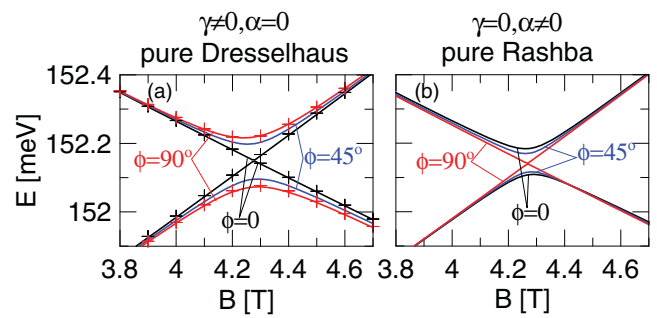


FIG. 3. (Color online) The energy levels near the anticrossing for pure Dresselhaus (a) and pure Rashba (b) couplings for different \mathbf{B} orientations. The black crosses are the results from a diagonalization of the matrix in Eq. (22) and the red crosses the results of diagonalization of Eq. (19). The magnetic field is oriented along the x direction ($\phi = 0$) for the black symbols and curves and along the y direction ($\phi = 90^\circ$) for the red symbols and curves.

$\gamma = 26.9 \text{ meV nm}^3$ is included. We denote the minimal energy difference between the anticrossing levels as E_{AC} . For the applied parameters, we obtain $E_{AC} = 146 \mu\text{eV}$. Outside the anticrossing the SO interaction does not modify the energy spectrum in a noticeable way, i.e., the black and red curves approximately coincide.

In the presence of the SO coupling, the anticrossing energy levels depend on the orientation of the magnetic field. In Figs. 3(a) and 3(b), we plot the energy levels obtained for pure Dresselhaus and pure Rashba interaction, respectively, for three different ϕ values. In both cases, clear dependence of the anticrossing width, E_{AC} , is observed with respect to the \mathbf{B} orientation. For pure Dresselhaus coupling the anticrossing is the widest when the magnetic-field vector is perpendicular to the y direction ($\phi = 90^\circ$) [the red curve in Fig. 3(a)]. When the field is aligned along the x direction ($\phi = 0$), the mixing between levels vanishes [the black curve in Fig. 3(a)] and there is crossing of the levels. With pure Rashba coupling the dependence is opposite; the anticrossing vanishes when \mathbf{B} is aligned along y , and E_{AC} is largest when \mathbf{B} is aligned along x .

The direction of the magnetic field for which the mixing between the states disappears can be inferred from the analytic form of the SO Hamiltonians utilizing the approximate symmetries of the wave functions of confined electron. Let us first inspect the case of pure Dresselhaus coupling and remind that for $\theta = 0$ the Hamiltonian in Eq. (4) has the same form in the x , y , and z coordinate system. Averaging the Hamiltonian in Eq. (4) over the z direction one obtains

$$H_{\text{BIA}}^{2\text{D}} = \gamma \langle k_z^2 \rangle [\sigma_x k_x - \sigma_y k_y] + \gamma [\sigma_y k_y k_x^2 - \sigma_x k_x k_y^2] + \gamma \sigma_z \langle k_z \rangle (k_y^2 - k_x^2). \quad (14)$$

The second term is the so-called cubic Dresselhaus term, which is negligible as long as the height is much smaller than the lateral size of the dot (i.e., until the value of $\langle k_x^2 \rangle$ or $\langle k_y^2 \rangle$ becomes comparable with $\langle k_z^2 \rangle$). For an infinite-quantum-well ground-state wave function in the z direction the last term in Eq. (14) vanishes³³ and

$$\gamma^{2\text{D}} = \gamma \langle k_z^2 \rangle = \gamma (\pi/R_z)^2. \quad (15)$$

The simplified Dresselhaus Hamiltonian takes now the following form:

$$H_{\text{BIA}}^{2\text{D}} = \gamma^{2\text{D}}(\sigma_x k_x - \sigma_y k_y). \quad (16)$$

$$\begin{pmatrix} E_{(+,\downarrow)} + \gamma^{2\text{D}}\langle\Psi_{(+,\downarrow)}|\sigma_x k_x - \sigma_y k_y|\Psi_{(+,\downarrow)}\rangle & \gamma^{2\text{D}}\langle\Psi_{(+,\downarrow)}|\sigma_x k_x - \sigma_y k_y|\Psi_{(-,\uparrow)}\rangle \\ \gamma^{2\text{D}}\langle\Psi_{(-,\uparrow)}|\sigma_x k_x - \sigma_y k_y|\Psi_{(+,\downarrow)}\rangle & E_{(-,\uparrow)} + \gamma^{2\text{D}}\langle\Psi_{(-,\uparrow)}|\sigma_x k_x - \sigma_y k_y|\Psi_{(-,\uparrow)}\rangle \end{pmatrix}. \quad (17)$$

The states $|\Psi_{(+,\downarrow)}\rangle$ and $|\Psi_{(-,\uparrow)}\rangle$ are separable into an orbital and spin part. Due to the action of the Pauli matrices on the states with a definite spin one gets

$$\begin{pmatrix} E_{(+,\downarrow)} - \gamma^{2\text{D}}\langle\Psi_{(+,\downarrow)}|\sigma_y k_y|\Psi_{(+,\downarrow)}\rangle & \gamma^{2\text{D}}\langle\Psi_{(+,\downarrow)}|\sigma_x k_x|\Psi_{(-,\uparrow)}\rangle \\ \gamma^{2\text{D}}\langle\Psi_{(-,\uparrow)}|\sigma_x k_x|\Psi_{(+,\downarrow)}\rangle & E_{(-,\uparrow)} - \gamma^{2\text{D}}\langle\Psi_{(-,\uparrow)}|\sigma_y k_y|\Psi_{(-,\uparrow)}\rangle \end{pmatrix}. \quad (18)$$

For the magnetic-field vector aligned parallel to the y direction, the components of the momentum-operator vector are $k_x = -i\frac{\partial}{\partial x} + eBz$, $k_y = -i\frac{\partial}{\partial y}$, and $k_z = -i\frac{\partial}{\partial z}$. Due to parity one obtains

$$\begin{pmatrix} E_{(+,\downarrow)} & -i\gamma^{2\text{D}}\langle\Psi_{(+,\downarrow)}|\sigma_x \frac{\partial}{\partial x}|\Psi_{(-,\uparrow)}\rangle \\ -i\gamma^{2\text{D}}\langle\Psi_{(-,\uparrow)}|\sigma_x \frac{\partial}{\partial x}|\Psi_{(+,\downarrow)}\rangle & E_{(-,\uparrow)} \end{pmatrix}. \quad (19)$$

The nonvanishing off-diagonal matrix elements mix the states $|\Psi_{(+,\downarrow)}\rangle$ and $|\Psi_{(-,\uparrow)}\rangle$, which results in an avoided crossing between the corresponding energy levels. By the red crosses

$$\begin{pmatrix} E_{(+,\leftarrow)} + \gamma^{2\text{D}}\langle\Psi_{(+,\leftarrow)}|\sigma_x k_x - \sigma_y k_y|\Psi_{(+,\leftarrow)}\rangle & \gamma^{2\text{D}}\langle\Psi_{(+,\leftarrow)}|\sigma_x k_x - \sigma_y k_y|\Psi_{(-,\rightarrow)}\rangle \\ \gamma^{2\text{D}}\langle\Psi_{(-,\rightarrow)}|\sigma_x k_x - \sigma_y k_y|\Psi_{(+,\leftarrow)}\rangle & E_{(-,\rightarrow)} + \gamma^{2\text{D}}\langle\Psi_{(-,\rightarrow)}|\sigma_x k_x - \sigma_y k_y|\Psi_{(-,\rightarrow)}\rangle \end{pmatrix}. \quad (20)$$

Due to spin one gets

$$\begin{pmatrix} E_{(+,\leftarrow)} + \gamma^{2\text{D}}\langle\Psi_{(+,\leftarrow)}|\sigma_x k_x|\Psi_{(+,\leftarrow)}\rangle & -\gamma^{2\text{D}}\langle\Psi_{(+,\leftarrow)}|\sigma_y k_y|\Psi_{(-,\rightarrow)}\rangle \\ -\gamma^{2\text{D}}\langle\Psi_{(-,\rightarrow)}|\sigma_y k_y|\Psi_{(+,\leftarrow)}\rangle & E_{(-,\rightarrow)} + \gamma^{2\text{D}}\langle\Psi_{(-,\rightarrow)}|\sigma_x k_x|\Psi_{(-,\rightarrow)}\rangle \end{pmatrix}. \quad (21)$$

For the magnetic field aligned along the x direction the components of the momentum operator vector are $k_x = -i\frac{\partial}{\partial x}$, $k_y = -i\frac{\partial}{\partial y}$, and $k_z = -i\frac{\partial}{\partial z} + eBy$. All integrals in Eq. (21) vanish due to the parity of the states and we finally obtain

$$\begin{pmatrix} E_{(+,\leftarrow)} & 0 \\ 0 & E_{(-,\rightarrow)} \end{pmatrix}. \quad (22)$$

Let us now consider the case of a magnetic field aligned parallel to the y direction and inspect matrix elements of the $H_{\text{BIA}}^{2\text{D}}$ Hamiltonian in a basis that include only the low-energy states $|\Psi_{(+,\downarrow)}\rangle$ and $|\Psi_{(-,\uparrow)}\rangle$ that exhibit an energy crossing without SO coupling. The matrix is given by

in Fig. 3 we plot numerically calculated eigenvalues of the matrix in Eq. (19). Note that the crosses and lines are in perfect agreement, proving that for our dot, with the assumed geometry, the $H_{\text{BIA}}^{2\text{D}}$ is, in fact, a good approximation to H_{BIA} .

Let us now consider the case of a magnetic field aligned parallel to the x ($\phi = 0$) direction. In this case, the low-energy states, for which energy levels cross without SO coupling, are $|\Psi_{(+,\leftarrow)}\rangle$ and $|\Psi_{(-,\rightarrow)}\rangle$, where the arrow denotes the electron spin aligned parallel (\rightarrow) and antiparallel (\leftarrow) to the magnetic-field vector, \mathbf{B} . The matrix of the $H_{\text{BIA}}^{2\text{D}}$ Hamiltonian in this two-state basis is

The matrix in Eq. (22) consists only of diagonal elements that are equal to the energy of the basis states. Thus the $|\Psi_{(+,\leftarrow)}\rangle$ and $|\Psi_{(-,\rightarrow)}\rangle$ states are not mixed by the Dresselhaus coupling in this configuration and there is no anticrossing of energy levels. We plot the eigenvalues of the matrix in Eq. (22) in Fig. 3(a) (represented by the black crosses).

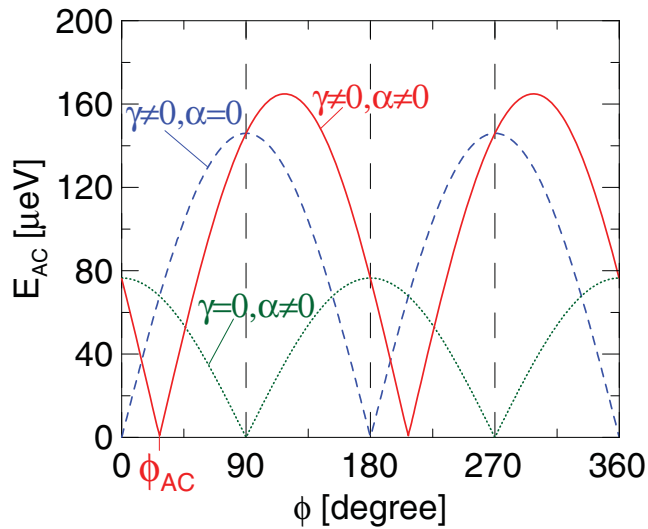


FIG. 4. (Color online) The spin-orbit-induced anticrossing width, E_{AC} , for pure Dresselhaus (blue dashed curve), pure Rashba (green dotted curve), and both (red solid line) interactions present. For $\gamma = 0$ the magnetic field is $B = 4.268$ T, for the two other cases, $B = 4.277$ T.

A similar analysis can be made for the Rashba Hamiltonian given by Eq. (2). Due to the fact that the analytic form of both Hamiltonians H_{SIA} and H_{BIA}^{2D} is similar, i.e., only the k_x and k_y are swapped (and the coupling constants are different), it is clear that the dependence of AC width on the magnetic-field direction is reversed, i.e., the mixing between the states vanishes when the magnetic field is aligned along the y direction.

C. Anisotropy in the presence of both SO couplings

Let us now consider the effect of both Dresselhaus and Rashba couplings. Figure 4 presents the avoided-crossing energy, E_{AC} , as a function of the angle ϕ between the x axis and the magnetic field. For pure Dresselhaus (the blue dashed curve in Fig. 4) and pure Rashba (the green dotted curve in Fig. 4) coupling the extrema are shifted by 90° , in agreement with our previous analysis. The curves in Fig. 4 are accurately described by $|\sin(\phi - \phi_{AC})|$, which is the same functional form as the one observed in the experimental work of Ref. 21 in Fig. 3(f) (where the behavior was described by $|\cos(\phi - \phi_0)|$). Moreover, the maximal value of E_{AC} is of the same order as the magnitude observed experimentally. When both SO interactions are present, the dependence of the anticrossing width is plotted in Fig. 4 by the red curve. The shape of the latter is the same as for pure Dresselhaus or Rashba coupling, with pronounced minima where E_{AC} is equal to zero. When the magnetic field is aligned along the x or y direction, the E_{AC} equals to the value for pure SO coupling. Note that the maxima are larger than the ones observed for pure couplings and its positions are now shifted and are no longer aligned along the axes of the dot. For $\alpha = 1.1$ nm² and $\gamma = 26.9$ meV nm³, the shift of the dependence is $\phi_{AC} = 27.8^\circ$. The latter value can be understood as follows. Let us denote the direction of the magnetic field for which the AC vanishes for pure Dresselhaus and pure Rashba couplings by the vectors \mathbf{d}_{BIA} and \mathbf{d}_{SIA} ,

respectively. Next, we estimate the strength of each interaction. The maximal induced anticrossing width is $E_{AC}^{BIA} = 146$ μ eV and $E_{AC}^{SIA} = 77$ μ eV for Dresselhaus and Rashba coupling, respectively. Thus the Dresselhaus interaction is 1.9 times larger than the Rashba coupling, which makes the vector \mathbf{d}_{BIA} 1.9 times longer than \mathbf{d}_{SIA} . Let us denote the magnetic field for which the effect of both spin-orbit couplings is zero by the vector $\mathbf{d}_{BIA+SIA} = \mathbf{d}_{BIA} + \mathbf{d}_{SIA}$. It is easy to show that this vector forms an angle $\phi = 27.8^\circ$ with the x axis. Thus when both couplings are present, the effect of the total spin-orbit coupling disappears when the external magnetic field is directed along this vector. In fact, that is exactly what we observe in our calculation (see position of the minimum of the dependence depicted with the red curve in Fig. 4). The formula $|\sin(\phi - \phi_{AC})|$ reflects the fact that the dependency obtained for both SO couplings present can be considered as an absolute value of a sum of the dependencies obtained for pure SO couplings, described by $-\cos\phi$ and $\sin\phi$ for pure Rashba and Dresselhaus couplings, respectively.

D. Dependence on the quantum dot orientation

Different in-plane orientations of the anisotropic potential of the dot with respect to the crystal host where the long axis of the dot forms an angle θ with $[100]$ are now considered. In Figs. 5(a)–5(c), we present the size of the AC as a function of the direction of the rotated magnetic field (note that the ϕ angle is defined as an angle between the magnetic-field vector and the long axis of the dot) for six different orientations of the dot. The dotted curves in Fig. 5(a) represent the result obtained for pure Rashba coupling. We observe that the E_{AC} dependencies are exactly the same as in Fig. 4 regardless of the dot alignment. The minimum of the E_{AC} does not change its position and the energy levels are not affected by the orientation of the dot. With the green diamonds we show, in Fig. 5(d), the ϕ_{AC} angle for which the $E_{AC} = 0$ as a function of the angle θ .

For pure Dresselhaus coupling, the E_{AC} dependencies [depicted by dashed curves in Fig. 5(b)] are shifted as the dot is rotated. For the case studied in the previous subsections

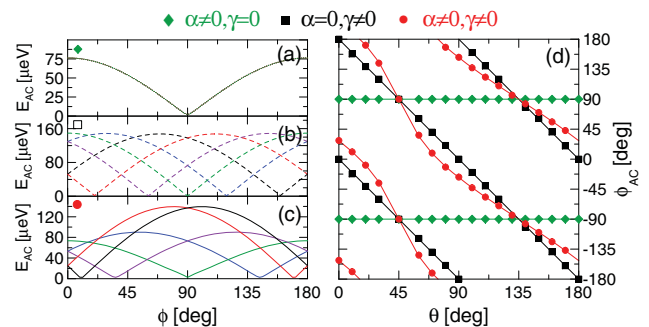


FIG. 5. (Color online) Avoided-crossing-energy width as a function of the direction (ϕ) for different orientations of the dot with $\theta = 10^\circ$ (black curves), 30° (blue curves), 45° (green curves), 60° (violet curves), and 80° (red curves). Results are shown for (a) pure Rashba, (b) pure Dresselhaus and (c) for both couplings present. (d) The value of the magnetic-field angle, ϕ_{AC} , at which $E_{AC} = 0$ as a function of the angle θ for pure Rashba (green diamonds), pure Dresselhaus (black squares), and both couplings present (red dots). The red curves are obtained from Eq. (23).

(where $\theta = 0$), the AC vanished when the magnetic field was aligned along the long axis of the dot ($\phi_{AC} = 0$). When the dot is oriented so that $\theta = 45^\circ$ (long axis oriented along the [110] direction), the anticrossing vanishes when the magnetic field is aligned along the short axis of the dot [see green dashed curve in Fig. 5(b)]. For $\phi_{AC} = 90^\circ$, the same behavior was observed as in pure Rashba case. We plot in Fig. 5(d) the angle ϕ_{AC} for pure Dresselhaus coupling (the black squares) for different orientations of the dot. We find that the angle exhibits a $\phi_{AC} = -2\theta$ dependence [black solid lines in Fig. 5(d)]. Moreover, we observe that for both cases, when only a single type of SO coupling is present the maximal value of the AC width remains unchanged.

In Fig. 5(c), we show the results when both SO couplings are present (the solid curves). The maximal values of E_{AC} and the angle ϕ_{AC} for which the minima are observed change when the dot orientation is varied. Both facts can be understood similarly as discussed in Sec. III C. We can justify the ϕ_{AC} values considering the orientation of the $\mathbf{d}_{BIA+SIA} = \mathbf{d}_{BIA} + \mathbf{d}_{SIA}$ vector. But now the orientation of the \mathbf{d}_{BIA} vector, assigned to the Dresselhaus coupling, is changed as the dot is rotated, i.e., \mathbf{d}_{BIA} forms an angle -2θ with the long axis of the dot. The rotation of the dot does not change the maximal value of E_{AC} when only a single type of SO coupling is present, and the previously derived value for the relative strength of both couplings remains unchanged (and thus also the ratio of the length of the \mathbf{d}_{BIA} and \mathbf{d}_{SIA} vectors). We take 1 as the length of \mathbf{d}_{SIA} and 1.9 as the length of \mathbf{d}_{BIA} . In Fig. 6, we schematically present the considered vectors and the angles they form with the axes of the dot. The angle between the $\mathbf{d}_{BIA+SIA}$ vector (see red arrow in Fig. 6) and the x direction can be easily calculated

$$\phi_{AC} = \arctan \left[\frac{1 + 1.9 \sin(-2\theta)}{1.9 \cos(2\theta)} \right]. \quad (23)$$

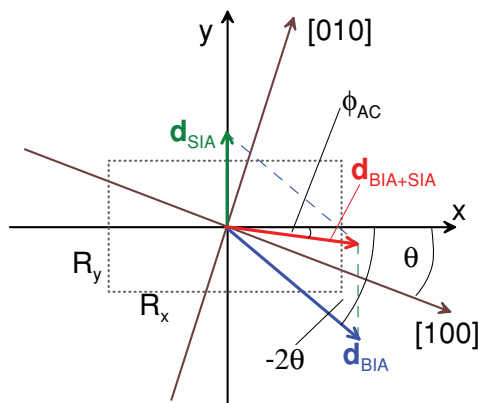


FIG. 6. (Color online) Schematics of the method of calculation of the angle ϕ_{AC} for which the the AC vanishes when both SO couplings are present and the quantum dot (dashed rectangle) is oriented with its long axis forming an angle θ with the [100] direction. The vectors depict the directions of \mathbf{B} for which $E_{AC} = 0$ for pure Rashba coupling (green arrow), pure Dresselhaus coupling (blue arrow), and both couplings present (red arrow). The coordinate system connected with the dot axes and the crystallographic directions is also shown.

With the red dots in Fig. 5(d) we plot the angle ϕ_{AC} obtained from our numerical calculation in the presence of both couplings for different orientations of the dot, which agree very well with the values (red curves) obtained from Eq. (23). Along with the changes of the orientation, the length of the $\mathbf{d}_{BIA+SIA}$ vector is changed, which results in the different values of the maximal AC width observed in Fig. 5(c).

A systematic study of the value of the ϕ_{AC} angle dependence on the SO coupling strengths and the dot alignment is given in Sec. III G where the two-electron case is studied.

E. Quantum dot with a square base

The above discussion was for a lateral anisotropic quantum dot. Now we study the case of a dot with a symmetrical base (we assume $R_x = R_y = 100$ nm) and $\theta = 0$, and we investigate if this has an influence on the anisotropy induced by the SO coupling. In the absence of the SO interaction and a magnetic field, the first-excited state is spin-doubly degenerate due to parity. The magnetic field lifts the spin degeneracy but the degeneracy due to parity is not removed. The inclusion of a single type of SO interaction induces a repulsion between the energy levels of the ground-state and one of the states from the parity doublet [see the red dashed curves in Fig. 7(a) for the case of pure Dresselhaus coupling and Fig. 7(b) for pure Rashba coupling]. The same configuration of energy levels is obtained regardless of the angle ϕ . In both Figs. 7(a) and 7(b), the black ($\phi = 0$), blue ($\phi = 45^\circ$), yellow dotted ($\phi = 22.5^\circ$), and red dashed curves ($\phi = 90^\circ$) coincide. The dependence of the energy levels on the magnetic-field orientation starts to appear already when the dot is elongated by a factor of 1%.

However, when both Rashba and Dresselhaus interactions are present the AC width varies with the rotation of the magnetic field, see Figs. 7(c) and 7(d). We observe that the anisotropy is most pronounced when α is increased by a factor of two—the case when both couplings have comparable strengths.^{23,34} In such a case, when the magnetic field is directed along the diagonal, i.e., $\phi = 45^\circ$ [see blue curves

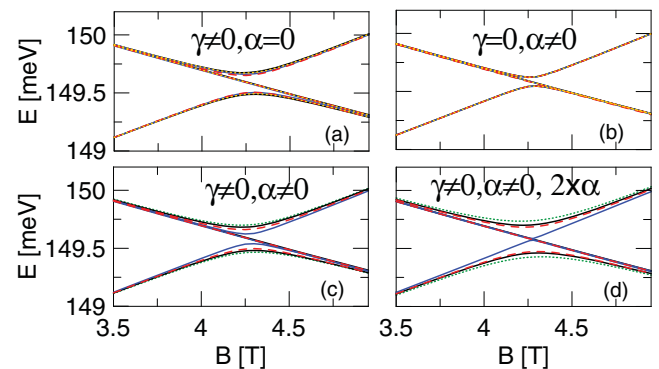


FIG. 7. (Color online) Energy levels of one-electron quantum dot with a square base with $R_x = R_y = 100$ nm. The black curves correspond to $\phi = 0$, the blue curves to $\phi = 45^\circ$, yellow dotted to $\phi = 22.5^\circ$, and the red dashed curves to $\phi = 90^\circ$. In (c) and (d), we additionally plot the energy levels obtained for $\phi = 135^\circ$ with green dotted curves. (a) Pure Dresselhaus coupling, (b) pure Rashba interaction, (c) both SO interactions are present, and (d) both SO interactions are present with α increased by a factor of two.

in Fig. 7(d)] the anticrossing between the energy levels of the ground state and both states from the parity doubled becomes very small.

F. Larger dot height

Let us now return to the case of the quantum dot with a rectangular base with $R_x = 100$ nm and $R_y = 60$ nm. For the previous dot with $R_z = 10$ nm no orbital effects from the magnetic field on the energy spectrum were observed [see the black curves in Fig. 2]. However, this is no longer true for larger R_z values. This can be seen from Figs. 8(a) and 8(b) where we plot the energy levels of a quantum dot with height $R_z = 20$ nm and $R_z = 40$ nm, respectively, in the presence of SO coupling (with both SO interactions present). The energy levels depend on the magnetic-field orientation even outside the anticrossing region. This is due to the elongation of the confinement potential in the x direction. The SO-induced anticrossing is shifted to lower magnetic fields as the value of the angle ϕ becomes closer to $\phi = 90^\circ$ [this is analogous to the experimental observation—compare with Fig. S7(a) from Ref. 28]. We calculated the anticrossing widths for different values of ϕ and we plot them as red dots in the insets of Fig. 8. Then we fitted the points with the function $A|\sin(\phi - \phi_{AC})|$, where $A = 86 \mu\text{eV}$ and $\phi_{AC} = 65^\circ$ for $R_z = 20$ nm and $A = 77 \mu\text{eV}$ and $\phi_{AC} = 82^\circ$ for $R_z = 40$ nm. Notice the agreement between the fitted curve and the data points. From this fact we conclude that in spite of the presence of orbital effects, the previously found dependence of the anticrossing width on the angle ϕ still holds, but with modified A and ϕ_{AC} values. The latter fact can be attributed to the reduction of the Dresselhaus coupling strength. This can be accounted for by considering the Dresselhaus coupling Hamiltonian in Eq. (16), in which the coupling strength decreases as $(1/R_z)^2$. In the calculation performed for pure Dresselhaus interaction, we obtain the maximal E_{AC} values: 146, 37, and $11 \mu\text{eV}$ for $R_z = 10, 20,$ and 40 nm, respectively—the obtained E_{AC} values decrease approximately as $(1/R_z)^2$ with the largest discrepancy for large R_z values (i.e., when the approximation of the coupling strength by Eq. (15) becomes inaccurate). The decrease of the Dresselhaus-coupling strength with increasing height of the dot results in a shift of the E_{AC} dependency on ϕ toward the one obtained for a flat quantum-dot with only Rashba interaction present compare the black curve in the inset of Fig. 8(b) with the green dotted curve in Fig. 4— ϕ_{AC} becomes close to 90° . Also the maximal E_{AC} value becomes closer to the one obtained for pure Rashba coupling— A tends to $77 \mu\text{eV}$ with increasing R_z . The shift in the ϕ_{AC} value [see insets of Figs. 8(a) and 8(b)] can be understood from the relative strengths of the Rashba and Dresselhaus couplings as discussed in Sec. III C.

G. Two-electron results

In a recent experiment [21], the ground state and excited states were measured provided that the latter entered into a finite but narrow transport window determined by the voltages applied to the source and drain electrodes. The avoided crossings that appear for a single-electron in the excited part

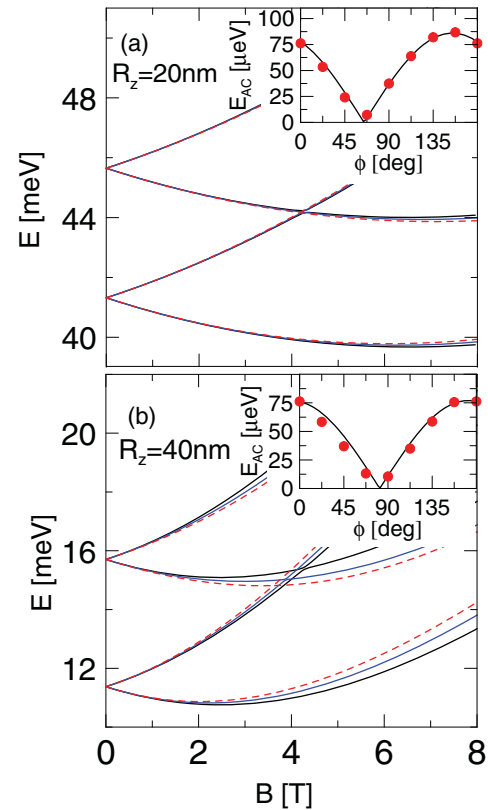


FIG. 8. (Color online) One-electron energy levels for a rectangular-based quantum dot with (a) $R_z = 20$ nm and (b) $R_z = 40$ nm for $\phi = 0, 45^\circ,$ and 90° plotted with the black solid, blue solid, and red dashed curves, respectively. The red dots in the insets of both plots present the anticrossing width, E_{AC} obtained from the energy spectrum for a given ϕ value; the black curves are the fitted $|\sin(\phi - \phi_{AC})|$ dependencies.

of the spectrum, which we described above, were outside the transport window.

In the two-electron regime and in the absence of both the magnetic field and the SO interaction, the ground state is a spin singlet and the first excited state is a spin triplet. Under the presence of an external magnetic field the ground-state singlet energy crosses the triplet energy. When we turn on the SO coupling it induces an avoided crossing between the states of opposite spin which was well resolved in the experiment [21].

Similarly to the one-electron case, the SO coupling is responsible for changes in the size of the anticrossing energy when the orientation of the magnetic field is varied. Figure 9 presents the low-energy spectrum of the two-electron quantum dot in the presence of both Rashba and Dresselhaus couplings for a dot aligned with its long axis along the [100] direction ($\theta = 0$). In the inset, we plot the energy levels in the vicinity of the AC. The anticrossing vanishes for exactly the same angle, $\phi_{AC} = 27.8^\circ$, as for the one-electron case discussed above (see the green curves in the inset of Fig. 9).

In Fig. 10(a), we plot the angular dependence of the anticrossing width, E_{AC} , for pure Dresselhaus, pure Rashba, and when both couplings are present by the blue dashed, green dotted, and solid red curves, respectively. Notice that all three

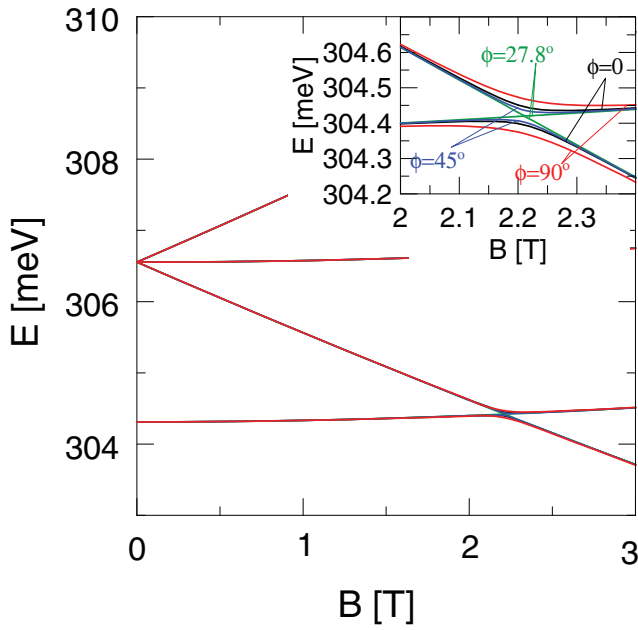


FIG. 9. (Color online) Two-electron energy spectrum in the presence of both Rashba and Dresselhaus SO coupling for angles $\phi = 0$ (black curves), 27.8° (green curves), 45° (blue curves), and 90° (red curves). The inset shows the energy levels in the vicinity of the anticrossing. The results are obtained for $\theta = 0$.

dependencies have the same shape as for the case of the one electron considered in Sec. III B (compare with Fig. 4), only the maximal E_{AC} values are about 1.5 times smaller.

As was presented in Sec. III C, for the anisotropic quantum dot the angle ϕ_{AC} depends on the relative strength of both SO interactions and the in-plane orientation of the dot (explained in Sec. III D). On the other hand, the ϕ_{AC} value can be measured experimentally²¹ and the orientation of the quantum dot with respect to the crystal directions can be obtained by inspecting the facets of the dot. This opens the possibility to employ such a measurement to evaluate the relative strength of the Rashba and Dresselhaus couplings for a dot with a given orientation with respect to the crystal host. Let us define the strength ratio of the SO interactions as the ratio of the effective coupling constants α^* and γ^{2D} . The Rashba coupling strength denoted with α^* is calculated as $\alpha^* = \alpha[\frac{\partial V}{\partial z}] = -\alpha|e|F_z$ and the Dresselhaus coupling γ^{2D} is obtained from Eq. (15).

We previously derived the angle ϕ_{AC} for given relative strength of the SO couplings for a given orientation of the dot [see Eq. (23)]. Let us substitute the $1/1.9$ value by α^*/γ^{2D} in Eq. (23) from which we obtain

$$\frac{\alpha^*}{\gamma^{2D}} = -\frac{\alpha}{\gamma} \frac{|e|F_z R_z^2}{\pi^2} = \cos(2\theta)[\tan(\phi_{AC}) - \tan(-2\theta)]. \quad (24)$$

This function is shown in Fig. 10(b) by the solid lines for different orientations of the quantum dot. With the black symbols we mark the angle ϕ_{AC} obtained from our numerical calculations for dots with different geometries (see Fig. 10 caption) with $\theta = 0$ for different SO coupling strengths. For such a case, with $\theta = 0$ (the dot oriented with its long axis along [100]) and pure Dresselhaus coupling ($\alpha^*/\gamma^{2D} = 0$) we obtain $\phi_{AC} = 0$. When the Rashba-coupling strength is

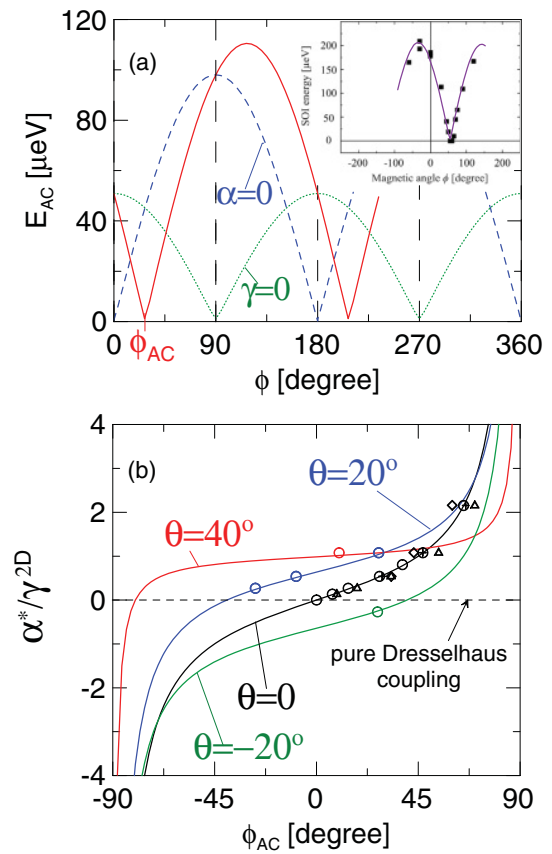


FIG. 10. (Color online) (a) Width of the singlet-triplet avoided crossing as a function of the angle ϕ for pure Dresselhaus coupling (blue dashed curve), pure Rashba coupling (green dotted curve), and for both couplings present (red solid curve). The inset shows the experimental results (symbols) of Ref. 21 together with the results of the present calculation (purple curve) with $\gamma = 29.58 \text{ meV nm}^3$ and $\alpha = 4.731 \text{ nm}^2$. The magnetic field is $B = 2.211 \text{ T}$ for pure Rashba coupling and $B = 2.209 \text{ T}$ for all the other cases. The dot is aligned with its long axis along [100], i.e., $\theta = 0$. (b) The ϕ_{AC} value for different strength ratios of the Rashba and Dresselhaus couplings for four different orientations of the dot. The symbols present the results of our numerical calculation and the curves represent the analytical result given by Eq. (24). The circles show the results obtained for $R_y = 60 \text{ nm}$ and $R_z = 10 \text{ nm}$, the crosses for $R_y = 30 \text{ nm}$ and $R_z = 10 \text{ nm}$, the triangles for $R_y = 20 \text{ nm}$ and $R_z = 10 \text{ nm}$, and the diamonds for $R_y = 60 \text{ nm}$ and $R_z = 20 \text{ nm}$. In all cases, R_x is 100 nm .

increased, the points move toward the angle $\phi_{AC} = 90^\circ$ obtained for pure Rashba SO coupling. The green, red, and blue symbols in Fig. 10(b) are the ϕ_{AC} values obtained from our two-electron numerical calculation for different orientations of the quantum dot.

In the above discussion, we assume that $\alpha^* = -\alpha|e|F_z$ and $\gamma^{2D} = \gamma\pi^2/R_z^2$ describe the strength of the spin-orbit interactions. For the Rashba coupling, given by the Hamiltonian in Eq. (3) (i.e., when an electric field is only present in the growth direction), the above α^* expression is valid regardless of the dot geometry. However, due to the fact that γ^{2D} originates from the Hamiltonian in Eq. (14), it describes the strength of the Dresselhaus coupling correctly only when

TABLE I. Calculated strength ratios of the SO couplings for $\phi_{AC} = 59^\circ$ and different orientations of the dot.

θ	α^*/γ^{2D}
0	1.66
40°	1.27
45°	...
75°	-0.94
90°	-1.66

the cubic term, $\gamma[\sigma_y k_y k_x^2 - \sigma_x k_x k_y^2]$, is negligible, which is the case when $R_x, R_y \gg R_z$ and the term with $\langle k_z \rangle$ is close to zero, i.e., for a dot with limited height.³³ All the symbols in Fig. 10(b) approximately coincide with the dependency given by Eq. (24). A discrepancy is seen in the limit of a narrow dot with $R_y = 20$ nm (the triangles) and for increased height of the dot for $R_z = 20$ nm (diamond symbols). We conclude that for anisotropic quantum dots with limited height the α^*/γ^{2D} ratio is a good measure of the relative strength of the Rashba and Dresselhaus spin-orbit couplings, which can be estimated from the analytic expression in Eq. (24).

The experiment of Ref. 21 found $\phi_{AC} = 59^\circ$, and we can use Eq. (24) to calculate the relative strength of the SO interactions. However, as the orientation of the anisotropic potential of the dot with respect to the crystal directions was not resolved in the experiment we need to assume a value for θ . We take $\theta = 0$ and by matching the absolute value of the SO-coupling constants (through the maximal value of E_{AC}) we obtained $\alpha^*/\gamma^{2D} \simeq 1.66$ by fitting the experimentally measured values for the AC width with our simulation results. In the inset to Fig. 10(a), we plot our results (purple curve) for the SO-coupling constants $\gamma = 29.58$ meV nm³ and $\alpha = 4.731$ nm² together with the data points from Ref. 21. However, as the relation between the crystal directions and the long axis of the dot is not known, the fit only proves the validity of the discussed process behind the anisotropy and not the exact value of the ratio α^*/γ^{2D} . Moreover, as the electrostatics of the actual device is complex the presented result is not the *exact* simulation of the experiment. Therefore, we present in Table I the strength ratios for different orientations of the dot. Note that Eq. (24) does not allow us to calculate the relative strength of the couplings for a dot aligned with long axis exactly along [110] or $[\bar{1}\bar{1}0]$. In such a configuration, for pure Dresselhaus as well as for pure Rashba coupling the AC vanishes for $\phi_{AC} = 90^\circ$ [compare dotted curves in Fig. 5(a) with green dotted curve in Fig. 5(b)] and because of that, for both couplings present simultaneously the minimum of the E_{AC} dependence on ϕ is not shifted irrespective of the coupling strength ratio.

IV. DISCUSSION

In the present paper we discussed the avoided crossings of energy levels induced by the presence of different SO couplings. Only for the case of a square-based quantum-dot [see Figs. 7(a) and 7(b)] the dependence of AC width on the magnetic-field direction was observed solely for both couplings present with comparable strength. This result is related to those of Ref. 23 where the spin-splitting of

single-electron energy levels in strictly *two-dimensional circular* quantum dots in the presence of a *small* in-plane magnetic field (before the crossings and avoided crossings appear) was calculated. When the Dresselhaus- and Rashba-coupling strengths are equal, a well-known high-symmetric case is found, which is beneficial for many spintronic applications.^{5,10} For that special case, the energy spectrum is not affected by SO-interaction effects and the spin in the [110] direction is strictly defined. The Zeeman interaction lifts this symmetry and results in a spectrum that depends on the orientation of the magnetic field as discussed in Ref. 23. Since for equal coupling strengths the spins in the [110] direction are well defined, the Zeeman interaction for \mathbf{B} oriented along [110] does not produce any AC between energy levels of spin-orthogonal states [see the blue curve in Fig. 7(d)].

On the other hand, in the presence of a vertically oriented magnetic field, the size of the Zeeman interaction induced lifting of the symmetry depends on the in-plane orientation³⁴ and also on the width³⁵ of the dot, which results in changes of both the AC width and the effective g factor, which are solely observed when both SO interactions are present with a comparable strength. However, changing the dot orientation is hardly achievable experimentally and therefore, in the present work, we considered an anisotropy that can be probed by changing the orientation of the magnetic field.

In the present work, we investigated the anisotropic dependence of the avoided-crossing width that occurs even for a single type of SO coupling [see Figs. 3(a) and 3(b)]. This effect is strictly connected to both the elongation of the confinement potential and the in-plane alignment of the magnetic field (see the discussion in Sec. III B). The exact shape of the confinement potential is not important for the studied phenomena, which is a generic propriety of a spin-orbit-coupled quantum dot. In our analysis, we indicated the trends that determined the dependence of E_{AC} on ϕ , in particular, the dependence on the dot geometry [for the dot with increased height and for different lateral sizes of the dot the black symbols in Fig. 10 still undergo the same analytical dependence Eq. (24) in spite of the different geometries of the dot] or the orientation of the quantum dot with respect to the crystallographic directions (which influences the position of the minima of E_{AC} purely due to Dresselhaus coupling—see discussion in Sec. III D).

The present study shows that for an elongated quantum dot with pure Rashba coupling the anticrossing vanishes always when the magnetic field is aligned along the short axis of the dot [see the minima of the dotted curves in Figs. 4 and 5(a), and 10(a)]. Only the presence of Dresselhaus coupling can result in a ϕ_{AC} value that is different from 90° . The magnetic-field direction ($\phi_{AC} = 59^\circ$) for which the anticrossing vanished in the experiment of Ref. 21 suggests that both SO couplings are present, contrary to the argumentation provided in Ref. 21. The authors suggested that the Dresselhaus coupling would not induce mixing between the two lowest-energy states due to their well-defined and different values of the total angular momentum $J_- = L - S$ in a high magnetic field. However, we found that due to the in-plane alignment of the magnetic field³⁶ the Dresselhaus coupling, in fact, induces avoided crossings in the energy spectrum of a flat quantum dot [see

Fig. 2] and leads also to a shift in the dependence of the AC width on the magnetic-field direction [see Figs. 3, 5(a), 5(b), and 8].

V. SUMMARY AND CONCLUSIONS

We presented a study of the energy spectrum of one and two-electron spin-orbit-coupled three-dimensional quantum dots in the presence of an external in-plane magnetic field. We found that the size of the avoided crossings in the one- and two-electron energy spectrum oscillates as a function of the orientation of the magnetic field. The oscillatory behavior could accurately be described by $|\sin(\phi - \phi_{AC})|$, which agrees with recent excited-state-spectroscopy measurements performed on an InAs gated self-organized quantum dot.²¹

For a quantum dot that is elongated in the [100] direction, and when only a single type of SO coupling is present, the avoided crossing vanishes for $\phi_{AC} = 0$ ($\phi_{AC} = 90^\circ$), i.e., when the magnetic field is aligned parallel to the long (short) axis of the dot for Dresselhaus (Rashba) coupling. We explain this behavior as a consequence of parity and spin-dependent mixing of the states caused by the SO interaction. When both couplings are present the ϕ_{AC} value varies between 0 and

90° and the ratio of the relative strength of the interactions follows a $\tan(\phi_{AC})$ dependence. The change of the in-plane dot orientation results in a change of ϕ_{AC} , which is observed only when the Dresselhaus coupling is present. We show that the experimentally measured ϕ_{AC} value²¹ along with the knowledge of the orientation of the dot can be used to determine the ratio of the strengths of the individual SO interactions in the case of anisotropic quantum dots.

ACKNOWLEDGMENTS

The authors thank S. Takahashi for helpful discussions. This work was supported by the “Krakow Interdisciplinary PhD Project in Nanoscience and Advanced Nanostructures” operated within the Foundation for Polish Science MPD Programme co-financed by the EU European Regional Development Fund, the Project No. N N202103938 supported by the Ministry of Science and Higher Education (MNiSW) for 2010–2013, and the Belgian Science Policy (IAP). W. J. P. has been partially supported by the EU Human Capital Operation Program, Polish Project No. POKL.04.0101-00-434/08-00. Calculations were performed in ACK–CYFRONET–AGH on the RackServer Zeus.

¹K. C. Nowack, F. H. L. Koppens, Yu. V. Nazarov, and L. M. K. Vandersypen, *Science* **318**, 1430 (2007).

²S. Nadj-Perge, S. M. Frolov, E. P. A. M. Bakkers, and L. P. Kouwenhoven, *Nature (London)* **468**, 1084 (2010).

³E. Ya. Sherman and D. J. Lockwood, *Phys. Rev. B* **72**, 125340 (2005).

⁴S. Z. Denega, T. Last, J. Liu, A. Slachter, P. J. Rizo, P. H. M. van Loosdrecht, B. J. van Wees, D. Reuter, A. D. Wieck, and C. H. van der Wal, *Phys. Rev. B* **81**, 153302 (2010).

⁵B. A. Bernevig, J. Orenstein, and S. C. Zhang, *Phys. Rev. Lett.* **97**, 236601 (2006); J. D. Koralek, C. Weber, J. Orenstein, A. Bernevig, S. Zhang, S. Mack, and D. Awschalom, *Nature (London)* **458**, 610 (2009).

⁶M. Scheid, M. Kohda, Y. Kunihashi, K. Richter, and J. Nitta, *Phys. Rev. Lett.* **101**, 266401 (2008).

⁷L. Meier, G. Salis, E. Gini, I. Shorubalko, and K. Ensslin, *Phys. Rev. B* **77**, 035305 (2008); L. Meier, G. Salis, I. Shorubalko, E. Gini, S. Schön, and K. Ensslin, *Nat. Phys.* **3**, 650 (2007).

⁸S. Bednarek and B. Szafran, *Phys. Rev. Lett.* **101**, 216805 (2008); P. Földi, O. Kálmán, M. G. Benedict, and F. M. Peeters, *Nano Lett.* **8**, 2556 (2008); P. Földi, B. Molnár, M. G. Benedict, and F. M. Peeters, *Phys. Rev. B* **71**, 033309 (2005).

⁹S. Datta and B. Das, *Appl. Phys. Lett.* **56**, 665 (1990).

¹⁰J. Schliemann, J. C. Egues, and D. Loss, *Phys. Rev. Lett.* **90**, 146801 (2003).

¹¹K. V. Kavokin, *Phys. Rev. B* **64**, 075305 (2001); **69**, 075302 (2004); S. C. Bădescu, Y. B. Lyanda Geller, and T. L. Reinecke, *ibid.* **72**, 161304 (2005); S. Gangadharaiah, J. Sun, and O. A. Starykh, *Phys. Rev. Lett.* **100**, 156402 (2008).

¹²D. Loss and D. P. DiVincenzo, *Phys. Rev. A* **57**, 120 (1998).

¹³M. P. Nowak and B. Szafran, *Phys. Rev. B* **82**, 165316 (2010).

¹⁴G. Dresselhaus, *Phys. Rev.* **100**, 580 (1955).

¹⁵Y. A. Bychkov and E. I. Rashba, *J. Phys. C* **17**, 6039 (1984).

¹⁶D. V. Bulaev and D. Loss, *Phys. Rev. B* **71**, 205324 (2005); L. Meza-Montes, C. F. Destefani, and S. E. Ulloa, *ibid.* **78**, 205307 (2008); F. Qu, G. L. Iorio, V. Lopez-Richard, and G. E. Marques, *Appl. Phys. Lett.* **95**, 083101 (2009); M. P. Nowak and B. Szafran, *Phys. Rev. B* **81**, 235311 (2010); F. Baruffa, P. Stano, and J. Fabian, *ibid.* **82**, 045311 (2010); S. Nadj-Perge, S. M. Frolov, J. W. W. van Tilburg, J. Danon, Yu. V. Nazarov, R. Algra, E. P. A. M. Bakkers, and L. P. Kouwenhoven, *ibid.* **81**, 201305(R) (2010).

¹⁷K. Shen and M. W. Wu, *Phys. Rev. B* **76**, 235313 (2007); T. Meunier, I. T. Vink, L. H. Willems van Beveren, K.-J. Tielrooij, R. Hanson, F. H. L. Koppens, H. P. Tranitz, W. Wegscheider, L. P. Kouwenhoven, and L. M. K. Vandersypen, *Phys. Rev. Lett.* **98**, 126601 (2007); L. R. Schreiber, F. R. Braakman, T. Meunier, V. Calado, J. Danon, J. M. Taylor, W. Wegscheider, and L. M. K. Vandersypen, e-print arXiv:1010.5682v1.

¹⁸P. Stano and J. Fabian, *Phys. Rev. Lett.* **96**, 186602 (2006); V. N. Golovach, A. Khaetskii, and D. Loss, *Phys. Rev. B* **77**, 045328 (2008).

¹⁹C. Fasth, A. Fuhrer, L. Samuelson, V. N. Golovach, and D. Loss, *Phys. Rev. Lett.* **98**, 266801 (2007).

²⁰A. Pfund, I. Shorubalko, K. Ensslin, and R. Leturcq, *Phys. Rev. B* **76**, 161308(R) (2007).

²¹S. Takahashi, R. S. Deacon, K. Yoshida, A. Oiwa, K. Shibata, K. Hirakawa, Y. Tokura, and S. Tarucha, *Phys. Rev. Lett.* **104**, 246801 (2010).

²²V. I. Fal’ko, B. L. Altshuler, and O. Tsypliyatsev, *Phys. Rev. Lett.* **95**, 076603 (2005); J. Königmann, R. J. Haug, D. K. Maude, V. I. Fal’ko, and B. L. Altshuler, *ibid.* **94**, 226404 (2005).

²³M. Valiyn-Rodriguez, A. Puente, and Ll. Serra, *Eur. Phys. J. B* **39**, 87 (2004).

- ²⁴The in-plane electric field, F_y , originating from the potential difference between the source-drain electrodes in Ref. 21, is of order of hundreds of V cm^{-1} , which is 50 times smaller than the electric field in the growth direction. The effect of F_y on the energy levels was found to be negligible.
- ²⁵M. Stopa and C. M. Marcus, *Nano Lett.* **8**, 1778 (2008).
- ²⁶The accuracy of the two-electron calculation for an infinite-quantum-well-confinement potential has been checked by comparing the present calculation in the two-dimensional limit (in the z direction we use an infinite quantum well with width of 1 nm) with the two-dimensional calculation on the grid showing an accuracy better than $1 \mu\text{eV}$ with ground state energy $E = 3.574 \text{ meV}$. For parabolic confinement we compared the present computational scheme with the center-of-mass approach obtaining differences in the energy of order of tenth of μeV with the ground-state energy $E = 248.15 \text{ meV}$.
- ²⁷P. W. Fry *et al.*, *Phys. Rev. Lett.* **84**, 733 (2000).
- ²⁸See supplemental online material for S. Takahashi, R. S. Deacon, K. Yoshida, A. Oiwa, K. Shibata, K. Hirakawa, Y. Tokura, and S. Tarucha, *Phys. Rev. Lett.* **104**, 246801 (2010).
- ²⁹Evaluated from gate voltage $V_g = -0.8 \text{ V}$ for which the first current peak in tunneling spectroscopy is observed [see Ref. 28].
- ³⁰E. A. de Andrada e Silva, G. C. La Rocca, and F. Bassani, *Phys. Rev. B* **55**, 16293 (1997).
- ³¹W. Knap *et al.*, *Phys. Rev. B* **53**, 3912 (1996).
- ³²M. Willatzen and L. C. Lew Yan Voon, *J. Phys. Condens. Matter* **20**, 345216 (2008).
- ³³The energetic contribution to the AC calculated for $R_z = 10 \text{ nm}$ from the second and third term in Eq. (14) is 4 and $9 \mu\text{eV}$, respectively, and does not change when the dot height is increased to $R_z = 40 \text{ nm}$.
- ³⁴M. P. Nowak and B. Szafran, *Phys. Rev. B* **83**, 035315 (2011).
- ³⁵S. Prabhakar, J. E. Raynolds, and R. Melnik, e-print arXiv:1011.1921v1.
- ³⁶In a sufficiently strong magnetic field, the diamagnetic term of the Hamiltonian becomes stronger than the confinement potential and, in consequence, the Hamiltonian eigenstates become identical to Fock-Darwin states. In particular, the ground-state and the first excited state acquire angular momenta 0 and -1 , respectively. However, in the problem studied in this paper, including strong confinement in the growth direction and in plane magnetic field orientation, this limit is not reached within the considered range of B . Namely, for quantum dot with dimensions $R_x = 100 \text{ nm}$, $R_y = 60 \text{ nm}$ and $R_z = 10 \text{ nm}$ in the absence of SO coupling at $B = 10 \text{ T}$ we obtain mean values of the angular momentum 0.1, 0.1, 0.1, and 0.09 for the ground and three lowest energy excited states, respectively. For the dot with increased height, $R_z = 40 \text{ nm}$, the values are 0.8, 0.7, 0.6, and 0.4.

9 Resonant harmonic generation and collective spin rotations in electrically driven quantum dots

Resonant harmonic generation and collective spin rotations in electrically driven quantum dotsM. P. Nowak,¹ B. Szafran,¹ and F. M. Peeters²¹AGH University of Science and Technology, Faculty of Physics and Applied Computer Science, al. Mickiewicza 30, 30-059 Kraków, Poland²Departement Fysica, Universiteit Antwerpen, Groenenborgerlaan 171, B-2020 Antwerpen, Belgium

(Received 30 April 2012; published 18 September 2012)

Spin rotations induced by an ac electric field in a two-electron double quantum dot are studied by an exact numerical solution of the time-dependent Schrödinger equation in the context of recent electric-dipole spin resonance experiments on gated nanowires. We demonstrate that the splitting of the main resonance line by the spin exchange coupling is accompanied by the appearance of fractional resonances and that both these effects are triggered by interdot tunnel coupling. We find that the ac-driven system generates residual but distinct harmonics of the driving frequency, which are amplified when tuned to the main transition frequency. The mechanism is universal for electron systems in electrically driven potentials and works also in the absence of electron-electron interaction or spin-orbit coupling.

DOI: [10.1103/PhysRevB.86.125428](https://doi.org/10.1103/PhysRevB.86.125428)

PACS number(s): 73.21.La, 03.67.Lx, 71.70.Gm, 75.70.Tj

I. INTRODUCTION

The idea¹ of processing quantum information stored in spins of electrons confined in quantum dots has motivated a significant theoretical and experimental effort within the last decade. One of the necessary prerequisites for quantum gating is coherent single-spin manipulation. Single-spin rotations can be performed using electron spin resonance–Rabi oscillations in external microwave radiation resonant with the Zeeman splitting of energy levels in a magnetic field (B). Electron spin resonance was implemented in a quantum dot² using an embedded on-chip microwave source. In gated quantum dots the microwave field has been successfully replaced by ac voltages.^{3–8} The periodic motion of the electron induced by the ac field subjects its spin to an oscillating momentum-dependent spin-orbit (SO) field,^{9,10} leading to electric-dipole spin resonance (EDSR).¹¹ The spin rotations are detected in two-electron double-quantum-dot systems^{2–8} using the Pauli blockade of the current flow which occurs when the dots become occupied by electrons with parallel spins. The rotation of the spin lifts the Pauli blockade when the frequency of the ac electric field is tuned to the resonant transition.

The detailed structure of the EDSR was recently resolved⁸ in a double dot produced in a gated InSb quantum wire with strong SO interactions. The experimental data [Fig. 2(b) of Ref. 8] include a double line corresponding to transitions from the spin-polarized triplet T_+ ground state to a doublet formed by (1) a singlet S , and (2) an unpolarized triplet T_0 , as well as a single line at half the resonant frequency. Half resonances were previously observed also in InAs quantum wire dots [Fig. 2(b) of Ref. 7] as well as in GaAs planar quantum dots.⁴ Analysis of the dipole moment induced by an ac field in the *singlet* subspace of two-electron systems was given in Ref. 12 in terms of flopping the pseudospin mode.

In this paper we report on the solution of the time-dependent Schrödinger equation for the two-electron system in an ac field induced by gates in the presence of SO coupling. We find spin transitions involving both Rabi oscillations for the resonant driving frequency as well as fractional resonances which are consistent with the experimental data.⁸ We show that the mechanism responsible for the appearance of the fractional

lines is the resonant amplification of the higher harmonics residually present within the driven system.

Solution of the time-dependent Schrödinger equation is one of the methods^{13–15} applied in theories of high-harmonics generation by atoms and molecules in intense laser fields^{16–18} in the quest for controllable sources of ultraenergetic photons. Noble gases or simple molecular systems (N_2 , O_2 , CO_2) generate *nonresonantly* high harmonics of the driving laser field of intensity 10^{11} W/m² with local field amplification by plasmonic metal nanostructures,¹⁹ or 10^{13} W/m² in standard conditions. The amplitude of the ac electric field applied in EDSR for quantum dots (a fraction of kV/cm) corresponds to a laser radiation of only 10^5 W/m². Nevertheless, we find a distinct—although residual—appearance of the second and third harmonics of the driving frequency ω_{ac} in the electron motion within the double dot. We demonstrate that the harmonics of the driving frequency are essentially reinforced when brought to resonance with the Rabi direct transition frequency. We indicate that this phenomenon is quite general for ac-driven electron systems confined in quantum dots, in particular that it appears also for a single electron and in the absence of SO coupling. As a result, the confined system is driven into an excited state by a frequency ω that is a fraction of the excitation energy ΔE , i.e., $\hbar\omega = \Delta E/n$, which is similar to n -photon optical transitions.²⁰

II. MODEL

The considered two-electron system is described by the Hamiltonian

$$H = h_1 + h_2 + \frac{e^2}{4\pi\epsilon_0\epsilon|\mathbf{r}|}, \quad (1)$$

with the single-electron energy operator

$$h_i = \frac{\hbar^2\mathbf{k}_i^2}{2m^*} + V(\mathbf{r}_i, t) + \frac{1}{2}g\mu_B B\sigma_{x_i} + H_{SO}, \quad (2)$$

with magnetic field B aligned along the x direction. The momentum operator is $\hbar\mathbf{k}_i = -i\hbar\nabla_i$ as we neglect the orbital effects of the magnetic field for low values of B and in strong confinement in the plane perpendicular to the x direction. $V(\mathbf{r}, t)$ stands for the confinement potential taken in a separable

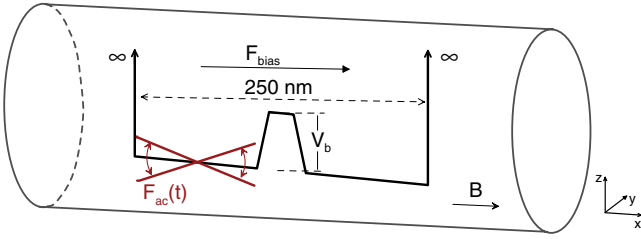


FIG. 1. (Color online) Schematic of the considered confinement potential of a nanowire double-dot system.

form $V(\mathbf{r}, t) = V_x(x, t)V_{y,z}(y, z)$. We include the Rashba SO interaction⁹ resulting from the electric field—generated by the system of gates from which the nanowire is deposited—which is assumed perpendicular to the wire (parallel to the z direction), $H_{SO} = \alpha(\sigma_x k_y - \sigma_y k_x)$. Figure 1 depicts the considered confinement potential. The structure is assumed 250 nm long, with

$$V_x(x, t) = V_{sx}(x) + eF_{\text{bias}}x + eF_{\text{ac}}xf(x)\cos(\omega_{\text{ac}}t). \quad (3)$$

The last term in Eq. (3) represents the ac field, which is applied to the left dot only (see [8]), i.e., $f(x) = 1$ in the left dot and 0 outside. V_{sx} is a double-quantum-well potential with a 30-nm-thick barrier of height V_b in the center. A constant $F_{\text{bias}} = -0.1$ kV/cm is taken for the 8 mV source-drain bias voltage.⁸ We assume a strong radial parabolic confinement in the (y, z) direction which freezes the lateral wave functions of both electrons into Gaussians $\Psi = (\sqrt{\pi}l)^{-1} \exp[-(y^2 + z^2)/2l^2]$, with $l = 30$ nm. Upon integration of (1) with the lateral wave functions one arrives at an effective Hamiltonian²¹

$$H = \sum_{i=1,2} \left[-\frac{\hbar^2}{2m^*} \frac{\partial^2}{\partial x_i^2} + V_x(x_i, t) - \alpha\sigma_{y_i}k_{x_i} + \frac{1}{2}g\mu_B B\sigma_{x_i} \right] + \frac{\sqrt{\pi/2}}{4\pi\epsilon_0\epsilon l} \text{erfcx} \left[\frac{|x_1 - x_2|}{\sqrt{2}l} \right], \quad (4)$$

which is used in this work. Unless stated otherwise we apply material parameters²² for InSb: $m^* = 0.014m_0$, $g = -51$, $\epsilon = 16.5$, and take the Rashba constant $\alpha = 50$ meV nm. The ac field amplitude $F_{\text{ac}} = 0.1$ kV/cm is assumed. All the calculations are performed within the finite-difference scheme on the (x_1, x_2) space with exact inclusion of the electron-electron correlation.

III. RESULTS

Figure 2(a) shows the energy spectrum of weakly coupled quantum dots ($V_b = 100$ meV). The fourfold degeneracy of the ground state at $B = 0$ is due to weak tunnel coupling between the dots. The degeneracy is lifted in nonzero B : the triplet energy levels with spin aligned parallel and antiparallel to the x direction— T_+ and T_- respectively²³ (plotted with the red and blue curves)—are split by the Zeeman interaction. The two other states— T_0 and S (plotted as the green solid and black dashed curves)—with zero value of the spin component in the x direction remain degenerate (with energy separation below 0.1 μeV).

We initialize the system in the T_+ state. For $B = 20$ mT and ac frequency tuned to the energy difference between the

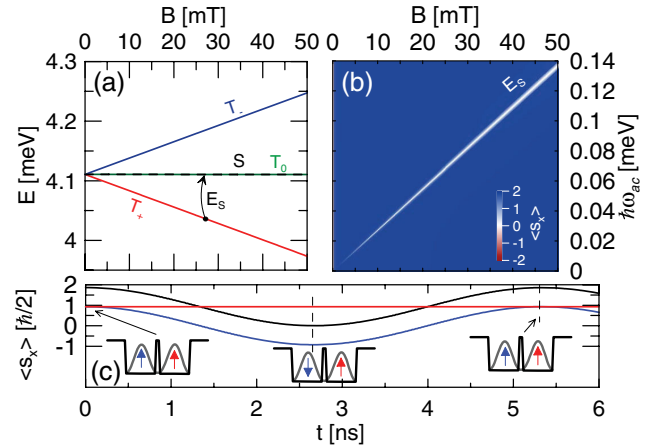


FIG. 2. (Color online) (a) Energy spectrum of coupled quantum dots with barrier height $V_b = 100$ meV. (b) Map of the spin transitions after 30 ns: the minimal value of the x component of the spin obtained during the simulation in units of $\hbar/2$ (the initial value is 2). (c) Evolution of the spin x component in the left (blue curve), right (red curve), and both dots (black curve) at the resonance marked with the black arrow in (a).

T_+ and S states ($\hbar\omega_{\text{ac}} = E_S \simeq 55$ μeV which corresponds to the oscillation period $\tau_{\text{ac}} \simeq 75$ ps) we see [Fig. 2(c)] that after about 2.7 ns the spin of the electron in the left dot—wiggled by the AC field—is inverted, while the spin in the right dot remains unaffected.

The EDSR experiments probe the spin rotations by measuring the map of current leakage through the spin blockade as function of the driving ac frequency ω_{ac} and external magnetic field magnitude B . Figure 2(b) shows the minimal value of the spin obtained during a time evolution of 30 ns as function of B and the driving frequency (the initial x component of the spin is 2 in units of $\hbar/2$). A single line corresponding to the $T_+ \rightarrow (S, T_0)$ doublet transition is obtained. Outside this resonant line the ac field does not influence the spin. Note that the transition $T_+ \rightarrow T_-$ is not observed since it requires rotation of both spins.

For stronger interdot coupling ($V_b = 17$ meV) the splitting of T_0 and S energy levels (the exchange energy^{1,24}) becomes nonzero, $J = E_{T_0} - E_S \simeq 5.6$ μeV [see the energy spectrum in Fig. 3(a)]. For ω_{ac} tuned to the $T_+ \rightarrow S$ transition we observe that the ac field applied to the left dot rotates the spins in *both* dots [Fig. 3(c)]. This is due to the spin exchange interaction which is now activated by the interdot tunneling. The characteristic spin swap time $\tau = \pi\hbar/J \simeq 370$ ps corresponds to the intervals between the local extrema of spins observed in Fig. 3(c). In the plot there are also fast oscillations of the spin component visible. Their period corresponds to the period of the ac field, i.e., $\tau_{\text{ac}} \simeq 63$ ps for $\hbar\omega_{\text{ac}} = 66$ μeV . They are due to spin precession²⁵ induced by the spatial electron oscillation driven due to stronger interdot tunnel coupling as compared to the $V_b = 100$ meV case. Near $B = 0$ we observe an avoided crossing of lowest-energy levels due to the SO interaction. For $B > 0.1$ mT they can be identified by their spin x component as S , T_+ , T_0 , and T_- ; see also the end of the section.

The map of minimal spin states encountered during a 30 ns simulation is presented in Fig. 3(b). At the diagonal

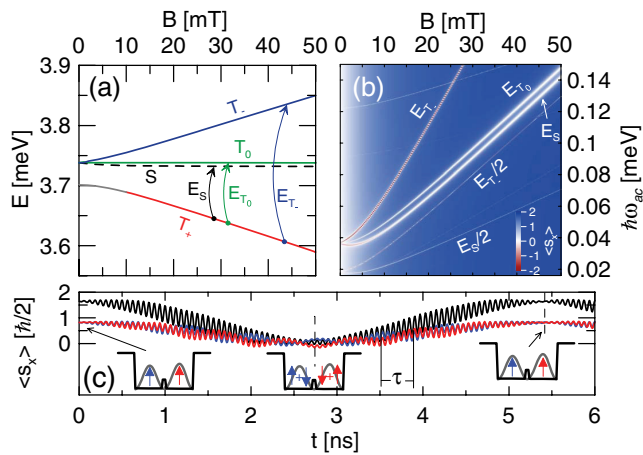


FIG. 3. (Color online) As Fig. 2 but for stronger interdot coupling, i.e., $V_b = 17$ meV.

of the plot two major lines emerge. They correspond to the transitions from the T_+ state to the S (for $\hbar\omega_{ac} = E_s$) and T_0 (for $\hbar\omega_{ac} = E_{T_0}$) states with 0 spin x components. This double line was observed in the experiments^{7,8} and attributed to different g factors in the dots with the assumption that a single spin responds to the ac field, and the local differences in g factor are due to variation of the confinement composition. In fact the present simulation shows that the lines are split when $J \neq 0$, which implies coupling between the spins in both the dots. Rotation of the spin in the left dot to which the ac field is applied results in the spin rotation of the other electron. When only the spin in the left dot is inverted, the final state corresponds to a spatial “spin density wave” which is not an eigenstate of the spin, but a superposition of S and T_0 states, which can be a stationary Hamiltonian eigenstate only provided that S and T_0 are degenerate as is the case in Fig. 2.

The transition $T_+ \rightarrow S$ lifts the Pauli blockade *directly*, while the $T_+ \rightarrow T_0$ transition lifts the blockade only *indirectly*²⁶ due to the mixing of S and T_0 states—which are close in energy—by the hyperfine field. The red curve in Fig. 3(b) obtained for $\hbar\omega = E_{T_-}$ corresponds to the transition to the T_- state, which requires the rotation of spins in both dots, and is therefore not visible for $V_b = 100$ meV [see Fig. 3(b)]. In nonzero B the T_- energy level is too far on the energy scale to mix with the S state via the nuclear spins. For that reason the transition to the T_- state does not unblock the current flow²⁶ and therefore this line is missing in the experimental data^{7,8} of the frequencies lifting the spin blockade of the current.

Besides the direct Rabi transitions additional ones for lower frequencies are clearly visible in Fig. 3(b). Let us focus on a cross section of the map Fig. 3(b) obtained for $B = 20$ mT, presented in Fig. 4(a). The transition probability is plotted in Fig. 4(b). The three broad peaks (marked with E_s , E_{T_0} , and E_{T_-}) correspond to direct Rabi transitions. The narrow resonances observed for lower ω_{ac} correspond to fractions of the frequencies of the direct transitions. The transition probabilities depicted in Fig. 4(b) exhibit one-half and one-third (those are not fully saturated in the plot resolution, i.e., $\hbar\Delta\omega_{ac} = 50$ neV) $T_+ \rightarrow S$ transitions (black curve) and fractional $T_+ \rightarrow T_-$ transitions (blue curve). The

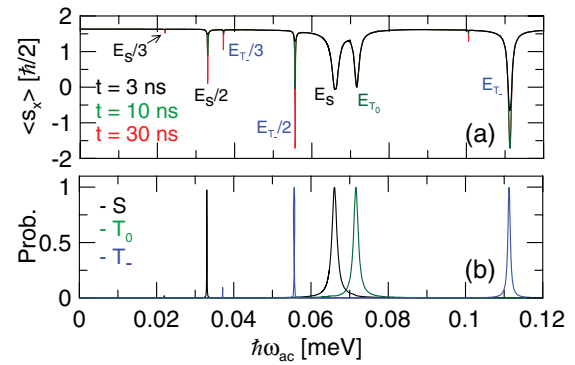


FIG. 4. (Color online) (a) Spin transitions obtained for $B = 20$ mT after 3 ns (black), 10 ns (green), and 30 ns (red) for $V_b = 17$ meV (the minimal x component of the spin acquired by the system subjected to the ac field with T_+ as the initial state). (b) Probability of transition to the S (black curves), T_0 (green curves), and T_- (blue curves) states after 30 ns.

fractional transition to the S state (for $\hbar\omega_{ac} = E_s/2$) is of particular importance as it lifts the spin blockade in the EDSR experiments, and this is the fractional resonant line that is visible in the experimental maps of Refs. 4, 7, and 8. The direct Rabi oscillations are rather slow²⁷ but the fractional ones are even slower. In Fig. 4(a) the transitions after 3, 10, and 30 ns are plotted. For 3 ns, the direct transitions are already fully resolved in contrast to the fractional ones. At the left upper corner of the map Fig. 3(b) one can observe an additional resonance line which is a fractional resonance to the fourth excited state.

Let us focus on the origin of the fractional transitions. First we consider the ac frequency $\hbar\omega_{ac}$ for which no transition occurs. The Fourier transform of the total momentum is presented in Figs. 5(b) and 5(c). We observe that when the electron is driven by an ac field its motion is periodic, consisting of (i) the driving frequency $\hbar\omega_{ac}$, (ii) its harmonics (marked with the red dashed lines in Fig. 5), and (iii) the resonant frequency corresponding to the direct $T_+ \rightarrow S$ transition (marked with the blue dashed line in Fig. 5). When the driving frequency is such that one of its harmonics matches the resonant one [Fig. 5(a)] its amplitude is greatly amplified and the system exhibits a resonant transition.

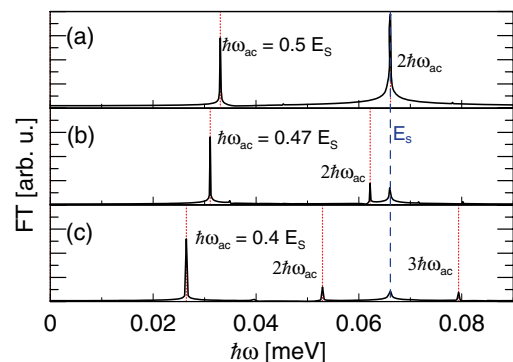


FIG. 5. (Color online) Fourier transform of the total momentum calculated for three different driving ac frequencies $\hbar\omega_{ac}$.

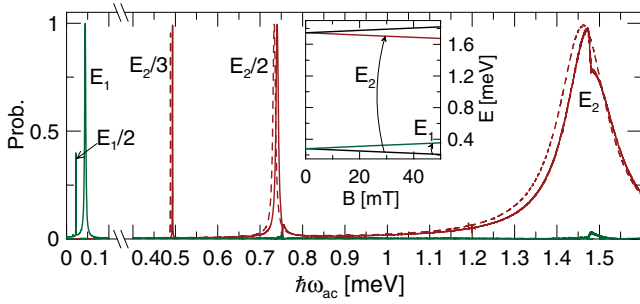


FIG. 6. (Color online) Transition probability to the first excited (green curve) and second excited (red curve) state after 10 ns for a one-electron single dot ($V_b = 0$) with (solid curves) SO coupling and without (dashed curve). The inset presents the single-electron energy spectrum with SO coupling included along with the direct Rabi transitions.

We find that there is a relation between the intensity of the fractional line in the transition maps and the probability of finding both electrons in the same dot in a given final state. In particular, for $V_b = 17$ meV the probabilities for subsequent states are S , 0.02, T_0 , 0.002, and T_- , 0.04. Both the transitions for $\hbar\omega_{ac} = E_s/2$ and $\hbar\omega_{ac} = E_{T_-}/2$ occur in $t \simeq 25$ ns with the half-width of the transition peak approximately 100 neV (the transition for $\hbar\omega_{ac} = E_{T_-}/3$ is as long as 200 ns with the half-width of the peak about 10 neV). The fractional transitions to T_0 are missing in Fig. 4 and we do not observe the generation of a residual frequency for $\hbar\omega = E_{T_0}$ in Fig. 5. In fact the fractional transition for $\hbar\omega_{ac} = E_{T_0}/2$ does occur but with a linewidth that is narrower than the plot resolution of 50 neV—the half-width of the peak is about 1 neV with the transition time more than $t = 1$ μ s. For nonzero double occupancy probability the electrons are at least partially driven over the entire double-dot area by the ac field and the generation of higher harmonics becomes effective. Consequently for $V_b = 100$ meV where the probabilities are as small as 10^{-4} no fractional transitions are observed.

The source of the fractional resonance observed in the experiments is the dynamics of a nonadiabatically driven electron system. In order to demonstrate that, let us reduce the problem to a single-electron one (we also lift the interdot barrier). The energy spectrum for such a system is presented in the inset to Fig. 6. The transition between the ground state and the first excited state is possible only through a spin rotation. The transition for $\hbar\omega_{ac} = E_2$ occurs between states of the same spin. In Fig. 6 we show the transition probabilities to the first and second excited states. We observe both the direct transitions and the fractional ones.

When we switch off the SO coupling the transition to the first excited state is blocked as the spin becomes decoupled from the electron motion. However, the transitions to the second excited state along with its fractional components are still present—see the red dashed curve in Fig. 6.

For completeness we present the case of weaker SO coupling—namely, we apply $\alpha = 25$ meV nm. The energy spectrum for strongly coupled dots (we chose $V_b = 27$ meV to obtain similar coupling strength between S and T_0 as previously, i.e., the exchange energy $J = 6.3$ μ eV) is presented in Fig. 7(a). For lower values of α one obtains a

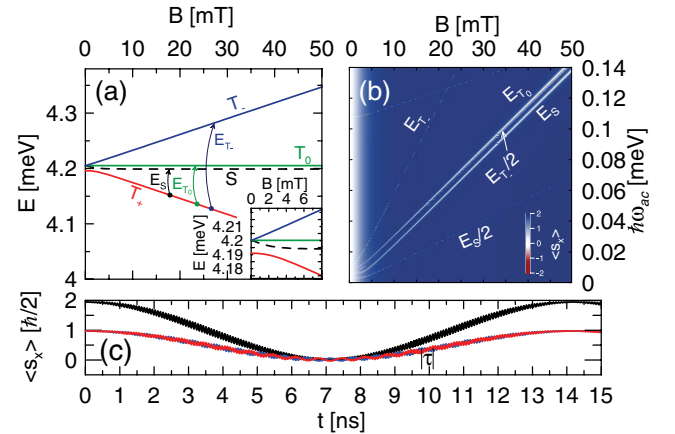


FIG. 7. (Color online) As Fig. 3 but for weaker SO coupling strength. The map in (b) is obtained after 60 ns.

singlet and a triplet energy level at $B = 0$ and the avoided crossing between the T_+ and S energy levels occurs at $B > 0$. Weaker SO interaction results also in a longer spin rotation time [see Fig. 7(c)] and now the $T_+ \rightarrow S$ transition occurs in 7 ns (compared to 2.7 ns in Fig. 3). The exchange-driven small-amplitude spin oscillations with $\tau = 328$ ps are visible in Fig. 7(c), along with fast oscillation due to spin precession. In the map of spin transitions Fig. 7(b), both the double central line and the half-frequency transitions to the S and T_- states appear. However, now the lines are narrower as compared to the case of stronger SO interaction (as the amplitude of the SO effective magnetic field that drives the spin transition is decreased). The half-frequency transitions occur in 54 ns (compared to 25 ns for $\alpha = 50$ meV nm). Otherwise the EDSR transition map remains qualitatively unchanged.

IV. CONCLUSIONS

In conclusion, we studied the electrically induced transitions between the electron states in quantum dots. We showed that the electron oscillations induced by an ac field are accompanied by residual harmonics of the driving frequency. We demonstrated that the fractional transitions observed in EDSR experiments involve resonant amplification of the harmonics in the electron dynamics when they match the Rabi transition frequency. Moreover, we indicated that the resonant amplification of higher harmonics is an intrinsic phenomenon of a driven electron system which occurs also for a single charge and without SO coupling.

In the two-electron system of the double dot when the ac field is applied to only one of the dots, a nonzero interdot tunnel coupling is necessary for the fractional transitions to appear as it triggers the motion of both electrons. A consequence of the nonzero exchange energy is the splitting of the main resonance line into T_0 and S final states. Thus the appearances of the double resonant line and the fractional resonance have a common origin.

ACKNOWLEDGMENTS

This work was supported by funds of the Ministry of Science and Higher Education (MNiSW) for 2012–2013 under

Project No. IP2011038671, and by PL-Grid Infrastructure. M.P.N. gratefully acknowledges support from the Foundation

for Polish Science (FNP) under START and MPD program cofinanced by the EU European Regional Development Fund.

-
- ¹D. Loss and D. P. DiVincenzo, *Phys. Rev. A* **57**, 120 (1998); G. Burkard, D. Loss, and D. P. DiVincenzo, *Phys. Rev. B* **59**, 2070 (1999); D. Awschalom, D. Loss, and N. Samarth, *Semiconductor Spintronics and Quantum Computation* (Springer-Verlag, Berlin, 2002); R. Hanson, L. P. Kouwenhoven, J. R. Petta, S. Tarucha, and L. M. K. Vandersypen, *Rev. Mod. Phys.* **79**, 1217 (2007).
- ²F. H. L. Koppens, C. Buizert, K. J. Tielrooij, I. T. Vink, K. C. Nowack, T. Meunier, L. P. Kouwenhoven, and L. M. K. Vandersypen, *Nature (London)* **442**, 766 (2006).
- ³K. C. Nowack, F. H. L. Koppens, Yu. V. Nazarov, and L. M. K. Vandersypen, *Science* **318**, 1430 (2007).
- ⁴E. A. Laird, C. Barthel, E. I. Rashba, C. M. Marcus, M. P. Hanson, and A. C. Gossard, *Phys. Rev. Lett.* **99**, 246601 (2007); *Semicond. Sci. Technol.* **24**, 064004 (2009).
- ⁵S. Nadj-Perge, S. M. Frolov, E. P. A. M. Bakkers, and L. P. Kouwenhoven, *Nature (London)* **468**, 1084 (2010).
- ⁶M. Pioro-Ladrière, T. Obata, Y. Tokura, Y.-S. Shin, T. Kubo, K. Yoshida, T. Taniyama, and S. Tarucha, *Nat. Phys.* **4**, 776 (2008); R. Brunner, Y.-S. Shin, T. Obata, M. Pioro-Ladrière, T. Kubo, K. Yoshida, T. Taniyama, Y. Tokura, and S. Tarucha, *Phys. Rev. Lett.* **107**, 146801 (2011).
- ⁷M. D. Schroer, K. D. Petersson, M. Jung, and J. R. Petta, *Phys. Rev. Lett.* **107**, 176811 (2011).
- ⁸S. Nadj-Perge, V. S. Pribiag, J. W. G. van den Berg, K. Zuo, S. R. Plissard, E. P. A. M. Bakkers, S. M. Frolov, and L. P. Kouwenhoven, *Phys. Rev. Lett.* **108**, 166801 (2012).
- ⁹Y. A. Bychkov and E. I. Rashba, *J. Phys. C* **17**, 6039 (1984).
- ¹⁰E. I. Rashba and A. L. Efros, *Phys. Rev. Lett.* **91**, 126405 (2003).
- ¹¹V. N. Golovach, M. Borhani, and D. Loss, *Phys. Rev. B* **74**, 165319 (2006).
- ¹²E. I. Rashba, *Phys. Rev. B* **84**, 241305(R) (2011).
- ¹³M. Awasthi, Y. V. Vanne, A. Saenz, A. Castro, and P. Decleva, *Phys. Rev. A* **77**, 063403 (2008).
- ¹⁴M. Abu-samha and L. B. Madsen, *Phys. Rev. A* **81**, 033416 (2010).
- ¹⁵M. F. Ciappina, J. Biegert, R. Quidant, and M. Lewenstein, *Phys. Rev. A* **85**, 033828 (2012).
- ¹⁶J. L. Krause, K. J. Schafer, and K. C. Kulander, *Phys. Rev. Lett.* **68**, 3535 (1992).
- ¹⁷K. J. Schafer and K. C. Kulander, *Phys. Rev. Lett.* **78**, 638 (1997).
- ¹⁸M. Lewenstein, P. Balcou, M. Y. Ivanov, A. L'Huillier, and P. B. Corkum, *Phys. Rev. A* **49**, 2117 (1994).
- ¹⁹S. Kim, J. Jin, Y.-J. Kim, I.-Y. Park, Y. Kim, and S.-W. Kim, *Nature (London)* **453**, 757 (2008).
- ²⁰Jon H. Shirley, *Phys. Rev.* **138**, B979 (1965).
- ²¹S. Bednarek, B. Szafran, T. Chwiej, and J. Adamowski, *Phys. Rev. B* **68**, 045328 (2003).
- ²²O. Voskoboynikov, C. P. Lee, and O. Tretyak, *Phys. Rev. B* **63**, 165306 (2001); C. F. Destefani, Sergio E. Ulloa, and G. E. Marques, *ibid.* **69**, 125302 (2004).
- ²³Note that in the presence of SO interaction the states do not have well-defined spin—we name them (S , T_+ , T_0 , T_-) after their character without SO interaction.
- ²⁴X. Hu and S. Das Sarma, *Phys. Rev. A* **61**, 062301 (2000); K. V. Kavokin, *Phys. Rev. B* **64**, 075305 (2001); A. Harju, S. Siljamäki, and R. M. Nieminen, *Phys. Rev. Lett.* **88**, 226804 (2002); K. V. Kavokin, *Phys. Rev. B* **69**, 075302 (2004); D. Stepanenko and N. E. Bonesteel, *Phys. Rev. Lett.* **93**, 140501 (2004); B. Szafran, F. M. Peeters, and S. Bednarek, *Phys. Rev. B* **70**, 205318 (2004).
- ²⁵M. P. Nowak and B. Szafran, *Phys. Rev. B* **82**, 165316 (2010).
- ²⁶F. H. L. Koppens, C. Buizert, I. T. Vink, K. C. Nowack, T. Meunier, L. P. Kouwenhoven, and L. M. K. Vandersypen, *J. Appl. Phys.* **101**, 081706 (2007).
- ²⁷D. V. Khomitsky, L. V. Gulyaev, and E. Ya. Sherman, *Phys. Rev. B* **85**, 125312 (2012).

10 Spin polarization anisotropy in a narrow spin-orbit-coupled nanowire quantum dot

Spin-polarization anisotropy in a narrow spin-orbit-coupled nanowire quantum dot

M. P. Nowak and B. Szafran

*AGH University of Science and Technology, Faculty of Physics and Applied Computer Science,
al. Mickiewicza 30, 30-059 Kraków, Poland*

(Received 29 October 2012; revised manuscript received 29 April 2013; published 24 May 2013)

One- and two-electron systems confined in single and coupled quantum dots defined within a nanowire with a finite radius are studied in the context of spin-orbit coupling effects. The anisotropy of the spin-orbit interaction is discussed in terms of the system geometry and orientation of the external magnetic field vector. We find that there are easy and hard spin-polarization axes, and in the quantum dot with strong lateral confinement electron spin becomes well defined in spite of the presence of spin-orbit coupling. We present an analytical solution for the one-dimensional limit and study its validity for nanowires of finite radii by comparing the results with a full three-dimensional calculation. The results are also compared with the recent measurements of the effective Landé factor and avoided crossing width anisotropy in InSb nanowire quantum dots [S. Nadj-Perge *et al.*, *Phys. Rev. Lett.* **108**, 166801 (2012)].

DOI: [10.1103/PhysRevB.87.205436](https://doi.org/10.1103/PhysRevB.87.205436)

PACS number(s): 73.21.La, 71.70.Gm

I. INTRODUCTION

There is a growing interest in gated semiconductor nanowires in the context of possible applications for spin-operating devices.¹⁻⁴ These structures provide a good basis for the creation of small electrostatic quantum dots with confinement introduced by external potentials. Energy spectra of such dots as determined⁵ by transport spectroscopy bear distinct signatures of strong spin-orbit (SO) interaction which results from the structure inversion asymmetry (Rashba SO coupling⁶) or the bulk inversion asymmetry (Dresselhaus SO interaction⁷). SO coupling mixes spin and orbital degrees of freedom, thus opening the possibility of fully electrical control of the electron spin.^{1-4,8,9} Moreover, SO coupling allows for electron spin relaxation mediated by phonons,^{10,11} and introduces anisotropic corrections to spin exchange interaction for electrons in double quantum dots.¹²

The SO coupling opens avoided crossings⁵ in the quantum dot energy spectra as a function of the external magnetic field (\mathbf{B}). The width of the avoided crossings between energy levels of different spin states depends on the orientation of the \mathbf{B} vector, which reveals the spatial anisotropy of the SO interaction.^{3,13-15} Moreover, the mixing of the spin states by SO coupling determines an effective Landé factor (g factor) and its anisotropy¹⁶ as a function of the magnetic field orientation. In nanowire quantum dots the effective g -factor was recently measured in electric dipole spin resonance (EDSR) experiments^{2,3} for a two-electron spin-blocked configuration or by magnetotransport measurements on electron¹⁷ and hole¹⁸ quantum dots. The anisotropy of SO interaction is a relevant issue for spin qubit manipulation¹ as well as for helical spin liquids¹⁹ which in the proximity of a superconductor can be used for observation of Majorana fermions.²⁰

It is well known that in the presence of SO coupling, the electron spin can be well defined in the stationary eigenstates only for equal Rashba and Dresselhaus SO coupling constants.²¹ This fact was exploited in a proposal of a nonballistic spin field effect transistor²¹ and for the prediction²² of a persistent spin helix.²³ In the present work, we demonstrate that in the limit of strong lateral confinement, the electron spins confined in the quantum dot become well

defined in the direction perpendicular to the wire axis and the external electric field vector in spite of the presence of the Rashba coupling. We show that in a general case, the extent of the electron spin polarization strongly depends on the orientation of \mathbf{B} reflecting the anisotropy of SO interaction.

For a description of narrow nanowires, a one-dimensional model is commonly used.²⁴ In this work, we present an analytical form of eigenstates for this approximation for a quantum dot defined in a nanowire. The analytical form of the SO-coupled wave functions accounts for the anisotropic spin polarization and explains the different strengths of the spin-splittings for varied orientation of the magnetic field. We study the applicability of the one-dimensional model for a nanowire with a finite radius by comparing its results with the three-dimensional calculation for various geometries of the nanowire quantum dot. To relate the model results to the experimental measurements, we study coupled two-electron quantum dots, i.e., the configuration that is used for EDSR and the spin exchange experiments. The obtained shape of the g factor and the avoided crossing width dependence on magnetic field orientation resemble the findings of the experiment of Ref. 3 on InSb nanowire quantum dots.

II. THEORY

We consider a single-electron quantum dot defined in a narrow nanowire described by the three-dimensional Hamiltonian

$$h = \frac{\hbar^2 \mathbf{k}^2}{2m^*} + V(\mathbf{r}) + H_{\text{SO}} + \frac{1}{2} g \mu_B \mathbf{B} \cdot \boldsymbol{\sigma}, \quad (1)$$

where $\mathbf{k} = -i\nabla + e\mathbf{A}/\hbar$ with the gauge $\mathbf{A} = B(z \sin \phi, 0, y \cos \phi)$. The magnetic field is aligned in the xy plane with an angle ϕ between \mathbf{B} and the x axis—in such a case, the Zeeman term stands for $\frac{1}{2} g \mu_B \mathbf{B} \cdot \boldsymbol{\sigma} = \frac{1}{2} \mu_B g B (\sigma_x \cos \phi + \sigma_y \sin \phi)$, $V(\mathbf{r})$ stands for the confinement potential which we take in a separable form $V(\mathbf{r}) = V_l(y, z) + V_L(x) + |e|\mathbf{F} \cdot \mathbf{r}$, where $V_l(y, z)$ is a 400-meV-deep two-dimensional circular quantum well of radius R , $V_L(x)$ is an infinite quantum well with width L (see Fig. 1), and \mathbf{F} stands for the external electric field. We account

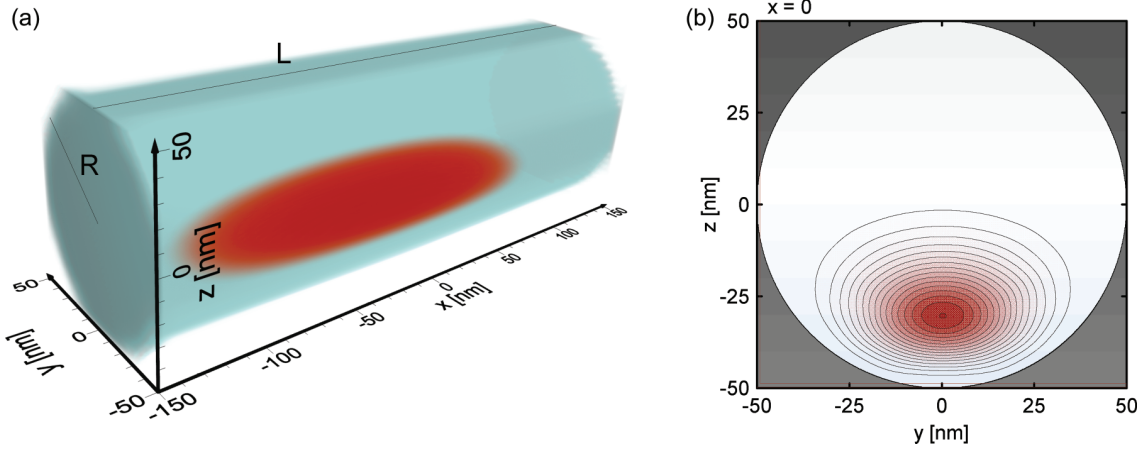


FIG. 1. (Color online) (a) Sketch of the confinement potential $V(\mathbf{r})$ of the nanowire quantum dot (with blue) and the single-electron charge density (with red) calculated for $F_z = 10$ kV/cm. (b) Cross section of the confinement potential and the charge density for $x = 0$.

for Rashba SO coupling $H_{SO} = \alpha_0 \frac{\partial V}{\partial r} \cdot (\boldsymbol{\sigma} \times \mathbf{k})$ as the main SO interaction type in the [111] grown InSb nanowires.³ Unless stated otherwise, we assume the electric field $\mathbf{F} = (0, 0, F_z)$ with a nonzero component in the z direction (perpendicular to the axis of the wire) due to the gating of the nanowire.¹⁻⁴ We assumed a hard-wall confinement potential of the wire. The electron wave function vanishes at the edge of a circular quantum well $V_l(y, z)$ [see Fig. 1(b)]. Therefore, the only part of the potential whose gradient overlaps with the wave function and thus gives rise to the SO coupling is the external electric potential, i.e., $H_{SO} = \alpha(\sigma_x k_y - \sigma_y k_x)$, where $\alpha = \alpha_0 F_z$.

To solve the Schrödinger equation, we rewrite the Hamiltonian Eq. (1) as $h = h_x + h_y + h_z + h_{ns}$, where

$$h_x = -\frac{\hbar^2}{2m^*} \frac{\partial^2}{\partial x^2} + V_L(x), \quad (2)$$

$$h_y = -\frac{\hbar^2}{2m^*} \frac{\partial^2}{\partial y^2} + V_B(y) + \frac{e^2 B^2}{2m^*} y^2 \cos^2 \phi, \quad (3)$$

$$h_z = -\frac{\hbar^2}{2m^*} \frac{\partial^2}{\partial z^2} + V_B(z) + \frac{e^2 B^2}{2m^*} z^2 \sin^2 \phi + |e| F_z z, \quad (4)$$

are separable in the x -, y -, and z -direction spin-independent parts. The infinite quantum wells $V_B(y)$ and $V_B(z)$ of width $2R$ define the computational box, and

$$h_{ns} = -\frac{i\hbar e B}{m^*} \left(z \sin \phi \frac{\partial}{\partial x} + y \cos \phi \frac{\partial}{\partial z} \right) + \frac{1}{2} g \mu_b B [\sigma_x \cos \phi + \sigma_y \sin \phi] + H_{SO} + V_l(y, z) \quad (5)$$

is the nonseparable part that contains the spin dependency and the potential of the cylindrical quantum well $V_l(y, z)$.

The calculation procedure proceeds as follows. We calculate eigenvectors of h_x , h_y , and h_z on meshes containing 1000 points and use them for construction of a basis (which consists of 8192 elements) in which the h Hamiltonian is diagonalized. As a result, we obtain three-dimensional spin orbitals $\psi(\mathbf{r}, \sigma)$. Note that introducing the infinite quantum wells V_B in the first step fixes the basis for the diagonalization of the complete Hamiltonian.

The solutions of the two-electron system described by the Hamiltonian

$$H = h_1 + h_2 + \frac{e^2}{4\pi \epsilon_0 \epsilon |\mathbf{r}_1 - \mathbf{r}_2|} \quad (6)$$

are found in the basis constructed from products of antisymmetrized single-electron spin orbitals $\psi(\mathbf{r}, \sigma)$,

$$\Psi(\mathbf{r}_1, \sigma_1, \mathbf{r}_2, \sigma_2) = \frac{1}{\sqrt{2}} \sum_{i=1}^M \sum_{j=i+1}^M c_{ij} [\psi_i(\mathbf{r}_1, \sigma_1) \psi_j(\mathbf{r}_2, \sigma_2) - \psi_i(\mathbf{r}_2, \sigma_2) \psi_j(\mathbf{r}_1, \sigma_1)], \quad (7)$$

where the coefficients c_{ij} are found by diagonalization of Hamiltonian Eq. (6) according to the configuration interaction method with $M = 20$. The scheme treats the Coulomb interaction in an exact manner. For the calculation of the Coulomb matrix elements, we use the two-step method that replaces six-dimensional integrations by calculation of the Poisson equation for the potential generated from single-electron wave functions and integrate it with the product of the wave function of the other electron.¹⁴

We adopt material parameters²⁶ for InSb, namely $m^* = 0.014m_0$, $g = -51$, $\epsilon = 16.5$, and $\alpha_0 = 5$ nm². In the bulk of the paper, we choose $F_z = 50$ kV/cm, which results in a SO interaction constant $\alpha = 25$ meV nm. Unless stated otherwise, we take $L = 300$ nm.

III. RESULTS

A. Single electron in a finite thickness nanowire quantum dot

The lowest part of the energy spectrum of the single-electron quantum dot is presented in Fig. 2. In the absence of the magnetic field, all the levels are Kramer's doublets. We include the residual magnetic field $B = 5$ mT and inspect the spin polarization along the magnetic field direction [calculated as $\langle s_B \rangle = \langle s_x \rangle \cos(\phi) + \langle s_y \rangle \sin(\phi)$]. In Fig. 3(a), we observe that the spin polarization undergoes oscillatory changes as a function of \mathbf{B} orientation. This reflects the presence of easy and hard spin-polarization axes in the system. For the magnetic field oriented perpendicular to the nanowire axis, the spin

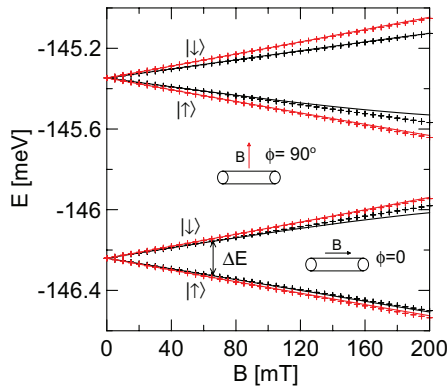


FIG. 2. (Color online) Single-electron energy spectrum for the SO coupled nanowire quantum dot with radius $R = 50$ nm and SO interaction constant $\alpha = 25$ meV nm plotted with lines for two orientations of the magnetic field. The crosses are the results obtained from the asymptotic one-dimensional solution—see the text. With $|\uparrow\rangle$ and $|\downarrow\rangle$ we mark the spin polarization of the states parallel and antiparallel to the magnetic field, respectively, as found without SO coupling.

is easily polarized—taking values close to $1 [\hbar/2]$. On the other hand, for \mathbf{B} oriented along the wire, the $\langle s_B \rangle$ is around $0.885 [\hbar/2]$. The amplitude of the oscillations depends on the nanowire radius [compare the curves in Fig. 3(a) for three values of R] and the oscillations are the strongest for a narrow

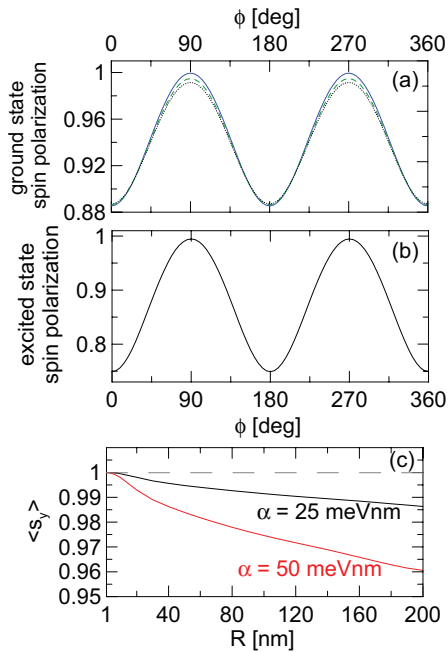


FIG. 3. (Color online) (a) Mean value of the spin along the magnetic field direction obtained for the ground state of the nanowire quantum dot with radius $R = 10$ nm (blue solid curve), $R = 50$ nm (green dashed curve), and $R = 100$ nm (black dotted curve). (b) Spin polarization of the second excited state for $R = 50$ nm. (c) Mean value of the spin- y component for the magnetic field aligned along the y direction as a function of the nanowire radius R . (a)–(c) are obtained for $B = 5$ mT. Results for $\alpha = 50$ meV nm correspond to $F_z = 100$ kV/cm.

nanowire with $R = 10$ nm. The spin polarization of the excited state is presented in Fig. 3(b). We observe that the amplitude of the oscillation is stronger than the one obtained for the ground state, but the spin polarization for $\phi = 90^\circ$ is again close to $1 [\hbar/2]$.

Let us inspect the degree of the maximal spin polarization at the easy axis $\phi = 90^\circ$. In Fig. 3(c), we plot the mean value of the spin- y component of the ground state versus the wire radius R . We observe that as the wire becomes narrower, the spin polarization becomes almost complete (i.e., $1 - \langle s_y \rangle 2/\hbar < 10^{-4}$ for $R = 1$ nm) despite the presence of the SO coupling. The existence of directions in which the spin can be exactly polarized should facilitate the qubit initialization and increase the spin coherence times. On the other hand, as the wire becomes wider, the spin polarization drops with the slope of the curves in Fig. 3(c) depending on the SO coupling constant α . Note that the extent of the wave function in the z direction is limited also by the applied electric field.

When the magnetic field is increased, it splits the doublets—see the energy levels in Fig. 2. The energy splittings obtained for the magnetic field perpendicular to the nanowire axis (red curves in Fig. 2) are stronger than those obtained for the magnetic field parallel to the nanowire axis (black curves in Fig. 2). In the following, we explain this observation.

B. Asymptotic solution (1D limit)

When the wire becomes narrow the energy of the states excited in the radial direction rises. It is reasonable then to inspect the case in which the radial degrees of freedom are decoupled from the longitudinal one (the x direction). Such a system is described by the one-dimensional (1D) Hamiltonian,^{24,25}

$$h_{1D} = \frac{\hbar^2 k_x^2}{2m^*} + V_L(x) - \alpha \sigma_y k_x + \frac{1}{2} \mu_B g B (\sigma_x \cos \phi + \sigma_y \sin \phi), \quad (8)$$

where $k_x = -i \frac{\partial}{\partial x}$.

Generally, the analytical solution for a SO coupled confined system are not known, with the exception of a special case of equal strength of Rashba and Dresselhaus coupling described in Ref. 21. Here we note, however, that in the absence of the magnetic field ($B = 0$) the Hamiltonian (8) commutes with the spin- y Pauli matrix and its eigenstates have definite y component of the spin. We find that for a quasi-one-dimensional nanowire, the spin orbitals (where N stands for the orbital quantum number and \pm denotes the spin polarization of the state) have the form

$$\Psi_{N\pm} = \frac{1}{\sqrt{2}} \begin{pmatrix} 1 \\ \pm i \end{pmatrix} \varphi_N(x) \exp \left[\pm \frac{i\alpha m^*}{\hbar^2} x \right], \quad (9)$$

where $\varphi_N(x)$ are spin-independent eigenstates of Hamiltonian (8) for $\alpha = 0$ and $B = 0$. The eigenenergies of the Hamiltonian (8) are $E_{1D} = E_{\alpha=0,N} + E_{SO}$, where $E_{SO} = -\alpha^2 m^* / (2\hbar^2)$ is the energy shift to the whole energy spectrum introduced by the SO interaction²⁷ and $E_{\alpha=0,N}$ is an energy level of the N th eigenstate obtained without SO coupling.

The magnetic field affects the energy levels of a strongly confined electron mainly through the Zeeman spin-splitting.

To investigate its influence on the SO eigenstates with an orbital excitation N , let us diagonalize h_{1D} for $B > 0$ in a basis consisting of a degenerate pair Ψ_{N+} and Ψ_{N-} . The Hamiltonian matrix is

$$\begin{pmatrix} \langle \Psi_{N+} | h_{1D} | \Psi_{N+} \rangle & \langle \Psi_{N-} | h_{1D} | \Psi_{N+} \rangle \\ \langle \Psi_{N+} | h_{1D} | \Psi_{N-} \rangle & \langle \Psi_{N-} | h_{1D} | \Psi_{N-} \rangle \end{pmatrix}, \quad (10)$$

where the diagonal elements are defined as follows:

$$\langle \Psi_{N\pm} | h_{1D} | \Psi_{N\pm} \rangle = E_{1D} \pm \frac{1}{2} g \mu_B B \sin \phi, \quad (11)$$

while the off-diagonal elements are

$$\begin{aligned} & \langle \Psi_{N\pm} | h_{1D} | \Psi_{N\mp} \rangle \\ &= \mp i \frac{1}{2} g \mu_B B \int |\varphi_N|^2 \left[\cos \left(\frac{2\alpha m^*}{\hbar^2} x \right) \mp i \sin \left(\frac{2\alpha m^*}{\hbar^2} x \right) \right] \\ & \quad \times dx \cos \phi. \end{aligned} \quad (12)$$

Let us denote $\lambda_N \equiv \int |\varphi_N|^2 \cos(\frac{2\alpha m^*}{\hbar^2} x) dx$ and $\kappa_N \equiv i \int |\varphi_N|^2 \sin(\frac{2\alpha m^*}{\hbar^2} x) dx$.

The eigenstates of the matrix (10) are

$$E_{N\pm} = E_{1D} \pm \frac{1}{2} g \mu_B B \sqrt{1 - (1 - \lambda_N^2 + \kappa_N^2) \cos^2 \phi}. \quad (13)$$

The energy difference between the states depends on the orientation of the magnetic field (angle ϕ) as well as the parameters λ_N and κ_N that control the strength of the anisotropy of the spin splittings for the rotated magnetic field. For the symmetric infinite quantum-well confinement along the wire (x direction), we obtain²⁹

$$\lambda_1 = \frac{\hbar^6 \pi^2 \sin(L\alpha m^*/\hbar^2)}{\alpha m^* L (\pi^2 \hbar^4 - \alpha^2 m^{*2} L^2)} \quad (14)$$

and

$$\lambda_2 = \frac{4\hbar^6 \pi^2 \sin(L\alpha m^*/\hbar^2)}{\alpha m^* L (4\pi^2 \hbar^4 - \alpha^2 m^{*2} L^2)} \quad (15)$$

and $\kappa_1 = \kappa_2 = 0$ for the two lowest orbital states. The λ_N depends on the quantum dot length and the SO strength. In Fig. 4, we present the λ_1 parameter as a function of L and α .

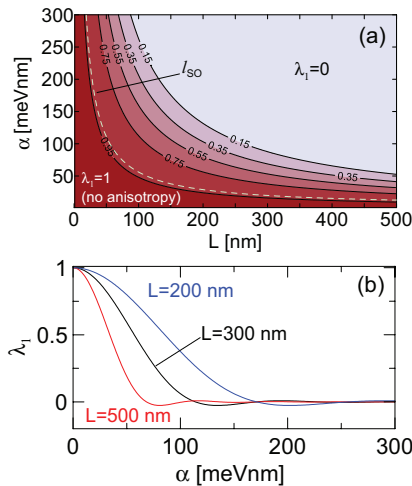


FIG. 4. (Color online) Parameter λ_1 as a function of the dot length L and SO coupling constant α . (b) Cross section of (a) for three different dot lengths L .

With the light-green dashed curve, we depict the SO length $l_{SO} = \hbar/(m^*\alpha)$. We observe that λ_1 drops quickly when the length of the dot becomes greater than the SO length. The shape of the λ_1 dependence on the SO strength for different quantum dot lengths is presented in Fig. 4(b), showing that the SO effects depend strongly on the quantum dot geometry and that λ_1 goes to 1 for vanishing SO coupling.

The smaller λ_N is, the stronger the SO coupling effects are. In particular, for the magnetic field parallel to the nanowire axis, the energy of the spin splitting is $E_S = g \mu_B B \lambda_N$. Consequently, the splitting can even go to 0 due to strong mixing of the spin states by the SO interaction [the light blue region in Fig. 4(a)].

When the magnetic field is aligned in the direction perpendicular to the nanowire axis, i.e., $\phi = 90^\circ$ or 270° , the off-diagonal elements of the matrix (10) vanish and the energy levels are split by Zeeman energy with the bulk value of the g factor. This is the reason for stronger spin splittings of the red curves in Fig. 2. For this configuration, the spin orbitals are separable into spin and orbital parts despite the presence of SO interaction and they have the exact form of Eq. (9). For any other orientation of the magnetic field, the off-diagonal elements mix the eigenstates (9). This results in decreasing the spin splittings by the SO interaction by an amount that depends on λ_N and κ_N parameters—the spatial extent of the wave function along the nanowire and the strength of the SO coupling. Moreover, the electron spin is no longer well defined as the electrons spin and orbital degrees of freedom are entangled.

We plot the energy spectrum obtained from Eq. (13) (shifted to match the energies obtained in the three-dimensional calculation at $B = 0$) with the crosses in Fig. 2. The spin splitting obtained from the one-dimensional model well describes the results of the three-dimensional calculation. The only discrepancy is visible for the energy levels of the first and the second excited states for $B > 100$ mT, which is due to mixing of these two states by the SO interaction.

As the magnetic field is rotated between the easy and hard axes, the spin polarization of the states changes, which results in changes of the spin-splitting strength. The latter term in Eq. (13) introduces Zeeman energy splitting between the energy levels of the two states. We can see that

$$g_N^* = g \sqrt{1 - (1 - \lambda_N^2 + \kappa_N^2) \cos^2 \phi} \quad (16)$$

is an effective g factor that is dependent on the orientation of the magnetic field with the angle ϕ . With the crosses in Fig. 5(a) we plot the effective g factor as obtained from Eq. (16) along with the values obtained in the three-dimensional calculation (calculated as $g^* = \Delta E/\mu_B B$, where ΔE is the energy difference between the energy of the first excited state and the ground state—see Fig. 2) for different nanowire radii. For the nanowire radius $R = 10$ nm, the analytical solution and the result of the three-dimensional calculation match. For larger values of R , the shapes of the dependences comply, only the amplitude is different, with the biggest discrepancy being for the wide nanowire with $R = 100$ nm. The effective g -factor dependence obtained from the two excited states as calculated from Eq. (16) is plotted in Fig. 5(a) with circles. We observe

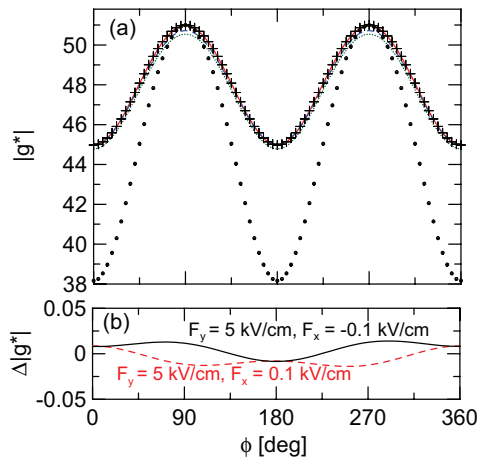


FIG. 5. (Color online) (a) Effective g factor obtained for a nanowire quantum dot with $R = 10$ nm (red solid curve), $R = 50$ nm (blue dashed curve), and $R = 100$ nm (green dotted curve) obtained for $B = 100$ mT. The symbols presents results obtained from Eq. (16) for the two lowest energy states $N = 1$ (black crosses) and for the second and third excited states $N = 2$ (black circles). (b) Difference between the g factor calculated for $F_x = F_y = 0$, $F_z = 50$ kV/cm, and calculated in the presence of the electric fields in the x and y directions as marked in the figure.

that due to the increased value of λ_2 , the amplitude of the oscillation is greatly increased.

C. Additional SO terms

Additional external electric fields in the device that results from, e.g., a source and drain voltage difference or from gating of the nanowire, can activate additional terms of the Rashba Hamiltonian, which takes the general form

$$H_{\text{SO}} = \alpha_0 [F_x(\sigma_y k_z - \sigma_z k_y) + F_y(\sigma_z k_x - \sigma_x k_z) + F_z(\sigma_x k_y - \sigma_y k_x)]. \quad (17)$$

We inspect the influence of these additional terms on the anisotropic g factor including in addition to $F_z = 50$ kV/cm the electric field in the x direction (resulting from the bias voltage) and assuming the electric field in the y direction $F_y = 5$ kV/cm. Figure 5(b) presents the difference between results obtained with additional fields F_x, F_y and results obtained for only F_z present. Only slight differences are observed with the highest magnitude at the easy axes, i.e., $\phi = 90^\circ$ and 270° .

D. Two-electron results

The experimentally probed anisotropy of the g factor is extracted from the slopes of resonance lines in EDSR experiments on double quantum dots in the two-electron regime.^{2,3} Figure 6(a) presents the two-electron energy spectrum of weakly coupled quantum dots defined in a nanowire with radius $R = 30$ nm obtained in the three-dimensional calculation. Results for the magnetic field oriented along the nanowire axis with $\phi = 0^\circ$ (perpendicular to the nanowire with $\phi = 90^\circ$) are plotted with solid (dotted) curves. The confinement potential includes now a potential barrier of 60 nm width that separates the electrons in adjacent dots both of

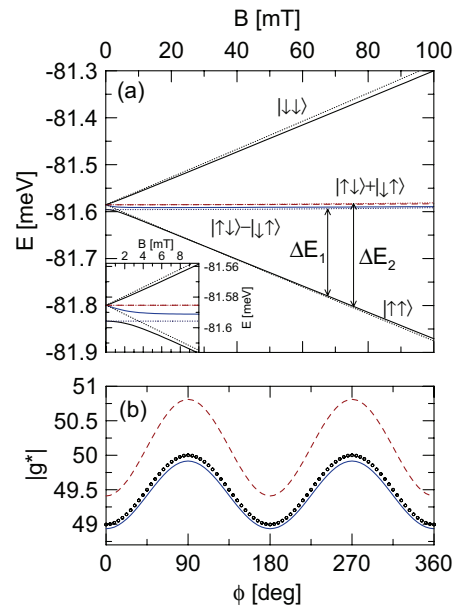


FIG. 6. (Color online) (a) Two-electron energy spectrum of coupled nanowire quantum dots with radius $R = 30$ nm. Solid curves present results for $\phi = 0^\circ$ and dotted curves for $\phi = 90^\circ$. With $|\uparrow\uparrow\rangle$, $|\downarrow\downarrow\rangle$, $|\downarrow\uparrow\rangle$, $|\uparrow\downarrow\rangle - |\downarrow\uparrow\rangle$, and $|\uparrow\downarrow\rangle + |\downarrow\uparrow\rangle$, we mark the spin configuration of the states parallel or antiparallel to the magnetic field as found without SO coupling. The inset presents the energy levels for low values of the magnetic field where the avoided crossing appears. (b) With the curves, the effective g factor is calculated from the energy splittings between the ground-state energy level and the energy levels depicted with blue solid (ΔE_1) and red dashed (ΔE_2) curves in (a) for $B = 200$ mT. The circles correspond to the effective one-electron g factor as obtained from Eq. (16) (shifted down by 1) for a single quantum dot with length $L = 120$ nm.

120 nm width. At $B = 0$, the ground state is a spin singlet ($|\uparrow\downarrow\rangle - |\downarrow\uparrow\rangle$) energy split from the degenerate triplet states [see the inset to Fig. 6(a)]. We tune the barrier height to 5 meV to match the singlet-triplet separation of $\simeq 5 \mu\text{eV}$ as measured in Ref. 3.

At $B = 3$ mT, an avoided crossing between the two lowest energy levels appears for $\phi = 0^\circ$ due to spin mixing by the SO interaction. The width of the anticrossing is $\Delta E \simeq 8.2 \mu\text{eV}$, which is similar to the value measured in Ref. 3, i.e., $\simeq 5 \mu\text{eV}$. The experiment performed in Ref. 3 established that the anticrossing vanished for $\phi = 90^\circ$ and 270° , which is also the case in the present results—the anticrossing vanishes when the magnetic field orientation is parallel to the easy axes of the spin polarization.

After the anticrossing, the magnetic field splits the energy levels of the two spin-polarized triplet states ($|\uparrow\uparrow\rangle$ and $|\downarrow\downarrow\rangle$) by the Zeeman energy. The blue solid and red dashed curves in Fig. 6(a) whose energy does not change (after the anticrossing) with B are the singlet ($|\uparrow\downarrow\rangle - |\downarrow\uparrow\rangle$) and triplet ($|\uparrow\downarrow\rangle + |\downarrow\uparrow\rangle$) states with zero spin component in the direction along the magnetic field. Those levels are split by exchange interaction²⁵ (additional splitting of those two energy levels occurs when the g factor along the structure is not constant²⁻⁴).

The magnetic-field orientation (angle ϕ) (i) influences the strength of the spin polarization of the triplet states $|\uparrow\uparrow\rangle, |\downarrow\downarrow\rangle$ which results in a change of the slope of the corresponding energy levels, and (ii) changes in the exchange energy (spacing between energy levels of $|\uparrow\downarrow\rangle - |\downarrow\uparrow\rangle$ and $|\uparrow\downarrow\rangle + |\downarrow\uparrow\rangle$ states, plotted with blue solid and red dashed curves in Fig. 6(a). These two effects lead to a dependence of the effective g factor on ϕ which we calculate from the energy splittings between the ground state and the first and second excited states and plot in Fig. 6(b) with the blue solid and red dashed curves, respectively. We find that the shape of both curves in Fig. 6(b) matches the shape of the single-electron dependence presented in Fig. 5; only the amplitude of the oscillations is lower. As described by Eq. (16) for the single-electron case, the amplitude of g -factor oscillations depends on the dot length. In the present case, each of the coupled quantum dots has a length of $L = 120$ nm. The effective g factor obtained for a *single* dot of this length as calculated from Eq. (16) is plotted with circles in Fig. 6(b). Obtained oscillations have a similar amplitude to that obtained for the two-electron system. This suggests that the low amplitude in the two-electron case results from the fact that each electron resides in a separate dot and the shape of the oscillations is controlled mainly by the single-electron spin-polarization anisotropy process described previously.

The shape of the g -factor dependence is similar to the one obtained in the experiment performed in Ref. 3. In particular, an agreement is obtained in the context of the slight change of the oscillation amplitude of the red dashed and blue solid curves in Fig. 6(b). This difference in amplitudes is due to a modification of the exchange energy that separates the energy levels of the singlet ($|\uparrow\downarrow\rangle - |\downarrow\uparrow\rangle$) and triplet ($|\uparrow\downarrow\rangle + |\downarrow\uparrow\rangle$) states by the rotated magnetic field. However, the experimental dependence of the effective g factor is shifted (with minima at $\phi = 124^\circ$ and 304°) with respect to the present result. We performed calculations for quantum dots in a nanowire of larger radius ($R = 100$ nm) ruling out the possible orbital effects of the magnetic field as a reason for the shift. Also the additional terms of Rashba coupling operator are not responsible for such a shift, as discussed in Sec. III C. On

the other hand, the g factor in quantum dots is affected by the local strain and asymmetries in the structure³⁰ which can influence the g factor as a concurrent process to the anisotropic spin polarization.

IV. SUMMARY AND CONCLUSIONS

In the present work, we studied the anisotropy of spin polarization in a narrow nanowire quantum dot in the presence of SO coupling. Solving the three-dimensional Schrödinger equation, we showed that the strength of spin polarization in the presence of Rashba SO interaction depends on the orientation of the magnetic field, and that there are hard and easy spin polarization axes. We explained the existence of these axes by the intrinsic tendency of SO coupling to polarize spins in the direction perpendicular to the nanowire. For the magnetic field aligned in this direction, the electron spin polarization can be nearly complete depending on the nanowire radius. We presented an analytical solution for the one-dimensional limit in which spin polarization can be complete, and we compared its results with the calculation for a finite thickness nanowire. Spin-polarization anisotropy results in an effective g -factor dependence on the magnetic-field orientation which is stronger for the excited states. The anisotropy of single-electron spin polarization results in changes of the avoided crossing width in the lowest part of the two-electron energy spectra. The magnitude and position of the extrema of this dependence match those found in the experiment. Also, the form of the g -factor dependence resembles that obtained in the experimental studies.

ACKNOWLEDGMENTS

This work was supported by funds from the Ministry of Science and Higher Education (MNiSW) for 2012–2013 under Project No. IP2011038671, and by PL-Grid Infrastructure. M.P.N. is supported by the Foundation for Polish Science (FNP) scholarship under START and the MPD Programme cofinanced by the EU European Regional Development Fund.

¹S. Nadj-Perge, S. M. Frolov, E. P. A. M. Bakkers, and L. P. Kouwenhoven, *Nature (London)* **468**, 1084 (2010).

²M. D. Schroer, K. D. Petersson, M. Jung, and J. R. Petta, *Phys. Rev. Lett.* **107**, 176811 (2011).

³S. Nadj-Perge, V. S. Pribiag, J. W. G. van den Berg, K. Zuo, S. R. Plissard, E. P. A. M. Bakkers, S. M. Frolov, and L. P. Kouwenhoven, *Phys. Rev. Lett.* **108**, 166801 (2012).

⁴S. M. Frolov, J. Danon, S. Nadj-Perge, K. Zuo, J. W. W. van Tilburg, V. S. Pribiag, J. W. G. van den Berg, E. P. A. M. Bakkers, and L. P. Kouwenhoven, *Phys. Rev. Lett.* **109**, 236805 (2012).

⁵C. Fauth, A. Fuhrer, L. Samuelson, V. N. Golovach, and D. Loss, *Phys. Rev. Lett.* **98**, 266801 (2007); A. Pfund, I. Shorubalko, K. Ensslin, and R. Leturcq, *Phys. Rev. B* **76**, 161308(R) (2007).

⁶Y. A. Bychkov and E. I. Rashba, *J. Phys. C* **17**, 6039 (1984).

⁷G. Dresselhaus, *Phys. Rev.* **100**, 580 (1955).

⁸K. C. Nowack, F. H. L. Koppens, Yu. V. Nazarov and L. M. K. Vandersypen, *Science* **318**, 1430 (2007).

⁹S. Datta and B. Das, *Appl. Phys. Lett.* **56**, 665 (1990).

¹⁰A. V. Khaetskii and Y. V. Nazarov, *Phys. Rev. B* **61**, 12639 (2000); V. N. Golovach, A. Khaetskii, and D. Loss, *Phys. Rev. Lett.* **93**, 016601 (2004); M. Florescu and P. Hawrylak, *Phys. Rev. B* **73**, 045304 (2006); S. Amasha, K. MacLean, Iuliana P. Radu, D. M. Zumbühl, M. A. Kastner, M. P. Hanson, and A. C. Gossard, *Phys. Rev. Lett.* **100**, 046803 (2008).

¹¹Y. Yin, *Semicond. Sci. Technol.* **25**, 125004 (2010); M. Wang, Y. Yin, and M. W. Wu, *J. Appl. Phys.* **109**, 103713 (2011).

¹²K. V. Kavokin, *Phys. Rev. B* **64**, 075305 (2001); S. C. Badescu, Y. B. Lyanda-Geller, and T. L. Reinecke, *ibid.* **72**, 161304(R) (2005); S. Gangadharaiyah, J. Sun, and O. A. Starykh, *Phys. Rev. Lett.* **100**, 156402 (2008).

¹³S. Takahashi, R. S. Deacon, K. Yoshida, A. Oiwa, K. Shibata, K. Hirakawa, Y. Tokura, and S. Tarucha, *Phys. Rev. Lett.* **104**, 246801 (2010).

- ¹⁴M. P. Nowak, B. Szafran, F. M. Peeters, B. Partoens, and W. J. Pasek, *Phys. Rev. B* **83**, 245324 (2011).
- ¹⁵M. P. Nowak and B. Szafran, *Phys. Rev. B* **83**, 035315 (2011).
- ¹⁶R. S. Deacon, Y. Kanai, S. Takahashi, A. Oiwa, K. Yoshida, K. Shibata, K. Hirakawa, Y. Tokura, and S. Tarucha, *Phys. Rev. B* **84**, 041302(R) (2011).
- ¹⁷H. A. Nilsson, P. Caroff, C. Thelander, M. Larsson, J. B. Wagner, L. E. Wernersson, L. Samuelson, and H. Q. Xu, *Nano Lett.* **9**, 3151 (2009).
- ¹⁸S. Roddaro, A. Fuhrer, P. Brusheim, C. Fasth, H. Q. Xu, L. Samuelson, J. Xiang, and C. M. Lieber, *Phys. Rev. Lett.* **101**, 186802 (2008).
- ¹⁹C. H. L. Quay, T. L. Hughes, J. A. Sulpizio, L. N. Pfeiffer, K. W. Baldwin, K. W. West, D. Goldhaber-Gordon, and R. de Picciotto, *Nat. Phys.* **6**, 336 (2010).
- ²⁰V. Mourik, K. Zuo, S. M. Frolov, S. R. Plissard, E. P. A. M. Bakkers, and L. P. Kouwenhoven, *Science* **336**, 1003 (2012).
- ²¹J. Schliemann, J. C. Egues, and D. Loss, *Phys. Rev. Lett.* **90**, 146801 (2003).
- ²²B. A. Bernevig, J. Orenstein, and S.-C. Zhang, *Phys. Rev. Lett.* **97**, 236601 (2006).
- ²³J. D. Koralek, C. P. Weber, J. Orenstein, B. A. Bernevig, S.-C. Zhang, S. Mack and D. D. Awschalom, *Nature (London)* **458**, 610 (2009).
- ²⁴Y. V. Pershin, J. A. Nesteroff, and V. Privman, *Phys. Rev. B* **69**, 121306(R) (2004); C. Flindt, A. S. Sorensen, and K. Flensberg, *Phys. Rev. Lett.* **97**, 240501 (2006); *J. Phys.: Conf. Ser.* **61**, 302 (2007).
- ²⁵M. P. Nowak and B. Szafran, and F. M. Peeters, *Phys. Rev. B* **86**, 125428 (2012).
- ²⁶O. Voskoboynikov, C. P. Lee, and O. Tretyak, *Phys. Rev. B* **63**, 165306 (2001); C. F. Destefani, S. E. Ulloa, and G. E. Marques, *ibid.* **69**, 125302 (2004).
- ²⁷The obtained energy shift is twice as small as the one obtained for two-dimensional systems in Ref. 28.
- ²⁸M. Valín-Rodríguez, A. Puente, and L. Serra, *Phys. Rev. B* **69**, 085306 (2004).
- ²⁹In general, the form of λ_N and κ_N can be provided for any confinement potential for which the analytical form of the wave functions is known, in particular for the harmonic-oscillator potential.
- ³⁰C. E. Pryor and M. E. Flatté, *Phys. Rev. Lett.* **96**, 026804 (2006).

11 Spontaneous and resonant lifting of the spin blockade in nanowire quantum dots

Spontaneous and resonant lifting of the spin blockade in nanowire quantum dots

M. P. Nowak and B. Szafran

AGH University of Science and Technology, Faculty of Physics and Applied
Computer Science,
al. Mickiewicza 30, 30-059 Kraków, Poland

E-mail: michal.nowak@fis.agh.edu.pl

Abstract. A complete description of the dynamics of a two-electron system confined in narrow nanowire quantum dots under oscillating electric field and phonon mediated relaxation is presented in the context of recent electric dipole spin resonance experiments. We find that spin-orbit coupling results in lifting the spin blockade by phonon mediated relaxation provided that the initial state is close in energy to the ground state. At higher magnetic field, after singlet-triplet anticrossing new channel for lifting the Pauli blockade opens which results in an appearance of additional resonance lines, as present in recent experimental results.

PACS numbers: 73.21.La, 03.67.Lx, 71.70.Gm, 75.70.Tj, 81.07.Ta, 63.22.Gh

1. Introduction

Coherent spin control is one of the prerequisites for creation of a solid-state quantum computer operating on spin qubits. In recent years gate defined nanowire [1] double quantum dots have been successfully used for experimental demonstration [2, 3, 4, 5, 6, 7, 8] of electrical control of single spins [9]. The spin rotations are performed by means of electric dipole spin resonance (EDSR) where spin-orbit (SO) interaction [10, 11] is used to electrically control the spin excluding the need for oscillating magnetic field in the device [12]. The spin oscillations are probed exploiting the spin blockade [20] of two-electron system where the current cycle $(0, 1) \rightarrow (1, 1) \rightarrow (0, 2) \rightarrow (0, 1)$ [the numbers denote number of electrons in the adjacent quantum dots] is blocked at the $(1, 1) \rightarrow (0, 2)$ transition when the spin configurations of the $(1, 1)$ and $(0, 2)$ states do not match. For low bias the only available $(0, 2)$ state is the spin singlet so the current is blocked if the system is initialized in one of the spin-polarized triplets. The blockade is lifted when the spin of oscillating electron is rotated such the total spin of the $(1, 1)$ state is changed from $S = 1$ to $S = 0$. Relaxation of the $(1, 1)$ state that follows the spin rotation opens the tunneling of the single electron through the double dot and is mediated by phonons that disperse the excess energy between the $(1, 1)$ and $(0, 2)$ states.

Strong SO coupling in InSb and InAs nanowires that is useful for effective control of the spins leads to spin relaxation [14, 15, 16] that results in lifting the spin blockade, limits the available magnetic fields for the EDSR [17] and results in the leakage current that exhibit dips or peaks at low magnetic field depending on the interdot coupling [18]. In the present work we study phonon mediated electron relaxation in electrically driven nanowire quantum dots. We find several unexpected features that are crucial for the mechanism of the spin blockade lifting: *i*) in all regions where the spin conserving $(1, 1) \rightarrow (0, 2)$ relaxation occurs the spin non-conserving relaxation from $(1, 1)$ triplet state with spins polarized along the magnetic field is of a very similar effectiveness. *ii*) For small magnetic fields where $(0, 2)$ singlet is the ground state this leads to the spontaneous lifting of the spin blockade from this triplet. *iii*) On the other hand the relaxation from triplet with spins oriented antiparallel to the magnetic field orientation is two orders of magnitude slower so the blockade is maintained. *iv*) At higher magnetic fields when the triplet becomes the ground state spin rotation accompanied by charge redistribution results in lifting spin blockade through direct transition to $(0, 2)$ singlet which is visible in recent experimental map [5].

Experiments with lifting the pauli blockade are performed in external magnetic field to induce the Zeeman splitting of electron energy levels. Since the Zeeman splitting of the nuclear levels is much smaller, the direct exchange of spins between the electron and the nuclei is suppressed. Changes of the nuclear field takes place in 10-100 microsecond [19] while in the present work we focus on the spin evolution in a time scale of order of tenths on nanoseconds. For that reason we do not consider effects of nuclear spin dynamics [5, 17, 20, 21, 22].

2. Theory

The considered two-electron system is described by the Hamiltonian $H(t) = \sum_i h^i(t) + e^2/(4\pi\epsilon\epsilon_0|\mathbf{r}_1 - \mathbf{r}_2|)$ where $h^i(t)$ is single electron energy operator. For a narrow nanowire the charge occupies ground state of lateral quantization (here taken in the Gaussian form $\psi(y, z) = (\sqrt{\pi}l)^{-1} \exp[-(y^2 + z^2)/2l^2]$, with $l = 20$ nm) which leads [23] to the two-electron Hamiltonian,

$$H_{1D}(t) = h_{1D}^1(t) + h_{1D}^2(t) + \frac{\sqrt{\pi/2}}{4\pi\epsilon_0\epsilon l} \operatorname{erfcx} \left[\frac{|x_1 - x_2|}{\sqrt{2}l} \right], \quad (1)$$

with single-electron energy operator

$$h_{1D}(t) = \frac{\hbar^2 k_x^2}{2m^*} + V(x, t) - \alpha\sigma_y k_x + \frac{1}{2}\mu_B g(x) B\sigma_x, \quad (2)$$

where $\hbar k_x = -i\hbar\nabla_x$ is momentum operator and $H_{SO1D} = -\alpha\sigma_y k_x$ stands for Rashba SO coupling which results from averaging the $H_{SO} = \alpha(\sigma_x k_y - \sigma_y k_x)$ Hamiltonian in the y -direction. We allow for position dependent g -factor in the device [2, 4, 5] and take $g(x) = g[1 + \beta H(x)]$ where $H(x)$ is Heavyside step function and $\beta = 0.1$ – g -factor in the right dot is 1.1 of the value in the left dot. The potential is separated into $V(x, t) = V_{QD}(x) + V'(x, t)$ where quantum dot confinement is described by $V_{QD}(x) = V_c(x) + eF_{bias}x$. V_c defines potential of two quantum dots of 138 nm width each separated by potential barrier of 25 nm width and 40 meV height. The driving AC electric field is assumed active in the left dot [2], so the time dependent part of the potential takes the form $V'(x, t) = eF_{AC}x f(x) \sin(\omega_{AC}t)$ where $f(x) = 1$ in the left dot and 0 outside – see the inset to Figure 1(a).

For the description of two-electron electric dipole spin resonance we first obtain the initial states for the time evolution. We calculate eigenstates of the Hamiltonian (1) for $t = 0$ using configuration interaction scheme where the n -th two-electron spin-orbital is constructed in a basis consisting slater determinants, i.e.,

$$\Psi^n(x_1, \sigma_1, x_2, \sigma_2, t = 0) = \sum_i^N \sum_{j=i+1}^N A_{ij}^n [\psi_i(x_1, \sigma_1, t = 0)\psi_j(x_2, \sigma_2, t = 0) - \psi_i(x_2, \sigma_2, t = 0)\psi_j(x_1, \sigma_1, t = 0)] \quad (3)$$

where the coefficients A_{ij}^n are found by diagonalization of Hamiltonian (1). Spin-orbitals $\psi(x, \sigma, t = 0)$ are found by exact diagonalization of $h_{1D}(t = 0)$ on a mesh with $N = 2 \times 201$ points. We use basis consisting of $N = 50$ single-electron orbitals which provides accuracy of two-electron energy levels better than $0.5 \mu\text{eV}$.

Time evolution is performed using time dependent perturbation theory. The two-electron Hamiltonian is separated into,

$$H_{1D}(t) = H_{1D} + H'_{1D}(t), \quad (4)$$

where H_{1D} is the time independent part and $H'_{1D}(t) = eF_{AC}[x_1 f(x_1) + x_2 f(x_2)] \sin(\omega_{AC}t)$ contains oscillating electric field F_{AC} .

The eigenstates $\Psi^n(x_1, \sigma_1, x_2, \sigma_2, t = 0)$ (with corresponding eigenenergies E^n) of Hamiltonian (1) are used for construction of a basis for time evolution where the two-electron spinor is expressed as

$$\Psi(x_1, \sigma_1, x_2, \sigma_2, t) = \sum_n^N c_n(t) \exp(-iE_n t/\hbar) \Psi^n(x_1, \sigma_1, x_2, \sigma_2, t = 0) \quad (5)$$

and the time evolution of each coefficient c_n is described by the equation

$$\frac{d}{dt} c_n(t) = -\frac{i}{\hbar} \sum_{m=1}^N c_m(t) \langle \Psi^n | H'_{1D}(t) | \Psi^m \rangle. \quad (6)$$

We use $N = 20$ basis states which provides agreement between the time evolution described above with an exact solution of the time dependent Schrödinger equation in the described system.

To describe the phonon mediated relaxation we allow for the transitions between the two-electron states with a rate given by the Fermi golden rule. The relaxation rate between the initial Ψ^i and final Ψ^f states is described by,

$$\tau_{if}^{-1} = \frac{2\pi}{\hbar} \sum_{\nu, i=1,2} \int_{\mathbf{q}} dq |M_{\nu}(\mathbf{q})|^2 \times |\langle \Psi^f | e^{-i\mathbf{q}\cdot\mathbf{r}_i} | \Psi^i \rangle|^2 \delta(|E^f - E^i| - E_q), \quad (7)$$

where the phonon dispersion relation is $E_q = \hbar c_{\nu} |\mathbf{q}|$ and c_{ν} is the sound velocity. The sum in (7) goes over three types of electron-phonon scattering (ν) due to: deformation potential with longitudinal mode[24] ($\nu = \text{LA-DP}$) with,

$$|M_{\text{LA-DP}}(\mathbf{q})|^2 = \frac{\hbar D^2}{2d c_{\text{LA}}} |\mathbf{q}|, \quad (8)$$

where D stands for the crystal acoustic deformation potential constant, d is density, and c_{LA} is sound velocity of phonon LA mode. Electron-LA phonon scattering due to the piezoelectric field [25] ($\nu = \text{LA-PZ}$),

$$|M_{\text{LA-PZ}}(\mathbf{q})|^2 = \frac{32\pi^2 \hbar e^2 h_{14}^2 (3q_x q_y q_z)^2}{\varepsilon^2 d c_{\text{LA}} |\mathbf{q}|^7}, \quad (9)$$

where h_{14} is PZ constant and electron-TA phonon scattering due to the piezoelectric field ($\nu = \text{TA-PZ}$),[25]

$$|M_{\text{TA-PZ}}(\mathbf{q})|^2 = 2 \times \frac{32\pi^2 \hbar e^2 h_{14}^2}{\varepsilon^2 d c_{\text{TA}}} \left| \frac{q_x^2 q_y^2 + q_y^2 q_z^2 + q_z^2 q_x^2}{|\mathbf{q}|^5} - \frac{(3q_x q_y q_z)^2}{|\mathbf{q}|^7} \right|, \quad (10)$$

where the multiplication by two results from two transverse phonon modes.

The relaxation is included into time dependent calculation such the amplitude $|c_n(t)|^2$ of each eigenstate is changed due to relaxation *to* all lower energy states and is increased due to relaxation *from* higher energy states with corresponding transition rates τ_{if} :

$$|c_n(t + \Delta t)|^2 = |c_n(t)|^2 + \sum_{m=n+1}^N \tau_{mn}^{-1} |c_m|^2 \Delta t - \sum_{m=1}^{n+1} \tau_{nm}^{-1} |c_n|^2 \Delta t. \quad (11)$$

This corresponds to 0K temperature where the energy instantly disperses and results in a half-life time of an i 'th state defined as $T_{1/2} = \ln(2)/\tau_{if}$ due to relaxation to f 'th state.

We assume material parameters for InSb, i.e. electron effective mass $m^* = 0.014$, $g = -51$, dielectric constant $\varepsilon = 16.5$ and take the Rashba constant $\alpha = 10$ meVnm. The AC field amplitude $F_{AC} = 0.05$ kV/cm is assumed. For calculation of phonon mediated relaxation we take [26] $D = 5775$ kg/m³, $h_{14} = 1.41 \times 10^9$ V/m after [25] and we take sound velocities: $c_{LA} = 3.9 \times 10^3$ m/s after [27] and $c_{TA} = 1.9 \times 10^3$ m/s from [28].

3. Results

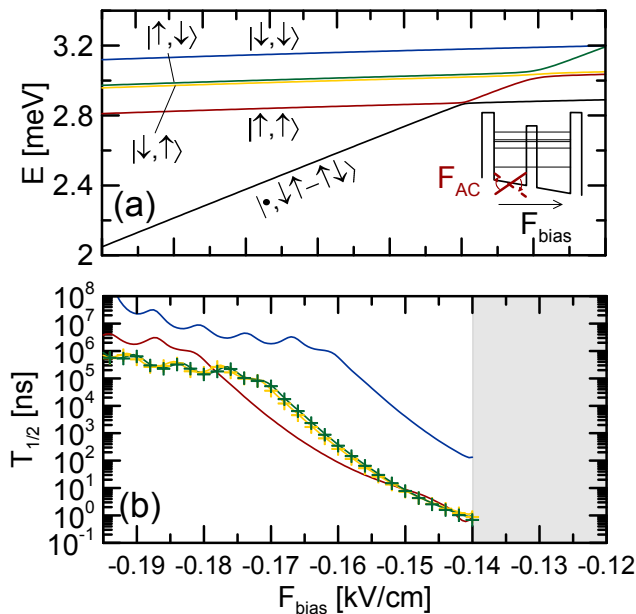


Figure 1. (a) Energy levels of two-electron double quantum dot as a function of bias electric field for $B = 50$ mT in the presence of spin-orbit interaction. The arrows present approximate spin polarization of electrons in the dots. The inset present schematics of the considered confinement potential. (b) Half-life time of excited states due to phonon mediated relaxation to the (0,2) singlet state. The colors of curves denote initial state of relaxation. The symbols (curves) corresponds to the results obtained without (with) SO interaction.

The charge distribution in the double dot is controlled by external voltages applied along the structure. Figure 1(a) presents the lowest part of the energy spectrum (the subsequent energy levels – of (0,2) triplets – are above 5 meV) as a function of bias electric field for $B = 50$ mT. For the most negative values of F_{bias} the ground state is a singlet $|\bullet, \downarrow\uparrow - \uparrow\downarrow\rangle$ state for which both electrons reside in the right dot [(0,2) configuration]. The four excited states correspond to single occupancy of each dot [(1,1) configuration] and energy of those states only weakly change as a function of bias electric

field. The two close in energy states, i.e. $|\downarrow, \uparrow\rangle$ and $|\uparrow, \downarrow\rangle$ correspond to definite and opposite spin configurations in each dot (i.e., in the $|\downarrow, \uparrow\rangle$ state spin of the electron in the right dot – where the g -factor takes the highest value – is polarized along the magnetic field) resulting from mixing spin-zero triplet with singlet state by the g -factor mismatch between the dots. The two triplets $|\uparrow, \uparrow\rangle$, $|\downarrow, \downarrow\rangle$ are split by Zeeman interaction.

Let us inspect relaxation times of the four excited (1,1) states. In Figure 1(b) we present half-life times of excited states due to relaxation to the ground state singlet. In the absence of SO interaction phonon scattering couples only states with the same total spin. Only the half-life times of $|\uparrow, \downarrow\rangle$ and $|\downarrow, \uparrow\rangle$ have finite values and they are presented with the crosses in Figure 1(b). At low values of F_{bias} the times are of order of milliseconds but when the energy differences between the initial states and (0,2) singlet become lower the half-life times rapidly drop allowing for (1, 1) \rightarrow (0, 2) spin-conserving relaxation within nanoseconds for $F_{bias} > -0.16$ kV/cm.

When SO coupling is included the spin polarization of the states becomes only approximate. The relaxation times of $|\downarrow, \uparrow\rangle$ and $|\uparrow, \downarrow\rangle$ states do not change – see the curves and crosses in Figure 1(b). However now relaxation from all the (1,1) states to (0,2) singlet is open. For most negative values of F_{bias} half-life time of triplet states is longer than tenths of milliseconds but when the bias field is increased the half-life time of $|\uparrow, \uparrow\rangle$ triplet becomes about the same as the two spin opposite states lifting the spin blockade. Only the $|\downarrow, \downarrow\rangle$ state remains effectively blocked with relaxation time longer by two orders of magnitude from the rest of the (1,1) states.

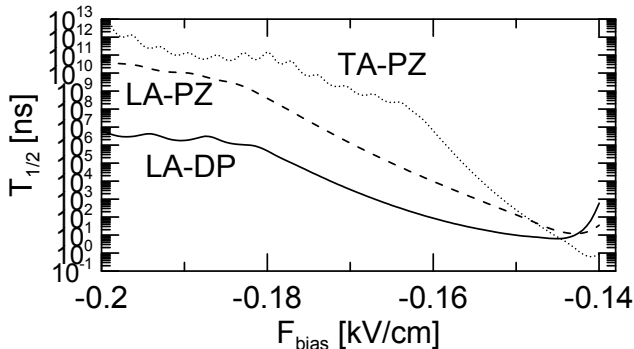


Figure 2. Half-life time of the $|\uparrow, \uparrow\rangle$ due to relaxation to ground state singlet mediated by different electron-phonon scattering types.

In Figure 2 we present impact of the individual electron-phonon coupling types on the relaxation time of the $|\uparrow, \uparrow\rangle$ to the $|\bullet, \downarrow\uparrow - \uparrow\downarrow\rangle$ state. We observe that LA-DP scattering dominates for almost all values of F_{bias} . Only when the energy separation between $|\uparrow, \uparrow\rangle$ triplet and the $|\bullet, \downarrow\uparrow - \uparrow\downarrow\rangle$ singlet becomes small [see Figure 1(a)] the TA-PZ term starts to dominate giving half-life times $T_{1/2} \simeq 1$ ns.

Discussed lifting of the blockade from $|\uparrow\uparrow\rangle$ triplet is not specific to particular parameters as we checked for different strengths of SO coupling and the dot size. We calculated half-life times of excited states as a function of bias voltage for different value of spin-orbit coupling strength [see Figures 3(a),(d)], length of the dots [see

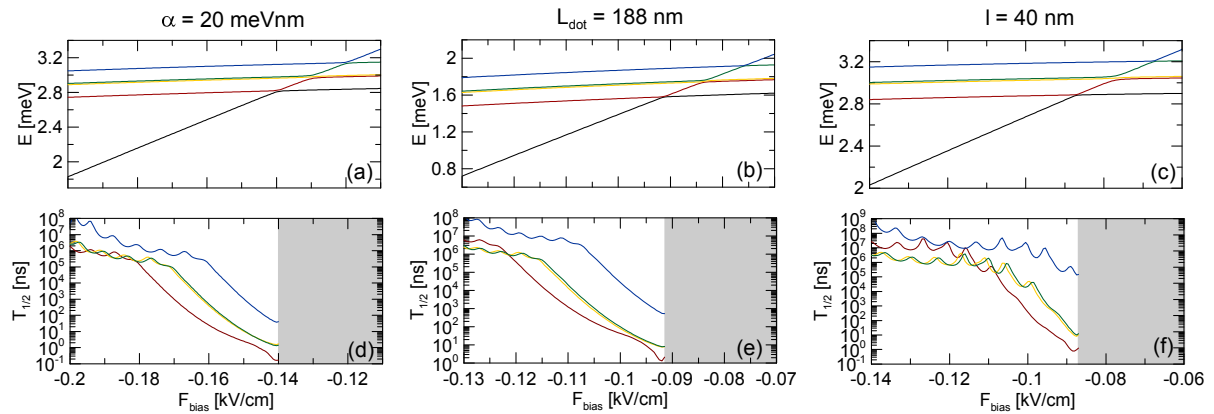


Figure 3. Lowest part of the energy spectrum obtained for (a) spin-orbit interaction constant increased to $\alpha = 20$ meVnm (b) length of each dot increased by 50 nm and (c) increased radius of the nanowire that results in an spread of wavefunction in the lateral direction such $l = 40$ nm. (d)-(f) present half-life times of excited states due to relaxation to ground state singlet $|\bullet, \downarrow\uparrow - \uparrow\downarrow\rangle$ obtained for parameters corresponding to upper plots.

Figures 3(b),(e)] and the nanowire radius that controls the spread of lateral gaussian wavefunction [see Figures 3(c),(f)]. We observe that in each case the situation is generally the same as described previously, i.e., either the relaxation from all excited states is at least of order of milliseconds or the relaxation from $|\uparrow, \uparrow\rangle$ triplet state with spins polarized along the magnetic field is faster than relaxation from $|\downarrow, \uparrow\rangle$ and $|\uparrow, \downarrow\rangle$ states effectively lifting the spin blockade from the former.

The experimental studies [7] report spin coherence time of order of tenths nanoseconds and coherent manipulation over a single spin up to 100 ns. We therefore focus on F_{bias} range where the relaxation times are of order of tenths of nanoseconds – hereafter we take $F_{bias} = -0.15$ kV/cm – that allow for deblocking of single-electron current through the double dot after spin rotation in EDSR experiments. In Figure 4(a) we plot energy levels as a function of the magnetic field B . For $B = 0$ the excited state is fourfold degenerate due to high interdot barrier – negligible exchange coupling. When the magnetic field is increased the energy levels of the two spin polarized triplets $|\uparrow, \uparrow\rangle$ and $|\downarrow, \downarrow\rangle$ are split by the Zeeman interaction. On the other hand the energy levels of the two spin-opposite states – $|\downarrow, \uparrow\rangle$ and $|\uparrow, \downarrow\rangle$ – are weakly split due to g -factor mismatch in the dots. At $B = 0.1$ T an anticrossing between the energy levels of triplet $|\uparrow, \uparrow\rangle$ and (0, 2) singlet states appear followed by the change of the ground state.

Figure 4(b) presents half-life times of excited states due to relaxation to (0,2) singlet. We observe that the relaxation from spin antiparallel $|\downarrow, \uparrow\rangle$ and $|\uparrow, \downarrow\rangle$ states occurs within few nanoseconds regardless of B value. As the energy separation between energy levels of $|\uparrow, \uparrow\rangle$ and (0,2) singlet decreases the relaxation time drops and after $B = 50$ mT the half-life time of this state is even lower than the half-life time of spin-antiparallel states. On the other hand relaxation from $|\downarrow, \downarrow\rangle$ state is slow and the half-life time grows for increasing magnetic field until $B = 0.1$ T. This shows that for magnetic field

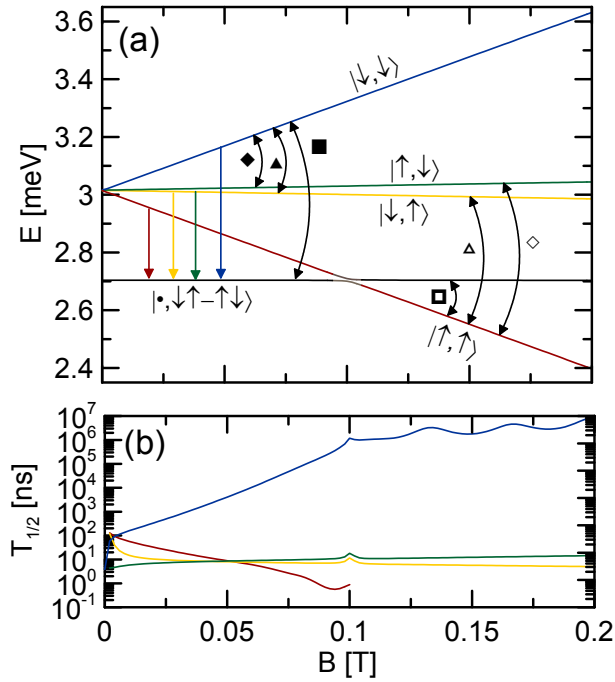


Figure 4. (a) Energy spectrum as a function of the magnetic field. Straight arrows denote transitions due to phonon relaxation. Curved arrows depict available EDSR resonances from the triplets. (b) Half-life time of excited states due to phonon mediated relaxation. Results obtained for $F_{bias} = -0.15$ kV/cm.

range before the anticrossing only the $|\downarrow, \downarrow\rangle$ triplet provides spin blockade as the $|\uparrow, \uparrow\rangle$, $|\downarrow, \uparrow\rangle$ and $|\uparrow, \downarrow\rangle$ states decay quickly into $|\bullet, \downarrow\uparrow - \uparrow\downarrow\rangle$.

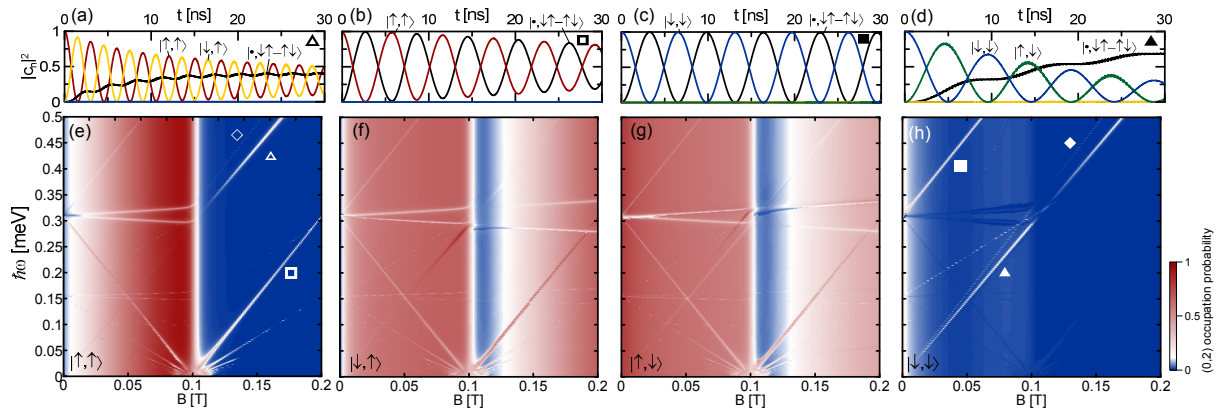


Figure 5. (a)-(d) Transitions between the eigenstates during the time evolution at the resonances marked with the symbols. (e)-(h) Probability of (0,2) occupation averaged during the 30 ns time evolution obtained for subsequent (1,1) states taken as the initial state of the time evolution – the spin configuration of the initial state is denoted in the left bottom corner of each plot.

In EDSR experiments the two-electron system can initialize in any of the low energy states within the transport energy window. We therefore study the time evolution taking

each of the (1,1) states with the energy levels depicted in Figure 4(a) as an initial state. In Figure 5(e)-(h) we present (0,2) occupation probability (which would allow for tunneling of one of the electrons outside the dot lifting the blockade) averaged during 30 ns time evolution as a function of the magnetic field and the electric field frequency.

For $|\uparrow\uparrow\rangle$ taken as the initial state the probability is presented in Figure 5(e). At the left part of the map we observe increasing probability in the background as a function of B due to spin relaxation that results in spontaneous lifting of spin blockade. At $B = 0.1$ T the phonon mediated spin-orbit relaxation to singlet (0,2) from $|\uparrow, \uparrow\rangle$ stops as the latter becomes the ground state – the background of the plot shows nearly zero (0,2) occupation probability. However we observe several resonance lines with an increased probability. The resonance line (Δ) corresponds to the spin rotation in the left dot ($|\uparrow, \uparrow\rangle \rightarrow |\downarrow, \uparrow\rangle$) accompanied by the phonon mediated relaxation to the $|\bullet, \downarrow\uparrow - \uparrow\downarrow\rangle$ singlet which results in an increase of the (0,2) occupation probability – see Figure 5(a) where we present the probability $|c_n|^2$ of finding the system in the n 'th state during the time evolution. The (\diamond) transition is related to the spin rotation in the right dot which is much less effective due to presence of the AC electric field only in the left dot and high interdot barrier which results in a narrow resonance line. The bottom line marked with (\square) corresponds to the direct transition to the (0,2) singlet that involves charge reconfiguration between the dots – see Figure 5(b). Note that line of increased probability due to $|\uparrow, \uparrow\rangle \rightarrow |\bullet, \downarrow\uparrow - \uparrow\downarrow\rangle$ transition is not observed for $B < 0.1$ T as in this region the spin relaxation of the triplet results in its fast deexcitation to the ground state with rate that exceeds the EDSR transition.

In Figures 5(f), (g) one can observe mainly nonzero (0,2) occupation probabilities due to fast spin-conserving relaxation of $|\downarrow, \uparrow\rangle$ and $|\uparrow, \downarrow\rangle$ to the $|\bullet, \downarrow\uparrow - \uparrow\downarrow\rangle$ state as discussed previously. In fact this relaxation is fast enough that one can observe lines of lowered probability when the system already relaxes into singlet (0,2) and is driven back to one of the excited states.

For the $|\downarrow, \downarrow\rangle$ triplet taken as the initial state outside the resonances the (0,2) occupation probability is nearly zero at Figure 5(h) as the phonon mediated relaxation from this state is slow – see the blue curve in Figure 4(b). The lines that go through the diagonal of the plot – (\blacklozenge), (\blacktriangle) – corresponds to the transition to the $|\downarrow, \uparrow\rangle$ and $|\uparrow, \downarrow\rangle$ states respectively accompanied by relaxation to $|\bullet, \downarrow\uparrow - \uparrow\downarrow\rangle$ [see Figure 5(d)] and the line at the left upper part of the plot – (\blacksquare) – is a direct transition to the (0,2) singlet that does not involve phonon mediated relaxation [see Figure 5(c)].

Note that in maps of Figure 5(a) and (d) also lines of increased probability at the half frequency of the (\square) and (\blacksquare) transitions are visible which is due to resonant harmonic generation by the driven electrons [29].

The experimentally [5] measured resonances at current maps are obtained from many sequential events of single electron transport through the structure. In each of them the system can initialize in any of the (1,1) states. We therefore calculate the total probability of (0,2) occupation by summing the results for initial states presented in Figures 5(e)-(h). For each value of B the probability obtained without the oscillating

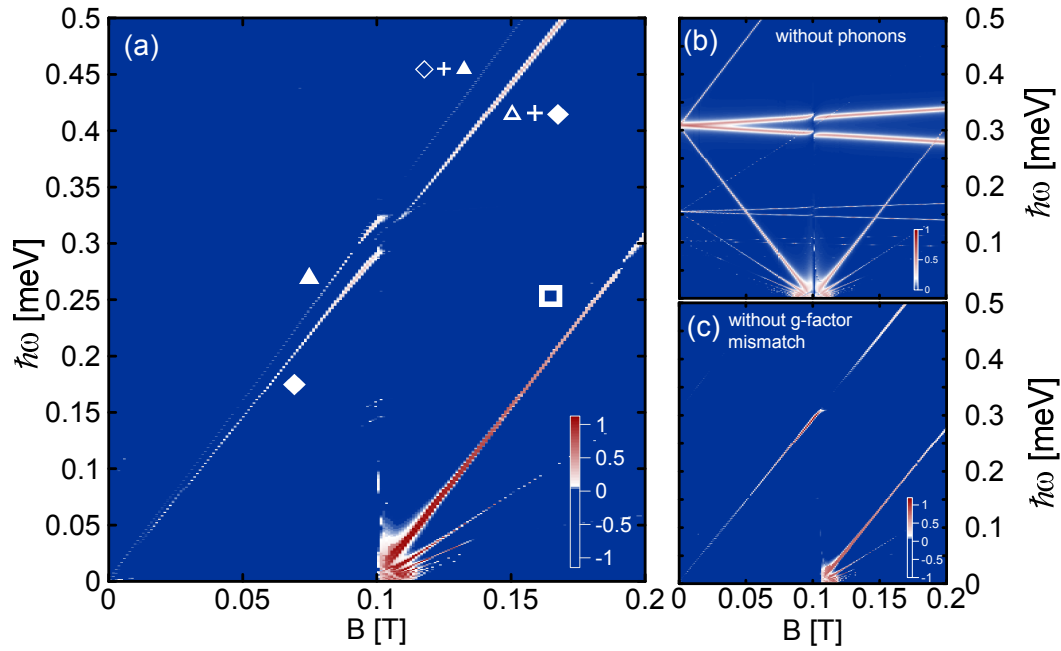


Figure 6. (a) Probability of (0,2) occupation averaged over the 30 ns time evolution calculated as a sum of results obtained for initial states with (1,1) occupation. For each B value the (0,2) occupation probability obtained for $\hbar\omega_{AC} = 0$ (in the absence of driving electric field) was subtracted from the results. (b) Same as (a) but without phonon mediated relaxation. (c) Same as (a) but without g-factor difference between the dots.

electric field (due to pure relaxation) is subtracted to mimic the experimental procedure of [5]. The (0,2) occupation probability is displayed in Figure 6(a). For low values of B we observe two lines at the diagonal of the map that corresponds to the transitions from $|\uparrow, \uparrow\rangle$ state – rotation of the spin down to spin up in the left dot (bright line) or in the right dot (faint line) accompanied by relaxation to (0,2) singlet. After singlet-triplet anticrossing at $B = 0.1$ T the lines correspond to transition from *both* the triplets. At $B = 0.1$ T additional resonance line starts at the bottom of the plot that corresponds to spin rotation with charge reconfiguration from $|\uparrow, \uparrow\rangle$ triplet. Note that there is no similar line corresponding to transition from the $|\downarrow, \downarrow\rangle$ state as it is compensated by the lowered probability obtained for evolution starting from $|\downarrow, \uparrow\rangle$ and $|\uparrow, \downarrow\rangle$.

To better expose the impact of the phonon mediated relaxation on the lifting of the blockade in EDSR we calculated map of (0,2) occupation probability with neglected phonon mediated relaxation and display the results in Figure 6(b). Now all of the resonances correspond to direct transition to S(0,2) induced by the AC electric field. We observe resonance lines which previously [compare with Figure 6(a)] were masked by the *spontaneous* relaxation to the S(0,2) state and are not present in Figure 6(a). Such lines are not present in the experimental maps [2, 3, 4, 5, 6, 7, 8]. Moreover the resonance lines at the diagonal of the plot which are found in all the experimental maps are present exclusively for active phonon mediated relaxation as it allows for the decay of the $|\uparrow, \downarrow\rangle$ and $|\downarrow, \uparrow\rangle$ states to the (0,2) singlet lifting the spin-blockade.

Results of Figure 6(a) seem to be related to the recent experimental work of [5] (Figure 2) that probed wider range on magnetic field as compared with the previous experimental studies [2, 3, 4, 6, 7]. Work [5] deals with EDSR involving dynamical nuclear polarization that compensates for the g -factor gradient within the structure. In such a case the two lines at the diagonal of the plot are merged into a single resonance line as presented in Figure 6(c) due to degeneracy of $|\downarrow, \uparrow\rangle$, $|\uparrow, \downarrow\rangle$ states. Although our modeling neglects the hyperfine field and its changes, our results indicate that the prominent features of the experimental data – in the background of EDSR spectra – are related to the ground-state singlet-triplet transition (the appearance of line that corresponds to (\square) direct transition) that in the present results occurs near $B = 0.1$ T. Note, that the critical B for the singlet-triplet transition in our modeling is lower due to higher value of the g -factor in InSb.

4. Conclusions

In conclusion we have presented the role that spin relaxation and EDSR plays on lifting the spin blockade in coupled nanowire quantum dots using numerical modeling that incorporates EDSR and phonon mediated relaxation. We found that spin relaxation can lead to spontaneous lifting of the spin blockade such that the resonances are observed only from a single spin-blocked triplet state. The change of the ground state in higher magnetic fields leads to spin blockade of both the triplets and reveals additional resonance to the (0,2) singlet that do not involve phonon mediated relaxation and which is present in recent experimental results.

Acknowledgements

This work was supported by the funds of Ministry of Science and Higher Education (MNiSW) for 2012 – 2013 under Project No. IP2011038671, and by PL-Grid Infrastructure. M.P.N. gratefully acknowledges the support from the Foundation for Polish Science (FNP) under START and MPD programme co-financed by the EU European Regional Development Fund.

References

- [1] Fasth C, Fuhrer A, Samuelson L, Golovach V N and Loss D 2007 *Phys. Rev. Lett.* **98** 266801; Pfund A, Shorubalko I, Ensslin K and Leturcq R 2007 *Phys. Rev. B* **76**, 161308(R).
- [2] Nadj-Perge S, Frolov S M, Bakkers E P A M and Kouwenhoven L P 2010 *Nature (London)* **468** 1084.
- [3] Schroer M D, Petersson K D, Jung M and Petta J R 2011 *Phys. Rev. Lett.* **107** 176811.
- [4] Nadj-Perge S, Pribiag V S, van den Berg J W G, Zuo K, Plissard S R, Bakkers E P A M, Frolov S M and Kouwenhoven L P 2012 *Phys. Rev. Lett.* **108** 166801.
- [5] Frolov S M, Danon J, Nadj-Perge S, Zuo K, van Tilburg J W W, Pribiag V S, van den Berg J W G, Bakkers E P A M and Kouwenhoven L P 2012 *Phys. Rev. Lett.* **109** 236805.

- [6] Petersson K D, McFaul L W, Schroer M D, Jung M, Taylor J M, Houck A A and Petta J R 2012 *Nature (London)* **490** 380.
- [7] van den Berg J W G, Nadj-Perge S, Pribiag V S, Plissard S R, Bakkers E P A M, Frolov S M and Kouwenhoven L P 2013 *Phys. Rev. Lett.* **110** 066806.
- [8] Pribiag V S, Nadj-Perge S, Frolov S M, van den Berg J W G, van Weperen I, Plissard S R, Bakkers E P A M and Kouwenhoven L P 2013 *arXiv:1302.2648*.
- [9] Nowack K C, Koppens F H L, Nazarov Yu V and Vandersypen L M K 2007 *Science* **318** 1430.
- [10] Bychkov Y A and Rashba E I 1984 *J. Phys. C* **17** 6039.
- [11] Dresselhaus G 1955 *Phys. Rev.* **100** 580.
- [12] Koppens F H L, Buizert C, Tielrooij K J, Vink I T, Nowack K C, Meunier T, Kouwenhoven L P and Vandersypen L M K 2006 *Nature (London)* **442** 766.
- [13] Ono K, Austing D G, Tokura Y and Tarucha S 2002 *Science* **297** 1313.
- [14] Golovach V N, Khaetskii A and Loss D 2004 *Phys. Rev. Lett.* **93** 016601.
- [15] Stano P and Fabian J 2006 *Phys. Rev. Lett.* **96** 186602.
- [16] Meunier T, Vink I T, Willems van Beveren L H, Tielrooij K-J, Hanson R, Koppens F H L, Tranitz H P, Wegscheider W, Kouwenhoven L P and Vandersypen L M K 2007 *Phys. Rev. Lett.* **98** 126601.
- [17] Pfund A, Shorubalko I, Ensslin K and Leturcq R 2007 *Phys. Rev. Lett.* **99** 036801.
- [18] Danon J and Nazarov Yo V 2009 *Phys. Rev. B* **80** 041301(R).
- [19] Hanson R, Kouwenhoven L P, Petta J R, Tarucha S and Vandersypen L M K 2007 *Rev. Mod. Phys.* **79** 1217.
- [20] Ono K and Tarucha S 2004 *Phys. Rev. Lett.* **92**.
- [21] Rudner M S and Levitov L S 2007 *Phys. Rev. Lett.* **99** 246602; Churchill H O H, Bestwick A J, Harlow J W, Kuemmeth F, Marcos D, Stwertka C H, Watson S K and Marcus C M 2009 *Nature Phys.* **5** 321; Kobayashi T, Hitachi K, Sasaki S and Muraki K 2011 *Phys. Rev. Lett.* **107** 216802; Baugh J, Kitamura Y, Ono K and Tarucha S 2007 *Phys. Rev. Lett.* **99** 096804.
- [22] Johnson A C, Petta J R, Taylor J M, Yacoby A, Lukin M D, Marcus C M, Hanson M P and Gossard A C 2005 *Nature (London)* **435** 925; Koppens F H L, Folk J A, Elzerman J M, Hanson R, van Beveren L H W, Vink I T, Tranitz H P, Wegscheider W, Kouwenhoven L P and Vandersypen L M K 2005 *Science* **309** 1346.
- [23] Bednarek S, Szafran B, Chwiej T and Adamowski J 2003 *Phys. Rev. B* **68** 045328.
- [24] Bockelmann U 1994 *Phys. Rev. B* **50** 17271.
- [25] Climente J I, Bertoni A, Goldoni G and Molinari E 2006 *Phys. Rev. B* **74** 035313.
- [26] Tsidilkovskii I M, Demchuk K M 1971 *Phys. Stat. Sol. (b)* **44** 293; Demchuk K M, Tsidilkovskii I M 1977 *Phys. Stat. Sol. (b)* **82** 59; Tukioka K 1991 *Jpn. J. Appl. Phys.* **30** 212.
- [27] Hebboul S E and Wolfe J P 1986 *Phys. Rev. B* **34** 3948.
- [28] *Group IV Elements, IV-IV and III-V Compounds. Part a - Lattice Properties Landolt-Börnstein - Group III Condensed Matter* Volume 41A1a 2001 pp 1-6.
- [29] Nowak M P, Szafran B and Peeters F M 2012 *Phys. Rev. B* **86** 125428.

References

- [1] S. Tarucha, D. G. Austing, T. Honda, R. G. van der Hage, and L.P. Kouwenhoven, *Shell Filling and Spin Effects in a Few Electron Quantum Dot*, Phys. Rev. Lett. **77**, 3613 (1996).
- [2] P. W. Shor, *Polynomial-Time Algorithms for Prime Factorization and Discrete Logarithms on a Quantum Computer*, Proceedings, 35th Annu. Symp. on the Foundations of Computer Science, 124 (1994).
- [3] L. K. Grover, *A fast quantum mechanical algorithm for database search*, Proceedings, 28th Annual ACM Symposium on the Theory of Computing, 212 (1996).
- [4] D. Loss and D. P. DiVincenzo, *Quantum computation with quantum dots*, Phys. Rev. A **57**, 120 (1998).
- [5] J. R. Petta, A. C. Johnson, J. M. Taylor, E. A. Laird, A. Yacoby, M. D. Lukin, C. M. Marcus, M. P. Hanson, and A. C. Gossard, *Coherent Manipulation of Coupled Electron Spins in Semiconductor Quantum Dots*, Science **309**, 2180 (2005).
- [6] F. H. L. Koppens, C. Buizert, K. J. Tielrooij, I. T. Vink, K. C. Nowack, T. Meunier, L. P. Kouwenhoven, and L. M. K. Vandersypen, *Driven coherent oscillations of a single electron spin in a quantum dot*, Nature (London) **442**, 766 (2006).
- [7] Y. A. Bychkov and E. I. Rashba, *Oscillatory effects and the magnetic susceptibility of carriers in inversion layers*, J. Phys. C **17**, 6039 (1984).
- [8] G. Dresselhaus, *Spin-Orbit Coupling Effects in Zinc Blende Structures*, Phys. Rev. **100**, 580 (1955).
- [9] Y. Kanai, R. S. Deacon, S. Takahashi, A. Oiwa, K. Yoshida, K. Shibata, K. Hirakawa, Y. Tokura, and S. Tarucha, *Electrically tuned spin-orbit interaction in an InAs self-assembled quantum dot*, Nature Nanotechnology **6**, 511 (2011).
- [10] B. Szafran, M. P. Nowak, S. Bednarek, T. Chwiej, and F. M. Peeters, *Selective suppression of Dresselhaus or Rashba spin-orbit coupling effects by the Zeeman interaction in quantum dots*, Phys. Rev. B **79**, 235303 (2009).

-
- [11] L. Meier, G. Salis, I. Shorubalko, E. Gini, S. Schön, and K. Ensslin, *Measurement of Rashba and Dresselhaus spin-orbit magnetic fields*, Nature Physics **3**, 650 (2007).
- [12] C. Fasth, A. Fuhrer, L. Samuelson, V. N. Golovach, and D. Loss, *Direct Measurement of the Spin-Orbit Interaction in a Two-Electron InAs Nanowire Quantum Dot*, Phys. Rev. Lett. **98**, 266801 (2007).
- [13] A. Pfund, I. Shorubalko, K. Ensslin, and R. Leturcq, *Spin-state mixing in InAs double quantum dots*, Phys. Rev. B **76**, 161308(R) (2007).
- [14] S. Takahashi, R. S. Deacon, K. Yoshida, A. Oiwa, K. Shibata, K. Hirakawa, Y. Tokura, and S. Tarucha, *Large Anisotropy of the Spin-Orbit Interaction in a Single InAs Self-Assembled Quantum Dot*, Phys. Rev. Lett. **104**, 246801 (2010).
- [15] K. C. Nowack, F. H. L. Koppens, Yu. V. Nazarov, and L. M. K. Vandersypen, *Coherent Control of a Single Electron Spin with Electric Fields*, Science **318**, 1430, (2007).
- [16] A. V. Khaetskii and Y. V. Nazarov, *Spin relaxation in semiconductor quantum dots*, Phys. Rev. B **61**, 12639 (2000).
- [17] V. N. Golovach, A. Khaetskii, and D. Loss, *Phonon-Induced Decay of the Electron Spin in Quantum Dots*, Phys. Rev. Lett. **93**, 016601 (2004).
- [18] W. Pan, K. Lai, S. P. Bayrakci, N. P. Ong, D. C. Tsui, L. N. Pfeiffer, and K. W. West, *Cyclotron resonance at microwave frequencies in two-dimensional hole system in AlGaAs/GaAs quantum wells*, Appl. Phys. Lett. **83**, 3519 (2003).
- [19] G. Burkard, D. Loss and D. P. DiVincenzo, *Coupled quantum dots as quantum gates*, Phys. Rev. B **59**, 2070 (1999).
- [20] M. P. Nowak, B. Szafran and F. M. Peeters, *Manipulation of two-electron states by the electric field in stacked self-assembled dots*, J. Phys.: Condens. Matter **20**, 395225 (2008).
- [21] K. V. Kavokin, *Anisotropic exchange interaction of localized conduction-band electrons in semiconductors*, Phys. Rev. B **64**, 075305 (2001).

-
- [22] N. E. Bonesteel, D. Stepanenko, and D. P. DiVincenzo, *Anisotropic Spin Exchange in Pulsed Quantum Gates*, Phys. Rev. Lett. **87**, 207901 (2001).
- [23] G. Burkard and D. Loss, *Cancellation of Spin-Orbit Effects in Quantum Gates Based on the Exchange Coupling in Quantum Dots*, Phys. Rev. Lett. **88**, 047903 (2002).
- [24] L. A. Wu and D. A. Lidar, *Universal quantum logic from Zeeman and anisotropic exchange interactions*, Phys. Rev. A **66**, 062314 (2002).
- [25] D. Stepanenko and N. E. Bonesteel, *Universal Quantum Computation through Control of Spin-Orbit Coupling*, Phys. Rev. Lett. **93**, 140501 (2004).
- [26] F. Baruffa, P. Stano, and J. Fabian, *Theory of Anisotropic Exchange in Laterally Coupled Quantum Dots*, Phys. Rev. Lett. **104**, 126401 (2010).
- [27] L. Wang, A. Rastelli, S. Kiravittaya, P. Atkinson, F. Ding, C. C. Bof Bufon, C. Hermannstädter, M. Witzany, G. J. Beirne, P. Michler, and O. G. Schmidt, *Towards deterministically controlled InGaAs/GaAs lateral quantum dot molecules*, New J. Phys. **10**, 045010 (2008).
- [28] T. Chakraborty and P. Pietiläinen, *Electron-electron interaction and the persistent current in a quantum ring*, Phys. Rev. B **50**, 8460 (1994).
- [29] J. I. Climente, J. Planelles, and J. L. Movilla, *Magnetization of nanoscopic quantum rings and dots*, Phys. Rev. B **70**, 081301(R) (2004).
- [30] V. M. Fomin, V. N. Gladilin, S. N. Klimin, J. T. Devreese, N. A. J. M. Kleemans, and P. M. Koenraad, *Theory of electron energy spectrum and Aharonov-Bohm effect in self-assembled $In_xGa_{1-x}As$ quantum rings in GaAs*, Phys. Rev. B **76**, 235320 (2007).
- [31] N. A. J. M. Kleemans, I. M. A. Bominaar-Silkens, V. M. Fomin, V. N. Gladilin, D. Granados, A. G. Taboada, J. M. Garcia, P. Offermans, U. Zeitler, P. C. M. Christianen, J. C. Maan, J. T. Devreese, and P. M. Koenraad, *Oscillatory Persistent Currents in Self-Assembled Quantum Rings*, Phys. Rev. Lett. **99**, 146808 (2007).

-
- [32] J. Splettstoesser, M. Governale, and U. Zülicke, *Persistent current in ballistic mesoscopic rings with Rashba spin-orbit coupling*, Phys. Rev. B **68**, 165341 (2003).
- [33] J. S. Sheng and Kai Chang, *Spin states and persistent currents in mesoscopic rings: Spin-orbit interactions*, Phys. Rev. B **74**, 235315 (2006).
- [34] T. Chwiej and B. Szafran, *Pinning of electron densities in quantum rings by defects: Symmetry constraints and distribution of persistent currents*, Phys. Rev. B **79**, 085305 (2009).
- [35] A. Fuhrer, S. Lüscher, T. Ihn, T. Heinzl, K. Ensslin, W. Wegscheider and M. Bichler, *Energy spectra of quantum rings*, Nature (London) **413**, 822 (2001).
- [36] Y. Aharonov and A. Casher, *Topological Quantum Effects for Neutral Particles*, Phys. Rev. Lett. **53**, 319 (1984).
- [37] P. Földi, B. Molnér, M. G. Benedict, and F. M. Peeters, *Spintronic single-qubit gate based on a quantum ring with spin-orbit interaction*, Phys. Rev. B **71**, 033309 (2005).
- [38] J. Nitta and T. Bergsten, *Time reversal Aharonov–Casher effect using Rashba spin–orbit interaction*, New J. Phys. **9**, 341 (2007).
- [39] P. W. Fry, I. E. Itskevich, D. J. Mowbray, M. S. Skolnick, J. J. Finley, J. A. Barker, E. P. O’Reilly, L. R. Wilson, I. A. Larkin, P. A. Maksym, M. Hopkinson, M. Al-Khafaji, J. P. R. David, A. G. Cullis, G. Hill, and J. C. Clark, *Inverted Electron-Hole Alignment in InAs-GaAs Self-Assembled Quantum Dots*, Phys. Rev. Lett. **84**, 733 (2000).
- [40] S. Nadj-Perge, S. M. Frolov, E. P. A. M. Bakkers and L. P. Kouwenhoven, *Spin–orbit qubit in a semiconductor nanowire*, Nature (London) **468**, 1084 (2010).
- [41] M. D. Schroer, K. D. Petersson, M. Jung, and J. R. Petta, *Field Tuning the g Factor in InAs Nanowire Double Quantum Dots*, Phys. Rev. Lett. **107**, 176811 (2011).

-
- [42] S. Nadj-Perge, V. S. Pribiag, J. W. G. van den Berg, K. Zuo, S. R. Plissard, E. P. A. M. Bakkers, S. M. Frolov, and L. P. Kouwenhoven, *Spectroscopy of Spin-Orbit Quantum Bits in Indium Antimonide Nanowires*, Phys. Rev. Lett. **108**, 166801 (2012).
- [43] K. D. Petersson, L. W. McFaul, M. D. Schroer, M. Jung, J. M. Taylor, A. A. Houck, and J. R. Petta, *Circuit quantum electrodynamics with a spin qubit*, Nature (London) **490**, 380 (2012).
- [44] S. M. Frolov, J. Danon, S. Nadj-Perge, K. Zuo, J. W. W. van Tilburg, V. S. Pribiag, J. W. G. van den Berg, E. P. A. M. Bakkers, and L. P. Kouwenhoven, *Suppression of Zeeman Gradients by Nuclear Polarization in Double Quantum Dots*, Phys. Rev. Lett. **109**, 236805 (2012).
- [45] J. W. G. van den Berg, S. Nadj-Perge, V. S. Pribiag, S. R. Plissard, E. P. A. M. Bakkers, S. M. Frolov, and L. P. Kouwenhoven, *Fast Spin-Orbit Qubit in an Indium Antimonide Nanowire*, Phys. Rev. Lett. **110**, 066806 (2013).
- [46] P. Stano and J. Fabian, *Theory of Phonon-Induced Spin Relaxation in Laterally Coupled Quantum Dots*, Phys. Rev. Lett. **96**, 186602 (2006).
- [47] T. Meunier, I. T. Vink, L. H. Willems van Beveren, K.-J. Tielrooij, R. Hanson, F. H. L. Koppens, H. P. Tranitz, W. Wegscheider, L. P. Kouwenhoven, and L. M. K. Vandersypen, *Experimental Signature of Phonon-Mediated Spin Relaxation in a Two-Electron Quantum Dot*, Phys. Rev. Lett. **98**, 126601 (2007).
- [48] A. Pfund, I. Shorubalko, K. Ensslin, and R. Leturcq, *Suppression of Spin Relaxation in an InAs Nanowire Double Quantum Dot*, Phys. Rev. Lett. **99**, 036801 (2007).
- [49] J. Danon and Yo. V. Nazarov, *Pauli spin blockade in the presence of strong spin-orbit coupling*, Phys. Rev. B **80**, 041301(R) (2009).

